Optical and Plasmonic Coupling in Linear and Nonlinear Regimes

By

Vincent Ng

A thesis submitted to Macquarie University
for the degree of Doctor of Philosophy
Department of Physics and Astronomy
April 2018

MACQUARIE
University
SYDNEY·AUSTRALIA

Contents

Abstract

Surface plasmon polaritons are electromagnetic surface waves that may be excited at the interface between metallic and dielectric materials. They confine light to subwavelength dimensions, and provide large field enhancement, making them useful for creating compact devices and sensing applications. Unfortunately, surface plasmons are difficult to utilise due to their characteristically large losses. They typically have propagation lengths from microns to hundreds of microns. Surface plasmon-to-optical coupling is also challenging, due to the inherent disparity in the size and wavevector of optical and plasmonic modes. In this thesis, we take two approaches to addressing these challenges.

The first approach is to explore second-order nonlinear effects. Nonlinear effects benefit from the plasmon field-enhancement, and can potentially be used to provide gain via parametric amplification. In our study, we experimentally consider the nonlinearity of gold in plasmon-to-plasmon second harmonic generation, as well as the dielectric nonlinearity in lithium niobate. In gold-coated lithium niobate crystals, we explore optical-to-plasmonic processes, using quasi-phase-matching for second harmonic generation, and birefringent phase-matching for parametric down conversion. We find that the large size disparity in optical and plasmonic modes strongly inhibits the efficiency of the nonlinear response, and diminishes the contributions made by phase-matching. We were unable to overcome the plasmonic absorption losses using second-order nonlinear effects in the nanosecond domain.

In our second approach, we consider directional coupling between optical and long-range surface plasmon waveguides using numerical methods. We then consider the design of a three-waveguide device, an adiabatic passage coupler with a plasmonic intermediate waveguide. By the use of a dark state, we show that light can be transported through the plasmonic waveguide without suffering plasmonic loss. This is achieved by supressing the surface plasmon amplitude. An analogous device, a digitised adiabatic passage coupler, is characterised experimentally, verifying the tolerance to loss in that design.

Statement of Candidate

This thesis is submitted in fulfilment of the requirements of the degree of Doctor of Philosophy at Macquarie University and has not previously been submitted for a degree, nor has it been submitted as part of requirements for a degree to any other univeristy or institution other than Macquarie University. I also certify that the thesis is an original piece of research and it has been written by myself. Any help and assistance that I have recieved in my research work and the preparation of the thesis itself have been acknowledged. In addition, I certify that all information sources and literature used are indicated in this thesis.

Vincent Ng

Acknowledgements

I would like to thank my supervisor, Judith Dawes. Your support and guidance helped me keep me on track, and I learnt a lot from your vision. I would also like to thank my co-supervisor David Coutts. Your experience and knowledge in the lab was were indispensable.

James Downes and Adam Joyce assisting me with the deposition of gold films and characterisation using the white light interferometer, respectively. Both were integral parts of my thesis. Thanks you both.

Aravindan M. Warrier, Jipeng Lin and David Spence and Aaron McKay were of great assistance in providing laser sources which made my nonlinear experiments possible. Thank you all.

I would also like to thank my collaborators: Jesse Vaitkus, Andrew Greentree, Mike Steel for their work in the design of the digital adiabatic passage devices, and Zachary Chaboyer for fabricating these devices.

Last, but not least, I would like to thank all the members of the Department: to Carol, Liz and Lisa for helping to keep the whole department running smoothly for most of the time I was here, and to the many academic staff who taught me, and inspired me.

1

Introduction

1.1 Surface Plasmons

Surface plasmon polaritons are electromagnetic surface waves that may be excited at the interface between metallic and dielectric materials. They arise due to the strong coupling between coherent oscillations of conduction band electrons within the metal and the electromagnetic fields that these oscillations generate. The existence of surface plasmon polaritions was first proposed by Sommerfeld [1] in 1899, and then by Zenneck [2] in 1907, in the context of radio waves propagating on metallic surfaces. The experimental demonstration of surface plasmons in the visible domain came much later, in 1968 by Kretschmann and Raether [3], and Otto [4].

Since then, surface plasmon polaritons have been the subject of much study. Surface plasmons are primarily of interest for their small mode sizes and their capacity for field localisation — the fields associated with a surface plasmon are confined to subwavelength dimensions, and provide a pathway to bring optics to the nanoscale. This field confinement makes a plasmon extremely sensitive to small perturbations at the metal's surface, leading to the very successful application of surface plasmons to sensing [5, 6]. The ability to tightly focus electromagnetic fields also makes plasmonics a natural path for generating high field densities. The has resulted in several applications for plasmonics— ranging from the relatively recent developments in plasmonic trapping [7], to the enhancement of optical nonlinearities as used in Surface-Enhanced Raman Spectroscopy (SERS) [8]. Here, the plasmonic hotspots generated on a roughened metal surface are used to enhance the scattered Raman signal by orders of magnitude.

Additionally, there is significant interest in the development of extremely compact on-chip plasmonic devices, as plasmonic waveguides can be fabricated with metal films that are ≈ 100 nm thick. These metallic waveguides could, in principle, support both electronic functions and plasmonic functions simultaneously, and bridge the gap between electronic and photonic devices [9, 10]. To this end, a range of on-chip plasmonic devices has been fabricated: including couplers, splitters and Mach-Zehnder interferometers [11, 12], ring-resonators [13], bragg reflectors [14, 15] and electro-optic modulators [16].

1.1.1 Plasmonic Loss

Unfortunately, there are several challenges associated with developing on-chip plasmonic devices. The first is that surface plasmons characteristically have large losses. Some of the losses are intrinsic, and are ohmic in nature. Other losses are extrinsic, and follow from the extreme sensitivity of the surface plasmon modes. This sensitivity leads to scattering off fabrication defects, such as surface roughness on the metal [17] or nanometer air gap inclusions [18, 19]. As a result of this loss, surface plasmons typically have propagation lengths ranging from microns to hundreds of microns. This constrains the size of devices that can effectively utilise plasmonic phenomena.

A number of studies have been carried out to address these losses [20], which may be divided into passive and active approaches. The passive approach consists of loss mitigation through waveguide engineering. Since a large component of the loss is ohmic in origin, the losses can be reduced by choosing waveguide geometries that redistribute the fields away from the metal. Examples of this approach are the Insulator-Metal-Insulator (IMI) waveguides. Using this approach, plasmonic propagation lengths as long as a centimetre have been reported [21]. Unfortunately, this reduction in loss, is accompanied by a reduction in field confinement, diminishing one of the key advantages of plasmonics[22–24].

In the active approach, gain is introduced into the plasmonic device [25–27]. This is commonly done through the introduction of different gain media. Optically excitable dyes [28–31] and fluorescent polymers [32] have been used. A gain of $420\,\mathrm{cm}^{-1}$ was achieved in [30] using Rhodamine 6G, leading to 30% loss compensation. Complete compensation (and slight gain) was achieved in [31, 32] for less confined long-range surface plasmons, however in [31] the gain began to decay after 5 mins, due to photo-bleaching of the dye. Electrically pumped semiconductors [33, 34] have also been investigated, due to the large gain densities afforded by this approach. This has also lead to the investigation of nanolasers and surface plasmon based lasers (or SPASERs) [35–42]. However, several studies have carried out by Khurgin and Sun [20, 24, 33, 40], call into question the practicality of true SPASER devices (where all interacting fields are plasmonic in nature). In particular, in [33], they demonstrate that for plasmonic configurations with semiconductor gain and subwavelength field confinement, the small mode volume causes a shortening of the recombination rate in the gain, through the Purcell effect. In order to compensate, they predict impractically high current densities in excess of $100\,\mathrm{kA/cm}^2$ are required in order to compensate. And so, despite the breadth of research, the topic of surface plasmon gain is still very much unresolved.

1.1.2 Plasmonic Coupling

The second key challenge that arises is coupling between light and surface plasmons. Surface plasmons are typically characterised by large wavevectors, making optical-to-plasmonic coupling a matter of phase-matching. Coupling is further complicated by the characteristic size-scale difference between optical and plasmonic fields, resulting in a poor mode overlap between the two. Together, these two factors restrict the configurations in which surface plasmons can be optically excited.

There are only a handful of configurations which are commonly used couple light from free space to plasmonic waveguides. These include prism coupling [3] (commonly called the Kretschmann coupling), grating coupling [17, 43] and end-fire coupling [44]. Each of these methods have different requirements and varying levels of coupling efficiency. For an example, Kretschmann coupling provides very efficient coupling to surface plasmons, but also

provides a very efficient route for the plasmons to re-radiate as light, significantly reducing the effective propagation length of the plasmons. Grating coupling provides reliable coupling in a small area, but requires nanostructures to be etched into the plasmonic waveguide. End-fire coupling is versatile, but is only efficient for configurations in which the surface plasmon confinement is weak. Additionally, both Kretschmann and grating coupling are out-of-plane coupling methods, making them difficult to interface with other integrated photonic devices.

The challenge of coupling also has implications for plasmonic detection. There are very few methods for direct plasmon detection, the most notable of them being Scanning Near-field Optical Microscopy (SNOM) [45, 46]. However, for surface plasmons propagating in dielectric materials, such as in integrated nanophotonic devices, or nonlinear dielectric crystals, the nearfields of the surface plasmon are inaccessible. Thus, surface plasmon behaviour must often be verified by far-field optical measurements via the coupling methods outlined above. This is particularly challenging in regimes where the plasmonic signal itself is weak.

1.2 Thesis Scope

In light of the challenges of plasmonic loss and optical-plasmonic coupling, we consider two distinct approaches in this dissertation. The first is an investigation of second-order nonlinear processes, in the form of second harmonic generation and parametric down conversion. The second approach is concerned with directional coupling between optical and plasmonic waveguides, and the application of directional coupling to more complex, three-waveguide devices such as adiabatic passage devices.

1.2.1 Active/Nonlinear Plasmonics

As mentioned above, the field localisation provided by surface plasmons results in enhanced field densities, and this can lead to a corresponding enhancement of optical nonlinear effects. These nonlinear effects offer the prospect of an alternate approach to both surface plasmon amplification and surface plasmon excitation.

The enhancement observed in SERS corresponds to the enhancement of a third-order effect. What is of interest here are second-order effects, which in principle are simpler, and already provide access to useful effects such as parametric down conversion—a process that can provide plasmonic gain. Unlike the cases of gain previously described, the magnitude of this nonlinear response is proportional to the field intensity and thus can potentially benefit from the plasmonic field confinement.

There have been several significant studies which have suggested plasmonic gain via parametric amplification. In one theoretical study [47], a configuration consisting of a guided optical pump (λ = 890.1 nm) and degenerate signal and idler plasmonic fields at (λ = 1780 nm) is studied. This is shown in fig. 1.1 (top), where the dielectric NLD2 corresponds to the nonlinear crystal lithium niobate, and the dielectric NLD1 is a 3 μm thick dielectric spacer on a silver film. In this configuration, with an optical pump of 50 MW/cm and a seed plasmonic signal of 1kW/cm, a plasmonic field amplification of almost 3 orders of magnitude is predicted. In [48], a simpler configuration consisting of plasmonic signal (λ = 850 nm)and idler waves (λ = 2.7625 nm) with an optical side pump (λ = 650 nm) was investigated, shown in fig. 1.1 (bottom). This study predicts an increase in propagation length of one or two orders of magnitude. Unfortunately, both of these studies are theoretical,
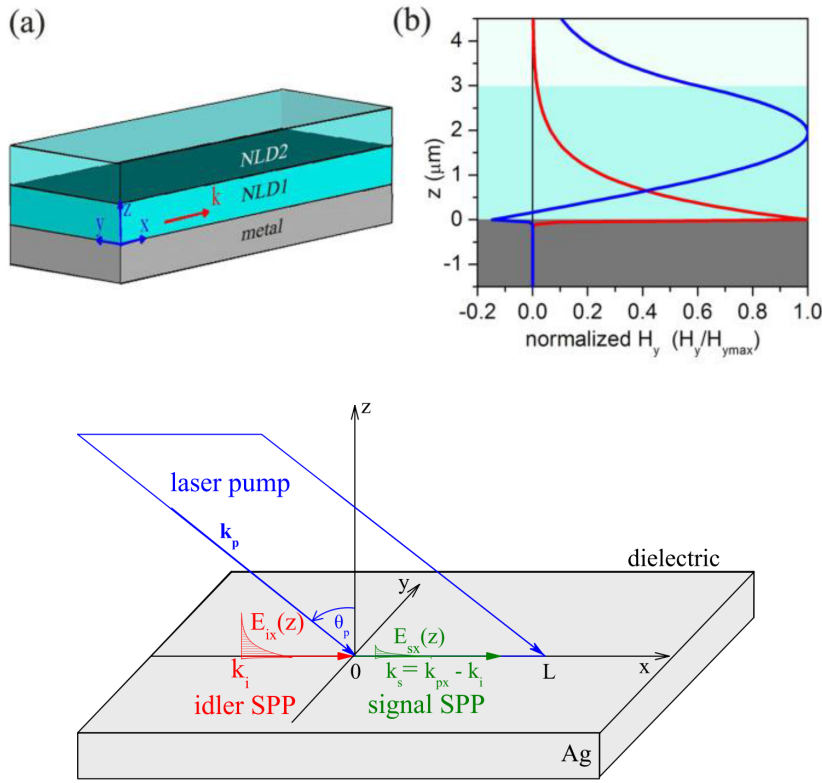
Figure 1.1: (Top) Configuration for parametric down conversion suggested by [47], using a guided optical pump, generating a degenerate down converted plasmon. (Bottom) Configuration for parametric down conversion suggested in [48], consisting of plasmonic signal and idler fields and an optical side pump.

and experimental studies have not emerged.

Many of the studies on second-order nonlinear effects in plasmonics have been instead focussed on plasmonic second harmonic generation, a much simpler effect. Here, there have also been several promising theoretical studies; taking advantage of nonlinearities from metals [49–51], nonlinear dielectrics (often lithium niobate) [52–57], or both [58]. Experimental demonstrations have since followed, using nonlinearities from metals [59–62], dielectrics such as quartz [63–65], polarisable dyes [66], and most recently, organic polymers [67]. However despite these experimental works, the predictions made by the theoretical studies have yet to be realised. This is in part due to the absorption of the harmonic by the metal [68].

This is also in part due to the broader scope of plasmonic nonlinearities; which have to consider the contributions from both plasmonic and optical fields, as well as contributions from metal and dielectric nonlinearities. There are also complications related to the plasmonic dispersion which arise when exciting surface plasmons in materials with a large nonlinear response, as these materials tend to be accompanied by large refractive indices. For these reasons, the topic of second-order nonlinearities in plasmonics is still very much an open topic.

In this dissertation, we investigate second order nonlinear effects, with the intention of introducing parametric gain into plasmonic devices. We investigate the interaction between metal and dielectric nonlinearities, starting with an investigation of the nonlinear metallic

contribution in plasmonic second harmonic generation, before moving onto methods of phase-matching in dielectrics. This latter study consists of a study of optically-pumped second harmonic generation using quasi-phase matching techniques, before moving onto birefringent phase-matching in optically-pumped parametric down conversion.

1.2.2 Plasmonic Directional Coupling and Adiabatic Passage

As an alternate approach to manage the plasmonic loss and phase mismatch, we also conducted a study on coupling between optical and plasmonic waveguides using a directional coupling approach. Directional coupling allows energy to be transferred from one waveguide to another via the overlap of the evanescent fields of the two modes. The main attraction of directional coupling here is that it is an in-phase approach and is compatible with the vision for monolithic nanophotonic devices. Once they have been designed and fabricated, they are also extremely robust. This has resulted in a number of studies investigating all plasmonic directional coupling [69–74] and photonic-plasmonic directional coupling: both theoretical [75–81] and experimental [82–88]. These studies demonstrate effective directional coupling between photonic and plasmonic waveguides of various geometries: some using high index dielectrics[84, 86–88], and some using complex layered dielectric/metallic structures[80, 81] to compensate the plasmonic dispersion. The limiting factor of this coupling approach is that the small plasmonic mode size requires that the waveguides be accurately fabricated, within 100's of nanometres of the specified in size and spacing. Furthermore, since directional coupling occurs over a characteristic distance, it must compete with plasmonic propagation losses. On the other hand, directional coupling can also be extremely useful, particularly as a basis for more complex devices. With additional waveguides, devices with additional functionality can also be constructed. In this work, we study one such device—a three waveguide adiabatic passage device.

An adiabatic passive waveguide device allows light from one waveguide to tunnel to another via an intermediate waveguide by continuous tuning of the coupling coefficients. Adiabatic passage has the particular property that throughout this coupling process, the intermediate waveguide remains dark, consequently making adiabatic passage devices extremely robust against loss or phase-mismatch in this intermediate waveguide. Adiabatic passage was first demonstrated experimentally in waveguide devices in [89], and has been applied to the design of optical couplers [90–95], and splitters [96–99].

Here, in an effort to address phase mismatch and simultaneously mitigate the plasmonic losses, we apply adiabatic passage to optical/plasmonic coupling, considering a geometry consisting of two optical waveguides coupled via an intermediate plasmonic waveguide.

1.3 Thesis Structure

This rest of this dissertation has been set out in 6 chapters:
Chapter 2 provides a review of surface plasmons, their properties and common excitation methods. This is followed by a discussion of plasmonic metals, the fabrication of plasmonic waveguides via the deposition of gold, and the characterisation of these films. Details of numerical modelling using the COMSOL Multiphysics software package are also included.
Chapter 3 provides a review of optical nonlinear effects and a discussion of their application to surface plasmons. Particular attention is drawn to the different behaviour of nonlinearities arising from well behaved nonlinear dielectric crystals, and nonlinearities arising from metal

surfaces, arising from symmetry breaking. The metallic nonlinearity is then utilised in an experimental study of the second-order nonlinear effect, plasmon-to-plasmon second harmonic generation. A strong harmonic response is observed, without phase-matching conditions having been satisfied.

Chapter 4 considers two optically-pumped nonlinear effects, second harmonic generation and parametric down conversion. Here we take advantage of dielectric nonlinearities to introduce phase-matching methods. We utilise quasi-phase matching and birefringent phase matching for the second harmonic and parametric down conversion experiments respectively. In both cases, introduction of phase-matching techniques is offset by the loss of confinement for the optical pump, resulting in the weak nonlinear response. These experiments are followed up by modelling, and the implications for optical gain in plasmonic devices is discussed.

Chapter 5 takes a different approach, considering photonic-plasmonic interactions via directional coupling. A brief overview of Coupled Mode Theory (CMT) is included, before numerically considering the behaviour of directional couplers under phase-mismatch and loss conditions found in plasmonics. This is accompanied a proposed design of a photonic-plasmonic directional coupler, and is characterised simulations carried out in COMSOL.

Chapter 6 provides a review of adiabatic passage couplers, a three waveguide device that is tolerant to phase mismatch and losses. Its performance is considered with respect to plasmonic waveguides, and is contrasted with the performance of the directional coupler proposed in chapter 5. This is followed by measurements of an analogous digital adiabatic passage device, designed by Jesse Vaitkus (RMIT), fabricated by Zachary Chaboyer (Macquarie University), and characterised by myself. These devices demonstrate the remarkable resilience of adiabatic passage devices against loss.

Chapter 7 provides a summary of the key conclusions and provides an outlook on future work.

2

Surface Plasmons: Background and Methods

2.1 Overview of Surface Plasmons
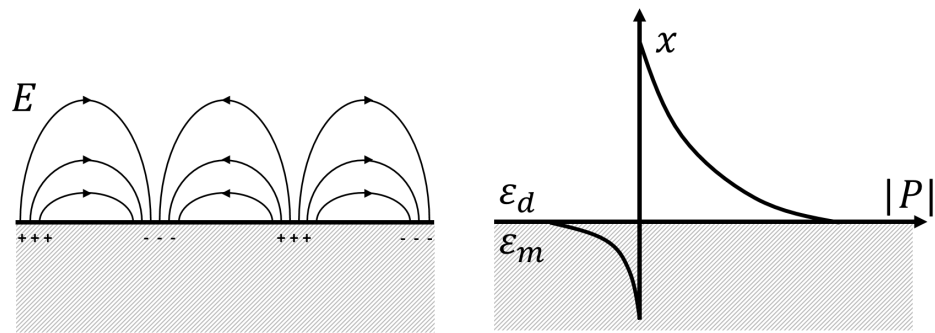
Figure 2.1: Two-dimensional sketch of the surface plasmon, showing the electric field distribution (left) and power density (right).

The behaviour of surface plasmon polaritons has been well characterised in [46, 100]. A surface plasmon polariton is a surface wave that propagates on the surface of metals or conductors. The surface wave is formed by the joint motion of an oscillating electromagnetic field and a corresponding electron density oscillation in the metal. Often, the response of the metal is simply modelled as a negative permittivity material, and in this picture, a surface plasmon may be viewed as an optical surface mode which exists at the interface between positive and negative permittivity materials. By using Maxwell's equations and considering the boundary conditions for such an interface, an expression for a propagating surface plasmon can be found. If we consider a surface plasmon propagating along a metal/dielectric interface in the yz plane, a surface plasmon propagating in the $\hat{z}$ direction can be described by its fields

in the form:

$$\vec{H} = \frac{A}{\mu_0 c} \begin{pmatrix} 0 \\ 1 \\ 0 \end{pmatrix} e^{i(\beta z - \omega t)} e^{-k_x^{(d)} x} \tag{2.1}$$

$$\vec{E} = A \frac{c}{\omega \varepsilon_d} \begin{pmatrix} \beta \\ 0 \\ -i k_x^{(d)} \end{pmatrix} e^{i(\beta z - \omega t)} e^{-k_x^{(d)} x} \tag{2.2}$$

in the dielectric, and

$$\vec{H} = \frac{A}{\mu_0 c} \begin{pmatrix} 0 \\ 1 \\ 0 \end{pmatrix} e^{i(\beta z - \omega t)} e^{k_x^{(m)} x} \tag{2.3}$$

$$\vec{E} = A \frac{c}{\omega \varepsilon_m} \begin{pmatrix} \beta \\ 0 \\ -i k_x^{(m)} \end{pmatrix} e^{i(\beta z - \omega t)} e^{k_x^{(m)} x} \tag{2.4}$$

where $\varepsilon_{d,m}$ is the permittivity in the dielectric and metal. The equations describing the surface plasmons are written differently than in [46, 100], as we've chosen to work in SI units, and we've written the scalar plasmon amplitude A in units of electric field. These equations describe a plasmon for a given frequency ω and propagation constant β, where β is complex. Here, the imaginary component of β corresponds to plasmonic loss. Notably, eq. (2.2) and eq. (2.4) define the polarisation of the surface plasmon with respect to the surface; there is no electric field in the $\hat{y}$ direction. The transverse spatial terms $k_x^{(d,m)}$ describe the mode profile of the surface plasmon, which decays exponentially from the metal/dielectric interface. The k_x's are related to the propagation constant β, and are given by:

$$k_x^{(i)} = \sqrt{\beta^2 - \varepsilon_i \left(\frac{\omega}{c}\right)^2} \tag{2.5}$$

In the simplest case, an analytic dispersion relation can be found by establishing the boundary conditions at the metal/dielectric interface using eqs. (2.2) and (2.4), and invoking eq. (2.5). The dispersion relation can then be found to be:

$$\beta = \frac{\omega}{c} \sqrt{\frac{\varepsilon_d \varepsilon_m}{\varepsilon_d + \varepsilon_m}}, \tag{2.6}$$

2.1.1   Properties of Plasmons

By using values for the metal permittivity found in the literature [101] with eqs. (2.2), (2.4) and (2.5), the dispersion of surface plasmons can be examined, as well as the plasmonic mode size. For the following calculations, we have assumed that the metal being used is gold. This choice of metal is discussed in more detail in section 2.2.

Surface Plasmon Dispersion

The surface plasmon dispersion is considered by examining the real part of eq. (2.6). Here, we consider surface plasmons propagating at an interface made up of gold and several different
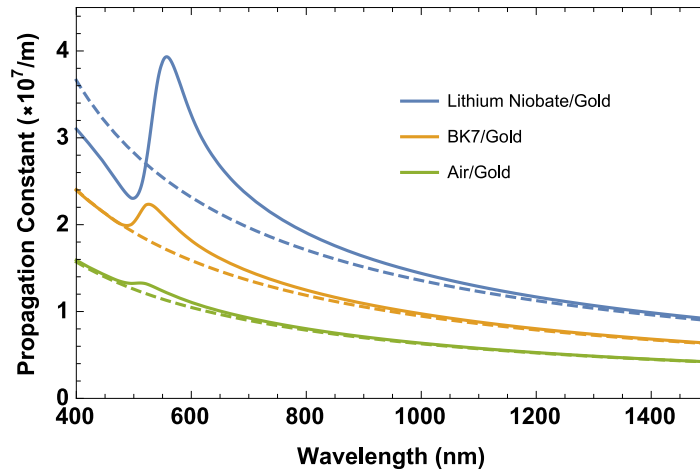
Figure 2.2: Plot of the real part of the surface plasmon dispersion relation. Plotted as a function of wavelength instead of angular frequency for convenience. The corresponding optical dispersion (dashed) is shown for comparison.

BK7			
B_1	1.03961212	C_1	$6.00069867 \times 10^{-3}$ μm^2
B_2	0.231792344	C_2	$2.00179144 \times 10^{-2}$ μm^2
B_3	1.01046945	C_3	1.03560653×10^{2} μm^2

Lithium niobate							
(o)				(e)			
B_1	2.6734	C_1	1.764×10^{-2} μm^2	B_1	2.9804	C_1	2.047×10^{-2} μm^2
B_2	1.2290	C_2	5.914×10^{-2} μm^2	B_2	0.5981	C_2	6.66×10^{-2} μm^2
B_3	12.614	C_3	4.746×10^{2} μm^2	B_3	8.9543	C_3	4.1608×10^{2} μm^2

Table 2.1: Sellmeier coefficients for the BK7 glass and lithium niobate. Coefficients sourced from [102] and [103] respectively.

dielectrics of interest. The dielectrics considered here are air ($n = 1$), a common glass (BK7, $n \approx 1.5$) and lithium niobate ($n \approx 2.1$), a high index dielectric often used for optical nonlinear effects[1]. The refractive index of these materials is precisely calculated by the Sellmeier equation:

$$n^2(\lambda) = 1 + \frac{B_1\lambda^2}{\lambda^2 - C1} + \frac{B_2\lambda^2}{\lambda^2 - C_2} + \frac{B_3\lambda^2}{\lambda^2 - C_3}, \tag{2.7}$$

where λ is the wavelength given in microns. The coefficients $\{B_1, B_2, B_3\}$ and $\{C_1, C_2, C_3\}$ for BK7 and lithium niobate are summarised in Table 2.1. The plasmonic dispersion eq. (2.6), including the dielectric dispersion in eq. (2.7), is plotted in fig. 2.2.

In each case, the surface plasmon dispersion has been plotted against the optical light-line for comparison. It can be seen that for long wavelengths in the near infrared, the surface plasmon wavevector β exceeds that of light at the same frequency. Towards the shorter wavelengths in the optical, this disparity increases up until a resonance is reached with the

---

[1]Lithium niobate is a birefringent material, but here for simplicity, we only consider the ordinary refractive index in this plot.

characteristic ω_p plasma frequency of the gold, at about 550 nm for gold. Past this resonance, the wavevector drops sharply, and the metal becomes dielectric in character.

The dispersion is one of the key constraints in plasmonics: the disparity between the optical and surface plasmon modes makes coupling between them difficult. There are only a handful of methods that are used to facilitate this coupling, which is discussed in greater detail in section 2.3.
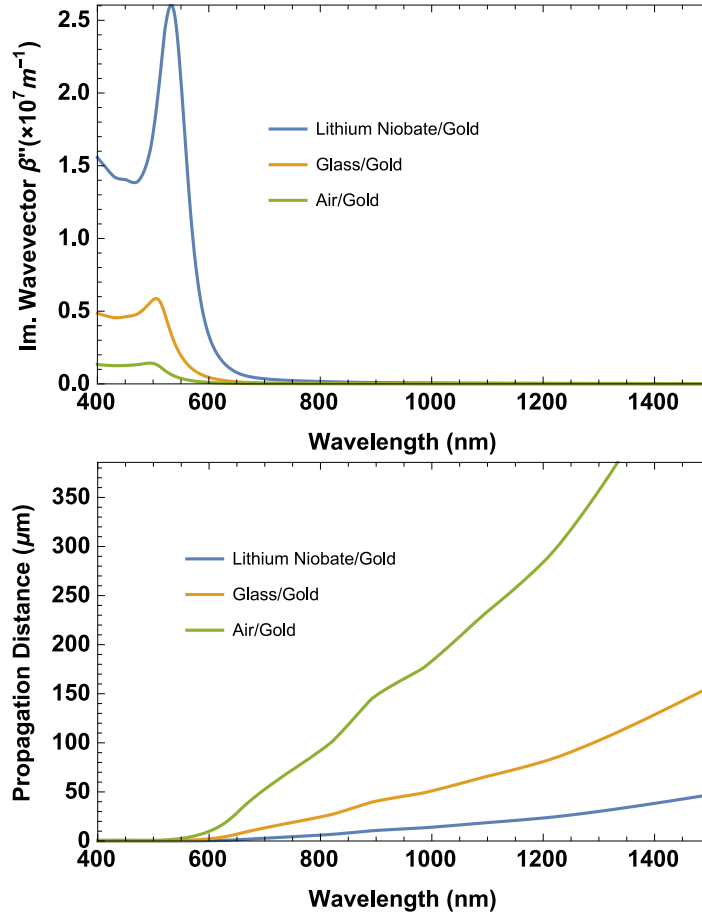
Figure 2.3: Plot of the decay constant (Top), and the corresponding propagation length in microns (Bottom).

The dispersion calculation also results in an imaginary component to the wavevector β'', and this component corresponds directly to the plasmonic loss, resulting in a propagation length given by $1/\mathrm{Im}(\beta)$. This has been plotted in fig. 2.3. Loss is an intrinsic characteristic of surface plasmons. It arises from ohmic losses in the metal. We can see that the losses are comparatively small for wavelengths longer than 700 nm, but at shorter wavelengths the losses increase rapidly. This coincides with the peak in the surface plasmon wavevector. This behaviour results in a huge range in propagation lengths for surface plasmons, depending on the wavelength of choice. In the near infrared, propagation lengths may reach many 100's of microns, whereas in the visible, the propagation length may be as small as several wavelengths. In addition to this intrinsic loss, practical plasmonic devices are also subject to external sources of loss, such as scattering losses from surface defects. This further reduces the effective propagation length of surface plasmons.

Plasmonic Mode Size

Where surface plasmons make up for the large losses and wavevector mismatch is in the plasmonic mode size. The large wavevector is accompanied by a mode distribution that falls off exponentially away from the interface, into both the metal and the dielectric. The exponent is given by eq. (2.5), and the resulting e^{-1} mode size of the surface plasmon given by $1/\text{Re}(k_x^{(d,m)})$. This mode size is strongly wavelength dependant, and is plotted in fig. 2.4, for the same dielectric materials. At long wavelengths, the field extending away from the interface extends on order of a micron into the dielectric. Towards shorter wavelengths this drops significantly, becoming more tightly bound to the surface. It should be noted that, in the visible, the plasmonic mode size lies below the local optical wavelength and therefore provides field confinement. The penetration of the field into the metal is orders of magnitude smaller, and increases by nanometres as the mode size in the dielectric decreases. The small mode size confers surface plasmons with several of the interesting properties; such as sensitivity of surface plasmons to surface perturbations, enhancement of optical fields and field localisation. These properties have led to sensing applications, the enhancement of local nonlinear effects, and the miniaturisation of photonic devices, which we discussed in chapter 1.

Figure 2.4: Surface Plasmon Mode size, extending into the dielectric (Top) and into the metal (Bottom). For comparison, the dotted lines show the corresponding optical wavelength $\lambda/n(\lambda)$.

Sensitivity to Refractive Index

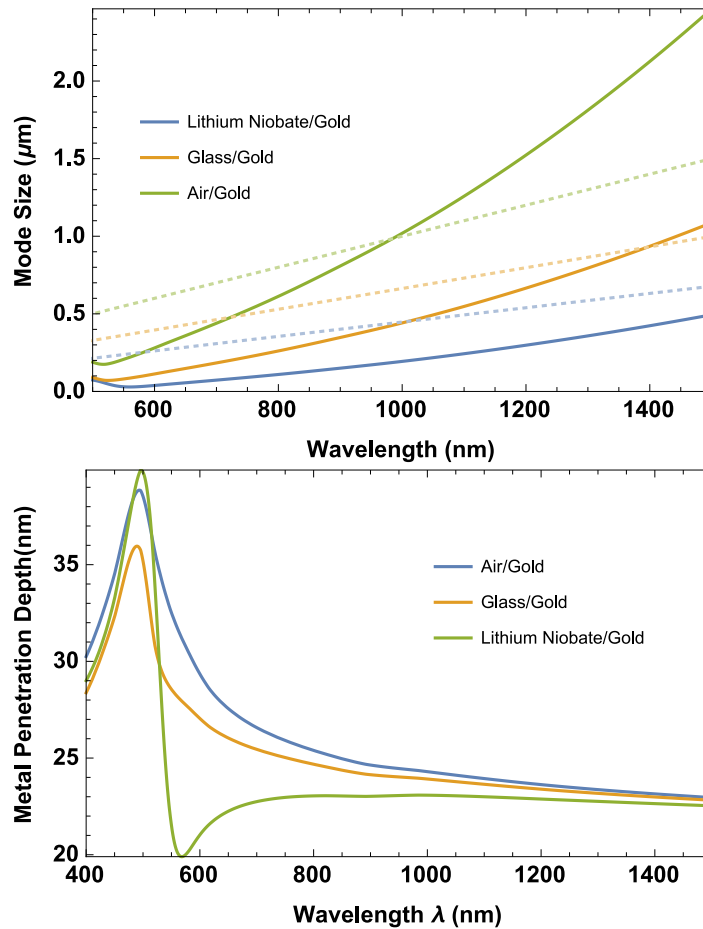It is worth noting that each of the properties outlined above are also strongly sensitive to the change in refractive index, and more so than in the standard optical case. This is also an important consideration when working with surface plasmons, as a change in dielectric can result in a change of size scales.

2.2   Plasmonic Materials

For surface plasmons propagating at the interface between a metal and a dielectric, the choice of the metal is very important, as the range of materials suitable for supporting surface plasmons is very limited. There are two primary factors involved in choosing the metal. The first is the number of free electrons available in the metal, which relates to the characteristic plasma frequency of the metal. The second is the conductivity of the metal. For surface plasmons in the visible, the two most common metals which possess both a sufficiently high plasma frequency and a high conductivity are silver and gold with plasma frequencies of $\omega_p = 1.375 \times 10^{16}$ Hz and $\omega_p = 1.32 \times 10^{16}$ Hz respectively [104]. The relative permittivity of both materials is plotted in fig. 2.5.

If we consider just the real component of the relative permittivity, gold and silver behave very similarly. What differentiates these two metals here is the imaginary component of the relative permittivity, which corresponds to loss. For all wavelengths the losses in gold are greater than that in silver. This is due to the material absorption bands which exist in the blue for the gold, but don't arise in the silver until the UV. Therefore, based on optical properties alone, silver is the metal of choice. On the other hand, silver is susceptible to oxidation, while gold is chemically stable. This is particularly pertinent due to the sensitivity of surface plasmons to surface conditions. As such, for many plasmonic applications, and indeed throughout this work, gold is the material of choice.

2.3   Plasmonic Coupling

The disparity in optical and surface plasmon dispersion makes efficient coupling to surface plasmon waveguides a key challenge in plasmonics. In order to bridge the wavevector mismatch, phase-matching methods are required. Plasmonic-photonic coupling is further complicated by the surface plasmon mode size, which leads to an additional size-scale mismatch. The three established coupling methods that are used are end-fire coupling, prism coupling and grating coupling. All three of these coupling methods require that the polarisation of the incident radiation coincides with the surface plasmon polarisation, which will be defined as transverse-magnetic (TM) with respect to the metal surface.

End-fire coupling

End-fire coupling is an in-plane coupling method which consists of focusing an optical field onto the edge of a plasmon waveguide. This method is intuitive and is similar to the method of launching light into most optical waveguides. It is extremely versatile in principle, requiring only a suitably polished facet and ordinary optical components. No additional microstructures are required. It is also largely insensitive to wavelength. In [44], Stegeman *et al* show that the most important parameter governing the efficiency of coupling is the spatial overlap

Relative Permittivity of Gold

Relative Permittivity of Silver
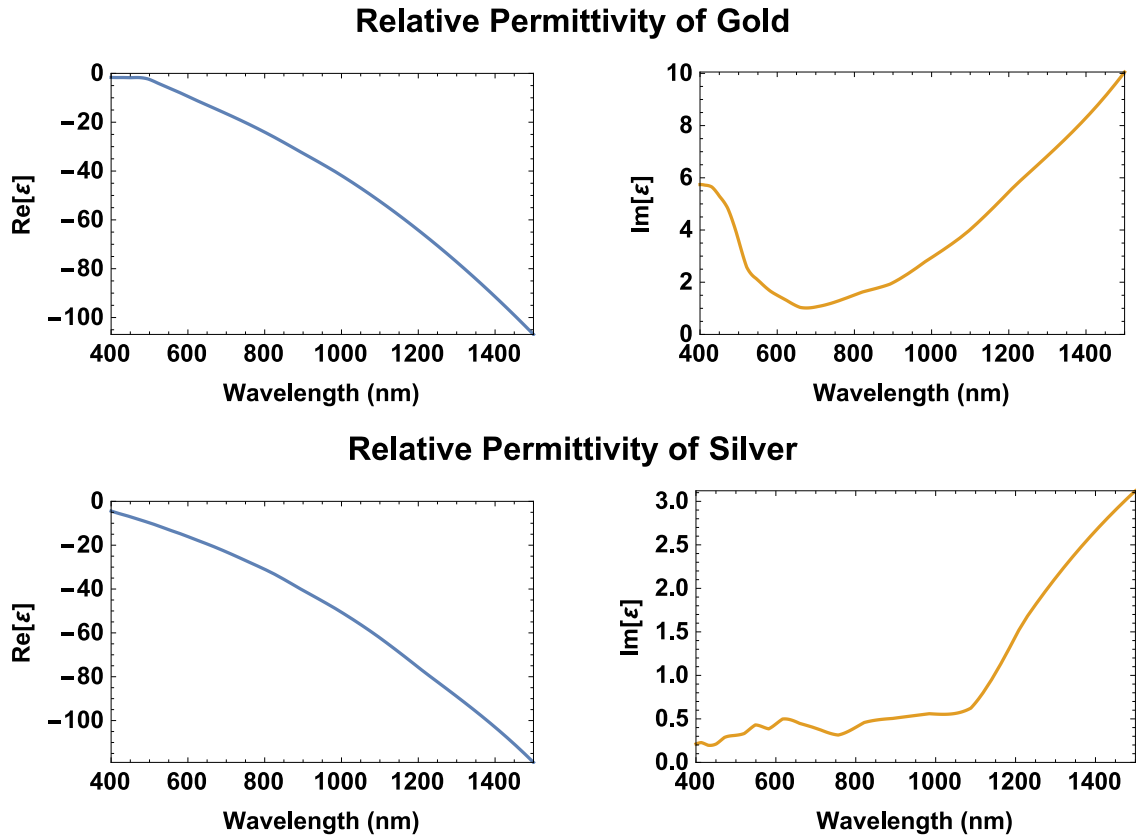
Figure 2.5: The relative permittivity of gold (top) and silver (bottom), divided into real (left) and imaginary (right) components, and plotted as a function of wavelength. Data from [101]. Note the difference in scale for the imaginary component for each metal.

between the input beam and the desired plasmon mode, as illustrated in fig. 2.6. This spatial overlap tends to have a more significant impact than phase-matching, and phase-matching is often disregarded. Recent work [105–107] has demonstrated, using numerical methods, that efficiencies as high as 80% can be achieved. End-fire coupling has also been observed in experiments [11], and has since been used routinely for exciting surface plasmons in a range of works.

The main concern when implementing end-fire coupling is in ensuring the spatial overlap of the input beam and plasmon mode. The aforementioned plasmonic mode size confinement places the plasmonic mode size on the order of the diffraction limit for the visible frequencies. For materials of a higher refractive index, the reduction in mode size is even more severe. The efficiency of end-fire coupling is therefore dependent on the use of extremely tight focussing and careful alignment. Furthermore, without the means to directly measure the surface plasmon, end-fire coupling is extremely difficult to optimise in the lab.

Prism coupling

Prism coupling is the primary method used in this work. This coupling configuration is shown in fig. 2.7. This method uses light incident from a high refractive index medium to phase match the surface plasmon mode in a lower index medium (usually in air). In the canonical Kretschmann configuration [3], this is achieved by using a prism with the metal
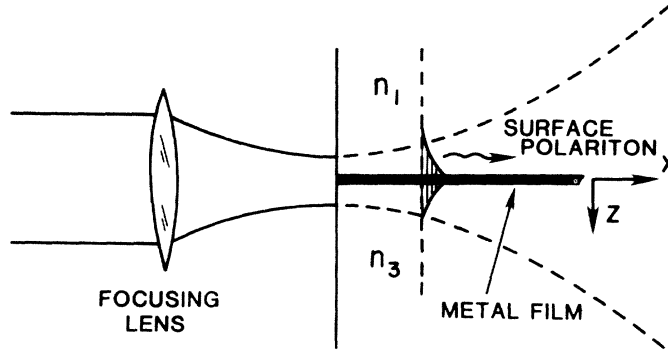
Figure 2.6: Illustration of a the end-fire technique, as shown in [44].

film deposited directly onto the hypotenuse face. The phase matching condition is satisfied by tuning the incident angle of the light such that the projection of the wavevector parallel to the surface matches that of the plasmon [100]:

$$k_{sp} - k_{opt} \sin \theta = 0 \qquad (2.8)$$

This angle is known as the Surface Plasmon Resonance (SPR)angle. At the SPR angle, some of the incident beam is reflected at the interface, but some of the beam tunnels through the gold film, exciting surface plasmons. By symmetry, eq. (2.8) also allows the leakage of surface plasmons back into light. Due to the phase acquired on reflection, reflected incident beam and the surface plasmon leakage destructively interfere. This supresses the plasmon leakage in the vicinity of the excitation beam and leads to highly efficient coupling, which approaches unity in the infrared. The acceptance angle of the prism coupling method is determined by the losses of the surface plasmon, making it strongly wavelength dependent.

In order to optimise prism coupling, the incident light must tunnel through the metal film, and this restricts the possible thickness of the gold film. A variation on this configuration, known as the Otto configuration [4], is also shown. Here, light instead tunnels across a thin dielectric gap, usually air. The advantage of this method is that it allows plasmon excitation on planar metallic films, without the need for nano-structuring, and with relatively simple alignment. It yields high coupling efficiencies, but also allows the surface plasmon to leak back out as optical radiation. This significantly reduces the effective propagation length of the plasmon. This coupling method is also extremely sensitive; the tolerance of the surface plasmon resonance angle typically being less than a degree.

Grating coupling

The last method that is commonly used to excite surface plasmons is grating coupling. A grating can coherently scatter the incident light, imparting a spatial wavevector. The condition for surface plasmon excitation via a grating is given by:

$$k_{opt} \sin \theta \pm \frac{2\pi n}{\Lambda} = 0, \qquad (2.9)$$

where Λ is the grating period and n is an integer. A particular strength of this method is that the grating period Λ can be chosen to enable a convenient incident angle θ for the input beam. As in the end-fire case, the coupling efficiencies that can be achieved are difficult to characterise.
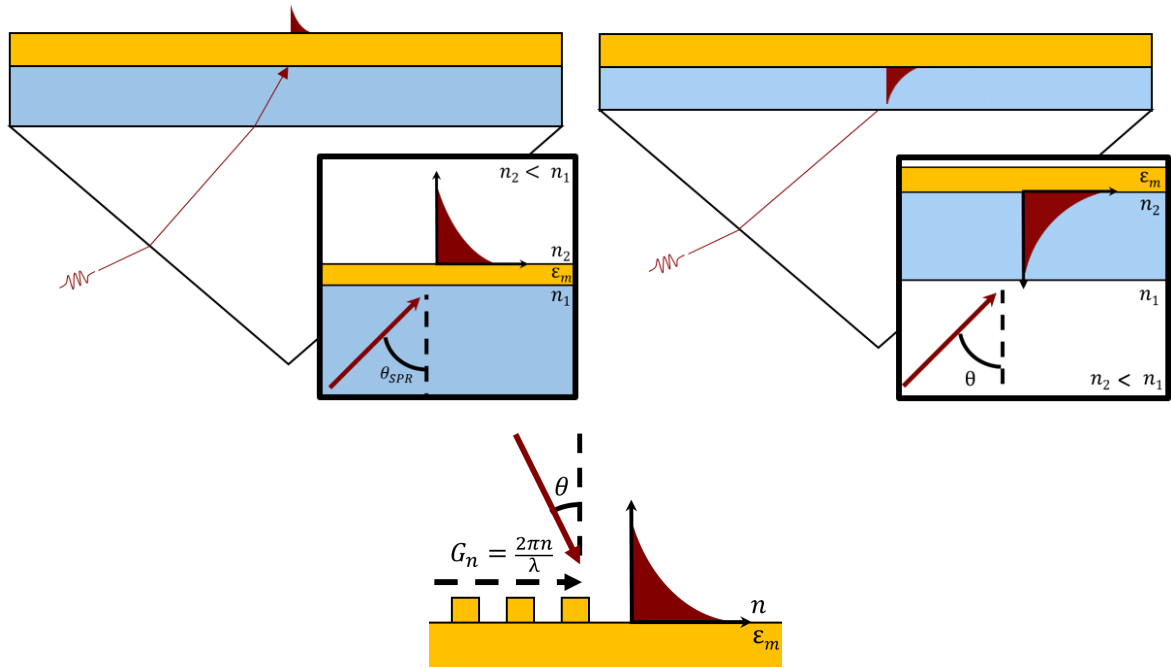
Figure 2.7: Typical plasmon launching schemes. (Top Left) Kretschmann configuration: Light tunnels from the high index medium to launch a plasmon on the low index side. (Top Right) Otto configuration: Similar configuration, where light tunnels across a low index layer. (Bottom) Grating coupling: Phase matching is achieved by a combination of the wavevector of the incident light and the wavevector of the grating.

There are many variations on the standard grating, including slanted [108], sinusoidal [109] and variable period [110] gratings, all of which have an impact on the coupling efficiency. In most cases, the gratings used are simple stepwise gratings, which can be written using either Focused Ion Beam (FIB) or E-Beam Lithography (EBL) methods. Here, the efficiency is a function of the duty cycle and the etch depth of the grating. Experimental studies of gratings [111] demonstrate that the coupling efficiency for surface plasmon excitation can reach 45% for an optimised grating.

2.4 Plasmon Waveguides

Surface plasmons travelling at an infinite metal/dielectric interface have been the focus of the discussion thus far, but this represents just the simplest case; there are other surface plasmon modes which arise for different geometries. These geometries allow the behaviour of the surface plasmon to be tuned in a variety of ways, and are therefore a powerful tool in engineering surface plasmon devices.

The next level of complexity for a surface plasmon mode arises when finite metal film thickness is considered, with a dielectric on either side. This is also commonly known as an Insulator-Metal-Insulator (IMI) configuration. For such a configuration, surface plasmons can be supported on both the top and bottom surfaces. When the metal film thickness is of the order of the skin depth of the metal itself, and if the dielectrics on either side of the metal are sufficiently similar, these two surface plasmon modes couple, forming surface plasmonic

supermodes. These two modes are shown in fig. 2.8. There is no analytic description of the dispersion for these modes, and the dispersion must be calculated numerically. However, these surface plasmon modes are known to have several defining properties. The odd mode possesses a node in the metal film and a larger mode size extending into the dielectric. This is associated with a lower propagation constant and smaller propagation losses. As such, this mode is commonly referred as the Long-Range Surface Plasmon Polariton. The even mode, on the other hand, has fields concentrated strongly in the metal film, with larger field densities, a further increased propagation constant and also higher losses. This is known as the Short-Range Surface Plasmon Polariton.

So far, these two modes have been presented here as planar waveguide modes, propagating on a thin film with an infinite extent in the yz plane. There has been a number of studies on finite metal films [112–115] and the resulting mode structures. Provided that the width of the waveguide is substantially wider than the local wavelength of light, the characteristic behaviour of the long-range and short-range surface plasmon polariton modes is maintained.

Due to the differing properties of the long-range and short-range modes, they are utilised in very different sets of applications. Here, we are interested in the long-range surface plasmon mode, which has garnered a lot of attention, and has been well characterised [11, 21, 116]. The larger mode size and smaller propagation constant of this mode make it easier to interface with optical fields. The propagation losses have also been demonstrated to be small enough to allow devices based on long-range surface plasmons to be created. In particular, losses as low as 0.1 dB/mm have been reported at $\lambda = 1550$ nm, corresponding to propagation lengths ≈ 3 cm [21]. The corresponding mode size is, however, drastically increased, and is of the order of ~ 7 μm^2 in this example [117], and is no longer confined to subwavelength dimensions. Nevertheless, studies in long-range surface plasmon waveguides has resulted in the fabrication of passive long-range surface plasmon devices such as splitters [12] and bragg gratings [14], as well as active devices utilising thermal [118] and electro-optic [16, 117, 119] effects. The long-range surface plasmon will be described in greater detail in chapter 5.

There are many other geometries for generating surface plasmon modes, some of which are mentioned here for completeness. Using the inverse Metal-Insulator-Metal (MIM) configuration, two similar modes also arise. Due to the large influence of the metal, both of these modes tend to be characterised by a large field confinement at the expense of larger losses. MIM waveguides are often considered where extreme field confinement is a priority, such as in plasmonic nanolasers [34, 35] and localised nonlinear effects [120]. Waveguide geometries which involve hybridised plasmon/optical modes on dielectric loaded plasmonic waveguides [72, 73, 121–123], allow a trade-off between optical and plasmonic properties. These waveguides can be difficult to implement, sometimes with nanometer tolerances on waveguide dimensions.

2.5   Fabrication/Thin Film Deposition

The gold films used throughout this thesis were deposited using the method of ion-assisted deposition [124]. This consisted first of mounting the substrates on a stainless steel plate (previously cleaned in an ultrasonic bath with acetone) and sealing it in a vacuum chamber, above a gold target. The chamber was then pumped down to 10^{-6} Torr. This takes at least 4 hours. Oxygen was introduced into the vacuum chamber at ≈ 6 SCCM (Standard Cubic Centimeters per Minute) and excited into a plasma using an ion gun. The voltage of the ion gun was varied until an an ion current density of $\sim 70 - 90 \mu A/cm^2$ was established. The
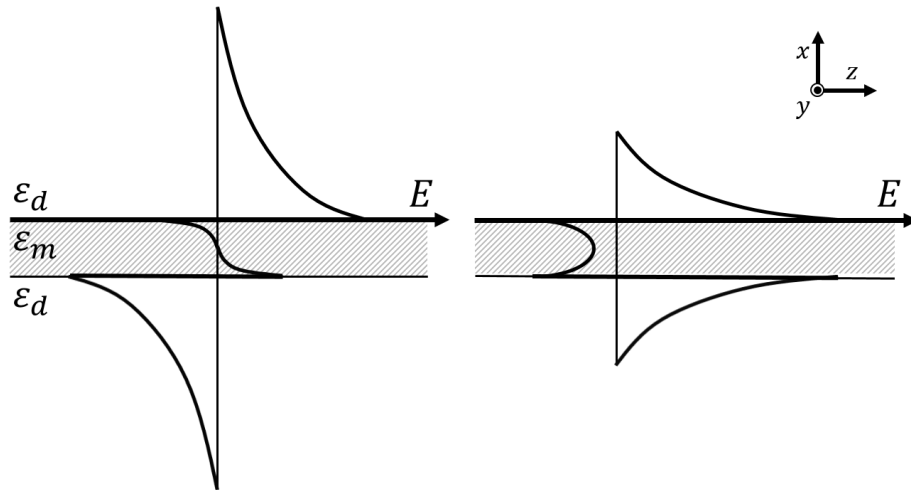
Figure 2.8: Sketch of the plasmonic mode distributions in an IMI configuration, showing both the long-range surface plasmon (Left)and the short-range surface plasmon (right).

oxygen plasma both cleans the substrate of organics adhered to the surface, and ionises the surface. Ionised sites act as nucleation sites for the gold, and for thin films, a high density of nucleation sites is preferred. The exposure to the plasma lasted ≈ 5 minutes. With the plasma present, 120 A was applied through a gold target, melting it and introducing a gold vapour into the chamber. The vapour expands in an approximately spherical front from the gold source. Far from the source, the deposition rate can be taken as uniform. Initially, the samples are shielded from the gold vapour, allowing the evaporation to reach a steady state. When this is achieved, the substrates are unshielded and the gold is deposited at a rate of $0.5 - 1$ Å/s, measured by a quartz crystal adjacent to the samples. The gold and oxygen plasma were simultaneously present for the first few nanometres (~ 6 nm) in order to densify the film and encourage adhesion to the substrate. Gold is deposited around nucleation sites, forming islands. These islands begin to coalesce around the 2-3 nm mark. The plasma was then turned off, and the gold film allowed to continue to grow to reach the desired thickness. Typically, this was between 30 nm and 100 nm. At 30 nm, the film is considered to have fully coalesced and additionally formed a smooth continuous surface, yielding a good film quality. At the upper end, films of ≈ 100 nm are more than 3 times thicker than the skin depth in the optical, and can be considered to be equivalent to an infinitely thick gold film for the purposes of surface plasmon propagation. A typical thin film deposition consumed ≈ 1.4 g of gold.

When the desired thickness was reached, the samples were shielded from the line of sight of the gold target, and the current running through the gold was removed to allow it to cool down. The chamber was then let back up to atmospheric pressure and the samples recovered. On inspection, a gold film that was deposited to a film thickness of ≈ 30 nm appears smooth and semi-transparent. Gold films that had been deposited to a film thickness of ≈ 100 nm are opaque, and appear as thick gold films.

2.6   Characterisation of Gold Films

Once removed from the chamber, it was important to be able to characterise the gold films that had been deposited. There were two main methods of characterising the surface quality
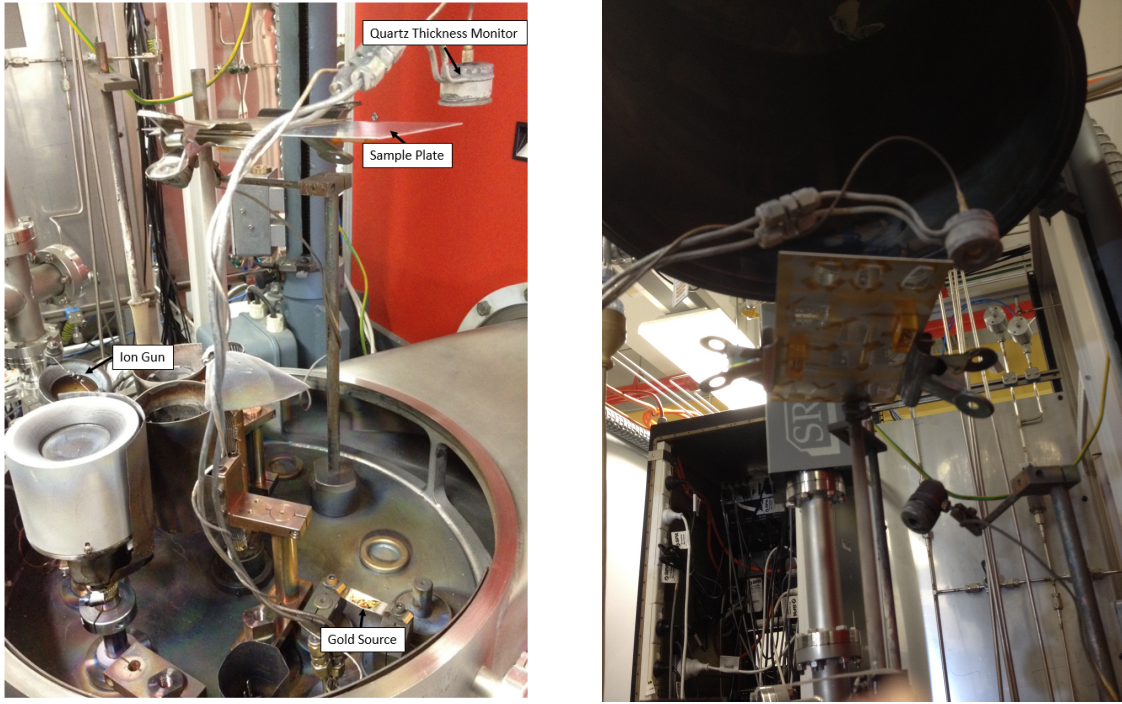
Figure 2.9: (Left) Annotated photo of the deposition chamber. (Right) Inverted sample plate.

of the gold film. The first was by using a white-light interferometer, and the second was by optical characterisation via reflectivity measurements.

2.6.1   White-Light Interferometer

The surface quality was assessed using a white light interferometer (Veeco Wyko NT98000), shown in fig. 2.10. Access to the white light light interferometer was kindly granted by Adam Joyce. The white light interferometer was used in a phase-shift interferometry mode, providing high resolution spatial imaging of the sample by interfering the reflected signal beam with a reflected reference beam. The length of the reference arm was varied in order to generate a series of interferograms which can be used to construct either a contour map or a 3D model of the sample surface, examples of which are shown in fig. 2.11. Using this method the white light interferometer has nanometre resolution height, but is diffraction-limited in the plane. The white light interferometer was able to determine the surface roughness of the gold films that had been fabricated. Using the arithmetic average, a surface roughness of $R_a \approx 1$ nm was found for a flat gold film.

2.6.2   Optical Characterisation

For the thin gold films, the gold was further characterised by analysing the linear optical properties of the thin film in reflection. The reflectivity of a thin film is well described by the Fresnel equations [125], where the reflection and transmission coefficients $\{r_{i,j}, t_{i,j}\}$, relating to the electric fields, are given as:

$$r_{ij} = \frac{k_{z,i}\varepsilon_j - k_{z,j}\varepsilon_i}{k_{z,i}\varepsilon_j + k_{z,j}\varepsilon_i}, \quad t_{ij} = \frac{2k_{z,i}\sqrt{\varepsilon_i\varepsilon_j}}{k_{z,i}\varepsilon_j + k_{z,j}\varepsilon_i}. \tag{2.10}$$
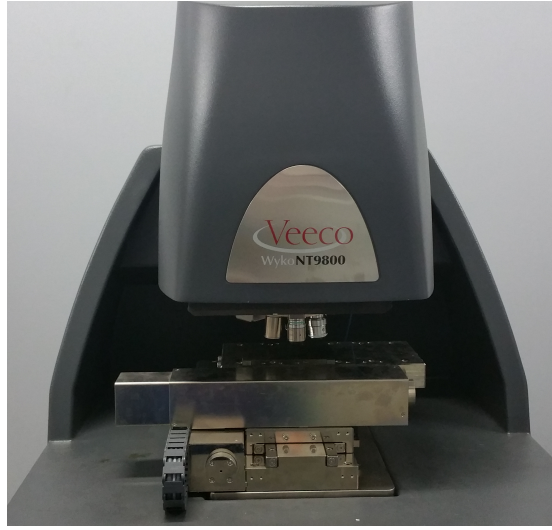
Figure 2.10: Photo of the Veeco Wyko NT9800. Included a high precision X-Y and tilt stage, and microscope objectives ranging from 15x to 228x.
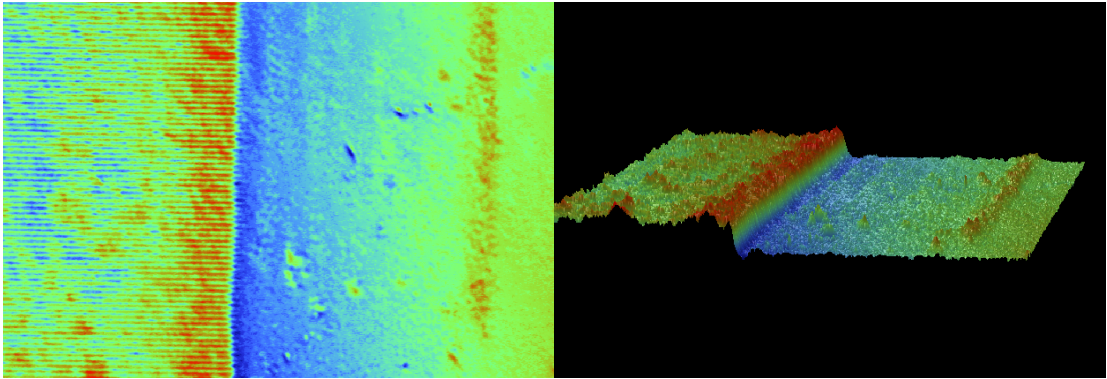
Figure 2.11: Example image from the white light interferometer, here showing a sample with a grating. Topographical information presented as a colour map (Left) and a 3D representation (Right).

Here, $k_{z,i} = k \cos \theta$ and is the wavevector perpendicular to the interface, and the ε's correspond to the relative susceptibilities at a particular wavelength.

The total reflectivity of the thin film is a linear combination of the reflection and transmission coefficients at each interface, with the addition of a phase term corresponding to propagation within the film. This gives the following result for the reflected power:

$$|R_{01}(\theta)|^2 = |\frac{r_{0m} + r_{m1}e^{2ik_{z,m}d}}{1 - r_{m0}r_{m1}e^{2ik_{z,m}d}}|^2, \tag{2.11}$$

where subscripts $\{0, m, 1\}$ refer to the substrate, metal (gold), and superstrate (air) and d is the film thickness.

By measuring the reflectivity of a gold film experimentally, and fitting the reflectivity to eq. (2.11), the permittivity and thickness of the gold film could be verified. These measurements were taken in a prism configuration, and the external incident angle on the
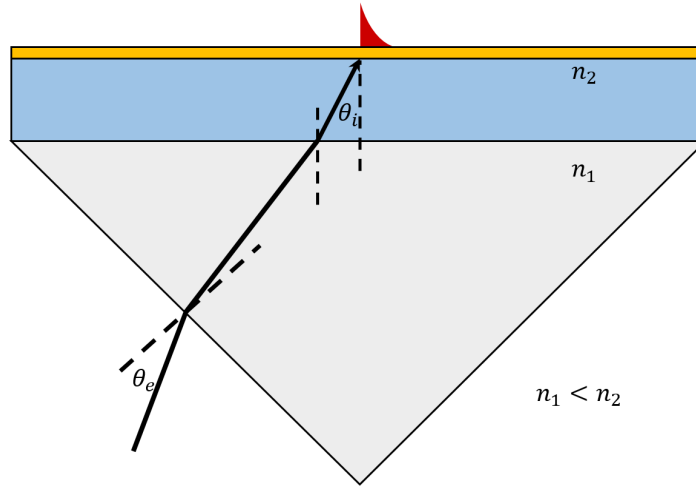
Figure 2.12: Schematic of the reflectivity measurement, showing the sign convention for the external angle θ_e.

prism θ_e was related to internal incident angle on the gold θ_i by:

$$\sin \theta_e = n_1 \, \sin \left(\frac{\pi}{4} - \arcsin(\frac{n_2}{n_1} \, \sin \theta_i) \right), \tag{2.12}$$

where $\{n_1, n_2\}$ are the refractive indices of the prism and substrate respectively. The sign convention for this calculation is shown in fig. 2.12.

The reflectivity of a typical gold film on a glass substrate and mounted on a glass prism (fig. 2.12), is shown in fig. 2.13, plotted using eq. (2.11). In the example shown above, the light source was a $\lambda = 642$ nm, and the corresponding relative permittivity of gold was taken to be $\varepsilon_m = -12.4333 + 1.15196i$. The reflected light was collected by a photodiode. The peak in reflection that is evident in the reflection scan corresponds to total internal reflection, and the dip in reflection is interpreted as a surface plasmon excitation, corresponding to excitation via the Kretschmann configuration. Both the angle at which this dip occurs and the width of the dip are sensitive to the thickness and permittivity of the gold. For all gold films deposited, it was found that the values for the bulk relative permittivity of gold given in [101] allows the gold film thickness to be determined within 1 nm of the expected value.

2.7   COMSOL Multiphysics

In this thesis, surface plasmons and coupling are explored through both experiments and modelling. One tool which has proven to be useful in simulating surface plasmons is COMSOL Multiphysics. COMSOL Multiphysics is an extremely versatile finite element method (FEM) simulation software. It can be used to simulate a range of physical phenomena including mechanical, electrical, fluid and optical phenomena, in both 2D and 3D geometries. In this work, COMSOL was mainly used with its Wave Optics Module for 2D simulations. This tool was extremely important since, for geometries more complex than a plasmon at an infinite metal/dielectric interface, no analytic solutions exist and numerical approaches are required.

COMSOL provides an interface which allows the user to define a geometry, and each domain of this geometry can be assigned material properties, such as refractive index or
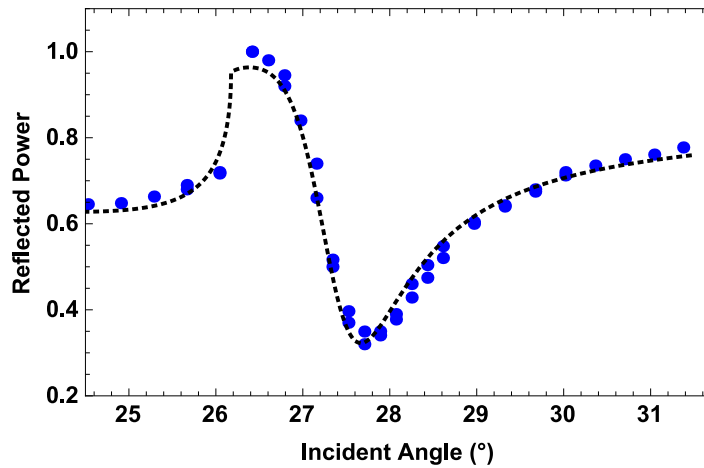
Figure 2.13: Example of a reflectivity measurement (blue), and the corresponding theoretical curve (dotted), calculated from the Fresnel equations. Peak corresponds to total internal reflection, and trough corresponds to plasmon excitation.

permittivity. Light of a specified frequency and spatial distribution could be injected into the geometry by introducing an excitation port. COMSOL would then be able to carry out a "frequency domain study", which consisted of full-wave simulations using Maxwell's equations at a well defined frequency, to determine how the light would propagate into the geometry. This method was useful in determining coupling between light and surface plasmons; via phase-matching techniques or scattering. Another useful application of COMSOL was to define a 2D geometry and treat it as a cross-section of a 3D structure. COMSOL is then able to perform a "mode analysis" of the geometry, and determine the modes and propagation constants of the structure.

2.7.1 Meshing

In either case, COMSOL calculates the field distribution by using finite-element methods, where the elements are defined on a mesh. The two key parameters of the mesh are the size of the mesh elements, and the shape of the basic element of the mesh. The meshing approach is extremely important when simulating optical-plasmonic phenomena due to the range of size scales involved. Ensuring that each region is sufficiently sampled is an important task: undersampling a region can result in artefacts in the simulation, and incorrect behaviour of the light. On the other hand, oversampling is computationally expensive, and drastically increases the time required for the simulation to complete.

In order to determine the appropriate scale for the mesh, we had to consider the behaviour of the fields in each material separately, and define different mesh sizes for each domain. The smallest size scale on which the electric fields can change in dielectrics is determined by the local wavelength λ_0/n. By defining a mesh size smaller than this, an accurate simulation can be ensured. For most of the simulations carried out, a mesh element size of $(\lambda_0/n)/8$ was chosen. Similarly, inside the metal the penetration depth of the electric field is ≈ 30 nm, and so a mesh size of 4 nm was chosen. The second major parameter of the mesh is the basic shape of the mesh. By default, these mesh elements are triangular in the 2D case or tetrahedral in the 3D case. Rectangular meshing elements are also available, however these are not as flexible. Triangular meshing elements are most useful for discretising domains

with curved or irregular shapes and also enable a smooth transition for mesh sizes across
domain boundaries. An example of this is shown in fig. 2.14.
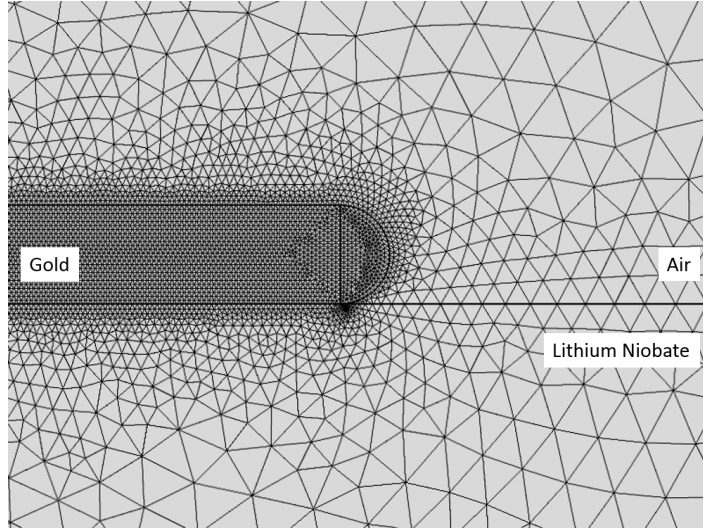
Figure 2.14: Example of a mesh generated in COMSOL, using tri-
angular mesh elements, showing interpolation of the mesh size from
fine to coarse.

To verify that our simulations were sufficiently accurate with these meshing parameters,
several additional simulations were carried out with smaller mesh sizes ($(\lambda_0/n)/16$ and 2 nm
respectively) were carried out and compared to the original simulations. No significant
change field distribution was observed between the two simulations with different meshes
and the power was not seen to vary significantly ($< 2\%$). To save computation time, the
coarser mesh size was generally adopted.

2.7.2   Boundary Conditions

Another important consideration for simulating surface plasmon behaviour is the boundary
conditions of the simulation. By default, COMSOL chooses perfectly conducting boundaries,
however, these boundary conditions reflect optical power back into the simulation and can
create artefacts. To avoid these artefacts, other boundary layers, called Perfectly Matched
Layers (PML), were introduced around the edges of the simulation. An example of a
Perfectly Matched Layer is shown in fig. 2.15. These boundary layers are required to be
several wavelengths thick and nominally have the same refractive index as the adjacent
region, however these layers have an additional loss coefficient. This causes most of the light
incident on the boundary to be rapidly damped within several wavelengths. These perfectly
matched layers are able to mitigate most of the reflections re-entering into the simulation,
but residual reflections are still present. To further reduce spurious effects from the residual
reflections, it is still necessary to choose a simulation size sufficiently large that any reflected
light is scattered far from any points of interest. This criterion is dependent on the simulation
being considered. However, generally the interesting behaviour occurred over a 1–3 μm
range, and a boundary box of 10×20 μm was adopted where possible. For wavelengths in the
visible, and in typical glasses ($n \approx 1.5$ this is more than 25× the size of the local wavelength.
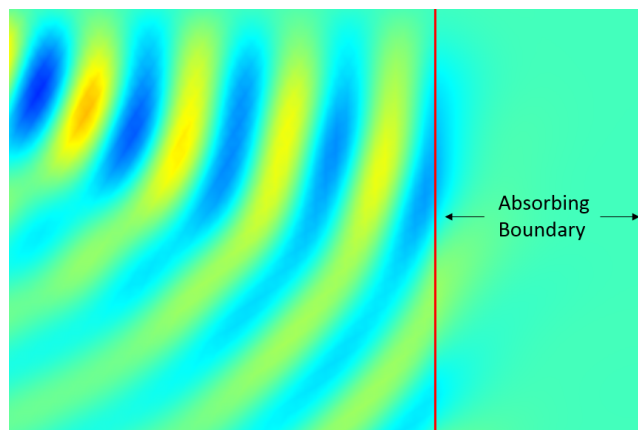
Figure 2.15: Example of a Perfectly Matched Layer (PML), used to absorb scattered radiation.

3

Plasmonic Second Harmonic Generation

3.1   Introduction

Our first study consisted of investigating second-order nonlinear effects in surface plasmons, through the simplest second-order nonlinear effect, second harmonic generation. Nonlinear effects arise when large field intensities induce a nonlinear polarisation in a material. This nonlinear polarisation can then re-radiate and and be used to excite surface plasmons at different frequencies.

In this chapter, we investigate the $\chi^{(2)}$ nonlinearity arising from the plasmonic interaction with metals, and excite plasmons using this nonlinearity for second harmonic generation. In section 3.2, we start with a discussion of nonlinearities observed in optics, and then their application to propagating surface plasmons in section 3.3. Lastly, in section 3.4, we use the $\chi^{(2)}$ nonlinearity of gold for plasmonic second harmonic generation, and calibrate the signal against the nonlinear response of lithium niobate.

3.2   Overview of Nonlinear Effects

Nonlinear optics is a field that has been studied thoroughly [126]. Here we include a brief overview of some of the relevant nonlinear effects. In nonlinear optics, nonlinear effects arise can be considered by taking a power series expansion of the polarisability of a medium. This polarisability $\tilde{P}$ can be written

$$\tilde{P} = \epsilon_0 \left(\chi^{(1)} \tilde{E} + \chi^{(2)} (\tilde{E} \cdot \tilde{E}) + \chi^{(3)} (\tilde{E} \cdot \tilde{E} \cdot \tilde{E}) ... \right), \tag{3.1}$$

where $\chi^{(1)}, \chi^{(2)}, \chi^{(3)}...$ are the susceptibility tensors, and $\tilde{E}$ is the complex electric field vector. Practically, due to the flexibility in choosing the material orientation, symmetries in nonlinear crystals and the choice of polarisation of the incident field, the susceptibility tensors $\chi^{(n)}$ can often be treated as scalar quantities. For low amplitudes of $\tilde{E}$, the higher order terms vanish and the polarisation is directly proportional to the excitation. Large field amplitudes are required in order to observe the emergence of the additional nonlinear effects.

The wave equation is given by:

$$\nabla^2 \tilde{E} = \frac{n^2}{c^2}\frac{\partial^2 \tilde{E}}{\partial t^2} + \mu_0 \frac{\partial^2 \tilde{P}}{\partial t^2}, \tag{3.2}$$

where n is the refractive index, and we have assumed the susceptibility $\mu = 1$. By taking the power expansion of the polarisation and substituting into eq. (3.2), the nonlinear effects can be described.

3.2.1 Second-Order Nonlinear Effects

Second-order nonlinear effects only emerge in materials which are not centrosymmetric (do not possess inversion symmetry), for which $\chi^{(2)} \neq 0$. The primary effects which emerge at this order are sum-frequency generation (SFG) and difference-frequency generation (DFG).

Sum-frequency generation and Second Harmonic Generation

Sum-frequency generation is the process by which two light fields of frequency ω_1 and ω_2, which are simultaneously incident on a nonlinear material, generate a component of the polarisation to oscillate at the sum frequency $\omega_1 + \omega_2$, which then re-radiates. Second harmonic generation (SHG) is the special case for which the two incoming optical waves are of the same frequency, $\omega_1 = \omega_2 = \omega$. In this case, we call this the fundamental frequency and the generated field is then the harmonic at 2ω.

We can use eq. (3.2) to determine the evolution of the fundamental and harmonic fields. In the simplest case, we can choose the form of the fundamental and the harmonic fields to be

$$\tilde{E} = \frac{1}{2}(E_1 e^{i(\beta_1 z - \omega_1 t)} + c.c.)$$
$$+ \frac{1}{2}(E_2 e^{i(\beta_2 z - \omega_2 t)} + c.c.), \tag{3.3}$$

where $c.c.$ is the complex conjugate and the subscripts $\{1, 2\}$ correspond to the pump and harmonic fields respectively. Here, E is the electric field amplitude, and β is the propagation constant given by

$$\beta_i = \frac{2\pi n_i}{\lambda_i} = \frac{\omega_i n_i}{c}, \tag{3.4}$$

where λ_i is the free space wavelength for pump and harmonic light. Using eqs. (3.2) and (3.3), and the slowly varying pump approximation ($\frac{\partial^2 E}{\partial z^2} = 0$), we find that the change in the amplitudes of the electric fields $\{E_1, E_2\}$ is given by:

$$\frac{\partial E_1}{\partial z} = i\frac{\omega_1}{cn_1}\chi E_1 E_2^* e^{-i\Delta z} \tag{3.5}$$

$$\frac{\partial E_2}{\partial z} = i\frac{\omega_2}{cn_2}\chi E_1^2 e^{i\Delta z}, \tag{3.6}$$

where $\Delta = 2\beta_1 - \beta_2$ is the phase matching condition and $\{E_1, E_2\}$ are the electric fields associated with the pump and harmonic respectively, and E_i^* is the complex conjugate. For simplicity, we've dropped the superscript on the second-order nonlinear susceptibility χ, and treated it as a scalar quantity: in practice it is a tensor and the effective susceptibility is

dependent on the orientation of the electric fields.

In the small gain limit, we can ignore the effect of the harmonic field on the pump field, and just consider the evolution of the harmonic (eq. (3.6)). Integrating along the propagation length L to find the electric field amplitude E_2 gives:

$$E_2 = i\frac{\omega}{cn_2}\chi E_1^2 \frac{e^{i\Delta L} - 1}{i\Delta} \tag{3.7}$$

$$= i\frac{\omega}{cn_2}\chi E_1^2 e^{i\frac{\Delta L}{2}} L\mathrm{Sinc}\left(\frac{\Delta L}{2}\right), \tag{3.8}$$

where $\mathrm{Sinc}(x) = \frac{\mathrm{Sin}(x)}{x}$. The harmonic electric field amplitude is related to the irradiance I by

$$I = \frac{1}{2}c\epsilon_0 n|E|^2, \tag{3.9}$$

and by combining eqs. (3.8) and (3.9), we find the well known equation for the second harmonic generation:

$$I_2 = \frac{\chi^2\omega^2}{\epsilon_0 c^3 n_1^2 n_2}I_1^2 L^2 \mathrm{Sinc}^2\left(\frac{\Delta L}{2}\right). \tag{3.10}$$

From the equation, we see that the harmonic irradiance increases quadratically with the irradiance at the fundamental frequency I_ω. The phase matching term Δ also has an important effect. When the phase matching term $\Delta = 0$, $\mathrm{Sinc}(\frac{\Delta L}{2}) = 1$ and the irradiance grows quadratically with the interaction length L. When $\Delta \neq 0$, the Sinc term limits the growth of the irradience, causing it to oscillate sinusoidally. This is caused by a phase difference accumulating between the fundamental and harmonic fields. When a π phase difference has accumulated, the harmonic field undergoes destructive interference and is converted back into the fundamental. The length over which this phase difference accumulates is called the coherence length, and occurs at a length equal to:
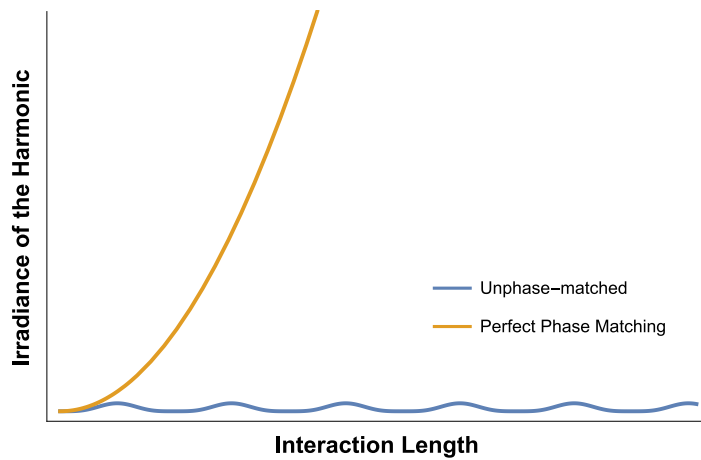
$$l_c = \frac{\pi}{\Delta} \tag{3.11}$$

Figure 3.1: Growth of the harmonic irradiance with interaction length L.

Difference-frequency generation

Difference-frequency generation is the inverse operation where an intense optical field of frequency ω_1, called the pump, may excite a polarisation of the material at two distinct frequencies, ω_2 and ω_3, which then radiate. These generated frequencies, generally called the signal and the idler, are constrained such that $\omega_1 = \omega_2 + \omega_3$. Similar equations can be found for growth of the amplitudes of these fields:

$$\frac{\partial E_1}{\partial z} = i\frac{\omega_1}{cn_1}\chi E_2 E_3 e^{-i\Delta z}, \tag{3.12}$$

$$\frac{\partial E_2}{\partial z} = i\frac{\omega_2}{cn_2}\chi E_1 E_3^* e^{i\Delta z}, \tag{3.13}$$

$$\frac{\partial E_3}{\partial z} = i\frac{\omega_3}{cn_3}\chi E_1 E_2^* e^{i\Delta z}, \tag{3.14}$$

Where $\{E_1, E_2, E_3\}$ are the corresponding electric fields of the pump, signal and idler respectively, * is the complex conjugate, and the phase matching condition for difference frequency generation is given by:

$$\Delta = \beta_1 - \beta_2 - \beta_3. \tag{3.15}$$

Difference frequency generation can occur spontaneously, but may also be stimulated by providing fields at either ω_2 or ω_3. The result is coherent amplification of the seeded field, and is thus known as optical parametric amplification or parametric gain.

3.2.2 Third-Order Nonlinearities

At higher powers, third order nonlinear effects can be accessed, which are mentioned here for completeness. There has been significant interest in third-order nonlinear effects in plasmonics, the third order susceptibility coefficient of metals are known to be relatively large. [127, 128]. The exact value of this nonlinearity is uncertain, as the experimentally measured values are strongly dependent on the measurement technique. The reported values vary between 10^{-20}–10^{-15} m^2/V^2 [129]. Third order nonlinearities include additonal effects such as the quadratic photorefractive effect (the Kerr effect) [130], cross-phase modulation and self-phase modulation. These effects have application in surface plasmon switching [70, 74, 131–133] and plasmonic self-focussing and soliton generation [134–139].

The effects which are pertinent for amplification and frequency generation fall under the umbrella of four-wave mixing. Using this approach, the excitation of surface plasmons on planar metal films has been modelled [140–142], and successfully demonstrated experimentally [143–145]. The inverse has also been demonstrated, using third order nonlinearities and surface plasmons to generate light in the far field [146] These schemes tend to be more complex than the second-order effects, due to the additional fields involved. Furthermore, the size of the third-order coefficient in gold is relatively large, but still small compared to second-order coefficients which tend to be of the order of 10^{-12}–10^{11} m/V. Hence, we only consider second-order effects in this thesis.

3.3 Considering Nonlinearities in Plasmonics

If we consider the polarisability model for nonlinearitiy as applied to surface plasmons, we would expect that surface plasmons naturally support nonlinear effects [128]; field confinement and large field densities are key characteristics of surface plasmons, and these are properties conducive to observing a strong nonlinear response. They suggest that plasmonic frequency conversion may be accessed with moderate powers.

This has resulted in a large body of work investigating plasmonics and the $\chi^{(2)}$ nonlinearity, mostly restricted to second harmonic generation. These studies include second harmonic generation from structured surfaces [147–151], nano particles and antennae [152–154], as well as from propagating surface plasmons. Some of these works are discussed in chapter 1.

Despite this effort, the study of the $\chi^{(2)}$ nonlinearity has not progressed much further than second harmonic generation. In part, this is due to some of the limitations of propagating surface plasmons. In chapter 2, we showed that losses result in plasmonic propagation lengths of tens of microns, whereas optical nonlinear frequency mixing is usually carried out over millimetres or centimetres. In second-order nonlinear effects, this restricts the possible interaction length, and makes it difficult to leverage the large intensities afforded by the small plasmonic mode size. Furthermore, a recent numerical study by Vincenti *et al.* [68] predicted that in the case of second harmonic generation, the amount of second harmonic absorbed by the metal is often as great, or even greater than the second harmonic that can be detected in the far field.

The plasmonic dispersion also becomes more complicated in the nonlinear regime, as the disparity in the propagation constants of optical and plasmonic waves becomes important for phase-matching considerations. The large phase-mismatch makes it difficult to apply conventional phase-matching techniques. This is discussed in greater depth in chapter 4.

The challenges in coupling also impede the detection of surface plasmons. Plasmonic phenomena are most commonly measured using optical techniques in the far field. But, without efficient conversion from a plasmon back into the optical domain, the detection of nonlinear plasmonic effects can be extremely challenging. This is especially true for experiments involving nonlinear effects, which tend to be pumped by large field intensities; these pump fields are often still detectable, despite any filtering, and this can often obscure the small nonlinear plasmonic signal.

There are also complications in the study of second harmonic generation stemming from the number of ways that this process may be approached. Whereas in the optical case, second harmonic generation consists of the mixing of two photons at the fundamental frequency to generate a single photon at the harmonic, in the plasmonic case, one or both of the photons may be substituted with a plasmon. The result of this interaction may also be either a photon or plasmon. The different possible combinations for second harmonic generation using light and plasmons are shown in fig. 3.2.

Each of these combinations presents different challenges, requiring the constraints of losses, phase-matching [61, 62] and detection to be reconsidered. This results in very different experimental configurations. In this thesis, we mainly consider fig. 3.2(a-c). Figure 3.2(a) is the typical optical nonlinear process, Figure 3.2(b) is the all-plasmonic second harmonic process, and Figure 3.2(c) is an optically pumped second harmonic generation process, resulting in the nonlinear excitation of a surface plasmon.

The all-plasmonic second harmonic generation process fig. 3.2(b) is the most straightforward analogue to optical second harmonic generation. This process takes advantage of the surface plasmon field confinement. And, the confinement of both the fundamental and
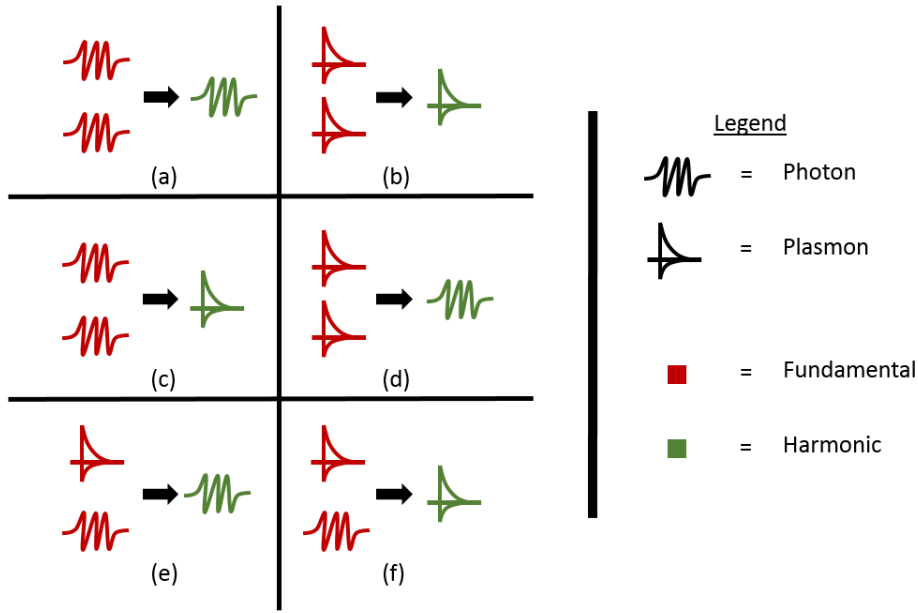
Figure 3.2: Options for second harmonic generation involving plasmons and photons.

harmonic fields to plasmonic modes results in strong modal overlap. Both of these factors are conducive to generating a large nonlinear response. However in this configuration, both the fundamental and harmonic fields are exposed to the plasmonic losses. Efficient coupling to the surface plasmon mode for the fundamental field is also necessary.

In contrast, surface plasmons excited by optically-pumped second harmonic generation fig. 3.2(c) have entirely different constraints. In this configuration, the optical field generating the nonlinear polarisation cannot take advantage of the field-enhancing properties of the surface plasmon, leading to a weaker interaction. On the other hand, there are also a number of potential benefits. Here, the pump field is not exposed to loss, nonlinear effects can be side-pumped to drive the nonlinear effect in a large area, and the optical excitation allows additional degrees of freedom in choosing the polarisation and incident angle of the pump.

3.3.1   Material Considerations and the Metallic Nonlinearity

The study of second-order nonlinearities and surface plasmons can also be divided into categories based on the source of the second-order nonlinearity. Surface plasmons can elicit a nonlinear response from either the dielectric or the metal on which they propagate.

Typically, in nonlinear optics, nonlinear effects are accessed through dielectric crystals. In this case, the $\chi^{(2)}$ nonlinearity is a property of the bulk crystal, and is described by a susceptibility tensor. This approach is still applicable in the plasmonic case, and is explored in detail in chapter 4.

While the dielectric nonlinearity can be made optional in plasmonic devices, the metallic nonlinearity is an intrinsic part of plasmonic waveguides. Unfortunately, the case of the metallic second-order nonlinearity is not as simple as the dielectric case. The metallic nonlinearity exists only at the surface of the metal and the usual treatment of nonlinearities is not applicable [49, 155]. In particular, in [58], instead of modelling the nonlinearity as a susceptibility tensor χ, the metal is considered using a hydrodynamic model for the

electrons. The model is strongly dependent on phenomenological constants a and b. The surface metallic nonlinearity can be divided into two main contributions [58, 156–158]: the first is a true surface term arising from symmetry breaking, and pertains to the electric field and currents perpendicular to the interface (corresponding to the phenomenological constant a). The second is a "bulk-like" term, which concerns the electric fields parallel to the interface (corresponding to the phenomenological constant b). The contribution of this term is strongly related to the skin depth of the metal for a given optical excitation. Both of these contributions have been optically measured [159–161]. The size of the surface second-order response has been shown to be extremely sensitive, to both the surface chemistry of the metal [59], and to surface structures and features [148, 162]. However, since the measured values for a and b are strongly dependent on the surface roughness of the metallic film, adsorbed species on the surface, and the penetration depth of the optical field into the metal, there is no consensus in the literature on the precise value of these parameters. There are not many applications for the metallic nonlinearity in optics, due to the briefness of the interaction that can be achieved between an optical field and a metallic surface on reflection. But for surface plasmons that are bound to the metal surface, the interaction can be significantly enhanced. Unfortunately, since the metallic nonlinearity is largely inaccessible, phase-matching techniques for the metal are largely absent.

3.4 Plasmonic Second Harmonic Generation via the Metallic Nonlinearity
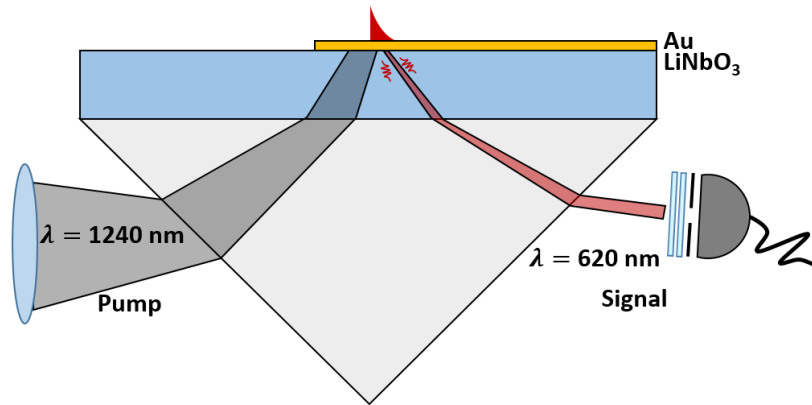
Figure 3.3: Schematic of the experiment with excitation based on a Kretschmann configuration.

In our first study of the interaction of surface plasmons with the second order nonlinearity, we considered the process of all-plasmonic second harmonic generation. We designed an experiment based on the Kretschmann configuration in order to ensure a strong coupling to the surface plasmon, and this is shown in fig. 3.3.

The experiment consisted of exciting surface plasmons with a pulsed $\lambda = 1240$ nm laser source on a thin film of gold deposited on a nonlinear lithium niobate substrate. Using a prism configuration, the plasmon was excited at the gold/air interface. This plasmon mode at the gold/air interface cannot interact with the nonlinearity of the lithium niobate, but can interact with the $\chi^{(2)}$ nonlinearity of the metal, generating a plasmon at the harmonic at $\lambda = 620$ nm. Due to the large dispersion of surface plasmons in the visible, this process

is not phase matched. However, due to the large field intensities provided by the plasmonic field confinement, some harmonic generation on short length scales is expected regardless.

This configuration has the advantage that, at the corresponding surface plasmon resonance angle $\theta_{SPR,\omega}$, it allows efficient coupling to the fundamental surface plasmon mode. The surface plasmon generated at the harmonic is also able to leak, and couple back into light: the same phase-matching conditions which allow optical-to-plasmon coupling in the Kretschmann configuration also allows the plasmon-to-optical leakage by symmetry. The angle of this leakage occurs at the surface plasmon resonance angle $\theta_{SPR,2\omega}$, which must be recalculated for harmonic wavelength. This enables us to use far-field detection methods.
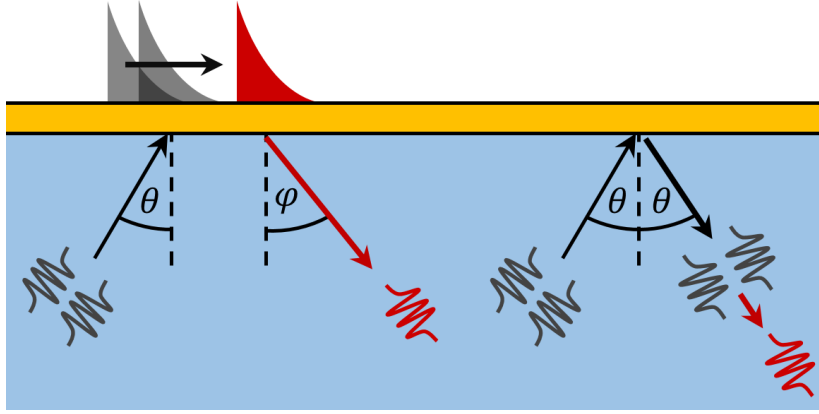
Figure 3.4: Schematic of the interactions being targeted in the experiment.

In addition to the plasmonic second harmonic response, the lithium niobate also generated an optical second harmonic signal, as shown in fig. 3.4. This process is well understood, and allows the strength of the plasmonic response to be gauged. Some of the design elements of the experiment are described in greater detail below.

3.4.1   Sample Preparation and Characterisation

The main material considerations in this experiment were the choice of lithium niobate as the nonlinear dielectric substrate, the choice of gold as the metal, and the film thickness.

Lithium Niobate

The nonlinear dielectric substrate that we chose as a calibration source for the plasmonic signal was lithium niobate. Lithium niobate is a well characterised crystal with 3m point symmetry that exhibits a broad array of properties: It is ferroelectric, piezoelectric, pyroelectric and electro-optic. It also has a wide transmission window through the visible and IR, and is an excellent nonlinear optical crystal. The second-order nonlinear polarisability tensor for lithium niobate is given by [126]:

$$P^{(2\omega)} = \begin{pmatrix} P_x \\ P_y \\ P_z \end{pmatrix}^{(2\omega)} = 2\epsilon_0 \begin{pmatrix} 0 & 0 & 0 & 0 & d_{31} & -d_{22} \\ -d_{22} & d_{22} & 0 & d_{31} & 0 & 0 \\ d_{31} & d_{31} & d_{33} & 0 & 0 & 0 \end{pmatrix} \begin{pmatrix} E_x^2 \\ E_y^2 \\ E_z^2 \\ 2E_y E_z \\ 2E_x E_z \\ 2E_x E_y \end{pmatrix}^{(\omega)}, \quad (3.16)$$

Lithium niobate							
(o)				(e)			
B_1	2.6734	C_1	$1.764 \times 10^{-2}\ \mu m^2$	B_1	2.9804	C_1	$2.047 \times 10^{-2}\ \mu m^2$
B_2	1.2290	C_2	$5.914 \times 10^{-2}\ \mu m^2$	B_2	0.5981	C_2	$6.66 \times 10^{-2}\ \mu m^2$
B_3	12.614	C_3	$4.746 \times 10^{2}\ \mu m^2$	B_3	8.9543	C_3	$4.1608 \times 10^{2}\ \mu m^2$

Table 3.1: Sellmeier coefficients for lithium niobate [103].

where, for lithium niobate, P_z is defined as the optic axis of the crystal. The nonlinear coefficients for lithium niobate are [126]: $d_{33} \approx 27$–30, $d_{31} = 4.5$, and $d_{22} = 2.7$ pm/V. Of particular note is the d_{33} component, which issignificantly larger than the nonlinearity observed for other similar crystals such as KTP ($d_{33} = 16.9$ pm/V), LBO ($d_{31} = 1.09$ pm/V), BBO ($d_{22} = 2.2$) pm/V [126]. This d_{33} component leads to a large nonlinear response along the optic axis $P_z^{(2\omega)}$ when the optical pump is co-polarised (corresponding to a large E_z^2). Lithium niobate is also a negative uniaxial crystal, and has a moderately high refractive index, with $n \approx 2.2$ in the visible. The sellmeier coefficients for stoichiometric lithium niobate were given in table 2.1, but are reproduced here for ease of use. The indices given by n_o and n_e are known as the ordinary and extraordinary indices. When light is travelling down the optic axis, its refractive index is given by n_0, regardless of the polarisation. When light is travelling at an angle θ to the optic axis, its refractive index is given by [163]:

$$n_{\text{eff}} = \frac{n_o n_e}{\sqrt{n_e^2 \cos^2(\theta) + n_o \sin^2(\theta)}} \tag{3.17}$$

Further information about lithium niobate may be found in [164], and its other optical properties in [165]. Due to the wealth of information available for lithium niobate, we considered it to be a reliable nonlinear crystal which could be used to calibrate the plasmonic nonlinear response.

The Gold Film

The source of the nonlinearity for the surface plasmon that we chose was the metallic nonlinearity of gold. The plasmonic coupling to the fundamental was optimised by the choosing the thickness of the gold film, and this process is elaborated below. The optimal thickness is predicted by the same Fresnel equations given in chapter 2.

When a sharp dip occurs in the reflectivity of the thin metallic film, a surface plasmon resonance can be inferred. The optimum film thickness then corresponds to the thickness at which the dip causes the beam to become extinct. The reflectivity for an incident wavelength of $\lambda = 1240$ nm is plotted in fig. 3.5, and it can be seen that the coupling is optimised for a gold film thickness between 30–40 nm. For this thickness, at an incident angle ≈ 27.25 the reflectivity approaches zero, indicative of a plasmon coupling efficiency approaching 1. In practice, the actual coupling efficiency is expected to be weaker, when taking into account the beam divergence and the narrow resonance of the coupling condition—it is only $\sim 0.1°$ wide.

As a result of this analysis, a sample was prepared consisting of a z-cut wafer of lithium niobate[1], partially coated in a gold film of thickness ≈ 30 nm deposited via ion-assisted thermal deposition [124]. A section of the lithium niobate wafer was masked during the

---

[1]A wafer of lithium niobate with its crystal axis (or z-axis) perpendicular to the surface of the wafer.
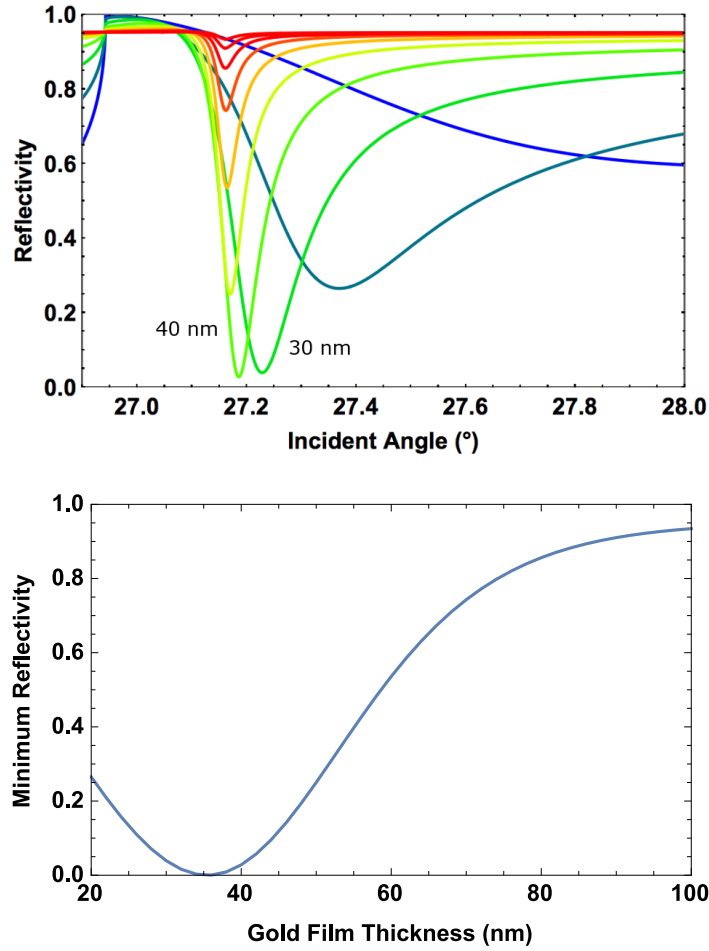
Figure 3.5: (Top) Calculations of the fresnel equations, showing reflectivity as a function of incident angle for a lithium niobate/gold/air setup, for a varying gold film thickness, at $\lambda = 1240$ nm. Gold film thickness varies from 10 nm (blue) to 100 nm (red) in 10 nm steps. (Bottom) Corresponding calculations of the minimum reflectivity as a function of gold thickness. Extinction of the incident light indicates strong plasmonic coupling.

deposition, allowing us to measure the second harmonic response of the sample with and without the plasmonic component by illuminating different sections of the sample. The deposited gold films were characterised using a white light interferometer (Wyko NT 98000), in order to verify the film thickness and quality. The findings were consistent with the gold films described in chapter 2, having a arithmetic surface roughness of $R_a = 1$ nm.

The quality of the gold film was further verified by comparing the reflectivity of the film, as a function of angle, back to the fresnel equations. In order to do this, the sample was mounted on a glass prism using index matching oil in a typical Kretschmann geometry, as detailed in section 2.3, and fig. 2.7. The reflected power from the film was measured near the harmonic wavelength, at $\lambda = 642 \pm 3$ nm, using a WhiteLase (SC400-4) supercontinuum source from Fianium. This light source proved to be much more stable than the source laser at $\lambda = 1240$ nm (described below), used for pumping the nonlinear effect. This was an important consideration for measuring the reflected power over large angular ranges at sub-degree resolution, ultimately allowing the thickness of the gold to be estimated.

Figure 3.6: Experimental reflectivity of gold at $\lambda = 642$ plotted with the theoretical curve using the fresnel equations for a gold film of 32 nm.

A comparison of the fresnel equations and the measured reflection is shown in fig. 3.6. The value for the relative permittivity of gold was taken as $\varepsilon_m = -12.4333 + 1.15196i$. Notably, the extinction in reflected power at the shorter wavelength of $\lambda = 642$ nm is less than at $\lambda = 1240$ nm, dropping to only 30%. the minima is also broadened, being $\a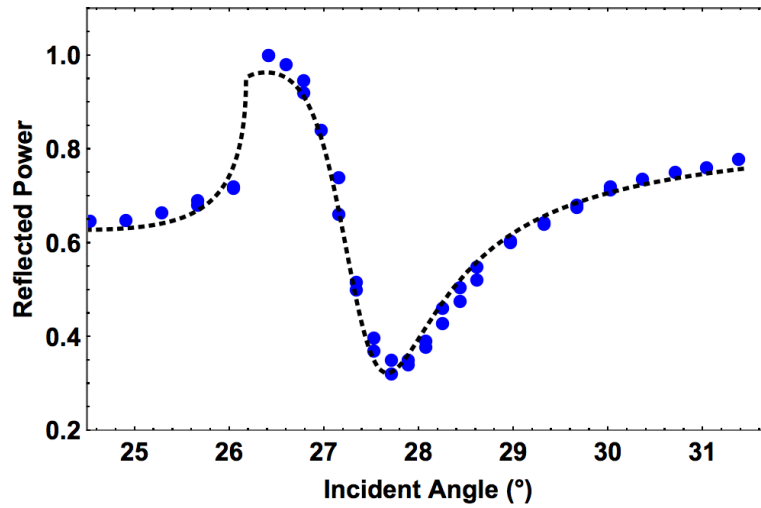pprox 0.1°$ at $\lambda = 1240$ nm, but $\approx 0.1°$ at $\lambda = 642$ nm. This is related to the increase in plasmonic losses in the visible. The comparison between the measured values and the fresnel curve suggest the samples possess good film quality, and that the effective permittivity of the gold closely matches the values found in the literature for bulk gold [101]. The slight deviation is consistent with a film thickness variation in the order of nanometres.

3.4.2 Experiment

Once the gold film on the lithium niobate had been characterised, the sample was probed for a nonlinear response. The laser source was provided by Dr. Aravindan M. Warrier, Dr. Jipeng Lin and A/Prof. David Spence, and was a diamond Raman laser at $\lambda = 1240$ nm with pulses of 6 ps, a repetition rate of 80 MHz and producing up to 600 mW of average power [166]. This laser source allowed large peak powers to be achieved, and was considered convenient for detection purposes: the generated harmonic field, at $\lambda = 620$ nm, lies in the visible part of the spectrum, simplifying the alignment of the detector. Additionally, the harmonic wavelength lies well within the sensitivity range of silicon based detectors, while the fundamental wavelength does not. This improves the detector's ability to discriminate between the pump and harmonic signals. Finally, the choice of the harmonic at 620 nm allowed us to avoid losses that occur at 550 nm which occur due to resonance with the plasma frequency of the gold.

The fundamental beam was focused onto the gold film using a $f = 10$ cm lens giving a beam waist of ≈ 50 μm. Focusing of the beam provides higher field densities but also increases the angular spread of the pump beam and reduces the plasmonic coupling efficiency. The sample itself was attached to a glass prism using index matching oil, and then mounted on a high precision rotation stage ($\pm 0.1°$), as shown in Fig. 3.7. measuring the extinction of the incident beam at the surface plasmon coupling angle, we estimated that the actual
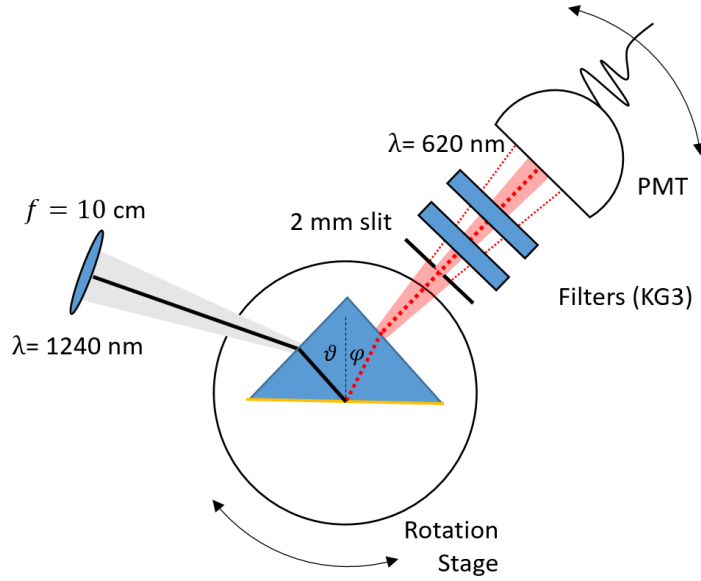
Figure 3.7: Schematic of the experimental setup. The incident angle θ was scanned while the detection angle ϕ was kept fixed with respect to the prism, at the harmonic plasmon leakage angle (27.6°)

coupling was only on the order of 25%. No optical damage occurred to the gold film and no plasma was observed during the experiments. The incident field was TM polarised to coincide with the surface plasmon polarisation. The angle of the incident beam was scanned through the surface plasmon resonance angle ($\approx 27.25°$) in order to observe the harmonic response of the gold film, as well as the harmonic response of the bulk lithium niobate. The incident angle was varied by an external angle of 3.6°, with measurements taken every 0.2°. This corresponded to a range of incident angles on the gold of 1.2°, with measurements taken every 0.075°. This range was limited by the laser power stability and the time required to take the measurements.

The second harmonic was detected using a photomultiplier tube (PMT)(Hamamatsu H10721-20) with a detection area 8 mm in diameter. The photomultiplier tube was sensitive to the $\lambda = 620$ nm harmonic, and insensitive to the $\lambda = 1240$ nm fundamental, as shown in fig. 3.8, providing some discrimination for the detector. Despite this, the fundamental was still detected by the photomultiplier tube, and two additional dielectric absorbing filters (Schott KG5) were required to suppress the pump signal. This PMT was placed at a fixed angle corresponding to the harmonic plasmon leakage angle.

3.4.3   Results

Some of the initial measurements of the second harmonic are plotted in fig. 3.9, showing a second harmonic signal arising in the angular vicinity of the surface plasmon resonance of the fundamental field. However, the width of the observed peak ($\approx 0.7°$) is several times greater than the width of the surface plasmon resonance ($\approx 0.1°$) which we expect to be driving the second harmonic response. Taking this into account, and considering the asymmetry of the observed peak, we surmised that this response was composed of more than a single contribution. To better resolve these components, the effective collection aperture of the detector was reduced. By itself, the photomultiplier tube, with a detecting surface 8 mm in diameter and ≈ 9 cm from the sample, collected light over a 5.1° range. This roughly
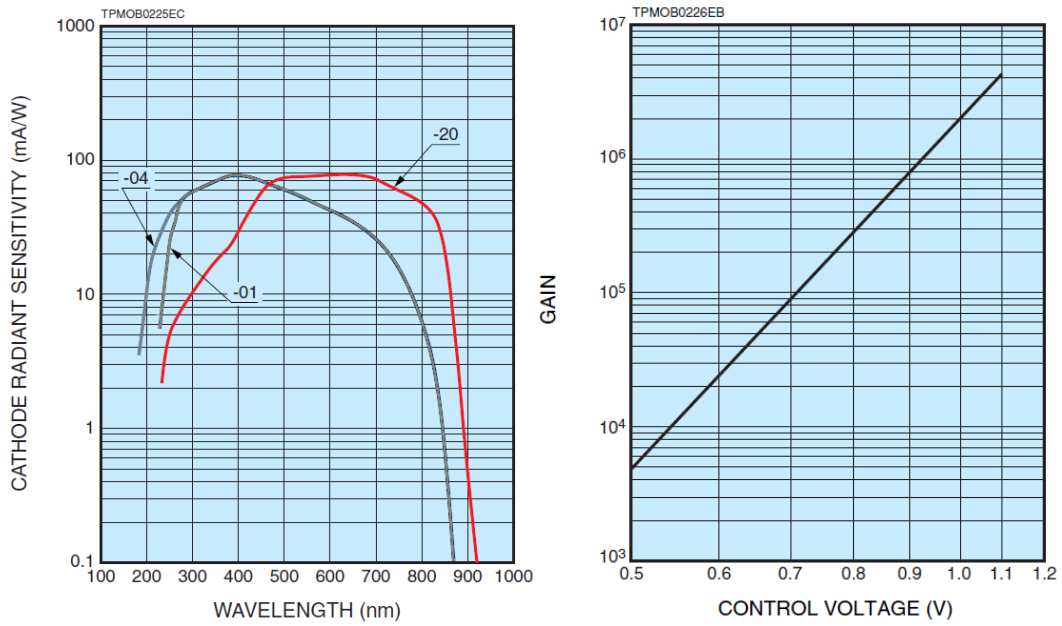
Figure 3.8: (Left) Responsivity curve of the photomultiplier tube (Hamamatsu H10721-20), as reported by the Hamamatsu catalogue. The responsivity curve corresponding to our detector is shown in red. (Right) Gain curve of the photomultiplier tube.

corresponds to a 2.6° range in the lithium niobate. A 2 mm slit was introduced, ≈ 5 cm away from the sample, reducing the angular collection range to 2.3° externally, or 1.2° inside the lithium niobate.

The measurements of the second harmonic response of the sample with the slit in place are shown in fig. 3.10, without any normalisation. The experimental results are shown for both the gold-coated lithium niobate, and bare lithium niobate. Two features are observed, one of which is due to the bulk interaction of the pump light with the lithium niobate, and is present in both experiments (27.2°). The second feature at 27.45° is only apparent in the presence of the gold film, which suggests that it is plasmonic in origin. This feature is offset from the expected angle (27.25°) by 0.2°, where the fundamental beam is optimised for plasmonic coupling. We attribute this to a small calibration error, and infer that this signal corresponds to plasmon-to-plasmon second harmonic generation.

What is immediately evident is that the two processes exhibit comparable efficiencies, as determined by detected levels of the second harmonic signals. At the angle 27.4°, where the plasmonic response was maximised, the pump power was scanned up to 800 mW. The output signal was confirmed to scale quadratically with the pump power as shown in fig. 3.10(bottom), indicative of a second-order nonlinear effect.

We now used the optical signal from the bulk lithium niobate to determine the power in the plasmonic signal. The harmonic field $E_{2\omega}$ generated by the bulk lithium niobate can be calculated by the equation for the second harmonic generation in a bulk dielectric found earlier eq. (3.10):

$$I_{2\omega} = \frac{\chi^2 \omega^2}{\epsilon_0 c^3 n_\omega^2 n_{2\omega}} I_\omega^2 L^2 \text{Sinc}^2 \left(\frac{\Delta L}{2} \right). \tag{3.18}$$

Far from the phase matched condition, which is $\Delta = 2\beta_\omega - \beta_{2\omega}$, the Sinc function simplifies

Figure 3.9: Coarse measurements of the second harmonic response.

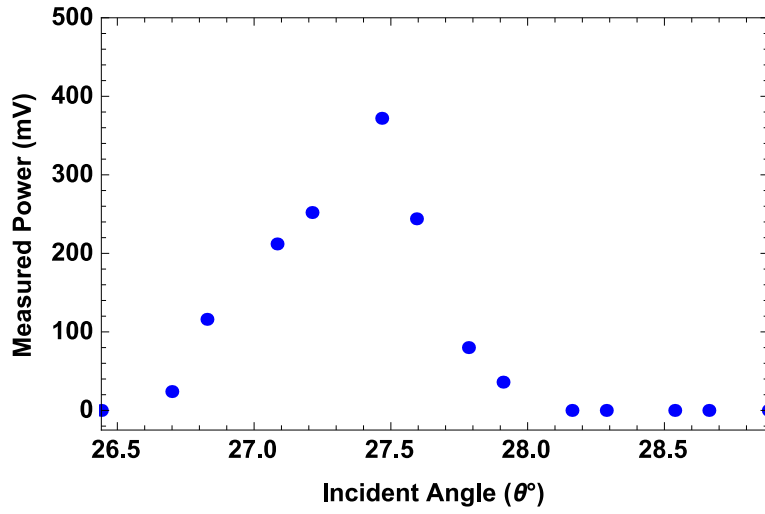to a sinusoidal term with a coherence length that can be calculated to be ≈ 4.8 μm. In this case, the thickness of the lithium niobate substrate (≈ 500 μm), being much greater than the coherence length, can be disregarded. The amplitude of this sinusoidal term can be characterised, and from this the second harmonic signals in fig. 3.10 can then be calibrated. For an average power of 600 mW, a pulse duration of 6 ps, a repetition of 80 MHz and a focal spot size of 50 μm, the peak optical irradiance is found to be 60 MW/cm^2. Using eq. (3.10), the optical harmonic process is found to generate a maximum of 54 μW/cm^2. This calculation allows us to convert the second harmonic signal detected in millivolts to optical intensities, rescaling the plasmonic peak power to 107 μW/cm^2.

We can further relate the detected far field power to the harmonic plasmon amplitude at the metal surface. In this manner, the plasmon-plasmon efficiency of the process can be determined. The measured plasmon power in the far field can be related to the plasmon amplitude by the Poynting vector, modified by a plasmon leakage rate. By using eq. (2.2) and eq. (2.4), we calculated the Poynting vector, integrated across the mode profile, as:

$$
\begin{aligned}
\int |\langle S \rangle| \, \mathrm{d}A &= \int \tfrac{1}{2} \mathrm{Re}[E \times H^*] \, \mathrm{d}A \\
&= \tfrac{1}{4} \frac{1}{\mu_0 c} |E|^2 \mathrm{Re} \left[\frac{1}{n_m k_{x,m}} + \frac{1}{n_1 k_{x,1}} \right],
\end{aligned}
\tag{3.19}
$$

where a constant amplitude E_ω has been assumed. This approximation is valid under the conditions that the pump length is much greater than the propagation length of the leaky plasmon and longer than the coherence length of the nonlinear process (7.5 μm). In this case, the second-harmonic generation can be expected to have reached a steady state value. Here, the pump length corresponds roughly to the illuminated spot size on the metal surface. The spot size is ≈ 50 μm and the propagation length is only several microns. Since the spot size is larger than both the propagation length and the coherence length, this approximation is valid. Subscripts $\{m, 1\}$ correspond to the metal and the air respectively, as before. For the plasmon leakage rate (α, it was found in [17] that this could be calculated as:

$$
\alpha = Im \left[r_{0m} \mathrm{e}^{2ik_{x,m}d} 2 \left(\frac{\omega}{c} \right) \left(\frac{\epsilon_m \epsilon_1}{\epsilon_m + \epsilon_1} \right)^{3/2} \frac{1}{\epsilon_1 - \epsilon_m} \right],
\tag{3.20}
$$

where the Fresnel reflection coefficient r_{0m} is the same as given in eq. (2.10). This leakage
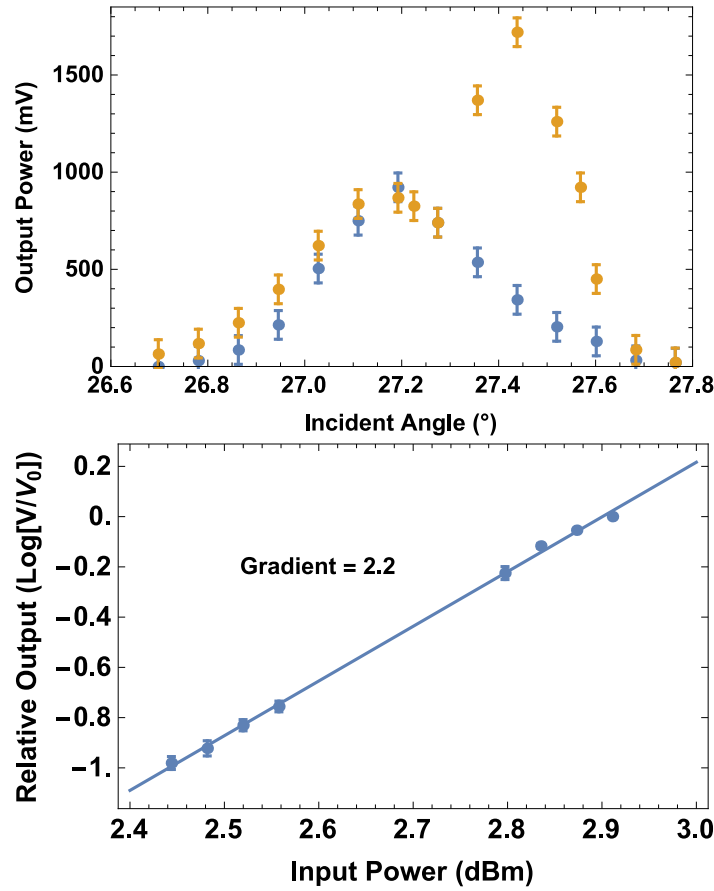
Figure 3.10: (Top) Second harmonic response of the sample as a function of incident angle, shown for bare lithium niobate (blue) and lithium niobate and gold (yellow). An upper bound of the measurement uncertainty has been included (70 mV) (Bottom) Output power as a function of input power, indicating a quadratic trend.

α competes with the plasmonic loss, given by the imaginary part of the plasmon wavevector (β''). We can calculate how much of the plasmon is lost as leakage rather than absorption by calculating:

$$\eta = \frac{\int_0^\infty e^{-2\beta'' z}(1 - e^{-2\alpha z})dz}{\int_0^\infty e^{-2\beta'' z}dz.} \tag{3.21}$$

By a straightforward integration, this simplifies to:

$$\eta = \frac{\alpha}{(\beta'' + \alpha)}, \tag{3.22}$$

giving us the total leakage efficiency. We can find that for $\lambda = 620$ nm, the leakage efficiency is as much as $\eta = 77\%$. Bringing eqs. (3.19) and (3.22) together, we can then relate the detected power to the harmonic plasmon amplitude at the output by:

$$\eta \int_a | \langle S \rangle | dA = P_{2\omega, out}. \tag{3.23}$$

Using this approach, we calculated that the signal detected in the far field of 107 μW/cm^2 corresponds to harmonic field amplitude of 2×10^2 V/m at the metal surface.

Determining the amplitude for the fundamental plasmon is much more straightforward. The plasmonic field amplitude at the fundamental, E_ω, is related to the electric field of the optical excitation $E_{opt,\omega}$ by the equation $E_\omega = T_{01}E_{opt,\omega}$, where T_{01} is the Fresnel transmission coefficient given by:

$$T_{01} = \frac{t_{1m}t_{m0}e^{ik_{x,m}d}}{1 - r_{m0}r_{m1}e^{2ik_{x,m}d}},\tag{3.24}$$

and t_{ij} and r_{ij} is given by eq. (2.10) as before. This approach is generally valid for a collimated, or weakly focused pump beam. However, in the near infrared, the plasmon resonance is extremely narrow, and we expect a significant portion of the excitation beam will not be coupled. Using the estimated coupling efficiency $\sim 25\%$ (section 3.4.2), an amplitude for the fundamental can be calculated at 4.8×10^8 V/m. With the harmonic field amplitude of 2×10^2 V/m, a conversion efficiency can then be estimated at $(A_{2\omega}/A_\omega)^2 = 2 \times 10^{-13}$.

3.4.4 Discussion

Having observed the nonlinear signal, the next step was to determine how the coupling efficiency could be improved. Two of the most significant factors are the short plasmonic propagation lengths and the lack of phase matching.
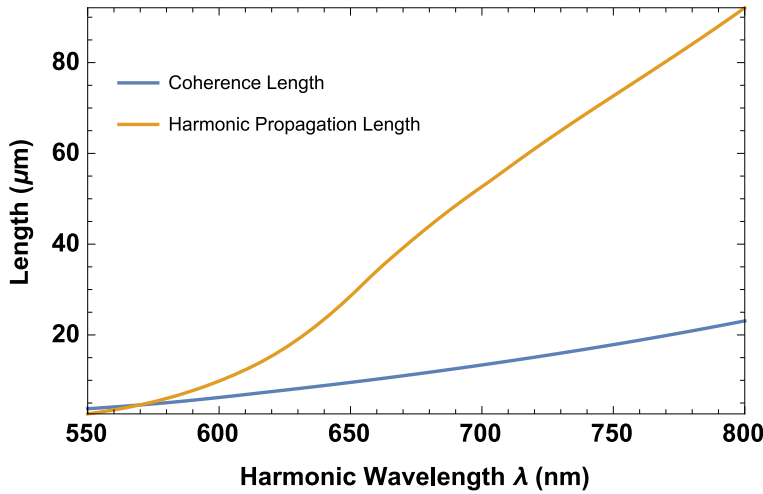
Figure 3.11: Comparison of the coherence length of plasmonic second harmonic generation and the propagation length of the plasmon at the harmonic.

We can compare these two limitations by plotting both the propagation length of the harmonic plasmon (β'') and the coherence length of the second harmonic process ($L_c = \frac{\pi}{|\Delta|} = \frac{\pi}{2\beta_{opt,\omega} - \beta_{plas,2\omega}}$). This is plotted in fig. 3.11. Here we can see that, of these two limitations, the phase-matching is the limiting factor. At the wavelength of 620 nm used in the experiment, the coherence length is only a quarter as long as the propagation length. Given that second harmonic generation is quadratic in length, then in a perfect phase-matching case, an enhancement $\approx 16\times$ might be expected. This enhancement can be seen to also apply for longer wavelengths towards the near IR.

3.5   Conclusion

In this chapter, we investigated plasmonic second harmonic generation in the Kretschmann configuration, drawing on the nonlinear response from the gold. This investigation demonstrated that the metallic nonlinearity, in conjunction with the plasmonic field confinement, is able to generate a second harmonic response similar to that of lithium niobate on short length scales.

However this experiment also highlighted several limitations with this approach. While a strong nonlinear response was observed, the short propagation length of plasmons at both the fundamental and harmonic frequencies severely limits the absolute conversion efficiency of the process. Additionally, the losses associated with the pump beam make this configuration impractical for exploring parametric gain. Processes where the pump was optical instead of plasmonic would allow gain to be provided to the plasmon over a much greater length.

The lack of phase-matching techniques was also a considered a limitation. However, many of the phase-matching techniques developed in nonlinear optics are not applicable for plasmons using the metallic nonlinearity. This prevents the second harmonic response from being scaled to larger lengths.

In light of these findings, we moved away from plasmonic second harmonic generation in metals to explore a more direct method of coupling light and plasmons using second order nonlinear effects in dielectrics where phase-matching could be achieved.

4

Phase-Matched Plasmonic Generation Using Dielectric Nonlinearities

4.1 Introduction

A promising approach to expand on second-order nonlinearities in plasmonics is to draw on the nonlinear response of dielectrics. In contrast to the metallic nonlinearity explored in chapter 3, the nonlinear response of dielectrics is often used in nonlinear optics and has been well characterised. Furthermore, in dielectric materials, numerous methods of phase-matching have been developed, which facilitate large conversion efficiencies.

There have been several studies which have investigated plasmonic second harmonic generation in dielectrics, in a variety of materials. Plasmonic second harmonic generation has been demonstrated using quartz for surface plasmons [63] and long-range surface plasmons [64] in a Kretschmann configuration. Similar configurations have been used for plasmonic second harmonic generation in polarisable dyes [60, 66] and organic polymers with large second order nonlinearities [67]. Notably, there is an absence of many of the more common nonlinear dielectric crystals, such as LBO, BBO, KTP and LiNbO$_3$ in these nonlinear plasmonic experiments. Furthermore, none of these studies has yet been able to draw on any phase-matching techniques to enhance the nonlinear response.

Here, we investigated two optical-to-plasmonic nonlinear processes, using two phase-matching techniques in the nonlinear crystal, lithium niobate (LiNbO$_3$). First, we investigated quasi-phase-matched second harmonic generation using surface poling techniques developed by Dr Andreas Boes and Prof. Arnan Mitchel (RMIT). This is followed by an investigation of parametric down conversion using birefringent phase-matching techniques.

4.2 Propagating Surface Plasmons in High Index Dielectrics

In order to understand nonlinear effects in surface plasmons, let us first treat the surface plasmon linear propagation in these materials. In the previous chapter, only surface plasmons propagating along gold/air interfaces were considered. But dielectric materials that exhibit

large nonlinearities are strongly correlated with high refractive indices [167]; this has a strong impact on the linear plasmonic properties. The propagation constant for surface plasmons propagating in air/gold, glass/gold and lithium niobate/gold have been reproduced from chapter 2 in fig. 4.1, using (eq. (2.6)).
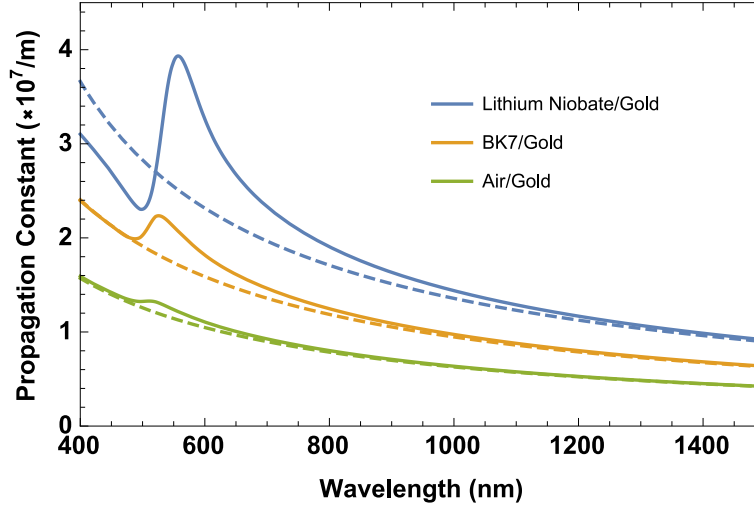

Figure 4.1: Propagation constants calculated for plasmons travelling at gold/air, gold/glass and gold/lithium niobate interfaces. Dotted lines correspond to the corresponding optical propagation constant.

From this plot, it can be seen that for wavelengths between the 500–600 nm, the surface plasmon propagation constant is extremely sensitive to the refractive index of the dielectric. It diverges strongly from the optical dispersion curve and at resonance has a propagation constant $\approx 40\%$ larger. This behaviour makes it difficult to optically phase-match a surface plasmon in high index materials. Unfortunately, as the nonlinear response of a material and its refractive index tend to be correlated, this becomes an essential challenge of nonlinear plasmonics in dielectric materials. It can be noted that at wavelengths shorter than the resonance, the plasmon propagation constant drops once more. However, at these wavelengths, the metal becomes dielectric in character, and the plasmonic properties are no longer evident.

The other key properties of surface plasmons are the propagation length and the mode size. The plasmonic loss is given by the imaginary part of the surface plasmon wavevector (β) and the propagation length is given by its inverse ($1/\beta''$). Similarly, if we consider a surface plasmon propagating on a 2D plane, the surface plasmon mode size is calculated as $1/\text{Re}(k_x^{(d)})$, where the transverse wavevector ($k_x^{(d)}$) is given by eq. (2.5). In the other transverse direction, surface plasmons provide no field confinement, and so will not be considered here. Both of these quantities are plotted in fig. 4.2. For a surface plasmon propagating on a lithium niobate/gold interface ($n \approx 2.1$), there is a drastic reduction in propagation length compared to a plasmon at an air/gold interface ($n = 1$), travelling less than 10% of the distance. On the other hand, the reduction in propagation length is accompanied by a reduction in plasmonic mode size. These subwavelength mode sizes are largely beneficial for nonlinear processes, providing a strong enhancement to the field intensity. In this case, the mode size of the plasmon at a lithium niobate/gold interface is 4× smaller than the corresponding plasmon at an air/gold interface.

The efficiency of second-order nonlinear processes such as second harmonic generation is quadratically dependent on both the interaction length and the field intensity. Given that
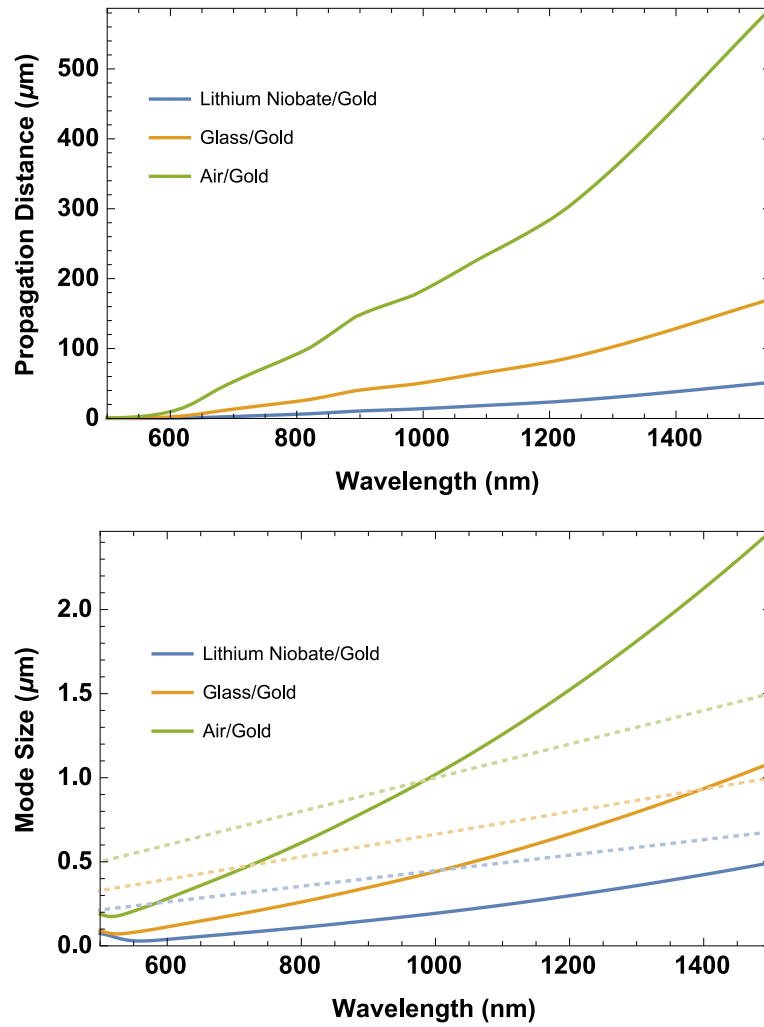
Figure 4.2: (Top) Propagation lengths (e^{-1}) of the surface plasmons in materials of different refractive index, plotted with respect to wavelength. (Bottom) Mode size of the surface plasmons, Dotted lines show the corresponding optical wavelength (λ/n).

the propagation length shrinks more than the plasmonic mode size, then on these considerations alone, a net reduction in efficiency might be expected when moving to high index dielectrics. Consequently, for phase-matching to be worth while, it must outweigh this limitation. Alternately, nonlinear processes that are not fundamentally limited by the plasmon propagation length can be considered, such as optical-to-plasmonic nonlinear processes. For optically-pumped processes, an arbitrarily large area can be illuminated. This can be used in a conjunction with phase-matching techniques to drive nonlinear processes. This is the approach that is taken in this chapter. Other methods to avoid this limitation also exist. For an example, waveguide engineering could be used to reduce plasmonic losses, while also taking advantage of nonlinear dielectrics and phase-matching. However, this was outside the scope of this thesis.

4.3   Quasi-phase-matching and Periodic Poling in Nonlinear Dielectrics

One of the phase-matching techniques that is explored here is quasi-phase-matching. Quasi-phase-matching is a well known technique [168], for overcoming the effects of mismatched wavevectors in second harmonic generation and parametric processes. Quasi-phase-matching consists of periodically inverting the sign of the nonlinear coefficient χ. The inversion of the nonlinear coefficient introduces a π phase shift, which is used to compensate for the phase mismatch between the interacting fields, thus allowing the second harmonic signal to continue to grow. If the nonlinear coefficient is periodically inverted over many coherence lengths, this introduces an effective wavevector component, similar to that of a grating, allowing the phase-matching condition to be rewritten as:

$$2\beta_\omega \pm m\frac{2\pi}{\Lambda} = \beta_{2\omega}, \qquad (4.1)$$

where $\{\beta_\omega, \beta_{2\omega}\}$ are the propagation constants of the fundamental and harmonic respectively, Λ is the poling period, and m is the poling order. For $m = 1$, corresponding to first-order periodic poling, we find that this new phase-matching condition is satisfied when $\Lambda/2$ is equal to the coherence length. For optical quasi-phase-matching of second harmonic generation, this is of the order of microns, to tens of microns.

Under quasi-phase-matching the growth of the second harmonic field growth acquires an undulated appearance, as shown in fig. 4.3, and this leads to an overall slower rate of growth compared to the perfectly phase-matched case. This corresponds to a lower effective nonlinear coefficient, which can be found by [126]:

$$d_{eff} = \frac{2d}{m\pi} \sin(m\pi D), \qquad (4.2)$$

where m is the poling order, d is a tensor component of the nonlinear coefficient χ and D is the duty cycle.

Physically, the poling is achieved by inverting the crystal orientation. This can be done in uniaxial nonlinear dielectric crystals, such as lithium niobate, without affecting the linear properties of the crystals. This modulation of the crystal structure can be achieved in bulk crystals using various methods: such as by stacking discreet crystals in alternating orientations [169, 170], or by direct growth of poling structures [171–173]. Poling may also be achieved by applying a strong external electric field, using either metal [174] or liquid [175, 176] electrodes. The electric field can induce the local crystal structure to invert, resulting in periodic poling structures in a monolithic crystal.

While the domain engineering of nonlinear crystals adds an additional level of complexity to the fabrication process, it facilitates phase-matching in configurations not accessible by other methods such as birefringent phase-matching. For lithium niobate in particular, quasi-phase-matching provides access to the d_{33} tensor component, along which lithium niobate exhibits its largest second-order nonlinear response.
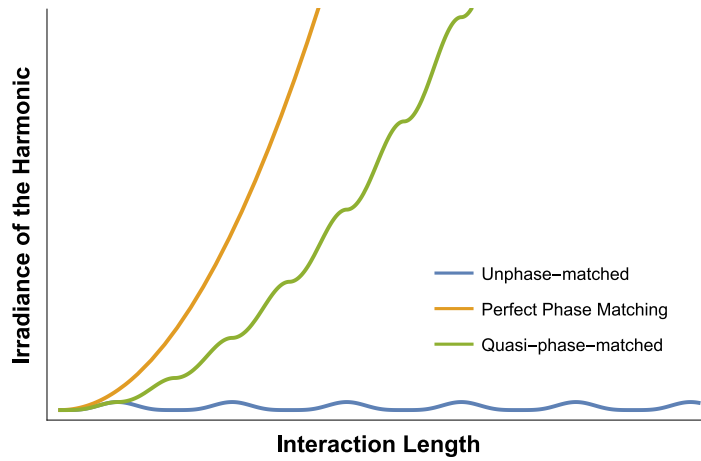
Figure 4.3: Schematic of harmonic field evolution. The field increases quadratically in the perfectly phase-matched case (orange), and oscillates in the unphase-matched case (blue). The quasi-phase matched case lies between these (green). A duty cycle of 50% has been assumed.

4.3.1 Periodic Poling and Surface Plasmons for Second Harmonic Generation

Quasi-phase-matching and periodic poling have been suggested in several studies as a method of introducing phase-matching to nonlinear surface plasmon interactions. In a study by Wu *et al.* [54], periodic poling was assumed in a model of plasmonic second harmonic generation for plasmons propagating on a lithium niobate/silver interface, where the fundamental wavelength was λ = 1550 nm and the corresponding harmonic was λ = 775 nm. This is shown in fig. 4.4 (top)(a). With a poling period of 2.89 μm, Wu *et al.* predicted an efficiency of 0.2% over an interaction length of 11.2 μm. This could be improved by moving towards a long-range surface plasmon configuration fig. 4.4 (top)(a) where, by reducing the losses and increasing the interaction length to 511 μm, a 15.2% conversion efficiency is predicted.

Another theoretical study [55] considered plasmonic-to-optical second harmonic generation, modelling a 500 nm×500 nm lithium niobate waveguide, separated by a 50 nm air gap from a silver interface. This configuration, shown in fig. 4.4 (bottom), results in a hybridised plasmonic mode, allowing some tuning of the plasmonic dispersion, facilitating the phase-matching to the optical mode in the lithium niobate. Using a poling period of 1.81 μm and an input power of 1 W, they predict conversion rates between 1–5%. Unfortunately, this conversion rate was critically dependant on the waveguide geometry and the size of the air gap spacing.

Despite these studies, the experimental demonstration of quasi-phase-matched nonlinear plasmonic effects has yet to be realised. This is largely due to the fabrication constraints required by both these schemes. The poling periods of 2.89 μm and 1.81 μm are significantly shorter than what is required in optical second harmonic processes, and shorter than can be fabricated by most conventional means. In order to obtain poling structures appropriate for plasmonic nonlinear effects, alternate poling processes were required.

Since propagating surface plasmons are confined within a micron or so of the dielectric surface, surface poling techniques become a viable solution. A novel surface poling technique has been used to fabricated poling periods in lithium niobate of the order of a micron or less.
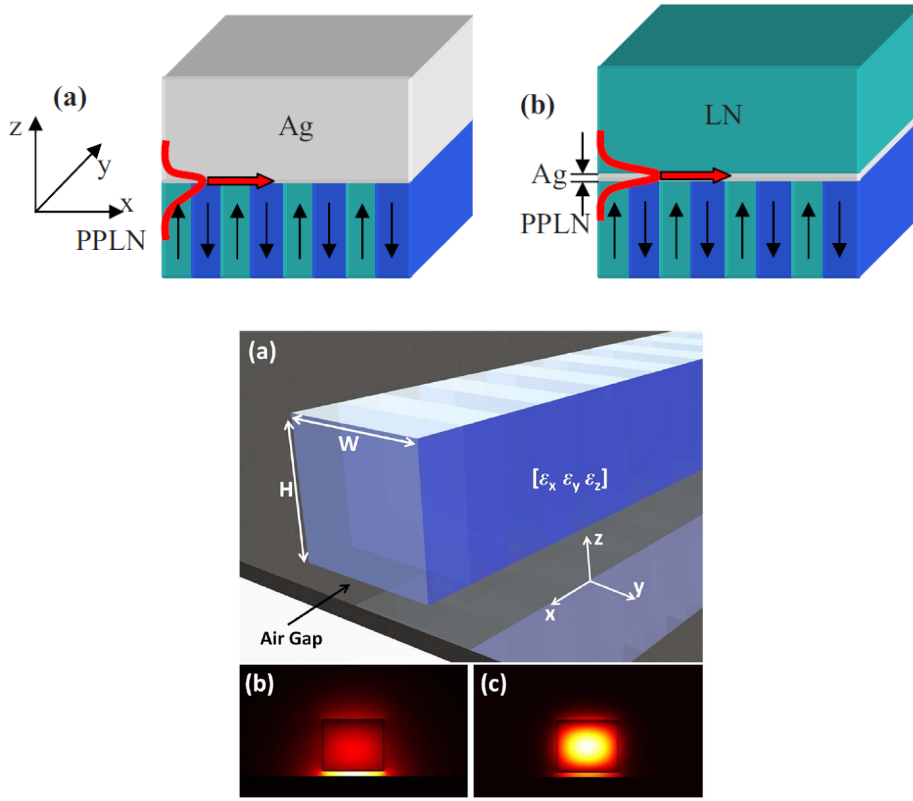
Figure 4.4: (Top) Configurations for quasi-phase matched second harmonic generation suggested by [54], using single interface (a) and long range surface plasmon modes (b). (Bottom) Configuration suggested in [55], consisting of a 500×500 nm periodically poled waveguide rib, 50 nm from the silver surface.

The surface poling techniques used by Dr. Andreas Boes are briefly discussed below.

4.3.2 Surface Poling Techniques

Recently, advances in surface poling techniques of lithium niobate have been demonstrated by Dr. Hendrik Steigerwald, Dr. Andreas Boes and Prof. Arnan Mitchell from the Royal Melbourne Institute of Technology (RMIT), resulting in a significant increase in resolution for periodically-poled structures. Two of the methods for generating surface-poled structures are detailed below. In the first, the poling pattern was created by direct illumination of the lithium niobate wafer with a UV light source [177]. In the second, the poling pattern was obtained by depositing patterned chromium on the surface, followed by UV exposure [178].

In the first case, a UV beam was used to cause local heating in the lithium niobate. Most of the beam is absorbed in the first ≈ 50 nm. At room temperature, a lithium niobate crystal possesses a spontaneous polarization along the c-axis and accumulates a static surface charge on the $-z$ and $+z$ faces. These charges have low mobility. The UV exposure excites free charge carries and, under local heating with the UV beam on the $+z$ face, thermal gradients and the corresponding thermoelectric fields cause the oxygen ions and charge carriers in the lithium niobate to drift and diffuse. The lithium niobate is required to reach temperatures greater than the curie temperature (1210 °C) for this to occur. As the crystal cools, this drift results in a local domain inversion in the heat-affected area. Note that no external electric
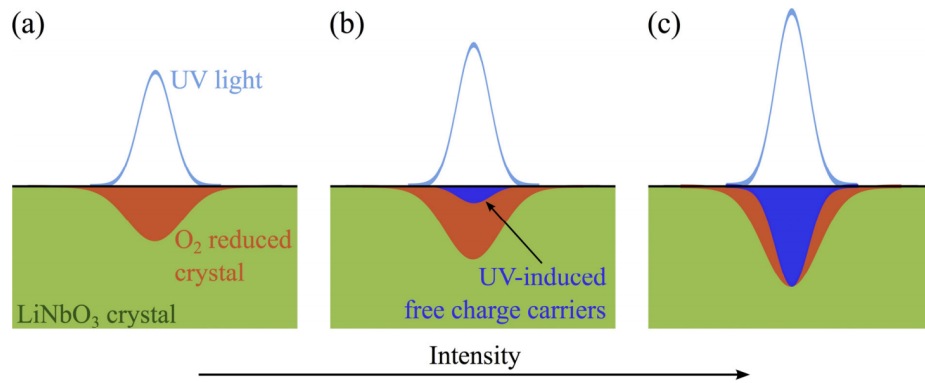
Figure 4.5: Schematic of the basic poling method using UV irradiation from [178]

field is required for this process. This process is shown schematically in fig. 4.5.

The domain size is determined by the size of the heating element or mechanism, and the thermal diffusion rate in the lithium niobate. In this case, the domain size is related to the beam spot size, hence, the limiting factor on domain size resolution is diffraction. The depth of the domain is restricted by the absorption depth of the UV beam, restricting the application of this technique to surface poling.

This technique was used to generate periods of 9–12 μm, using a 244 nm beam with 125–150 mW of power. The cross-sectional profiles of these domains were roughly semicircular, being half as deep as they were wide. Usually, poled structures in lithium niobate leave no visible change to the surface of the lithium niobate, and have to be visualised by permanently etching the lithium niobate in hydrofluoric acid. However, in this case, the poled regions were visible by eye, suggesting surface deformation by the UV beam. The deformation was found to be $\approx$ 3 nm in height, using the white light interferometer (Veeco Wyko NT9800). Additionally, cracks were observed in some cases, probably due to the excess thermal loading. These cracks are shown in fig. 4.6. With plasmonic propagation lengths of the order of microns in the visible, these periods were considered to be too large to facilitate quasi-phase-matching, and furthermore, the cracks would also exacerbate the plasmonic propagation losses.
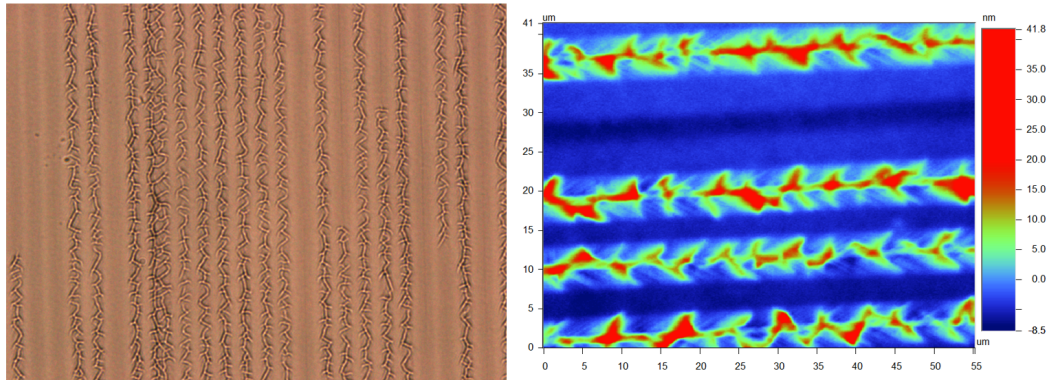
Figure 4.6: Microscopy Images of the 9 μm poling using optical microscopy at 100$\times$ magnification (left) and the white light interferometer at 115$\times$ magnification (right). Damage is clearly visible, and damage sites contain protrusions up to 40 nm above the sample surface.

The second technique consisted of depositing 60 nm of chromium onto the lithium niobate, and patterning the chromium using electron beam lithography [178]. Illumination of the sample with UV light then allows the remaining chromium structures to act as heaters, raising the temperature to ~600–700°. The presence of the hot chromium on the lithium niobate is believed to cause the out-diffusion of oxygen into the chromium layer, accompanied by the opposite motion of lithium ions on the lithium niobate surface. The induced electric field resulting from this defect gradient, in conjunction with the aforementioned thermoelectric field leads to local domain inversion. This method has an advantage for the domain size: the domain size here is related to the size of the chromium structures, and is therefore limited in resolution by the electron beam lithography step. This allows domains 100's of nanometres wide to be defined, corresponding to a minimum poling period of 200 nm for a 50% duty cycle. Since this minimum poling period is much smaller than the effective wavelength of an optical excitation, this technique should be able to satisfy any possible periodic poling configuration. The lower temperatures also reduce the risk of thermal damage to the surface, and generally lead to structures of higher quality. This technique was used to generate poling structures ranging from 200–600 nm. A further discussion of the quality of the fabricated structures is given below. It should be noted that both of these poling techniques are relatively new, and the longevity of the poled domains are uncharacterised. This is particularly difficult as, (ideally) there is no visual change to the crystal caused by the poling. We have assumed that these poling domains were stable throughout the experiments conducted.

4.3.3   Sample Design and Characterisation

Using surface poling techniques, poled structures to facilitate optical-to-plasmonic second harmonic generation could be generated. We calculated the poling periods that would be required for this using eq. (4.1) and this is shown in fig. 4.7. For comparison, the poling periods required in the purely optical case are also shown. We immediately see that the poling periods for optical-to-plasmonic second harmonic generation are significantly smaller than the optical case, and for a fundamental wavelength in the near IR, poling periods shorter than 1.5 μm are needed. In these calculations, we assumed that the optical excitation and propagating plasmon signal were collinear. However, practical considerations demand that the poled structures be illuminated at an angle, shifting the required poling periods to even lower values.

In light of these calculations, two samples of lithium niobate with poling periods ranging from 200–625 nm were generated by Dr. Andreas Boes with a 50% duty cycle, in a variety of configurations including linear gratings, circular gratings, square and hexagonal arrays. One of the final samples is shown in fig. 4.8. The square and hexagonal arrays are not considered in detail here. On visual inspection, a dark line can be seen running down the length of the chip. This is the result of an error in the EBL operation, causing damage to many of the short poled structures. Each poled region was 100 μm × 100 μm, corresponding to the field of view available during the electron beam lithography step. These domains were assumed to be extremely shallow, also with a semicircular cross-section and half as deep as they are wide. The corresponding depth of the poled regions ranged from ≈50–160 nm, making them significantly smaller than the decay length of the plasmon evanescent field. Since the non-poled region is not phase-matched, destructive interference cancels out any contribution. Thus, the shallow domains lead to a reduction in the effective thickness of the nonlinear medium. This then reduces the effective nonlinearity encountered by the plasmon. It was observed that, in places, the surface of the lithium niobate was darkened. This is believed to
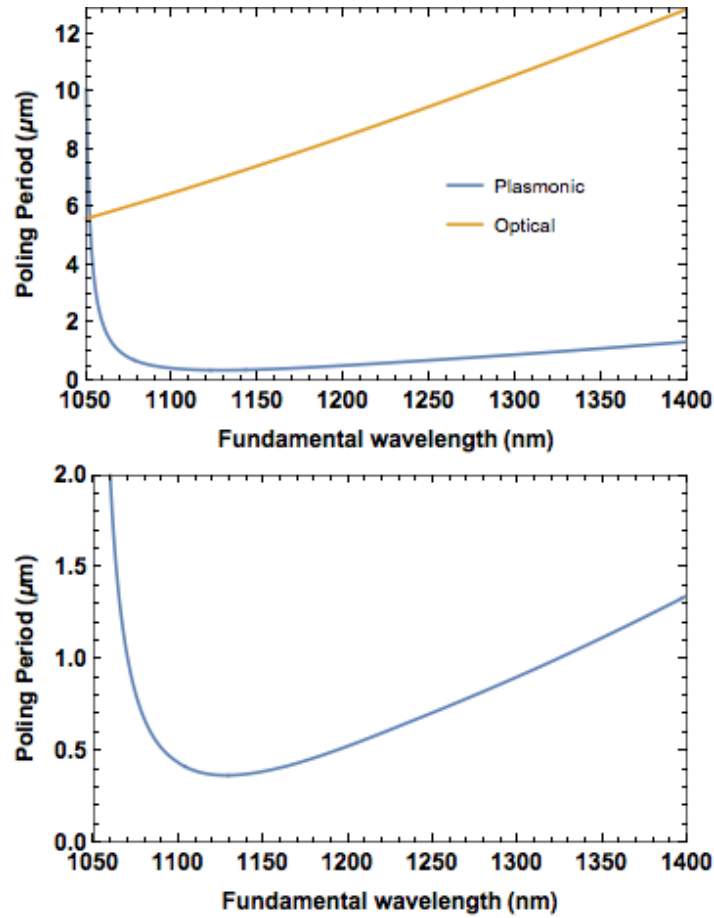
Figure 4.7: Poling periods required in order to achieve first order quasi-phase-matching in lithium niobate, assuming collinear propagation for both the optical-to-optical and the optical-to-plasmonic cases (top). The plasmonic case is also rescaled and plotted separately for clarity (bottom).

be a result of the out-diffusion of the oxygen, and suggests a change to the optical properties of the poled regions [178].

Prior to the deposition of the 100 nm gold film, the lithium niobate was also etched using hydrofluoric acid to depths of 80 nm and 50 nm respectively on the two lithium niobate samples. The differential etching between the $+z$ and $-z$ faces causes the poling structures to be revealed as a physical relief. This served two purposes. The first was to act as an optical/physical grating in order to be able to detect the signal generated by the poling. This is discussed further below. Secondly, the hydrofluoric etch allowed the quality of the poling structures to be assessed using the white light interferometer to measure their physical profile.

Images of a selection of the structures are shown in fig. 4.9. The poling process can be seen to have been very successful in some cases, such as the 525 nm and 625 nm gratings, resulting in highly ordered structures. Others have only partial structures, such as the 575 nm grating and the 600 nm circular grating. Others still failed completely, such as the hex array. The success of the process does not strictly appear to be tied to poling periods, but it was assumed that larger periods were easier to fabricate. This is largely due to the discrepancy between the actual UV dosage used to write the structures, and the effective UV dosage. While the lithium niobate was exposed to a uniform UV dosage, the ideal exposure is dependent on the poling

period–the area of the chromium determining the total energy absorption. Consequently, not all structures were written to the same quality and we decided to work with the structures with longer periods, avoiding the poled structures with a period $\approx$ 200 nm.

Finally, the structures were coated in 100 nm of gold. Notably, this gold deposition was not carried out locally at Macquarie University, and the ion-assisted deposition method was not used. Instead, a chromium adhesion layer several nanometres thick was deposited on the lithium niobate first. We expect this chromium layer to affect the surface plasmon mode and introduce some uncertainty into the plasmon parameters.
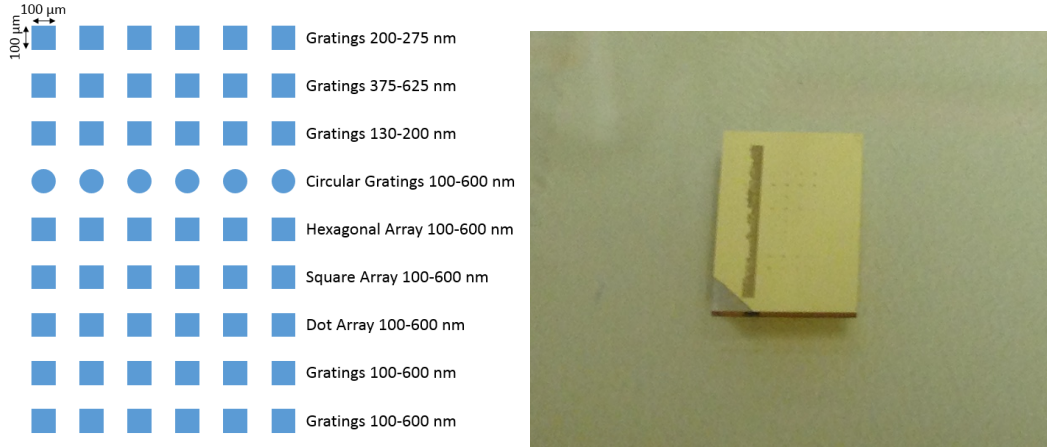
Figure 4.8: (Left) Layout of the lithium niobate surface structures. Structures were 100 μm×100 μm each, separated by 500 μm. (Right) Photograph of a gold coated surface poled lithium niobate chip. Damage is evident on the left side, obstructing the short period structures.

4.3.4   Experimental Design

Using these samples of gold-coated lithium niobate, we then explored optical-to-plasmonic second harmonic generation with quasi-phase-matching. For this experiment, we needed to excite the second harmonic plasmon mode propagating at the lithium niobate/gold interface. The 100 nm layer of gold is more than 3 times the penetration depth of gold (30 nm) and so was considered sufficiently thick in order to remove any interactions between this plasmon mode and the plasmon mode at the air/gold interface. The second harmonic process consisted of targeting the fundamental beam to interact with the poled structures, causing the excitation of a surface plasmon at the harmonic wavelength. This process would only be phase-matched at a particular angle θ, determined by the phase-matching condition:

$$2\beta_{\omega,opt} \sin\theta + \frac{2\pi n}{\Lambda} = \beta_{2\omega,plas}, \tag{4.3}$$

where $\{\beta_{\omega,opt}, \beta_{2\omega,plas}\}$ are the propagation constants of the optical fundamental and the plasmonic harmonic respectively, Λ is the poling period and θ is defined with respect to the surface normal. We have also chosen $n = 1$ for first order poling. The harmonic surface plasmon excited by this process would then interact with the physical grating generated by the HF etch, and would scatter back into a photon at a well defined angle ϕ, given by:

$$\beta_{2\omega,opt} \sin\phi + \frac{2\pi}{\Lambda} = \beta_{2\omega,plas}. \tag{4.4}$$
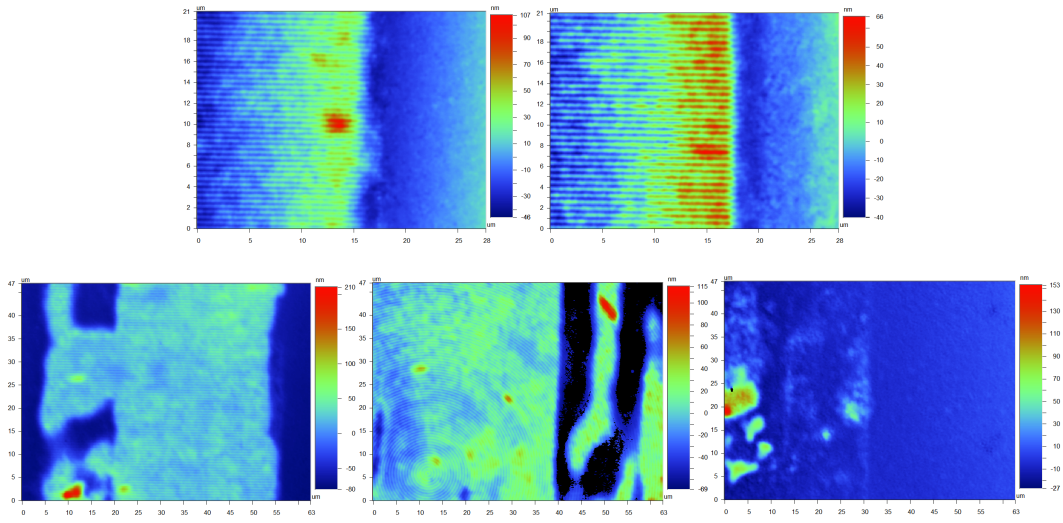
Figure 4.9: A selection of white light interferometer images of the surface poled structures on the sample HF etched to a depth of 50 nm. Imaged using the white light interferometer.(Top Left) 525 nm and (top right) 625 nm grating structures that are clearly visible. (Bottom Left) 575 nm grating and (middle) 600 nm circular grating are only partially written. (Bottom Right) hex structure which failed to write.

Note that, due to the fabrication method, the grating period Λ is the same as the poling period. This coupling scheme is illustrated in fig. 4.10. Both the coupling angle θ and the harmonic
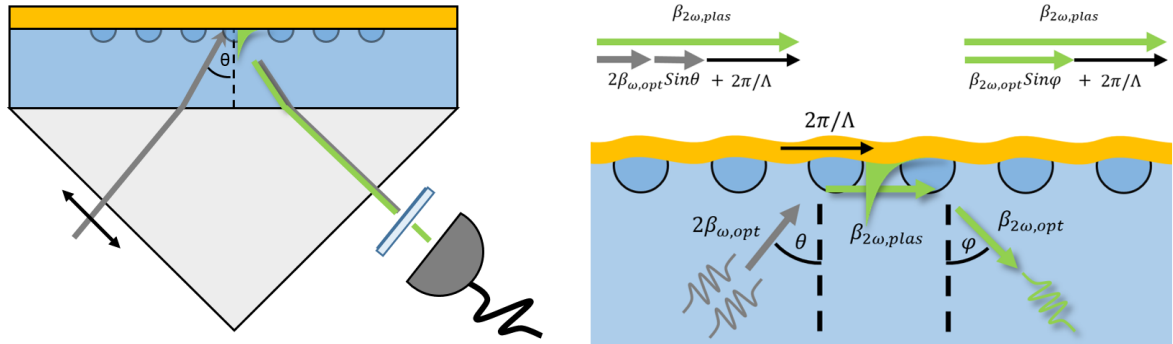
Figure 4.10: (Left) Schematic of the optically-pumped second harmonic process. (Right) Detailed schematic showing the key parameters. The incident angle θ of the 1064 nm beam was swept, while the angle of the detector was fixed at the surface plasmon scattering angle ϕ.

scattering angle ϕ are functions of the chosen fundamental and harmonic wavelengths, as well as the grating periods available. Initially, the poling periods were intended for use with a $\lambda = 1550$ nm laser source, placing the corresponding harmonic at $\lambda = 775$ nm. At this harmonic wavelength, the propagation length is sufficiently long to interact with the poling. However due to the availability of laser sources, an excitation wavelength of $\lambda = 1064$ nm was used instead. This wavelength is not optimal for this experiment, since the harmonic plasmon at 532 nm is close to the plasma frequency of the gold. Consequently, it has a propagation length of 100's of nanometres. Nevertheless, the corresponding angle for the

excitation of optical-to-plasmonic second harmonic generation was calculated for 1064 nm. The code for this calculation has been included in appendix A. This is plotted alongside the scattering angle for the harmonic in fig. 4.11. Note that the excitation angle (and therefore the angle of reflection) of the 1064 nm beam is almost identical to the 532 nm surface plasmon scattering angle.

Eight of the poling periods produced on the sample had excitation angles and detection angles that were accessible. Based on the quality of the structures we decided to focus on one of the longer poling periods, and chose a poled region with a period of 400 nm. For 400 nm poling, the corresponding excitation angle is 35.5° with a harmonic scattering angle of 34°.
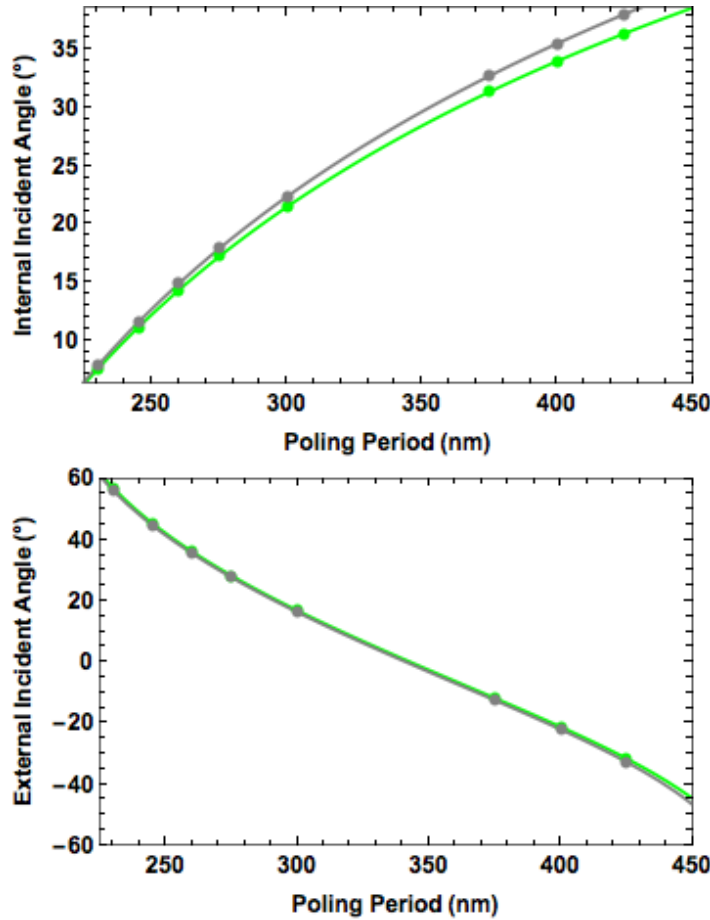
Figure 4.11: Coupling angle for the 1064 nm (grey) and the corresponding exit angle of the 532 nm harmonic (green), as a function of poling period. Angles are shown with respect to the internal angle on the gold (top) and external angle on the prism (bottom). Dots indicate periods corresponding to fabricated structures.

4.3.5   Experiment

The gold-coated lithium niobate structures were mounted on a right-angle prism in order to access the calculated phase-matching angle. The prism was mounted on a rotation and X-Y translation stages in order to ensure that the correct structure was targeted at the correct angle.

The laser source used was a Nd:YAG laser (Ekspla NL220) at 1064 nm with ≈ 5 ns pulses, a repetition rate of 1 kHz, and an average power of 5 mW. The beam was focussed

down to a ≈ 100 μm spot, with a peak power density of 1.6 MW/cm^2. Using a flat section of the gold film, it was determined that this power density did not cause any visible damage to the sample.

A photomultiplier tube (Hamamatsu H10721-20, the same as used in chapter 3), with an 8 mm diameter detecting surface, was fixed in position at the expected harmonic scattering angle. As before, the detector needed to be isolated from the pump beam. This was particularly pertinent due to the similarity of the exit angles for the fundamental at 1064 nm and the harmonic at 532 nm, as shown in fig. 4.11 (bottom). While largely insensitive to the pump beam at 1064 nm, a strong signal could still be detected due to the power in the pump, and the large gain being used. The photomultiplier tube was isolated using a 1064 nm dielectric mirror.

4.3.6   Results
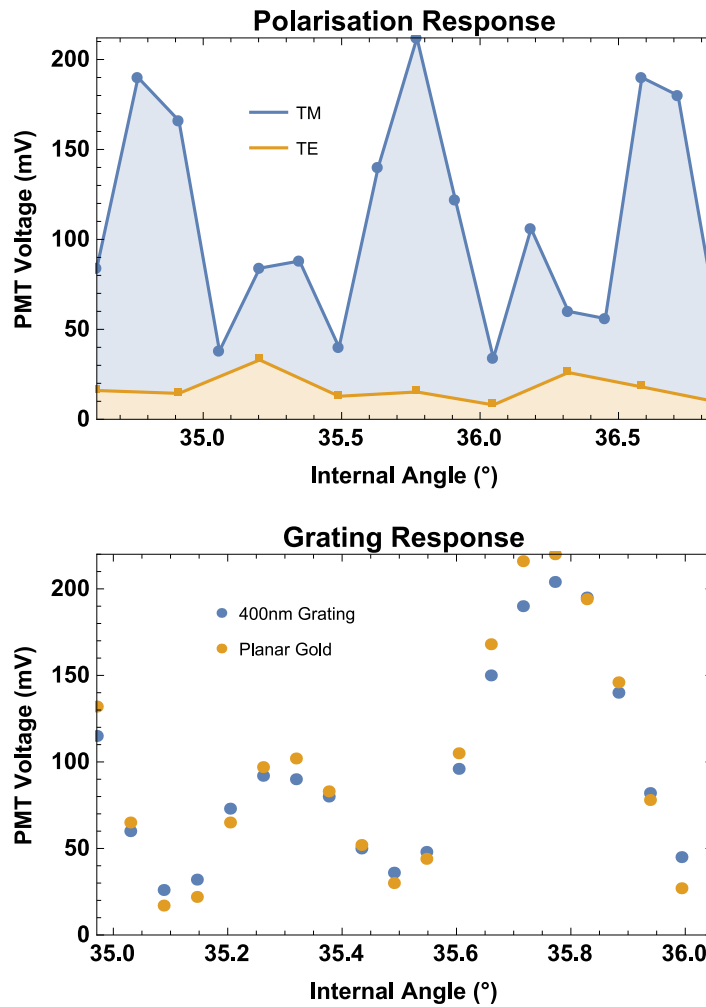
Figure 4.12: Second harmonic signal as a function of input angle. (Top) The signal for TE and TM polarisations. The signal is shown to be much stronger in the TM case. (Bottom) The signal on and off the grating using the TM polarisation. The signal is shown to be almost identical regardless of the grating.

The incident 1064 nm beam was swept over the 400 nm grating for a range of angles in

the vicinity of the harmonic excitation angle and is shown in fig. 4.12. A harmonic signal can be seen at all incident angles for the TM polarisation. The period was found to be consistent with incoherent second harmonic generation in the lithium niobate bulk. Alternating peak heights are also seen, and the cause of this is not known. To test if any component of this signal was plasmonic in nature, the polarisation was rotated $90°$. Using a TE polarisation, no surface plasmons can be excited due to the polarisation restriction of surface plasmons (eqs. (2.2) and (2.4)). Indeed, using a TE polarisation resulted in a significantly diminished second harmonic signal. However, while this is consistent with a plasmonic response, lithium niobate has one strong nonlinear tensor component, d_{33}. This tensor component is accessed by exciting along the crystal axis. Rotation of the input polarisation is therefore also consistent with tuning off the d_{33} tensor component of the second order nonlinearity in lithium niobate, and therefore a reduction in signal is expected regardless of any plasmonic behaviour. Thus this test was not conclusive.

The conclusive test was to measure the harmonic response on and off the grating structures, which would change the appropriate phase-matching conditions for plasmon excitation. The harmonic signals measured in both cases were almost identical (fig. 4.12(Bottom)), and it was concluded that the poling and the grating produced no plasmonic effect.

4.4   Discussion

The experiment on optical-to-plasmonic second harmonic generation resulted in no detectable plasmonic phenomena. We believe this to be largely due to the use of sub-optimal wavelengths because of the lack of a suitable laser source. Due to the short plasmonic propagation length at the wavelength used, we expect that there was insufficient interaction with either the poling or the grating. This would prevent any signal from being detected in the far field. A longer, and therefore stronger, interaction could be achieved by a longer wavelength laser source. Unfortunately, this experiment remains inconclusive.

4.5   Birefringent phase-matching and Parametric Down Conversion in Nonlinear Dielectrics

The final study on plasmonic nonlinear effects consisted of an investigation of birefringent phase-matching techniques through the second-order effect, parametric down conversion. In this case, we could not study second harmonic generation, the simpler process, as the large phase-mismatch resulting from the plasmonic dispersion made it incompatible with birefringent phase-matching techniques.

For parametric down conversion, the plasmonic dispersion presents much less of a challenge, since, at the longer wavelengths being generated, the plasmonic dispersion tends towards the optical dispersion. We therefore conducted our study of birefringent phase-matching focussing instead on down-conversion processes. This study also allows us to directly consider concepts of plasmonic gain.

Birefringent phase-matching takes advantage of the fact that many dielectric crystals which exhibit strong nonlinearities are also birefringent. The polarisation-dependent refractive index provides additional degrees of freedom to control the phase-matching conditions. This has lead to a widespread application of birefringent phase-matching in optics [126]. In uniaxial birefringent crystals such as lithium niobate, light that is polarised orthogonally to

the plane of the propagation direction and the crystal axis is considered an ordinary wave, and its refractive index is given by n_o. For light that is polarised in the plane of the propagation direction and the crystal axis, the light is considered an extraordinary wave, and the effective refractive index is determined by the angle θ between the propagation direction and the crystal axis (eq. (3.17)). By choosing the correct configuration of propagation directions and polarisations, the phase-matching conditions can be met.

There may be many possible configurations that may satisfy the phase-matching conditions, but most can be assigned to two categories which are denoted as type I and type II. In parametric down conversion, type I phase-matching describes configurations where the signal and the idler fields have the same polarisation. This includes cases where both fields are ordinary waves with respect to the optic axis of the nonlinear crystal, as well as cases where both waves are extraordinary waves. Generally, the pump field is in an orthogonal polarisation to the other two waves. On the other hand, Type II describes the configurations where the signal and idler are orthogonally polarised: with the pump being either an ordinary wave or an extraordinary wave.

Birefringent phase-matching can be used for phase compensation for cases where the phase mismatch is equal or less than the total birefringence of the nonlinear crystal Δn. Birefringent phase-matching is also limited by the symmetry of the dielectric crystal and the resulting the second-order susceptibility tensor. These determine the strength of the nonlinear response for a given combination of polarisation states. From an experimental perspective, birefringent phase-matching can be challenging to implement. Each input beam is required to be prepared in a separate polarisation state and combined with a high spatial and temporal overlap. For pulsed laser sources, which are often required to generate the large peak powers, the temporal overlap can be particularly challenging. This requires that short pulse times, and pulse timing jitter and beam quality all be well controlled.

4.5.1 Birefringent phase-matching and Surface Plasmons

When considering the application of birefringent phase-matching to surface plasmons, there are two main concerns. The first is of course the plasmonic dispersion. In order for the plasmonic dispersion to be overcome, nonlinear materials that possess a large birefringence are required. This is particularly true if surface plasmons in the visible are involved in the interaction. Due to this restriction, up-conversion processes like second harmonic generation are largely incompatible with this approach.

Another significant constraint is the polarisation of the surface plasmon. The surface plasmon polarisation is constrained with respect to the interface on which it propagates, and does not have the degrees of freedom needed to implement this method. As a result, in a purely plasmonic nonlinear ineraction, birefringent phase-matching is not viable. Indeed when considering birefringent phase-matching for surface plasmons, optical-to-plasmonic configurations are the only viable solutions.

In the remainder of this chapter, we design and perform an experiment, applying birefringent phase-matching techniques to an optically-pumped plasmonic parametric down conversion process. Our configuration consisted of 620 nm optical pump and 1064 nm signal pulses being coincident on a lithium niobate/gold surface, with the intention of generating a surface plasmon at 1485 nm. The choice and details of this configuration are discussed below.

4.5.2   Experimental Design

Lithium Niobate

Our initial choice of lithium niobate was based on our past experience, and the wide availability of the material. In order to determine whether lithium niobate had a sufficiently high birefringence to facilitate birefringent phase-matching, some basic modelling was carried out. We first considered degenerate parametric down conversion, targeting the near-infrared around the telecommunications band. This wavelength band has a number of advantages: surface plasmons in this wavelength range have lower losses than in the visible and the plasmon wavevector diverges much less. Furthermore, by targeting telecommunications wavelengths, we would also be able to take advantage of mature detector technology made for this wavelength range.

Using this assumption, the phase-matching conditions were calculated using eqs. (2.6) and (3.15), and the properties of lithium niobate given in section 3.4.1. Since the birefringence of lithium niobate is small ($\Delta n_{\lambda=1550} = 0.07$) compared to the refractive index ($n_{\lambda=1550} = 2.2$), the birefringence was ignored during these initial calculations, allowing us to make no assumptions about the orientation of the incident light. The phase-mismatch, plotted in terms of Δn, is shown in fig. 4.13. From this plot, we can see that for parametric down conversion, the phase-mismatch is significantly smaller than in the purely optical case. Furthermore, all values in this range fall below $\Delta n = 0.01$, which is much less than the birefringence of lithium niobate ($\Delta n \approx 0.09$). From this we could conclude that birefringent phase-matching using lithium niobate was feasible for plasmonic nonlinear processes.

For comparison, it is illustrative to plot the phase-matching condition for second harmonic generation. In this case, the optical-to-plasmonic curve instead lies far above the optical curve. In particular, we can consider the case of second harmonic generation from 1064 nm light to produce plasmons at 532 nm. Here, the phase mismatch term is $\Delta n \approx 0.21$, falling well above the total birefringence of lithium niobate. This large phase mismatch demonstrates the difficulty in using birefringent phase matching for plasmonic second harmonic processes.

Wavelengths

Now that lithium niobate was determined to be a suitable nonlinear crystal, the wavelengths had to be selected. We pursued an arrangement consisting of a pump wavelength of 620 nm and a signal wavelength of 1064 nm, yielding an idler at 1485 nm. These particular wavelengths were chosen, as they could both be generated by the same laser source: the 1064 nm field could easily be accessed using a Nd:YAG laser, while the 620 nm field could be obtained by a combination of frequency doubling and Raman shifting in diamond. By choosing wavelengths that could be generated by the same pulsed laser source, we could ensure that the pulses were synchronised in time, and could more easily be overlapped at the sample.

Configuration,

To determine the phase-matching for this combination of wavelengths, we chose to model a Type I configuration, as shown schematically in fig. 4.14. This configuration allows the plasmon-enhanced wavevector to be compensated by the birefringence. Since lithium niobate is a negative uniaxial crystal, the pump was chosen to be an extraordinary wave, and its corresponding wavevector is tuned by rotating the crystal orientation θ. The signal and the plasmonic idler field are polarised perpendicularly to the crystal axis. As ordinary waves,
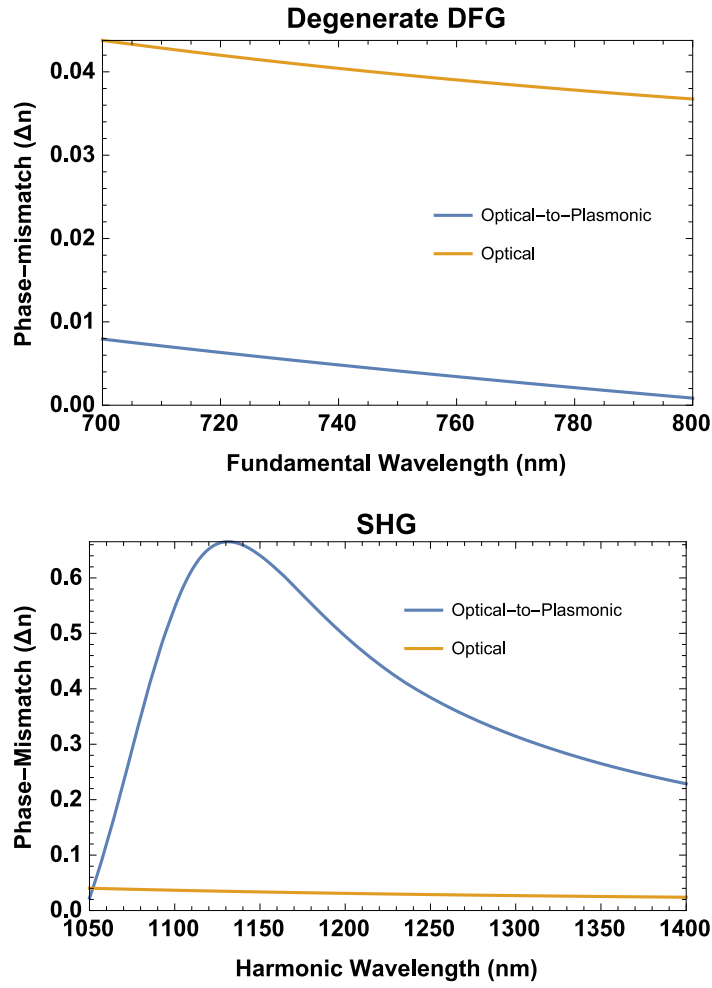
Figure 4.13: Phase mismatch required for phase-matching second harmonic generation (Top) and degenerate difference frequency generation (Bottom), plotted in terms of effective index Δn. Optical and optical-to-plasmon cases are shown for comparison. Note the difference in vertical scales.

their wavevectors $\{\beta_{s_{opt}}, \beta_{i,plas}\}$ are largely insensitive to the crystal rotation. The pump and signal fields were also assumed to be incident on the lithium niobate crystal at a small angle ϕ, ensuring that the entire beam is incident on the lithium niobate/gold interface. Thus, the signal is not truly an ordinary wave.

The phase-matching condition for this configuration can be described by:

$$\cos(\phi) \left(\beta_{p,opt}(\theta) - \beta_{s,opt}(\theta, \phi) \right) - \beta_{i,plas} = 0$$

$$\sin(90 - \phi) \left(\frac{2\pi}{\lambda_p} n_p(\theta) - \frac{2\pi}{\lambda_s} n_s(\theta, \phi) \right) - \beta_{i,plas} = 0, \tag{4.5}$$

where $\{\lambda_p, \lambda_s\}$ are the free space wavelengths of the pump and the signal, and $\beta_{i,plas}$ is the propagation constant of the plasmonic idler. Here, the phase-matching condition has been modified to consider only the projection of the pump and signal fields along the metallic interface. The angular dependence is written as $\sin(90 - \phi)$ in order to keep with convention, defining the incident angle on a surface with respect to the surface normal. For the pump,
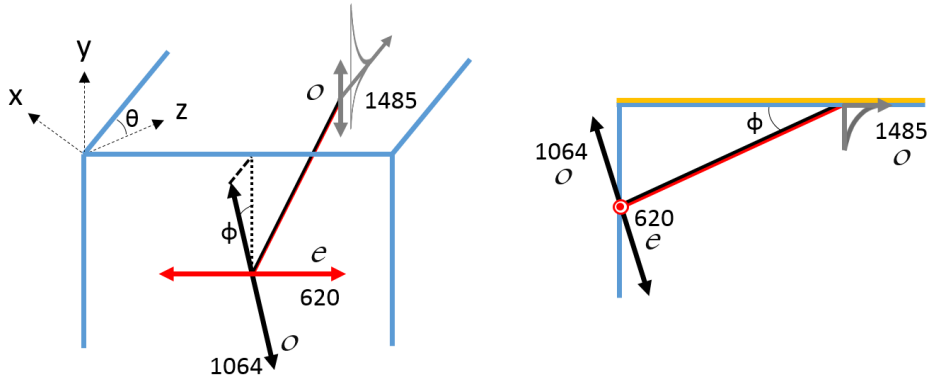
Figure 4.14: (Left) Polarisations of the pump (red), signal (black) and idler (grey) fields. Here, ϕ corresponds to the small angle of the incident fields with respect to the crystal, (blue). The angle θ defines the crystal orientation, where $\hat{z}$ corresponds to the crystal c axis. (Right) The side view of the crystal with coincident pump and signal fields at an angle ϕ to the crystal surface with the gold film (yellow)

the effective index $n_p(\theta)$ is simply dependent on θ, and is given by the regular equation for uniaxial crystals eq. (3.17). For the signal, the effective index is dependent on both the crystal angle θ and the angle of incidence ϕ. By using geometric arguments, the effective index $n_s(\theta, \phi)$ can be found to be:

$$n_s(\theta, \phi) = \frac{n_o\, n_e}{\sqrt{n_o^2 \cos^2 \theta\, \sin^2 \phi + n_e^2 (1 - \cos^2 \theta\, \sin^2 \phi)}}, \quad (4.6)$$
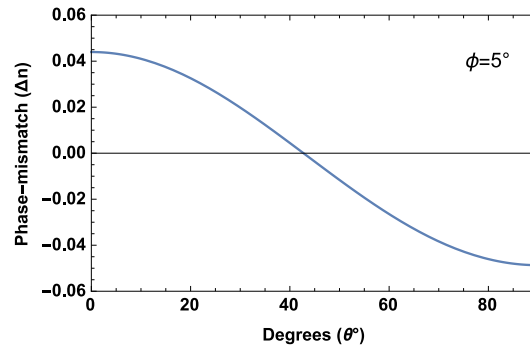
Figure 4.15: Phase-mismatch as a function of crystal angle θ for the configuration shown in fig. 4.14. The phase-mismatch has been normalised by the optical wavevector of the idler $k_{i,opt}$, giving phase-mismatch in terms of Δn.

The phase-matching condition is shown in fig. 4.15, plotted as a function of crystal angle, and the code for this calculation has been included in appendix A. Here the pump and signal fields are assumed to be incident at a grazing angle (5°). Under these conditions, we determined that phase-matching occurs in this Type I configuration for a crystal angle of $\theta = 43°$. For this combination of crystal angle and polarisations of the 620 nm and 1064 nm beams, the corresponding nonlinear tensor component is the d_{31} component, and the effective

nonlinear coefficient is 3 pm/V.

4.5.3   Numerical Modelling of Detection

In addition to ensuring the correct conditions for parametric down conversion were met, the method for detecting the generated plasmon had to be determined. The surface plasmon being excited here is tightly bound and, in the ideal case, has no natural leakage modes. The usual approach is to out-couple via a grating, however this was considered impractical in our case. Most gratings used in plasmonics are restricted to areas of around 100×100 microns, which is determined by the field-of-view of the fabrication technique being used (focussed ion beam or electron beam lithography). These small areas would be difficult to target reliably using free space optics, and introduce unnecessary uncertainties into the experiment. The other obvious method of detection in the far field is to rely on scattering caused by the surface roughness of the gold film. However this was deemed unreliable, as this results in non-directional scattering, making it difficult to collect efficiently with a far-field optical detector.

Instead, we decided to investigate scattering off a simple sharp edge of the gold. If the scattering behaviour proved favourable, this approach would be simple to implement and robust. To determine the scattering behaviour of such an edge, a simulation was constructed in COMSOL, consisting of a propagating surface plasmon and a sharp rectangular gold edge.
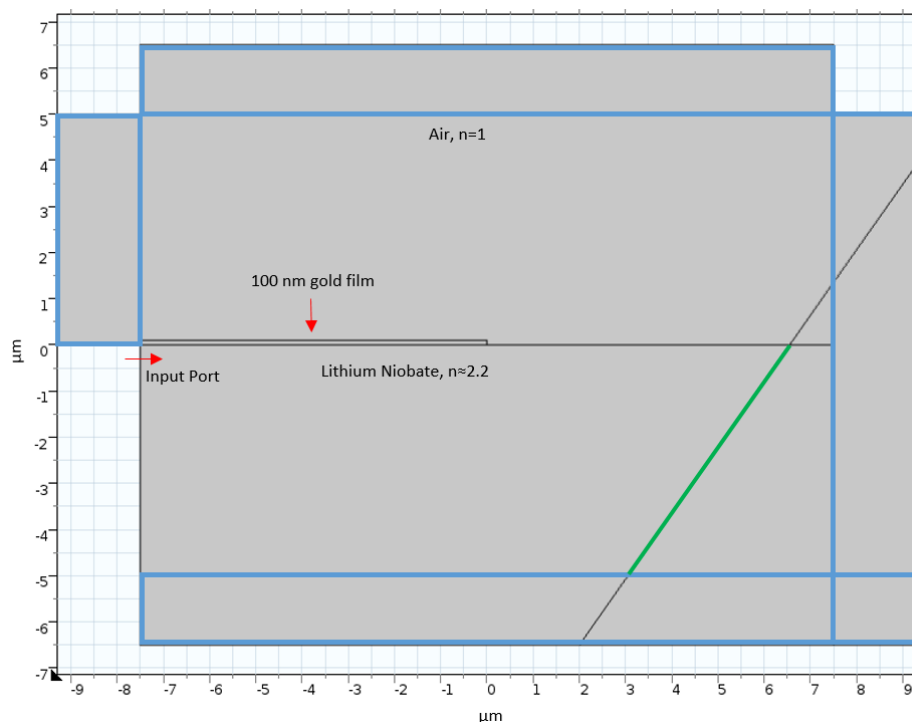
Figure 4.16: Scattering configuration simulated in COMSOL in 2D. Absorbing boundaries are indicated in blue. Radiated power was later calculated by integrating along the line indicated in green.

The simulation configuration is shown in fig. 4.16. It consisted of a 2D, 15×10 μm simulation box, with a gold film that is 100 nm thick and terminated with a rectangular edge. In the third dimension, the simulation assumes homogeneity, allowing the simulation to only consider a 2D problem. This drastically reduces the meshing elements required, as well as the computation time. The gold layer sits on top of a layer with a fixed refractive index of $n \approx 2.2$,

approximating the behaviour of lithium niobate. In this simplified model, the birefringence is not included. On top of the gold was a layer with a refractive index of $n = 1$, corresponding to the air. At the input port on the left, an electromagnetic wave can be injected into the simulation, and by choosing the field distribution of this wave to be consistent with a plasmon mode distribution (eqs. (2.2) and (2.4)), light can be launched into a surface plasmon mode. Most of this light is expected to couple to the plasmon mode, however some of the light is expected to scatter due to discontinuities at the simulation boundary. The surface plasmon propagates along the gold film, scatters at the gold edge, and then leaves the simulation via the absorbing boundaries (indicated in blue). The relatively small size and the simplicity of the simulation allows a dense mesh to be used without incurring large computation times. The maximum distance between mesh elements in the metal was set to be 4 nm in the gold, and $\lambda/(8n)$ in the rest of the simulation box. Both of these mesh element sizes were well below the effective wavelength of the light in the respective materials, ensuring the accuracy of the simulation. The quality of the simulation was later verified by doubling the density of the mesh. The field distribution remained constant between simulations, and no significant change in power was observed (<2%).
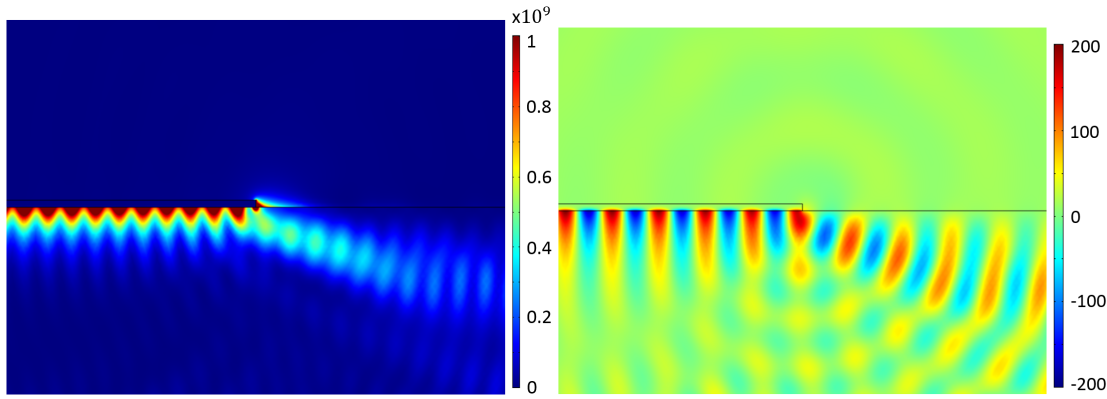
Figure 4.17: COMSOL simulation of the surface plasmon scattering off a rectangular edge. The colour map is shows $|E|^2$ (Left) and H_z (Right).

The results of this simulation are shown in fig. 4.17, showing both $|E|^2$, which is proportional to power, and H_z, in order to visualise the fields. On encountering the edge of the gold, some light can be seen to radiate into the air, however the majority of the scattering occurs into the higher index material. The surface plasmon scattering into the lithium niobate scatters in a semi-directed cone, at an angle approximately 22° from the surface. This scattering angle is sufficiently different from the intended angle of incidence for the 620 nm and the 1064 nm optical beams (chosen to be 5° in section 4.5.2), affording a level of angular discrimination between the plasmonic optical effects. This cone is approximately 13° wide on leaving the lithium niobate crystal. Interference fringes can be seen along this radiated cone.

The power radiated in this cone can be estimated by integrating $|E_{rad}|^2$ along the line indicated in green in fig. 4.16, and comparing it to the input power. The input power was found in a separate simulation, without the abrupt gold edge, by integrating $|E_{in}|^2$ across the input port. This step was necessary in order to remove any power reflected from the gold edge from being included in the integration. From this, the fraction of power that is radiated from the gold edge can be estimated to be $|E_{rad}|^2/|E_{in}|^2 = 35\%$. Given the amount of radiated power and the semi-directional nature of the cone, we considered this method for scattering

surface plasmons to be sufficient for detection in the far field.
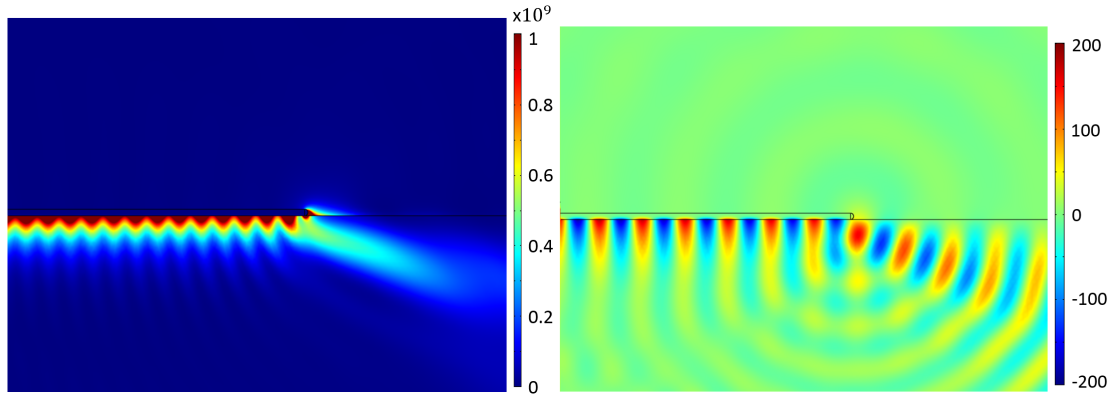
Figure 4.18: Plasmon scattering off a rounded edge, plotted in (left) $|E|^2$ and in (right) H_z.

Two other similar simulations were also carried out in COMSOL: the first was a simulation of surface plasmon scattering off a gold film with a rounded edge, with a radius of 50 nm, and the second was surface plasmon scattering off a slit in the gold. The simulation of the rounded edge was to investigate how the shape of the gold edge might affect the scattering pattern. Due to the the thickness of the gold film and the deposition method, direct control over the profile of the gold edge was not possible, and we wanted to investigate how this might influence the scattering behaviour. The results of this simulation are shown in fig. 4.18. In the rounded edge case, the scattering is extremely similar to the previous case, with forward scattering in a narrow cone, at angle of 22°. The main difference is the lack of interference fringes in the radiated cone, which allows us to infer that these fringes are related to the morphology of the gold edge. However, as the scattering angle was preserved, we concluded that the shape of the gold edge would not strongly affect the detection of the surface plasmon.
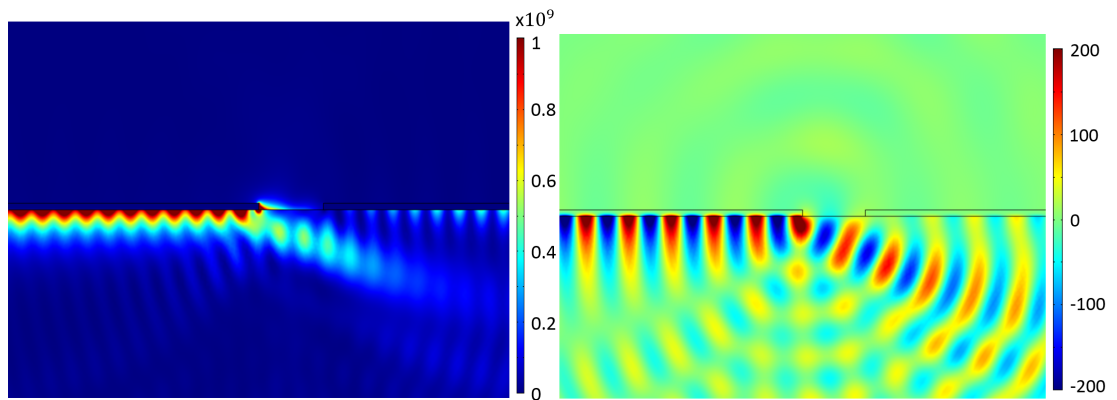
Figure 4.19: Surface plasmon scattering off a 1 μm slit, plotted in (left) $|E|^2$ and in (right) H_z.

The other simulation that was carried out involved a surface plasmon scattering off a slit. Slits in gold films have been shown to be useful under certain circumstances for launching surface plasmons [179], and so we wanted to investigate their ability to scatter plasmons. The simulation of a surface plasmon scattering off a 1 μm slit is shown in fig. 4.19. A 1 μm slit is wider than is typically used for exciting surface plasmons, but corresponds to an optimistic

estimate of what might be achievable in our lab. The simulation shows that the scattering off the slit is similar to the original scattering simulation: light scatters off the initial gold edge, radiating in a cone. In addition, surface plasmons can be seen to couple from one gold film to the other. Overall, very little change is observed in the far field radiation behaviour. For smaller slit widths below 1 μm, coupling across the slit gets stronger, and the scattering gets weaker. This is consistent with end-fire coupling from waveguide to waveguide. From this simulation, we concluded that using a slit appeared to confer no benefits for plasmon scattering.

As a result of these simulations in COMSOL, we concluded that a gold edge was sufficient to induce plasmon scattering, and that the semi-directed nature of this scattering should enable far-field detection using an near IR detector.

4.5.4   Sample Preparation and Characterisation

As a result of the phase-matching calculations and the COMSOL modelling, two 9×9×25 mm lithium niobate crystals, with the crystal cut at an angle of 43°, were obtained from Castech. These crystals were polished by the supplier on four of the six faces to allow optical access during the experiment. We deposited gold on the top face to a thickness of 100 nm as before,
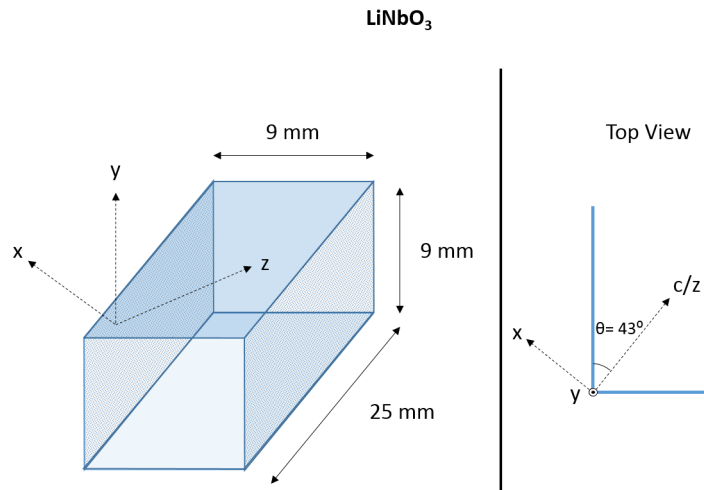
Figure 4.20: Crystal orientation for mixing 620 nm and 1064 nm, generating 1485 nm. The top, bottom, front and back surfaces were polished.

using the ion-assisted gold deposition method. During the deposition, both lithium niobate crystals were partially masked using Kapton tape, resulting in partial coverage of the gold and an edge on which the surface plasmons could be scattered. The edge was also used to verify the thickness of the gold film, finding the actual gold film thickness to be of the order of 80 ± 5 nm with a surface roughness (arithmetic roughness) of $R_a \approx 1$ nm. Although the gold film was thinner than anticipated, this is expected to have little effect on the surface plasmon, as the film thickness is still several times greater than the plasmon decay length into the gold. Indeed, additional simulations carried out in COMSOL showed no change in surface plasmon scattering angle, and no change in power(<2%) was observed. This is due to the fact that the scattering behaviour is dominated by the interaction at the interface, and not the gold bulk. The white light interferometer also revealed roughness along the gold edge

with features on the order of 10 microns, as shown in fig. 4.22. We expect that these features introduce additional scattering, and reduce the directionality of the scattered cone.
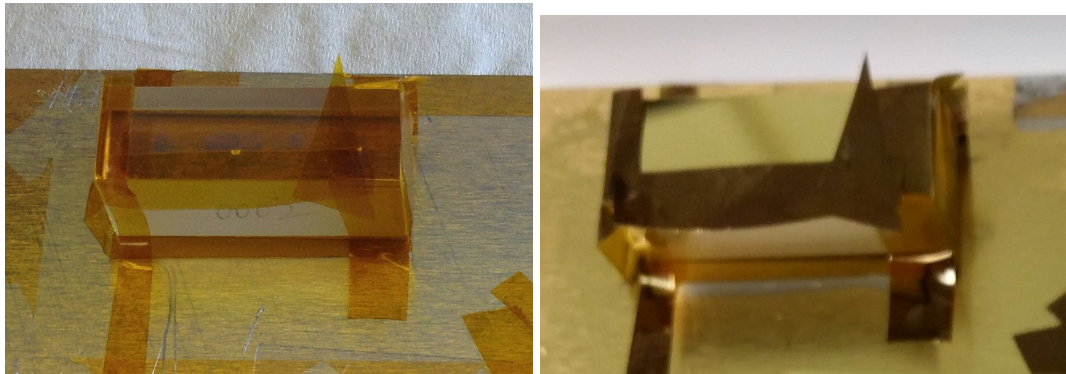
Figure 4.21: Photos of the lithium niobate crystals, before (left) and after (right) the gold deposition.

4.5.5 The Experimental Setup

The Laser Source

The experiment set up for probing parametric down conversion in the lithium niobate samples is shown in fig. 4.23. Similar to the previous experiment, and relying on lasers available in the lab, the laser source used to generate both the pump and the signal pulses was a Ekspla NL220, consisting of a Q-switched Nd:YAG laser with $\lambda = 1064$ nm, producing 6 ns pulses at a 1 kHz repetition rate. The nanosecond pulse duration differs from previously reported studies of nonlinear plasmonics which commonly use pulse durations with ≈ 100 fs (notably [67]). The longer pulses used here result in lower peak powers, compared to the femtosecond case, and in general provide a weaker nonlinear response. The longer pulse times also lead to an increase in pulse energy, increasing the likelihood that thermal effects will be observed. However, the longer pulse duration makes it much easier to temporally overlap the pulses, making the experimental setup more robust; this was considered essential.

The Ekspla NL220 contains an internal doubling crystal and can simultaneously output both the fundamental ($\lambda = 1064$ nm) and the harmonic ($\lambda = 532$ nm) beams. The power in each arm could be tuned internally, as well as externally, using a combination of half-waveplate and polarising beam splitters. The 532 nm beam was then Raman shifted using a diamond crystal (with a Stokes shift of 1332 cm^{-1} [180]) to the second Stokes wavelength, in order to obtain a beam at $\lambda = 620$ nm. This was achieved with the help of Dr. Aaron Mckay. To maximise the second Stokes output, the 532 nm beam polarisation was rotated to coincide with the (111) crystal axis of the diamond, taking advantage of the highest Raman gain coefficient. Additionally, the diamond crystal was placed in a low Q cavity. The input mirror of this cavity had a radius of curvature of 500 mm and was transmissive at 532 nm and highly reflective at the first and second Stokes wavelengths. The output mirror was highly reflective at 532 nm and the first Stokes, and 50% reflective at the second Stokes. The resulting second Stokes pulses had a pulse duration estimated at ~ 3 ns, and an average power up to $\sim$25 mW. The 620 nm light was separated from any remaining 532 nm light after the cavity using a narrowband 532 nm dielectric mirror. It was then collimated using a $f = 50$ cm lens, resulting in a beam width of ≈ 2 mm.
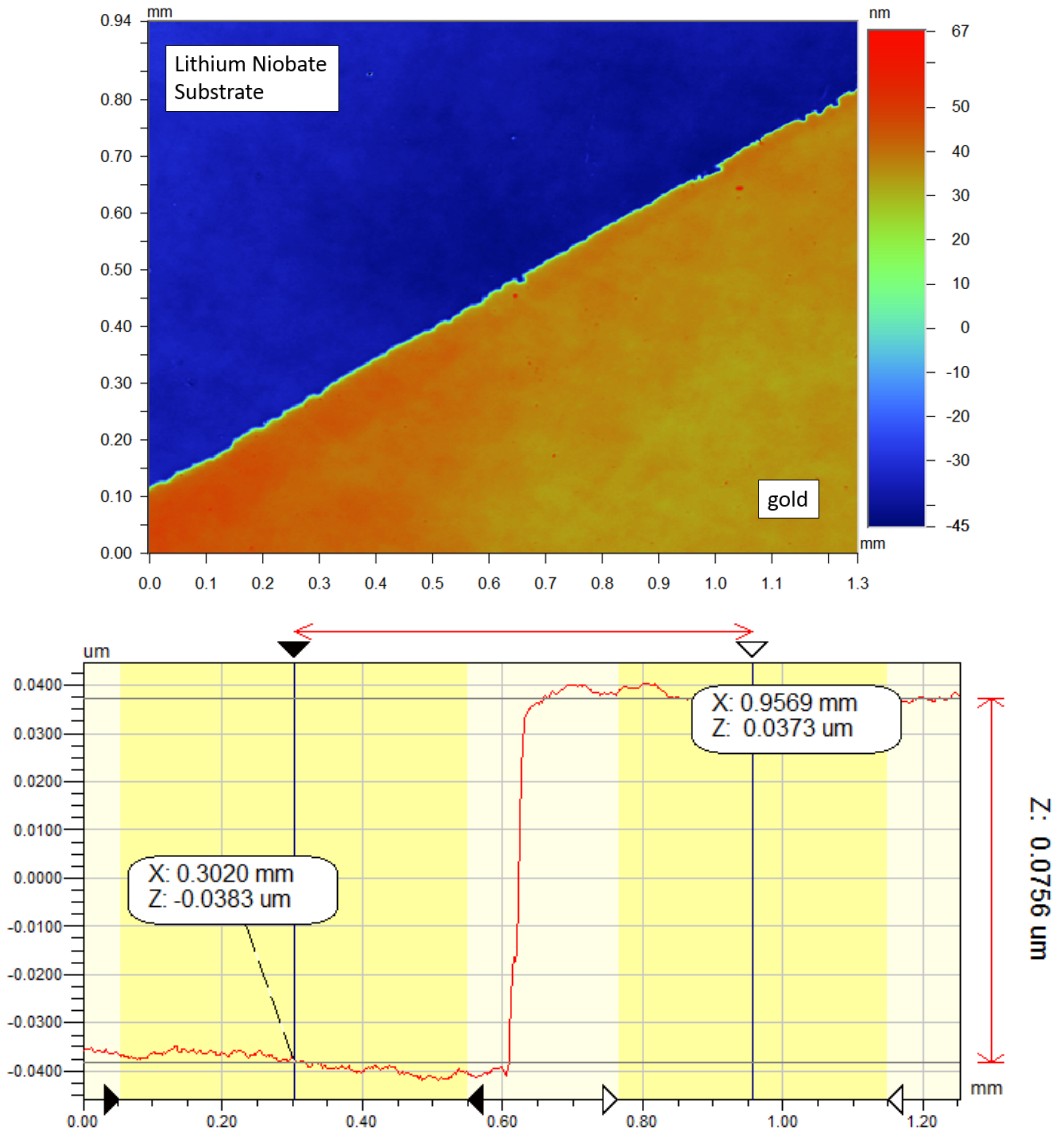
Figure 4.22: (Top) Image of the gold edge, taken using the white light interferometer. (Bottom) Line profile taken across the gold edge, showing a film thickness around 75 nm.

The $\lambda = 1064$ nm beam, with a larger beam width of ≈ 3 mm, was path-length-matched with the 532 nm/620 nm arm to ensure temporal overlap, before being combined using a dichroic mirror. The beams were required to have a beam spot size ≈ 200 μm in order to reach the required power densities. This could be achieved by a focal length in the range of 40 cm. In practice, the beams were focused down using a combination of a $f = 1000$ mm lens and a $f = 750$ mm lens, separated by ~ 1 cm, generating an effective lens with an effective focal length of ≈ 43 cm, calculated using the following equation:

$$\frac{1}{f_{eq}} = \frac{1}{f_1} + \frac{1}{f_2} - \frac{d}{f_1 f_2}, \tag{4.7}$$

where f_1 and f_2 are the focal lengths of the individual lenses and d is the lens separation. This effective lens focuses the beams down to a focal width of ≈ 200 μm calculated using the
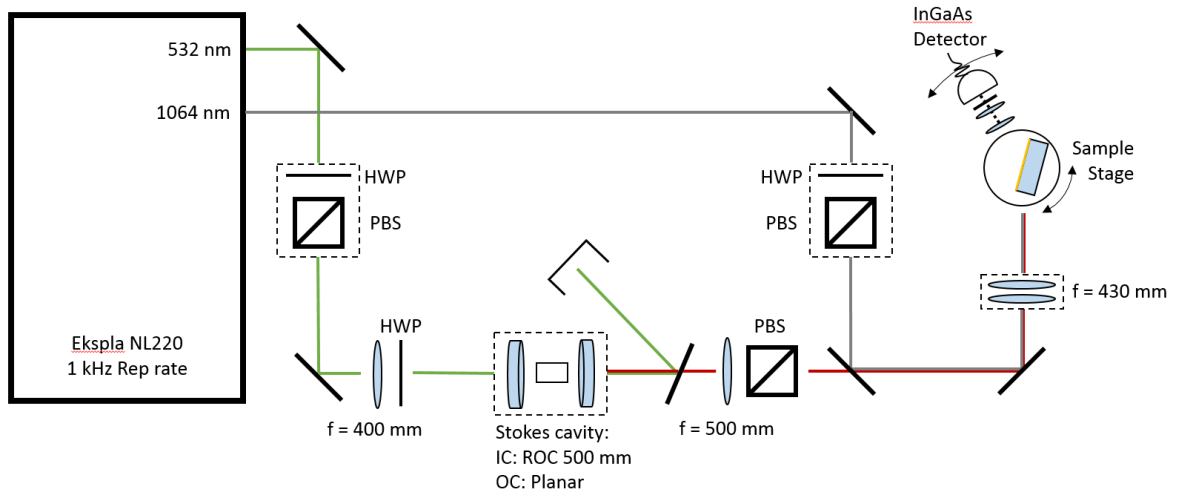
Figure 4.23: Schematic of the experimental configuration.

equation:

$$w = \frac{\lambda f}{\pi w_0} \tag{4.8}$$

where w is the collimated beam half-width, f is the focal length, and w_0 is the desired focal width. This yields a power density up to 100's MW/cm^2 for the 620 nm beam, which is expected to be sufficient to observe the nonlinear effect.

The sample stage was placed at the focal point with similar mounting as used in section 4.3.5. The sample stage was capable of x-y translation, as well as full rotation. The stage could be rotated by a micrometer allowing sub-degree accuracy. The lithium niobate crystal sample was bonded to an aluminium sample plate by wax such that the sample surface lay at the centre of rotation of the stage. This allowed the illuminated area to remain fixed under rotation of the stage. The sample plate was fixed in place by 6-mm poles screwed into the stage, and vertical translation could be achieved by placing spacers below the plate.

We simultaneously verified the spatial and temporal overlap of the signal and idler beams, as well as the position of the sample stage, by placing a BBO crystal on the stage and optimising for the equivalent optical process. Using the phase-matching equations for optical parametric down conversion eq. (3.15), we found that optical parametric down conversion for the same wavelengths could be produced in BBO for a crystal orientation of 20.8°. This angle orientation was achieved using a 2 mm thick BBO crystal cut at 24° and angle tuning. The output radiation was then collected by a spectrometer (DWARF-Star NIR spectrometer, StellarNet), allowing the 1485 nm signal to be identified and optimised.

Detection

Once the lithium niobate sample had been replaced on the sample stage, a 25.4 mm lens and a 75 mm lens, both with anti-reflection coatings, were used to collect the forward-scattered light from the surface and image it onto a detector, at which the 1485 nm idler field would be detected.

The primary detector being used was an InGaAs transimpedence amplified detector (PDA20CS, ThorLabs). Much like the second harmonic generation experiment, a very sensitive detector was required, as the idler was expected to be extremely weak. However, due to the wavelength of the idler, the photomultiplier tube used previously was not appropriate.

A transimpedance amplified detector allows the photocurrent generated at the active surface to be output as an amplified voltage by applying a large impedance. This InGaAs detector was sensitive to light between 800–1700 nm, with a sensitivity $\approx$ 1 A/W at the idler wavelength of 1485 nm. It also had a relatively large active area, with a diameter of 2 mm. This was considered an important feature given the spread of the scattered idler field. The transimpedance amplified detector also had switchable gain, which made the detector versatile and sensitive over a large range of optical powers. Unfortunately, both the impedance applied and the large active area have adverse effects on the response time of the detector. Given that the pulse duration of the laser is only $\sim$ 5 ns, the significant increase in response time results in the sensitivity of the detector plateauing for higher gain settings. Both of these factors also affect the dark current of the detector.

This detector was preceded by two long-pass filters (FEL1250 and FEL1200, ThorLabs). The long-pass filters consisted of dielectric reflective coatings on absorbing glass, and served to isolate the detector from ambient room light as well as the 620 nm and 1064 nm beams. Given that the 1064 nm beam falls within the sensitivity range of the detector, an additional 1064 nm narrowband dielectric mirror was also included. Each of these detectors were characterised by a Cary spectrophotometer, and the transmission of these components at the idler wavelength of 1485 nm was measured to be 83%, 78% and 90% for the FEL 1250, FEL1200 and 1064 nm dielectric mirror respectively.

This combination of lenses, filters and the detector were placed on an arm that could rotate about the sample, collecting light scattered at different angles. The detector was setup to collect light scattering at a 22° internal angle from the gold edge, corresponding to an external angle at $\approx$ 55°.

4.5.6   Results

When both 620 nm beams and 1064 nm beams were incident on the sample and the detector angle was swept, a strong signal could be detected on the transimpedance amplified detector. However, as the signal persisted in the absence of the 620 nm beam, this was identified as the 1064 nm beam. When the 620 nm beam was coincident, no significant change in this signal was observed, allowing us to conclude that, while the detector was not sensitive to the 620 nm beam, no 1485 nm signal could be observed.

Several alternate approaches were attempted in order to try and recover any 1485 nm signal. The first was to use a spectrometer in order to spectrally resolve the signal, removing interference from the 1064 nm beam. This method had several complications: Firstly, the spectrometer being used (DWARF-Star NIR spectrometer, StellarNet) had low sensitivity when compared to the transimpedance amplified detector. In order to compensate for this, long integration times had to be used. Secondly, the spectrometer was fed by a multimode fibre, resulting in a small collection aperture 100's of microns across. Even with focusing optics, it was not possible to ensure that the 1485 nm signal would be collected by the fibre. Ultimately, no 1485 nm signal could be identified using this approach.

The second approach was to introduce a lock-in amplifier and chopper in conjunction with the transimpedance amplified detector. The lock-in operates by taking the output of the detector, multiplying it by a known frequency and integrating. In doing so, components of the detector output at frequencies other than the specified frequency tend to integrate to zero, leaving behind the contribution from the single frequency component. This makes lock-in amplifiers very effective at detecting small signals in noisy environments.

In our case, the chopper was used to modulate the 620 nm beam, while the 1064 nm beam

was left to operate as before. Since the detecting apparatus was insensitive to the 620 nm beam, any signal detected at the chopper frequency would have to correspond to a signal generated by the interaction of the 620 nm and 1064 nm beams, ie. the 1485 nm signal. The one complication with this setup was that on top of the chopper modulation, the laser itself is modulated, with a 5 ns pulse and a 1 kHz repetition rate. This interaction with the laser pulse train and the chopper was expected to result in a reduction in the output of the lock-in by orders of magnitude.

To test the premise of this detection method, the sample was once again replaced by a BBO crystal to generate an optical parametric conversion response at the same wavelength. It was determined that by using the lock-in, the apparatus was indeed sensitive to the 1485 nm signal generated, even when strongly attenuated by the use of ND filters.

Despite this, when the BBO was replaced with the gold-coated lithium niobate sample, no 1485 nm signal could be detected.

4.5.7 Modelling of Plasmonic Parametric Down Conversion

Given the lack of signal from the plasmonic parametric down conversion process, we turned to modelling to determine the strength of the signal which might have been expected. Using the same approach as in chapter 3, we can find an approximate expression for the idler in parametric down conversion. Starting from the wave equation eq. (3.2), and choosing the electric field E_3 to follow the form of a surface plasmon eqs. (2.2) and (2.4), we arrive at:

$$\frac{\partial E_3}{\partial z} = \frac{2i}{\beta_3}\left(\frac{\omega_3}{c}\right)^2 \chi E_1 E_2^* \kappa - E_3 \beta''$$ (4.9)

where ω_3 and β_3 are the frequency and propagation constant of the plasmonic idler field, β'' is the imaginary component of the propagation constant, corresponding to the surface plasmon loss, and κ is an overlap integral. Equation 4.9 is completely analogous with the equations for optical parametric down conversion (eqs. (3.12) to (3.14)), and in the case where the losses are neglected ($\beta'' = 0$), are identical. In this calculation, we have taken a paraxial approximation for the optical beams. This approximation is valid as long as the optical beams are not approaching the diffraction limit. The surface plasmon mode has been treated exactly in this model. We can also assume that the experimental configuration has satisfied the phase-matching condition, and so this has not been included in the model. The pump and idler fields $E_{\{1,2\}}$ are related to the incident powers via the intensity $I_{\{1,2\}}$:

$$P_{\{1,2\}} = \int I_{\{1,2\}}\, \mathrm{d}A$$

$$= \int \frac{c n_i \epsilon_0}{2} |E_{\{1,2\}} \Psi_{\{1,2\}}|^2\, \mathrm{d}A,$$ (4.10)

where $\Psi_{\{1,2\}}$ is a Gaussian mode distribution of the form

$$\Psi_{\{1,2\}} = \frac{1}{\psi_{\{1,2\}}} e^{-\left(\frac{x^2}{2\sigma^2}\right)} e^{-\left(\frac{y^2}{2\sigma^2}\right)}.$$ (4.11)

Here, σ is related to the beam half-width, which we have chosen to be identical for the signal and idler, and ψ_i is the normalisation constant such that

$$\int |\Psi|^2 = 1. \tag{4.12}$$

Given the grazing incidence angle of the optical beams, and that the illuminated surface area is many times larger than the propagation length of the plasmon, we have also chosen to neglect any angular effects of the optical beams, and assumed collinear propagation.

A similar calculation to the above can relate the plasmonic field amplitude E_3 back to a plasmonic mode power P_3 by means of the time-averaged Poynting vector:

$$\begin{aligned}
P_3 &= \int | \langle S_3 \rangle | \, dA \\
&= \frac{1}{2} \mathrm{Re}\left(E_3 \times H_3^* \right) \\
&= \frac{|E_3 \Psi_3|^2}{2 n_3 \mu_0 c},
\end{aligned} \tag{4.13}$$

where the corresponding mode profile is chosen to be

$$\Psi_3 = \frac{1}{\psi_3} e^{-k_x^{(d)} x} e^{-\left(\frac{y^2}{\sigma^2}\right)}, \quad x > 0. \tag{4.14}$$

The $k_x^{(d)}$ describes the exponential plasmonic mode profile as before, and in the $\hat{y}$ direction, it was assumed that the plasmon mode follows the square of the Gaussian beams being used for excitation. The overlap integral κ is given as where

$$\kappa = \int_0^\infty \Psi_1 \Psi_2^* \Psi_3^* \, dx \tag{4.15}$$

Given that the source of nonlinearity being considered here is from the dielectric, we neglect the contribution from the metal here, and therefore only take the integral from $0 \rightarrow \infty$. This approximation is further justified by the fact that, at the wavelength of $\lambda = 1485$ nm, the power of the surface plasmon in the metal is $\approx 3\%$, and most of the power resides in the dielectric. The code for this calculation has been included in appendix A.

By using eqs. (4.9), (4.10) and (4.13) and numerically integrating, the power that can be expected to be generated by the experimental configuration can be estimated. The results of this calculation are shown in fig. 4.24. Here, the plasmon power at 1485 nm increases rapidly in the first 100 μm, and then saturates at a peak output power of 0.2 μW. The growth of the idler field saturates when the parametric gain matches the surface plasmon loss. The limited parametric gain can be explained by the overlap integral (eq. (4.15)). If we consider two gaussian beams (the 620 nm and the 1064 nm beams) with a full beam width $2\sigma = 100$ μm, overlapped with a surface plasmon at 1485 nm with a mode size of $1/\mathrm{Re}(k_x^{(d)}) = 0.48$ μm, the overlap integral yields a value two orders of magnitude smaller than in the purely optical case, resulting in a large reduction in the nonlinear response.
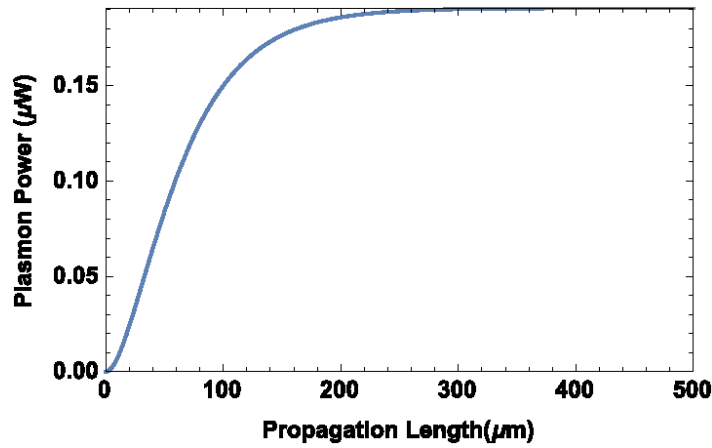
Figure 4.24: Numerical calculation of the mode power generated via the parametric down conversion process.

4.5.8 Discussion

We can take the peak power calculated from the model and estimate how much power could be expected at the detector. If we account for the scattering efficiency of the edge ($\approx 35\%$), the peak power of 0.2 μW reduces to 70 nW that can be detected in the far-field. If we further account for the detection efficiency, we have to consider the transmission of the 1064 nm dielectric mirror (90%), the 1200 nm long pass filter (78%) and the 1250 nm long pass filter (83%). This reduces the maximum detectable power at the detector to 60% of the scattered power, reducing the detectable power to ≈ 40 nW. While nanowatts of power is not impossible to detect, especially using the lock-in amplifier, it would require the experimental setup to be optimised and very precisely aligned. Without the feedback of an easily detectable signal, this can be very difficult to achieve. This challenge of detection is further compounded by the intense optical pump beams which further obscure the idler field.

Given the small peak powers being generated, this experiment could be made more feasible by moving to picosecond or femtosecond pulse durations. This would result in greater peak powers, and therefore generate a larger nonlinear response. While this would in principle make detection easier, shorter pulse durations would also have more stringent path length matching requirements, making the experimental configuration much more complex. Additionally, for the higher peak powers involved, damage by ablation becomes more of a concern than thermal effects. Lastly, this would also require a very different laser source. Given the time constraints and difficulty to access such laser sources, this was not pursued.

4.6 Conclusion

In this chapter, we took advantage of dielectric nonlinear materials in order to implement phase-matching techniques in optically-pumped plasmonic second-order nonlinear effects. We investigated quasi-phase-matching in the context of second harmonic generation, and birefringent phase-matching in the context of parametric down conversion. In these configurations, we were able to take advantage of the extra degrees of freedom afforded by the optical pumping beams. However in both cases, we were not able to identify a nonlinear optical-to-plasmon interaction. We partly attribute this to the poor overlap between the optical and plasmonic fields, which results in low conversion efficiencies. Ultimately, these nonlinear

processes are unable to compete with the plasmonic losses. Due to this limitation, we also conclude that optically-pumped nonlinear processes are impractical; both for implementing plasmonic gain, and for exciting surface plasmons via the second order nonlinearities.

This limitation can be lifted by returning to all-plasmonic nonlinear processes, such as explored in chapter 3, in the context of metallic nonlinearities. In this case, the mutual confinement of the surface plasmon modes ensures a good spatial overlap, which should enable stronger conversion efficiencies. The appropriate phase-matching mechanisms for plasmonic nonlinear effects also have to be reconsidered. Methods such as birefringent phase-matching are no longer applicable, due to a reduction in the degrees of freedom of the surface plasmons, and only in-plane methods like quasi-phase-matching remain viable for enhancing plasmonic nonlinear effects.

By focusing on plasmonic second-order effects, there is also an assumption that the surface plasmons of multiple wavelengths can also be excited simultaneously and efficiently. However, experimentally, this is not always simple. This is particularly true in nonlinear dielectric materials, which tend to have high refractive indices, exacerbating the plasmonic dispersion. In addition to the challenge of optical excitation of surface plasmons, there was also the inverse challenge of plasmon-to-optical coupling. It became apparent during our investigation that far-field optical methods of plasmonic detection were often insufficient, particularly for three-wave mixing experiments, where strong optical pumping fields are also present. For these reasons, we decided that our next study would focus on a method of ensuring stronger optical and plasmonic interactions, and an alternate means of optical to plasmonic coupling.

5

Photonic-Plasmonic Directional Couplers

5.1 Introduction

A directional coupler consists of two waveguides separated by a small gap. Evanescent coupling allows light to tunnel from one waveguide to the other over a characteristic length. The direct application of directional coupling to plasmonics is limited by this characteristic length: most have a characteristic coupling length on the order of millimetres, while the propagation length of plasmons is of the order of microns. However, other existing methods of coupling to surface plasmons (section 2.3) also possess significant limitations. In particular, grating coupling and prism coupling are both out-of-plane techniques, and are difficult to integrate with other photonic devices. On the other hand directional coupling naturally lends itself to photonic integration, while also producing monolithic devices. This makes them very stable and reliable couplers. As such, directional coupling using plasmonic waveguides is a topic that has been extensively studied.

All-plasmonic directional couplers have been studied [69–74] and in particular, a plasmonic directional coupler with a coupling length as short as $410 \ \mu$m has been demonstrated for long-range surface plasmons at a wavelength of $\lambda = 1550$ nm [69]. These waveguides were separated by 4 μm. A number of studies have also been conducted on photonic-plasmonic directional coupling: both theoretical [75–81] and experimental [82–88]. These studies demonstrate effective directional coupling between photonic and plasmonic waveguides of various geometries: some using high index dielectrics [84, 86–88], and some using complex layered dielectric/metallic structures [80, 81] to compensate the plasmonic dispersion.

In this chapter, we focus on a simpler planar design, modelling a plasmonic-dielectric directional coupler consisting of a photonic waveguide made of the dielectric photoresist SU-8 and a gold waveguide supporting long-range surface plasmons. These waveguides were embedded in the polymer PMMA. The implication of plasmonic loss in directional couplers is first investigated using coupled mode theory. Then, waveguide theory is used to select the appropriate waveguide geometries. Finally, a full-wave simulation of the design is carried out in COMSOL Multiphysics. This study formed the basis for the further study on more complex couplers, such as the three-waveguide Adiabatic Passage couplers explored in chapter 6.
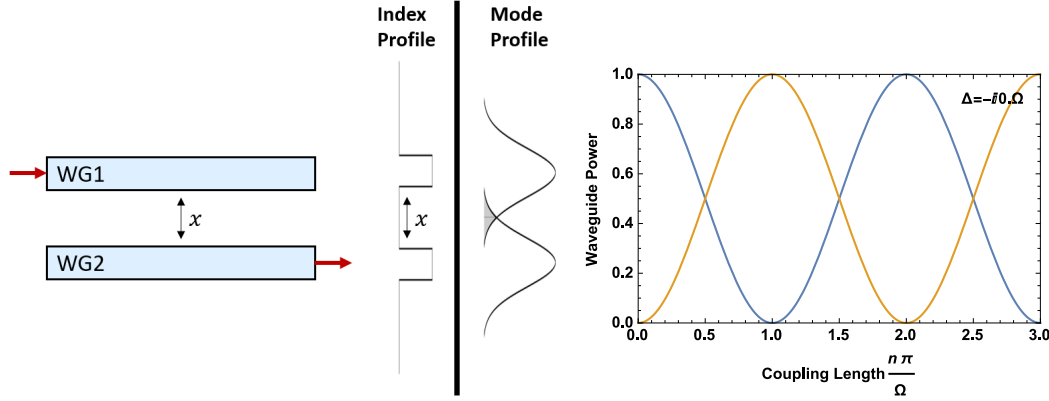
5.2   Coupled Mode Theory

Figure 5.1: (Left) Sketch of a directional coupler consisting of two parallel waveguides. (Middle) Corresponding refractive index profile of the directional couplier, as well as a sketch of the mode profiles. Coupling is driven by the overlap of the two modes. (Right) The corresponding power evolution, with power transferred from the input waveguide (blue) to the output waveguide (yellow) and transferred back over several coupling lengths.

In order to model plasmonic-photonic directional couplers, we first turned to the well established coupled mode theory [181, 182]. If we consider the two waveguides separately, the evolution of optical waves in these waveguides can be described by the equations:

$$\frac{\mathrm{d}\tilde{E}_1}{\mathrm{d}z} = i\beta_1\tilde{E}_1$$

$$\frac{\mathrm{d}\tilde{E}_2}{\mathrm{d}z} = i\beta_2\tilde{E}_2, \tag{5.1}$$

where $\{\tilde{E}_1, \tilde{E}_2\}$ are the electric fields in the waveguides, and $\{\beta_1, \beta_2\}$ are the propagation constants. These can be related to the mode powers by $P \propto |E|^2$ When the waveguides are brought sufficiently close and the modes waveguides modes are perturbed. In the limit of weak coupling, the equations are rewritten as:

$$\frac{\mathrm{d}\tilde{E}_1}{\mathrm{d}z} = i\beta_1\tilde{E}_1 - i\Omega_{12}\tilde{E}_2 \tag{5.2}$$

$$\frac{\mathrm{d}\tilde{E}_2}{\mathrm{d}z} = i\beta_2\tilde{E}_2 - i\Omega_{21}\tilde{E}_1.$$

We can define $\bar{\beta} = (\beta_1 + \beta_2)/2$ and, without loss of generality, choose $\beta_1 > \beta_2$ and define $\Delta = (\beta_1 - \beta_2)/2$. Then, by choosing $\tilde{E}_i = E_i e^{i(\bar{\beta}z - \omega t)}$, eq. (5.2) can be rewritten the matrix form:

$$i\frac{\mathrm{d}}{\mathrm{d}z}\begin{pmatrix} E_1 \\ E_2 \end{pmatrix} = \frac{1}{2}\begin{pmatrix} -\Delta & \Omega_{12} \\ \Omega_{21} & \Delta \end{pmatrix}\begin{pmatrix} E_1 \\ E_2 \end{pmatrix} \tag{5.3}$$

where E_1, E_2 are scalar amplitudes of the electric field in each waveguide. The coupling

coefficients Ω_{ij} are determined by the overlap of modes of these two waveguide:

$$\Omega_{ij} = \frac{1}{4}\sqrt{\frac{\varepsilon_0}{\mu_0}} \int (n^2 - n_j^2)\Psi_i^* \cdot \Psi_j \, dA, \qquad (5.4)$$

where the Ψ_i are the normalized mode profiles of the electric fields, and the Ψ^* is the complex conjugate. The Ψ's are vectors, however by choice of polarisation, can generally be treated as scalar. The total refractive index profile is given by n, and n_j is the refractive index profile of a particular waveguide. The asymmetry of the waveguides and the waveguide modes is captured in these parameters n_i and Ψ respectively. In the case where $\Delta = 0$, the physical interpretation of these coupling coefficients is simple—after a characteristic length $L_c = \pi/\Omega$, the light in one waveguide can be seen to have completely transferred to the other waveguide. This is shown in fig. 5.1.
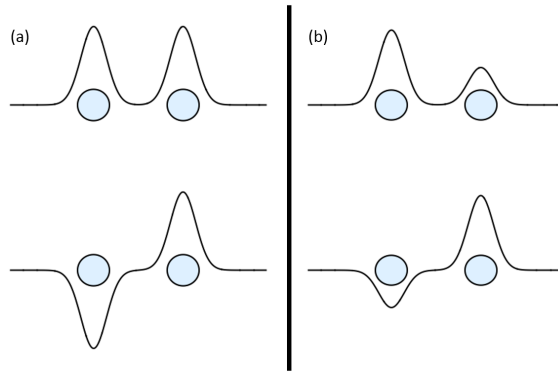

Figure 5.2: (a) Even and odd supermodes of a pair of identical waveguides. (b) Weighted even and odd supermodes for waveguides which are not phase-matched.

Alternately, the coupling behaviour can be understood by expressing the matrix in terms of the eigenstates of the system. For the case where $\Delta = 0$, the coupling coefficients are symmetric ($\Omega_{12} = \Omega_{21} = \Omega$) and real, and the eigenvalues reduce to $\varepsilon_\pm = \pm\frac{1}{2}\Omega$. The corresponding eigenstates are just the odd and even supermodes [182] shown in fig. 5.2(a). The coupling coefficient Ω in this case reduces to the difference in propagation constants of the supermodes $\Omega = \varepsilon_+ - \varepsilon_- = \beta_{even} - \beta_{odd}$. Thus, the coupling from one waveguide to the other corresponds to the beating between these two modes. This case represents a typical, optical directional coupler. Usually, the waveguides would be spaced by tens of microns, yielding $\Omega \sim 1000 \text{ m}^{-1}$, or equivalently a characteristic coupling length of millimetres.

5.2.1 Propagating Plasmons in Coupled Mode Theory

When introducing surface plasmons into the coupled mode equations, the material properties and mode distribution are inherently included in the calculation of Δ and Ω. In particular, since the wavevector of the surface plasmon is complex, as a result of the complex relative permittivity of the metal, then the quantity $\Delta = (\beta_1 - \beta_2)/2$ is also complex. We first consider the effect of having a non-negligible real part for Δ. For optical-plasmonic directional couplers, it is not realistic to take the case where $\text{Re}[\Delta] = 0$ case. The dispersion properties and mode profiles of the photonic and plasmonic waveguides are inherently different and dissimilar. This difference in dispersion can lead to a large phase-mismatch and a non-zero
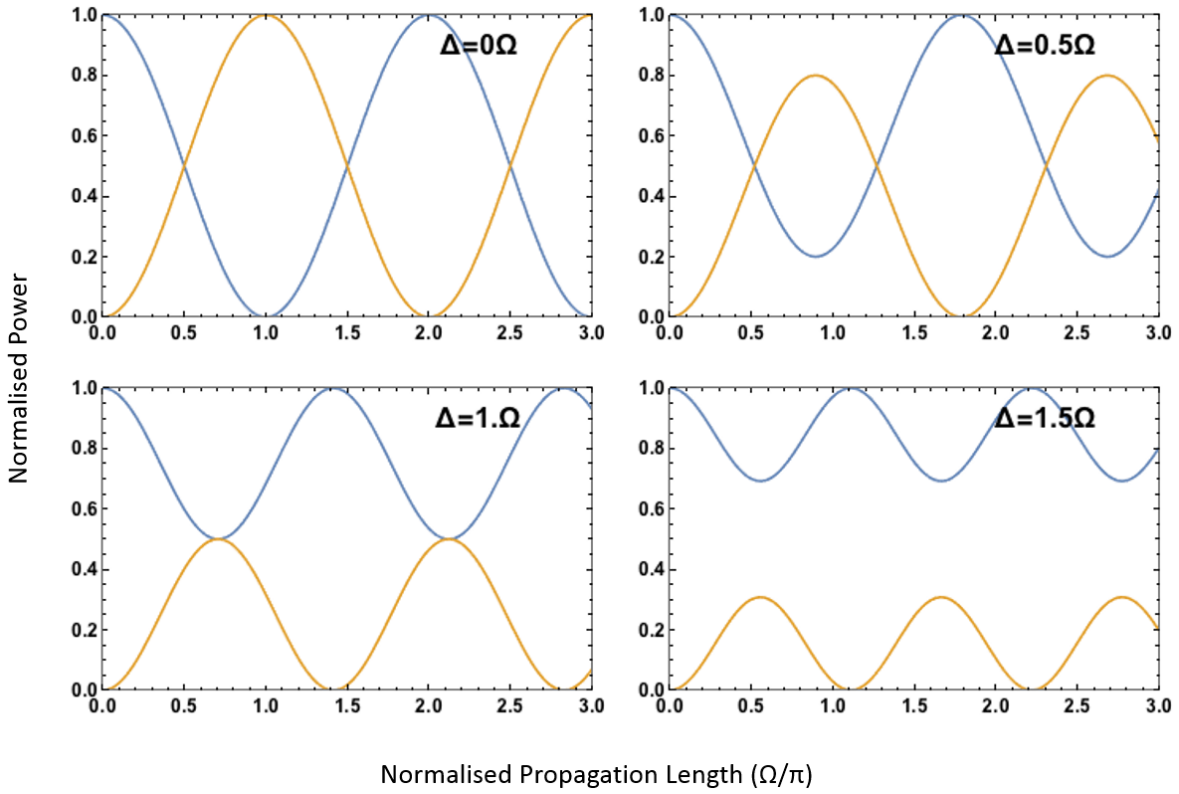
Figure 5.3: Behaviour of a directional coupler as the phase mismatch between the waveguides Re[Δ] is increased, with respect to the coupling coefficient Ω, which has been normalised to 1.

Δ term, however the exact value depends on the particular choice of waveguide geometry. When Δ is large, light remains in the initial waveguide, and the maximum power transferred by the directional coupler diminishes. This is shown in fig. 5.3, where the phase mismatch has been expressed in terms of Ω, which provides the characteristic length scale. In the eigenmode picture, the supermodes are no longer even, but rather weighted superpositions of the individual waveguide modes (fig. 5.2(b)), and the beating of these weighted modes do not result in light completely transferring from waveguide to waveguide. It can also be seen in fig. 5.3, that for a phase-mismatch $\Delta = \Omega$, the efficiency of the directional coupler reduces to half. For a typical optical dielectric coupler with a coupling strength of $\Omega \sim 1000 \, \text{m}^{-1}$, this would correspond to a phase-mismatch of the same order. For comparison, we can consider a surface plasmon propagating at a glass/gold interface, and the corresponding optical wave. At $\lambda = 633$ nm, the refractive index of the glass is $n \approx 1.52$, and the corresponding permittivity of the gold is $\epsilon = -11.8053 + 1.227i$. We can calculate the real part of the propagation constant(eq. (2.6)) for the plasmon to be Re(β) $= 1.67 \times 10^7$, and the corresponding optical propagation constant to be $k_o = 1.50 \times 10^7$. This corresponding phase-mismatch is then 1.7×10^6, and is three orders of magnitude larger than can be tolerated by the directional coupler.

This quick calculation highlights one of the challenges of implementing directional coupling between optical and surface plasmon waveguides. In order to ensure that maximum power is transferred between optical and plasmonic waveguides, either stronger coupling must be used, corresponding to much smaller waveguide separations, or the phase mismatch Δ must be reduced significantly. This latter option can be achieved by choosing higher index

materials for the optical waveguide, or by choosing plasmonic waveguide geometries with modes that naturally produce smaller propagation constants.
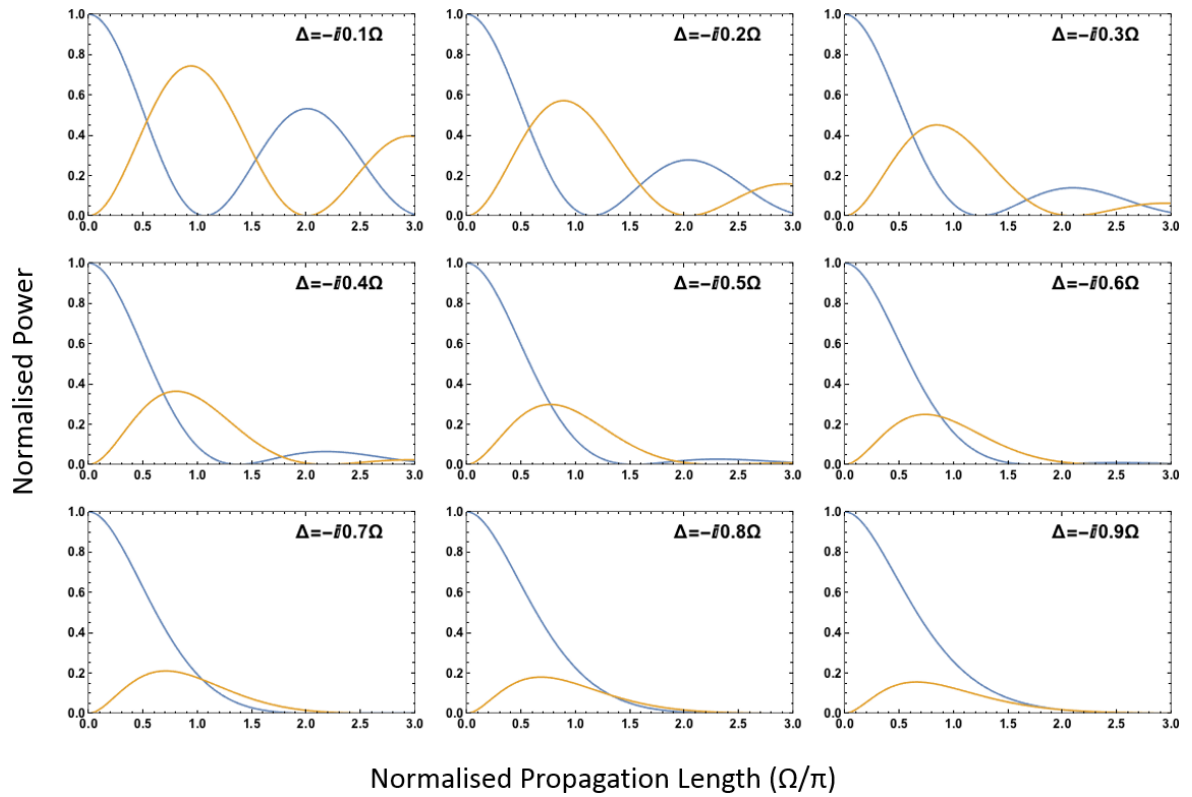
Figure 5.4: Behaviour of a directional coupler as the size of the loss (corresponding to an imaginary Δ) is increased, with respect to the coupling coefficient Ω which has been normalised to 1.

Phase matching is further complicated by plasmonic loss. As before, this loss corresponds to a negative imaginary component of the propagation constant β for the surface plasmon, which produces here a complex phase-mismatch Δ. The effect of the loss is shown in fig. 5.4. Here, we can see that loss can be detrimental to the transfer of power, and in particular, a loss of $|\Delta| = 0.3\Omega$ can halve the coupling efficiency of the directional coupler. For a typical optical dielectric coupler with a coupling strength of $\Omega \sim 1000$ m^{-1}, this would correspond to propagation length of around 3 millimetres. We can make a similar comparison as above, for a surface plasmon at a wavelength of $\lambda = 633$ nm propagating at a glass/gold interface. Using the propagation constant from eq. (2.6), we can find the propagation length to be $\frac{1}{\text{Im}(\beta)} \approx 5$ μm. This again demonstrates the difficulty in implementing directional coupling between optical and surface plasmon waveguides. Either much stronger coupling is required in order to compensate the effect of the losses, or plasmonic waveguide geometries with much smaller losses are required.

5.3 Design

In light of the constraints from this simple analysis, we considered a design of an optical-to-plasmonic directional coupler, a schematic of which is shown in fig. 5.5. For this coupler, we established the need for surface plasmon waveguides that provide a smaller propagation

Figure 5.5: 2D schematic of the proposed structure of the directional coupler, infinite in the $\hat{y}$ direction.

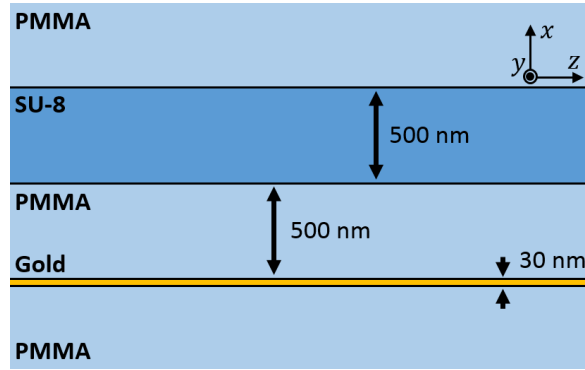constant and longer propagation lengths. These criteria can generally be met with Insulator-Metal-Insulator (IMI) waveguides [21, 112–115], which consist of a thin metal film with a dielectric cladding on either side. These waveguides are well studied, and are known to support long-range surface plasmons, as discussed in chapter 2.

For the optical waveguide, we chose a moderately high index dielectric to match the surface plasmon. The photoresist SU-8 [183] possesses a relatively high refractive index of $n \approx 1.57$. It is more than 95% transmissive between wavelengths of 400 nm and 1600 nm [184] and can be readily deposited by spin-coating techniques to a thickness of a micron or less. At these dimensions, it has been shown that SU-8 can be phase-matched to an IMI waveguide[79]. Based on these considerations, we chose to use SU-8 for the dielectric waveguides in our directional coupling and adiabatic passage studies.

For the background dielectric, we chose polymethyl methacrylate (PMMA), which has a refractive index $n \approx 1.49$, and is also compatible with spin coating techniques.

5.3.1   Calculation of the Waveguide Dispersion

For the chosen configuration and materials, we calculated the waveguide dispersions, in order to determine the wavelength and waveguide dimensions at which they would be phase-matched for efficient coupling.

The dispersion for a long-range surface plasmon is not governed by the same equation as given in chapter 2 for a plasmon at an infinite interface (eq. (2.6)). Instead, it is governed by the implicit equation [46]:

$$\left(\frac{\varepsilon_m}{\varepsilon_1} \frac{k_x^{(1)}}{k_x^{(m)}} + 1 \right) \left(\frac{\varepsilon_x}{\varepsilon_2} \frac{k_x^{(2)}}{k_x^{(m)}} + 1 \right) = \left(\frac{\varepsilon_m}{\varepsilon_1} \frac{k_x^{(1)}}{k_x^{(m)}} - 1 \right) \left(\frac{\varepsilon_m}{\varepsilon_2} \frac{k_x^{(2)}}{k_x^{(m)}} - 1 \right) e^{-4k_x^{(m)}d}, \qquad (5.5)$$

where $k_x^{(i)} = \sqrt{\beta^2 - \varepsilon_i \left(\frac{\omega}{c} \right)^2}$, and the superscripts $\{1, 2, m\}$ correspond to the transverse wavevectors calculated in the upper dielectric, lower dielectric, and the metal respectively. Here, the plasmon is propagating in the $\hat{z}$ direction. Equation 5.5 can be solved numerically by root finding methods. However, in order to avoid artefacts, these solutions need to be checked, to ensure that the correct solution has been reached. For the long-range surface plasmon below the plasma resonance point, it must be ensured that the propagation constants lie below the value for a plasmon propagating at a single interface, and above the value of an equivalent optical wave in the corresponding dielectrics. Note that for an infinitely thick

film thickness d, this relation reduces to two separate plasmons on either side of the film, and the dispersion reduces to eq. (2.6) once more. The effective index for a gold film embedded in PMMA is plotted in fig. 5.6, where the gold height has been varied. The code for this calculation has been included in appendix A.
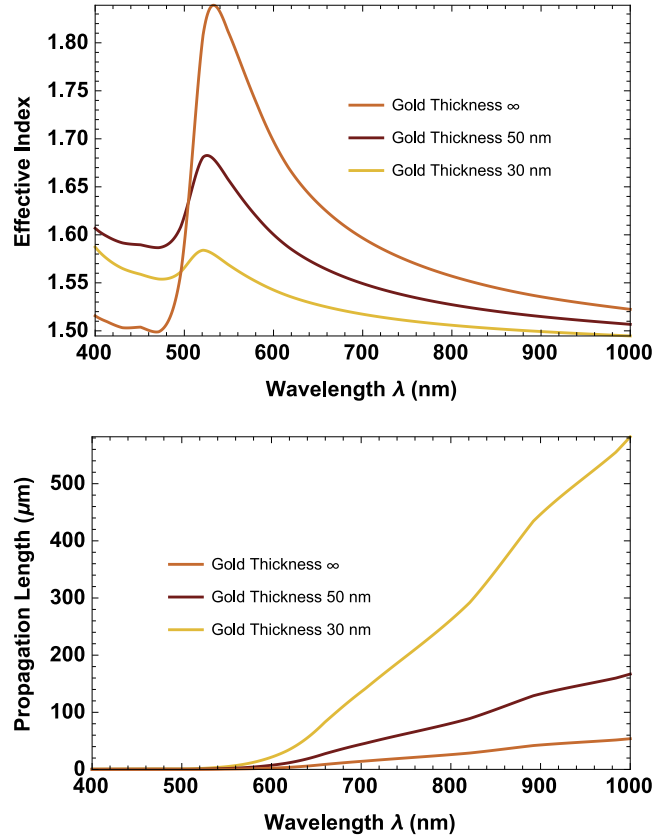
Figure 5.6: (Top) Effective index for the long-range surface plasmon at different gold film thicknesses. (Bottom) Corresponding propagation lengths at the same gold film thicknesses.

The behaviour of the effective index of the long-range surface plasmon is well understood: at longer wavelengths and far from the plasma frequency of the gold, the dispersion lies close to the optical refractive index. Approaching the plasma frequency at around ~ 530 nm, the effective index increases significantly. And for wavelengths exceeding the plasma frequency, the metal becomes dielectric in character, and the effective index of the plasmon reduces once more.

Reducing the gold film thickness has the effect of pushing the mode field distribution out into the dielectric. This shifts the dispersion of the long-range surface plasmon towards the optical curve. Notably, the reduction in the effective index of the long-range surface plasmon is accompanied by dramatic increase in propagation length, almost reaching millimetres in the near IR. Conversely, increasing the thickness of the gold allows a greater proportion of the field into the metal, and has the effect of shifting the dispersion curve to higher effective indices. This continues until the gold thickness is significantly greater than the penetration depth into the gold. At this point, the long-range surface plasmon tends towards the behaviour of an ordinary plasmon. Here, we are interested in having a small film thickness, a lower effective index, and longer propagation lengths. The gold film thickness of 30 nm is the thinnest gold film that we are confident in depositing that results in a continuous film of good

quality.

A similar set of equations is used to calculate the optical waveguide propagation constants. To couple to the plasmonic waveguide, we require that the optical waveguide is co-polarised with the surface plasmon, and therefore we solve for the mode primarily polarised in the $\hat{x}$ direction (the TM mode.) The transverse wavevector for the optical field $k_{x,opt}$ can be found for the TM modes by calculating the numerical solution to the following equation [185]:

$$\frac{\varepsilon_{core}}{\varepsilon_{clad}}\sqrt{\frac{\omega^2\mu_0\varepsilon_0(\varepsilon_{core}-\varepsilon_{clad})}{k_{x,opt}^2}-1} = \begin{cases} \tan(k_{x,opt}d) & \text{for even modes} \\ -\cot(k_{x,opt}d) & \text{for odd modes.} \end{cases} \tag{5.6}$$

Here, each solution corresponds to an additional waveguide mode. A similar equation exists for the TE waveguide modes, but since only the TM modes can couple to the surface plasmon modes, they are not considered here. The transverse wavevector can be related to the waveguide propagation constant by the equation:

$$\beta_{opt} = \sqrt{\left(\frac{2\pi}{\lambda}n_{core}\right)^2 - k_{x,opt}^2}, \tag{5.7}$$

which can then be used to determine the phase-matching condition for coupling to the surface plasmon waveguide. The solution to eq. (5.7) is plotted in fig. 5.7 for a SU-8 waveguide 500 nm thick, embedded in PMMA.
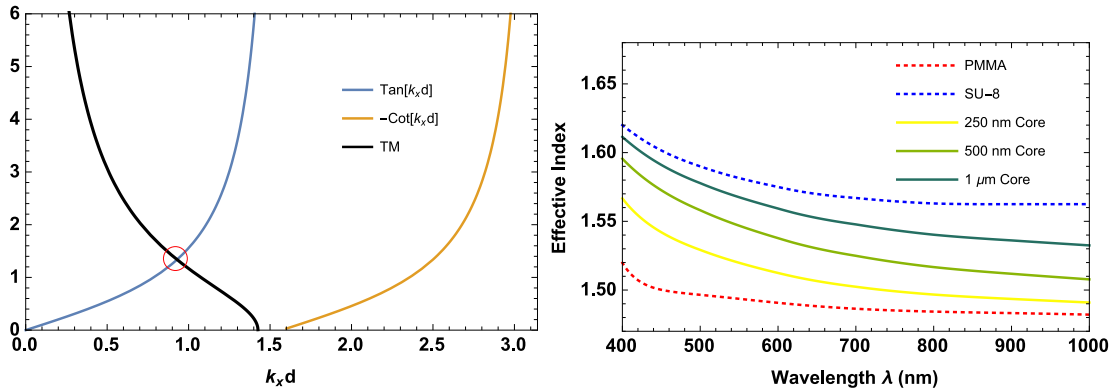
Figure 5.7: (Left) Graphical solution to eq. (5.6), for a 500 nm thick SU-8 waveguide. The numeric value of the left-hand side of eq. (5.6) is plotted in black, and the right-hand side is plotted in blue and yellow for the odd and even modes. For this particular case, there is only one crossing (red), indicating that this waveguide supports a single mode. (Right) Effective index of a guided optical mode in a SU-8 waveguide embedded in PMMA. The bulk refractive indices of the core (SU-8) and cladding (PMMA) are shown for reference (dotted).

For the optical waveguide, we can see that at longer wavelengths, when the waveguide thickness h is of the order of the wavelength $h \sim \frac{\lambda}{n}$, and the effective index is dominated by the cladding, PMMA in this case. And at short wavelengths the effective index tends to the bulk index of the core material, here given by SU-8. This dispersion curve can be tuned by slight changes in the waveguide dimensions—increasing the waveguide thickness shifts the whole curve higher, towards the core index. However this also allows the introduction

of higher order modes, and adds additional degrees of freedom. Decreasing the waveguide thickness shifts the whole effective index curve lower, towards the cladding. The thickness of 500 nm lies at the lower limit of what can realistically be fabricated using spin coating techniques. We can see in fig. 5.7 (left) that, at this waveguide thickness, only a single mode is supported.

Figure 5.8: Plot of effective index for 500 nm SU-8 waveguide and 30 nm gold waveguide. Crossings indicate phase-matched wavelengths.

Finally, we can make direct comparisons between long-range surface plasmon waveguides and the SU-8 waveguide. In fig. 5.8, the effective indices for the 30 nm gold waveguide and the 500 nm SU-8 waveguide have been plotted together. Using these dimensions, we ca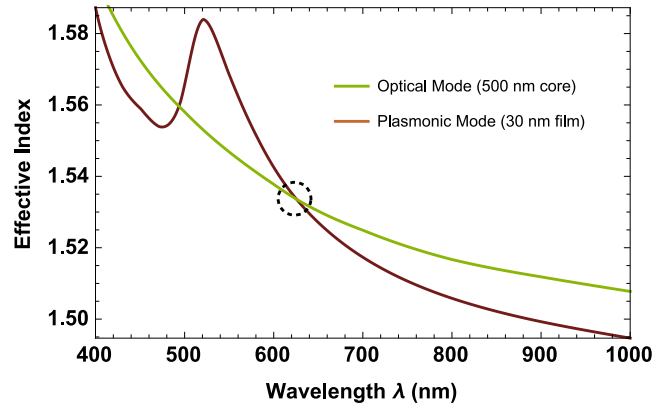n see that these two curves cross at $\lambda \approx 630$ nm and the two propagating modes can be phase-matched. This wavelength was considered optimal for our purposes. Working in the infrared would have increased the surface plasmon propagation lengths by several times, however working in the visible at $\lambda = 630$ allowed the use of convenient light sources, and simple alignment. Furthermore, this wavelength can be used to excite common dyes. In principle, this could allow fabricated devices to be dye doped, and the coupling in the waveguides to be directly imaged. At this wavelength, the long range surface plasmon has a propagation length in the range of 20 μm, requiring a coupling strength of the order of 10^5 m^{-1} in order for significant coupling to occur.

5.4 Simulations in COMSOL Multiphysics

Once the appropriate dimensions for the SU-8 and gold waveguides had been established, numerical simulations were carried out using COMSOL Multiphysics in order to determine the mode field distributions and the appropriate waveguide separation for directional coupling to occur. The simulations retrieved from COMSOL could then be compared to results found using coupled mode theory. COMSOL is also a useful tool in providing insight into other contributions not taken into account by coupled mode theory, such as scattering.

5.4.1 Simulation parameters

A 2-dimensional model of the directional coupler was constructed, as shown in fig. 5.9. The model consisted of a 20×7 μm boundary box, with a refractive index of $n = 1.48899$,
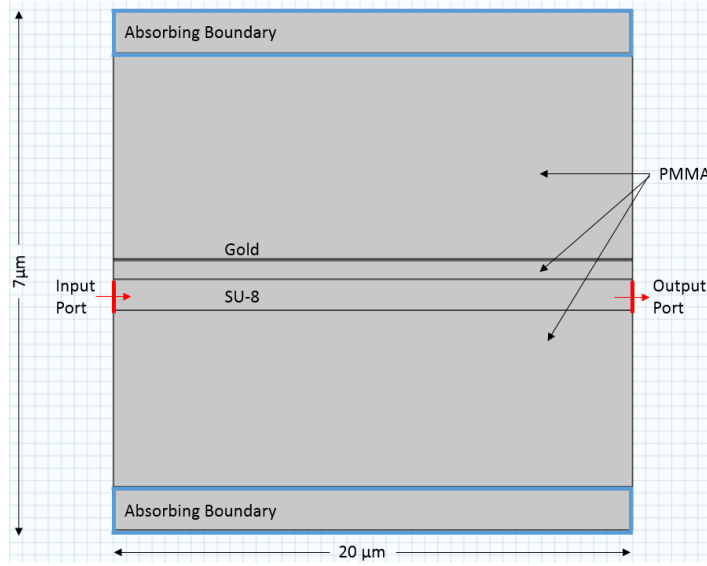
Figure 5.9: Directional coupling configuration simulated in COM-
SOL. Absorbing boundaries (blue) and the output port (red) allowed
scattered light to leave the simulation.

corresponding to PMMA. A 500 nm thick waveguide with a refractive index of $n = 1.57159$
was included, corresponding to the optical SU-8 waveguide, and a 30 nm thick layer with
a permittivity of $\epsilon = -11.595 + 1.25345i$ corresponded to the gold. Initially, the two
waveguides were separated by a 300 nm gap. Continuous-wave light was injected into the
SU-8 waveguide, through an input port, with a wavelength $\lambda = 630$ nm. The light was given
a Gaussian beam distribution by defining the E and H fields. The width of the Gaussian
was chosen to match the thickness of the optical waveguide, approximating the optical
waveguide mode. As this was only an approximation, not all of the injected light coupled
into the waveguide mode. However, this did not significantly affect most of the results of the
simulation, as discussed below. The light was then allowed to propagate for 20 μm. Given
that the light exiting the simulation would have a well defined wavevector, the waveguide was
terminated with a phase-matched port. This allowed the majority of the light to leave the
simulation,and not be reflected at the boundary. Absorbing boundaries were also placed on
the sides of the simulation cell to allow any scattered light to exit. As before, the maximum
element size of the mesh was set to 4 nm in the gold, and to $\lambda/8n$ in the dielectrics. When the
mesh element density was doubled, no qualitative changes to the simulation were observed,
ensuring the consistency and quality of the simulation.

The result of the 2D COMSOL simulation is shown in fig. 5.10(left). In order to extract
and quantify the strength of the fields in the optical and plasmonic waveguides, a cross-
section was also taken through the center of the optical waveguide, and 50 nm above the
plasmonic waveguide (to capture the power in the evanescent fields), resulting in the plot
in fig. 5.10 (right). Coupling behaviour is evident in fig. 5.10, where light launched into
the optical waveguide is seen to couple to the plasmonic waveguide after a characteristic
length of ~ 10 μm. At this point, the electric fields in the surface plasmon are more intense
than the initial fields in the optical waveguide, owing to the plasmonic field confinement.
After this point in the coupler, the light begins to couple back to the optical waveguide.
In this particular case, light from the optical waveguide is almost completely extinguished,
indicative of directional coupling behaviour. Some structure is also evident at the input to
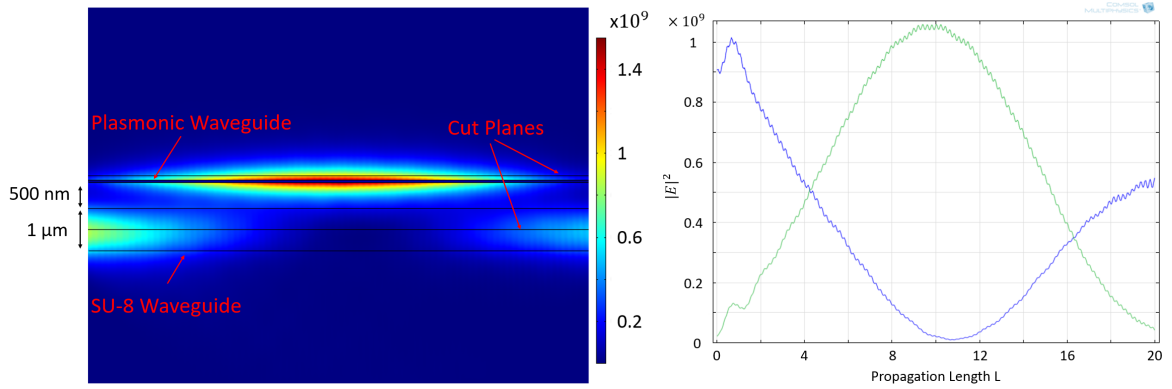
Figure 5.10: (Left) COMSOL simulation of the proposed dielectric coupler with a 500 nm SU-8 waveguide coupling to a 30 nm plasmonic gold film (fig. 5.9). Colour map is showing $|E|^2$. (Right) Plot of the electric fields obtained by taking a line cross-section through the waveguides.

the simulation. This behaviour also appears to damp well before $\sim 4\ \mu$m into the device, and should not affect the overall behaviour of the device. Additional simulations were carried out, where the plasmonic waveguide was introduced later, and in these cases, it was verified that the introduction of the gold film did not cause significant scattering from the optical waveguide (as shown in fig. 5.11).
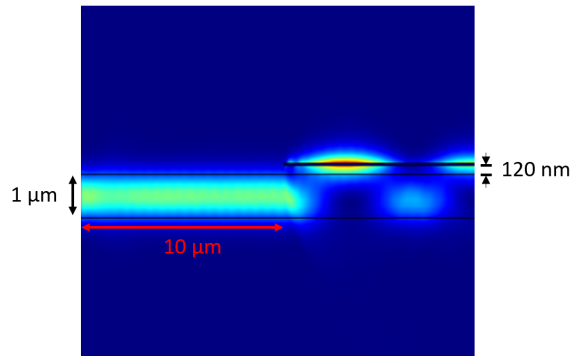
Figure 5.11: Simulation allowing the light to propagate in the optical waveguide for 10 μm, in order to observe any scattering or perturbations introduced by the gold film. In this particular simulation, the waveguide separation is 120 μ m

5.4.2   Simulating Fabrication Tolerances

After establishing that the key features of directional coupling were evident, several parameters were swept in order to determine the tolerances of the device. The parameters that were swept included: the excitation wavelength, the metal film and optical waveguide thickness and the waveguide spacing. In most cases, the range of the parameter sweeps reflects the expected variation during fabrication. The results are shown below.
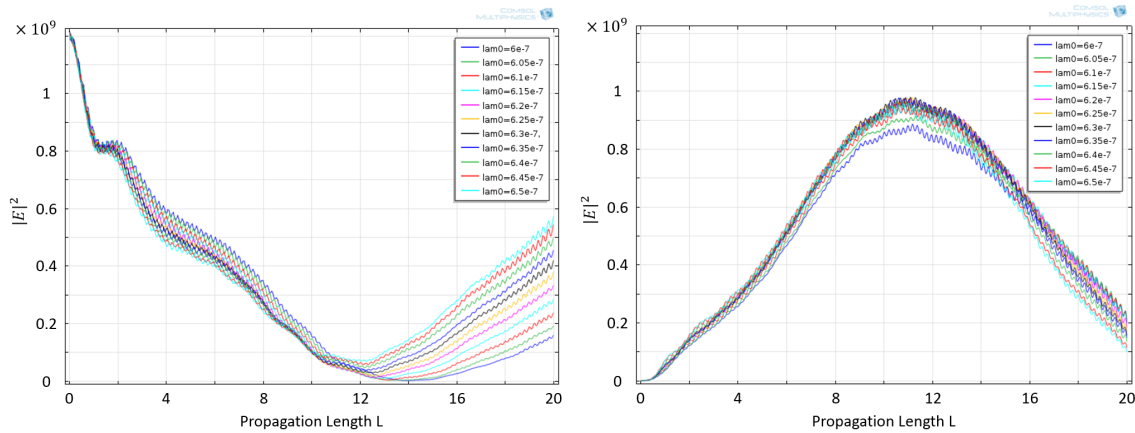
Figure 5.12: Simulation of the directional coupler, varying the wavelength launched into the device. The wavelength is varied from 600 nm (blue) to 650 nm (teal), with the nominal launch wavelength of 620 nm (pink). (Left) Field in the optical waveguide, (right) field in the plasmonic waveguide. In the plasmonic waveguide, the coupled intensity varies from $0.88{\times}10^9$ to $0.98{\times}10^9$.

Sensitivity to Wavelength

In fig. 5.12, the input wavelength was swept from 600–650 nm, in 5 nm increments in order to determine the optimal excitation wavelength, as well as the sensitivity to changes in the excitation wavelength. Over the 50 nm range, the maximum intensity accumulating in the plasmonic waveguide varies by no more than $\approx 10\%$, which can be related to a 10% change in efficiency. A slight improvement in performance is seen towards 600 nm. This is shifted from the predicted phase-matched wavelength of 620 nm, further suggesting perturbations to the modes caused by strong coupling.

Sensitivity to Metal Film Thickness

In fig. 5.13, the gold film thickness was varied from 30–40 nm in 1 nm increments. The behaviour of the propagating plasmon is strongly dependent on the metal film thickness. An increase in film thickness of 10 nm can be seen to reduce the coupling to the surface plasmon of the directional coupler by 40%. This would be due to both the increased losses with the increased film thickness, as well as an effect of tuning the waveguide parameters farther from the phase-matched point. In practice, this sensitivity is expected to play only a small role in the performance of the device; gold is deposited at a rate of 0.5 Å/s, resulting in a gold film thickness accurate to within nanometres.

Sensitivity to SU-8 Film Thickness

In fig. 5.14, the dielectric waveguide thickness was varied between 450–550 nm in 10 nm increments. The efficiency of the directional coupler in coupling light to the plasmonic waveguide was seen to change little over this 100 nm range. However, a small variation in optimal coupling length was observed, changing by 2 μm.

Figure 5.13: Simulations of the directional coupler, varying the gold film thickness. The film thickness varies from 30 nm (blue) to 40 nm(teal). The nominal thickness is 30 nm. (Left) Field in the optical waveguide, (right) field in the plasmonic waveguide. As the thickness increases, the maximum intensity in the plasmonic waveguide decreases by 50%.

Sensitivity to Waveguide Separation

Finally, the waveguide separation was varied from 300–700 nm, and this is shown in fig. 5.15. For this simulation, the simulation was expanded to 80 μm in order to account for the longer coupling lengths at greater separations. Over the 400 nm range studied, the coupling length varies from 12–30 μm. The change in coupling length is accompanied by a change in coupling efficiency of 80%, due to plasmonic losses coming into play; the surface plasmon propagation length is only $\approx$ 20 μm. The best coupling was achieved by a waveguide separation of 300 nm, however this lies at the lower limit of what can be fabricated using spin-coating, and a separation $\sim$ 500 nm is closer to what may be expected. At a separation of 500 nm, the coupling length is on the order of 20 μm, corresponding to a coupling strength $\Omega \sim 1.6 \times 10^5$, which is in the range which we require to achieve substantial coupling. In these simulations, the intensities are seen to possess structure not consistent with directional coupling between the two waveguides. This structure becomes more pronounced at larger waveguide separations. We attribute these features to the imperfect coupling method used. The optical waveguide mode was approximated by a Gaussian, resulting in imperfect coupling to the optical mode. As a result, light which did not couple to the optical waveguide mode between the two waveguides would be partially guided, before being lost to absorption in the gold or scattering.

These parameter sweeps provided insights into the feasibility of fabrication for the directional couplers They demonstrate that many of the fabrication requirements lie within expectation, and that only the waveguide spacing layer should represent a challenge during fabrication.
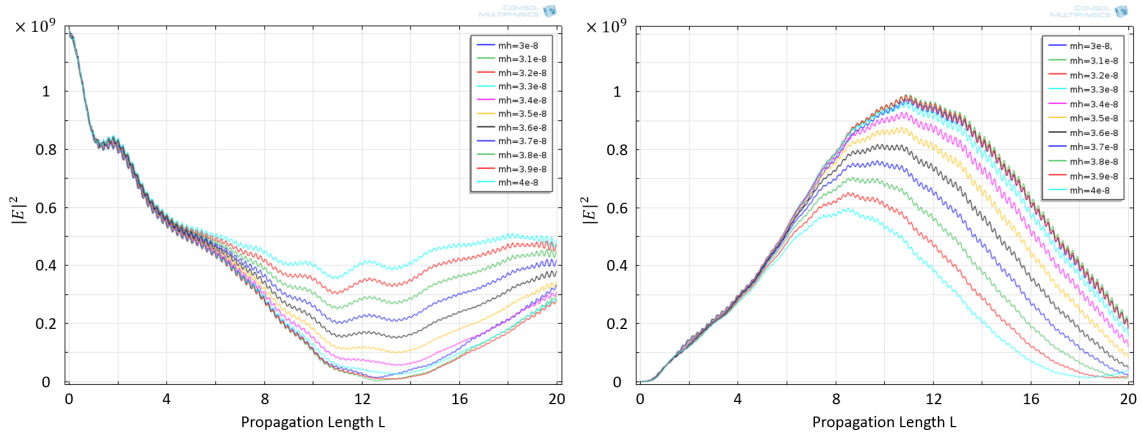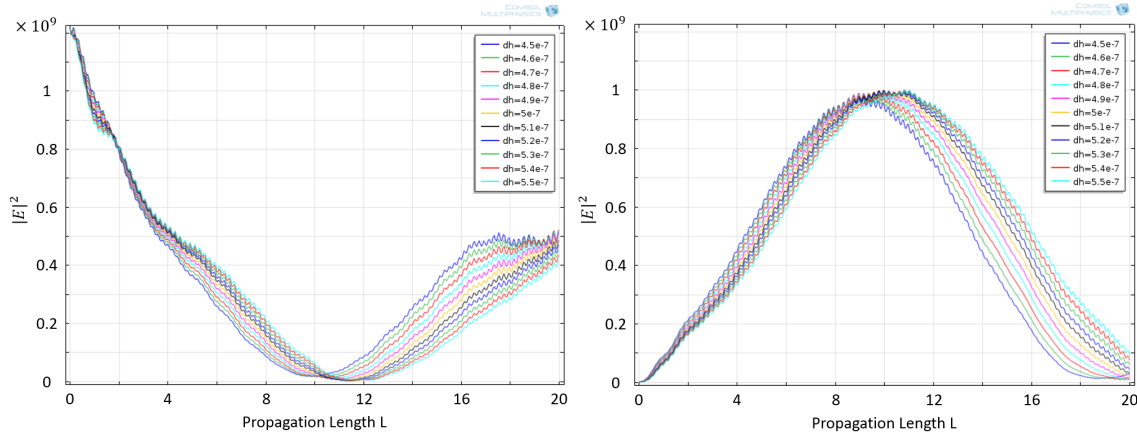
Figure 5.14: Simulations of the directional coupler, varying the SU-8 waveguide thickness. The thickness varies from 450 nm (blue) to 550 nm (teal), from the nominal thickness of 500 nm. (Left) Field in the optical waveguide, (right) field in the plasmonic waveguide. As the thickness of the waveguide is increased, the maximum intensity in the plasmonic waveguide changes by less than 5%, but the coupling length increases by $\approx 2~\mu$m

5.5   Fabrication

We intended to follow up our modelling by fabricating these directional couplers using a combination of spin coating and ion-assisted gold deposition techniques. However, complications during fabrication prevented directional coupling devices from being completed. The method of fabrication that was attempted is outlined below.

The PMMA and SU-8 layers were deposited using a spin coating approach. Spin coating allows the deposition of polymer layers with a range of refractive indices, generating films with a thickness on the order of a micron. During spin coating, a glass substrate is mounted on a vacuum chuck, upon which several droplets of the polymer solution are deposited. The substrate is then spun; the centrifugal force causes the droplets to spread out across the substrate with a final thickness related to the spin speed and the viscosity of the initial polymer solution. The solvent rapidly evaporates throughout the spinning process, leaving behind a solid polymer film.

In order to fabricate films of the appropriate thickness, the viscosity of the initial solution was varied, and the spin speed had to be varied, until the correct final thickness was achieved. Starting with PMMA950 from MicroChem, the (polymerised) PMMA dissolved in a solvent (anisole) was further diluted using dichloromethane to reduce the viscosity. Using a PMMA:dichloromethane mixture in a 1:10 ratio, and spun at 3000 rpm for 1 minute, PMMA films with a thickness of ~ 300 nm were fabricated. The surface roughness of the PMMA films were not as good as achieved with the gold films, with the arithmetic surface roughness $R_a < 10$ nm. We fabricated films with a trace amount of dye dissolved in the solution (Oxazine Perchlorate 170). This dye was intended to act as a tracer for the plasmonic mode. The dye has a fluorescent spectrum centred at 637 nm, which would allow the behaviour of the optical-plasmonic directional coupler to be directly imaged. Similarly, SU-8 films were fabricated using the GMI1030 SU-8 solution (Gersteltec). Here, we primarily varied the spin speed, and a spin speed between 3500–4000 rpm, resulted in SU-8 films ≈ 600 nm thick, with a similar arithmetic surface roughness ($R_a < 10$ nm). The preparation of the SU-8 films were
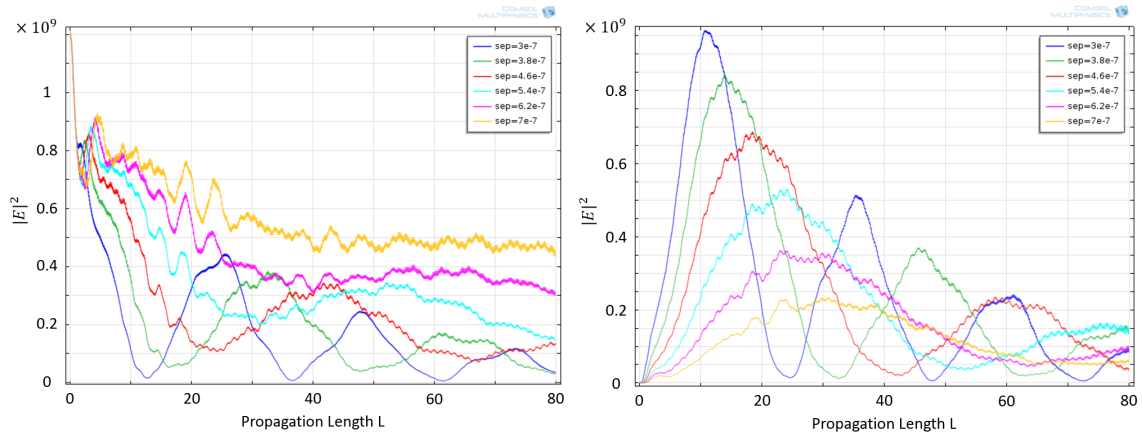
Figure 5.15: Simulations of the directional coupler, varying the separation between the two waveguides. The separation is varied from 300 nm (blue) to 700 nm (yellow). (Left) Field in the optical waveguide, (right) field in the plasmonic waveguide. As the separation increases, the maximum intensity drops by 75% and the coupling length increases from 10 to 30μm

then completed following the procedure in [183]. This consisted of a soft-bake in two steps: at 65° for 2 minutes, and then at 95° for 2 minutes, where the temperature was ramped at 2°/min between stages. This soft-bake was followed by a UV exposure to cause cross-linking in the SU-8 film. The UV exposure consisted of using a λ = 266 nm UV lamp, and exposing the film for 7 seconds, to achieve ~ 100 mJ/cm^2. Finally, the film was post-baked at 65° and 95° for 5 minutes each. The final SU-8 film thickness was thicker than specified by the design outlined above (500 nm), but was considered close enough that it did not strongly affect the efficiency of the coupling.

In conjunction with our existing gold deposition techniques, these spin-coating recipes enabled us to fabricate each of the individual layers of the directional coupler. Unfortunately, fabrication of the complete directional coupler failed due to interactions that occurred between fabrication steps. The fabrication of the second PMMA layer on top of the gold film resulted in the severe damage to the gold film, shown in fig. 5.16.

We believe the gold damage is due to the following process: the dichloromethane, used as a solvent for the PMMA, penetrates through nano-holes in the gold film, through to the underlying PMMA layer. The dichloromethane is then able to dissolve the underlying PMMA film. This causes the the gold film to de-laminate, and it is then lifted off the substrate by the spinning process. As the PMMA mixture was already polymerised, the film could not be thermally cured to avoid this outcome. Due to this, we were unsuccessful in experimentally testing our design.

5.6   Summary

In this chapter, we reviewed coupled mode theory in the context of optical-plasmonic coupling, considering the effects of phase-mismatch and plasmonic loss. We then designed an optical-plasmonic directional coupler and simulated it in COMSOL. In this modelling, we were able to show substantial coupling could be achieved to the plasmonic waveguide. However, the device was extremely sensitive to the waveguide separation. This parameter was also required

Figure 5.16: Damage to the underlying gold layer as a result of PMMA deposition. From the left, slide 2 to 4 were completely covered in gold prior to PMMA deposition. After the PMMA deposition, the gold on slide 2 is almost completely peeled off, and cracking is evident. Partial destruction of the gold film is seen in slide 3 and 4.

to be of the order of 500 nm or less in order to achieve the coupling strength required, and this can be extremely challenging to implement practically. This model serves as a baseline for comparison in the next chapter, where we investigate three-waveguide adiabatic passage coupling devices.

6

Plasmonic-Photonic Couplers based on Spatial Adiabatic Passage

6.1 Introduction

The modelling of plasmonic-optical dielectric couplers allowed us to consider more complex waveguide configurations. Here, we consider adiabatic passage couplers. These consist of three evanescently coupled waveguides, where the coupling strength has been modulated along the length of the device. Adiabatic passage has been demonstrated to be resilient to variations in the central waveguide, such as phase-mismatch and losses. Thus, adiabatic passage can be used to directly address some of the challenges in photonic-plasmonic couplers. This is discussed in more detail in the following sections. In this chapter, we first consider adiabatic passage using coupled mode theory in numerical models. We then consider a device consisting of two optical waveguides on either side of a surface plasmon waveguide by introducing loss and phase mismatch into the coupled mode equations, comparing these models to the directional couplers in chapter 5.

The second half of this chapter concerns digital adiabatic passage waveguide devices. Though these devices are purely optical, they experimentally demonstrate the robustness of the adiabatic passage framework against spatial phase modulation and losses; forming a complimentary study to the interaction between adiabatic passage and surface plasmons. These optical devices were designed by Jesse Vaitkus and Prof. Andrew Greentree (RMIT), fabricated by Zachary Chaboyer (MQ) using a laser inscription technique, and optically characterised by myself.

6.2 Adiabatic Passage

Adiabatic passage [186] is related to the Stimulated Raman Adiabatic Passage (STIRAP) process [187, 188]. The STIRAP process allows the coherent excitation of molecules to a specific energy state in a protocol which is tolerant, flexible and efficient. It involves three energy states ($|1\rangle, |2\rangle, |3\rangle$), and by tuning the nearest neighbour coupling strengths

$\{\Omega_p(t), \Omega_s(t)\}$ in time, the molecules can transferred from their ground state $|1\rangle$ to the excited state $|3\rangle$ through an intermediate state $|2\rangle$. Throughout this process, the intermediate state remains dark, as illustrated in fig. 6.1.

The obvious application of such a process is in situations in which the ground and excited states can not be coupled directly, but STIRAP possesses several other useful properties. Firstly, the process is not sensitive to small variations in coupling strengths, relaxing the precision required in implementing this process. Secondly, since the intermediate state $|2\rangle$ remains unoccupied in the ideal case, the constraints on choosing an appropriate intermediate state are also relaxed. The intermediate state can be lossy, or slightly detuned from the coupling fields, without affecting the quality of the STIRAP process. These characteristics come with the trade-off that STIRAP must be executed on relatively long time scales (much longer than a Rabi oscillation in this case).
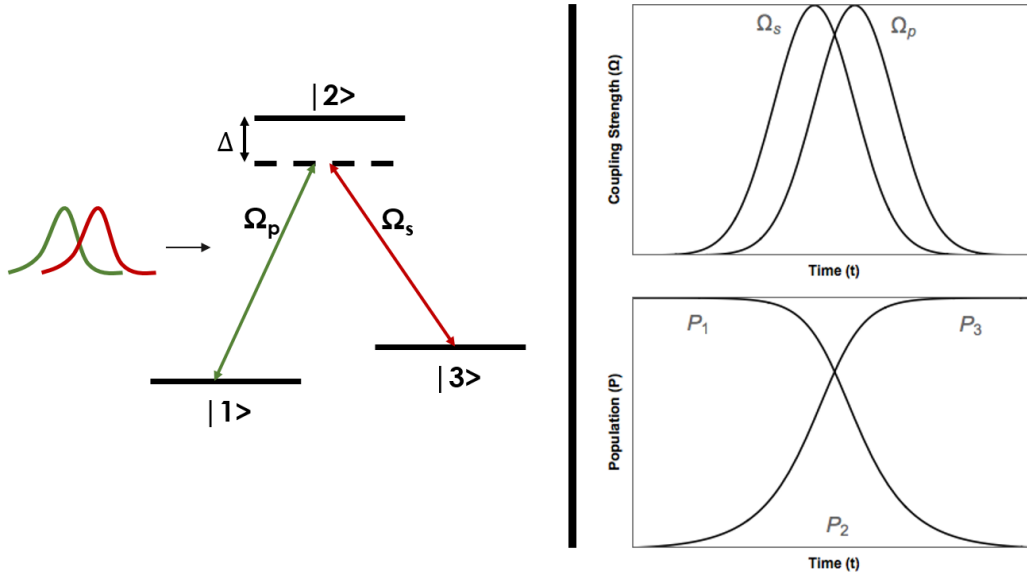
Figure 6.1: Typical STIRAP setup.

The STIRAP process can be abstracted from the molecular case, and in the more general context it is may be referred to as Coherent Tunneling Adiabatic Passage (CTAP) or simply Adiabatic Passage [189, 190]. It has become an attractive method for population transport for cases in which the population may be susceptible to noise or loss [186]. Such applications range from quantum information transport in semiconductor devices [191–194], to optical frequency conversion [195–198] and to optical couplers [89–97, 99] the current context, we are interested in designing a adiabatic passage device in an optical/plasmonic configuration, in order to facilitate plasmonic coupling. Here, the three states $\{|1\rangle, |2\rangle|3\rangle\}$ now correspond to three waveguides, where the intermediate waveguide $|2\rangle$ is a surface plasmon waveguide. Such devices would allow the coupling of optical and plasmonic fields, without being sensitive to the usual fabrication constraints, or the plasmonic loss.

6.3   Coupled Mode Theory and Adiabatic Passage

Adiabatic passage can be described by coupled mode theory by considering three coupled waveguides $\{|1\rangle, |2\rangle, |3\rangle\}$. Similar to eq. (5.2), the evolution of the light in the coupler can

be captured by the electric fields $\tilde{E}$, and in the three waveguides can be written as:

$$\frac{d\tilde{E}_1}{dz} = i\beta_1\tilde{E}_1 - i\Omega_{12}\tilde{E}_2$$

$$\frac{d\tilde{E}_2}{dz} = i\beta_2\tilde{E}_2 - i\Omega_{21}\tilde{E}_1 - i\Omega_{23}\tilde{E}_3 \tag{6.1}$$

$$\frac{d\tilde{E}_3}{dz} = i\beta_3\tilde{E}_3 - i\Omega_{32}\tilde{E}_2,$$

$$\tag{6.2}$$

where the coupling terms Ω_{nm} (given by eq. (5.4)) are introduced as a linear term, which is valid in the weak coupling regime. We have also assumed only nearest neighbour coupling ($\Omega_{13} = \Omega_{31} = 0$). The mode power is proportional to $P \propto |E|^2$. Since we are interested in a photonic-plasmonic-photonic coupler configuration, we can take the propagation constants of waveguides $|1\rangle$ and $|3\rangle$ to be equal ($\beta_1 = \beta_3 = \beta$). Again, it is helpful to define $\bar{\beta} = (\beta_1 + \beta)/2$ and $\Delta = (\beta_2 - \beta)/2$. Then, by choosing the electric field to be $\tilde{E}_i = E_i e^{i(\bar{\beta}z - \omega t)}$, we can rewrite the equations as a matrix:

$$i\frac{d}{dz}\begin{pmatrix} E_1 \\ E_2 \\ E_3 \end{pmatrix} = \frac{1}{2}\begin{pmatrix} -\Delta & \Omega_{12} & 0 \\ \Omega_{21} & \Delta & \Omega_{23} \\ 0 & \Omega_{32} & -\Delta \end{pmatrix}\begin{pmatrix} E_1 \\ E_2 \\ E_3 \end{pmatrix}. \tag{6.3}$$

Where $\{E_1, E_2, E_3\}$ are now the electric field amplitudes. We can take Δ out as a global phase, arriving at:

$$i\frac{d}{dz}\begin{pmatrix} E_1 \\ E_2 \\ E_3 \end{pmatrix} = \frac{1}{2}\begin{pmatrix} 0 & \Omega_{12} & 0 \\ \Omega_{21} & 2\Delta & \Omega_{23} \\ 0 & \Omega_{32} & 0 \end{pmatrix}\begin{pmatrix} E_1 \\ E_2 \\ E_3 \end{pmatrix}, \tag{6.4}$$

The Δ is canonically called the detuning in adiabatic passage literature, but here it corresponds to the phase mismatch parameter for the central waveguide $|2\rangle$. Under the assumptions of symmetric and real-valued coupling coefficients ($\Omega_{12} = \Omega_{21}$ and $\Omega_{23} = \Omega_{32}$), and $\Delta = 0$, the matrix may be solved for its eigenvectors $\{\lambda_0, \lambda_+, \lambda_-\}$ and eigenstates $\{v_0, v_+, v_-\}$:

$$\lambda_0 = 0, \qquad v_0 = \frac{1}{\sqrt{\Omega_{12}^2 + \Omega_{23}^2}}\begin{pmatrix} \Omega_{23} \\ 0 \\ -\Omega_{12} \end{pmatrix} \tag{6.5}$$

$$\lambda_\pm = \mp\frac{1}{2}\sqrt{\Omega_{12}^2 + \Omega_{23}^2}, \qquad v_\pm = \frac{1}{\sqrt{2(\Omega_{12}^2 + \Omega_{23}^2)}}\begin{pmatrix} \Omega_{12} \\ \pm\sqrt{+\Omega_{12}^2 + \Omega_{23}^2} \\ \Omega_{23} \end{pmatrix}. \tag{6.6}$$

Thus, there is an eigenstate with the eigenvalue $\lambda_0 = 0$, for which the light may occupy the first and last waveguide, but the second waveguide remains dark. In order to implement adiabatic passage, we then require that the coupling coefficients are varied in time ($\{\Omega_{12}, \Omega_{23}\} \rightarrow \{\Omega_{12}(t), \Omega_{23}(t)\}$). For the spatial adiabatic passage case, this is equivalent to allowing the coupling coefficients to be tuned along the length of the device ($\{\Omega_{12}, \Omega_{23}\} \rightarrow \{\Omega_{12}(z), \Omega_{23}(z)\}$). By doing so, there exists a configuration where the eigenstate v_0 corresponds to the transfer of light from one waveguide to the other. In particular, for the transfer of light from $|1\rangle \rightarrow |3\rangle$, we require that the coupling coefficients are varied in the

opposite order: $\Omega_{23}(0) \gg \Omega_{12}(0) \rightarrow \Omega_{12}(L) \gg \Omega_{23}(L)$, where L is the length of the device. This is the core principle behind adiabatic passage, and the coupling order is known as the counter-intuitive coupling scheme [186, 187]. If the coupling is tuned in the opposite order, known as the intuitive coupling scheme, then no smooth transition of power is observed; light is seen to oscillate between all three waveguides. This corresponds to the beating of the $\nu_{\pm}$ eigenmodes. The only additional constraint on adiabatic passage is that the tuning of the coupling coefficients ($\partial \Omega_{ij}/\partial z$) must be adiabatic, or slow, with respect to the coupling coefficients (Ω_{ij}) themselves, in order to implement adiabatic passage. This ensures that the ν_0 and $\nu_{\pm}$ eigenstates remain orthogonal throughout the process. If the coupling is tuned too rapidly, oscillatory behaviour, similar to the intuitive case, is observed.

Canonically, the coupling coefficients are tuned to follow a Gaussian profile. This case follows directly from STIRAP, where the energy states were coupled using optical pulses. However, there are many waveguide configurations which satisfy both the counter-intuitive coupling order and the adiabaticity condition, and this leads to the flexibility of design and implementation of adiabatic passage devices.

Mathematically, this constraint of adiabaticity can be addressed by defining an adiabatic parameter:

$$\mathcal{A} \equiv \frac{\langle \nu_i | \dot{\nu}_j \rangle}{|\langle \nu_i | \nu_i \rangle - \langle \nu_j | \nu_j \rangle|^2}, \tag{6.7}$$

where $\nu_{i,j}$ are any two of the eigenstates. The adiabaticity condition then demands that the adiabatic parameter $\mathcal{A} << 1$.

6.4   Modelling

In order to test the robustness of the adiabatic passage process, we first need to determine how the coupling coefficients varied with waveguide separation, and then we may choose a waveguide configuration that satisfies the requirements of adiabatic passage. We used COMSOL to do this. These values were then used with the coupled mode equations eq. (6.4). COMSOL was not able to carry out full-wave simulations for these devices due to the prohibitively long lengths of adiabatic passage devices.

Since waveguides are represented in coupled mode theory by propagation constants and coupling coefficients, we can initially treat optical and surface plasmon waveguides as interchangeable. We start with a model of adiabatic passage using propagation constants consistent with optical waveguides. This simplified model also allows us to investigate the adiabatic passage process itself. The initial simulation geometry and corresponding mesh are shown in fig. 6.2. The waveguides consisted of 1×1 μm square waveguides with waveguide separations between 1–3μm. The refractive index of the waveguide was 1.57159, corresponding to SU-8, excited with a wavelength of 630 nm as before. The structures were embedded in a background refractive index of 1.4963, corresponding to PMMA. This served as the cladding. The coupling coeffcients were extracted in COMSOL using an inbuilt mode solver, reducing the simulation to a 2 dimensional cross-section of the waveguides. The waveguides were placed in the centre of a large boundary box (20×10 μm) with perfectly conducting boundary layers. The boundary box needed to be much larger than the waveguides to ensure that the simulated waveguide modes were not affected by the simulation boundaries. Due to the relative simplicity of this mode-solving simulation, a high density mesh was used around the waveguides, with a maximum mesh element distance being defined as $\lambda/10n$, where n is the refractive index. A low density mesh ($\sim \frac{\lambda}{n}$) was used near the boundaries where
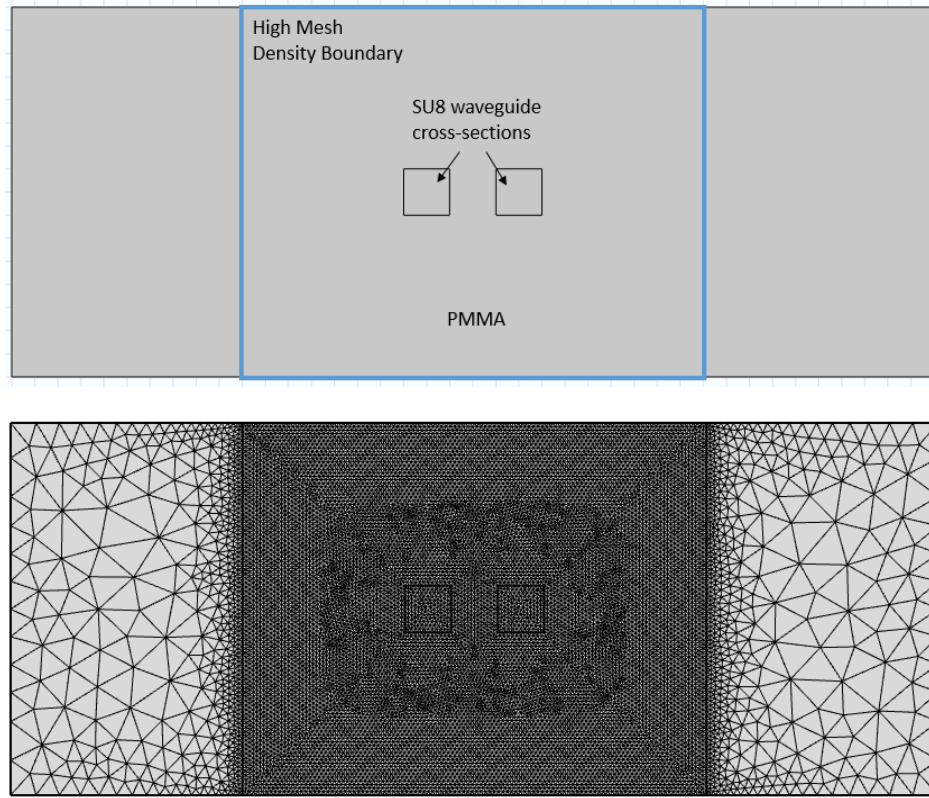
Figure 6.2: (Top) Mode analysis simulation of two SU-8 waveguides. (Bottom) Corresponding mesh.

no significant field was expected. An example of the results from these mode simulations is shown in fig. 6.3.

The propagation constants of the odd and even supermodes is provided by the Comsol simulations, and the coupling coefficient Ω can then be calculated by taking their difference $\Omega = |\beta_{odd} - \beta_{even}|$. This could be done for several waveguide separations, and then it was fitted with an exponential curve. This is shown in fig. 6.4

Once the range of coupling coefficients had been determined, a tuning profile was selected. Initially, the tuning profile of the coupling was chosen to be Gaussian of the form:

$$\Omega(z) = \Omega_{max} e^{\frac{-(z-z_0)^2}{2\sigma^2}} \tag{6.8}$$

where the offset z_0 is given by

$$z_0 = \frac{1}{2}(z_{max} \pm \sigma). \tag{6.9}$$

Here, σ is the width of the Gaussian. The width, and even the shape of the tuning profile, can be chosen almost arbitrarily provided that adiabaticity is maintained. The Gaussian tuning profile was chosen here since they have been thoroughly characterised in the literature in the context of STIRAP [187]. Using this form for $\Omega(z)$, we then numerically integrated eq. (6.4) using Mathematica to determine the field evolution of the electric fields in the device design. We can then take $P = |E|^2$. This model served as a baseline for an adiabatic passage optical device, and is plotted in fig. 6.5. The waveguide layout, corresponding to the chosen Gaussian coupling profile has also been calculated using fig. 6.4, and is also shown in fig. 6.5. Here, we chose a detuning $\Delta = 0$. We also chose a maximum device length of 40 mm, corresponding to
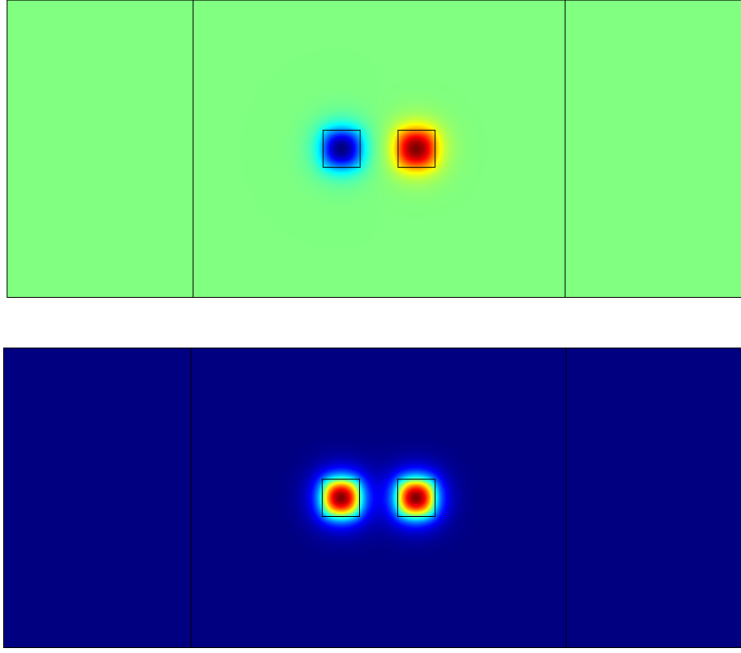
Figure 6.3: Solved modes of a standard directional coupler simulation, showing the (Top) odd and (Bottom) even supermodes.
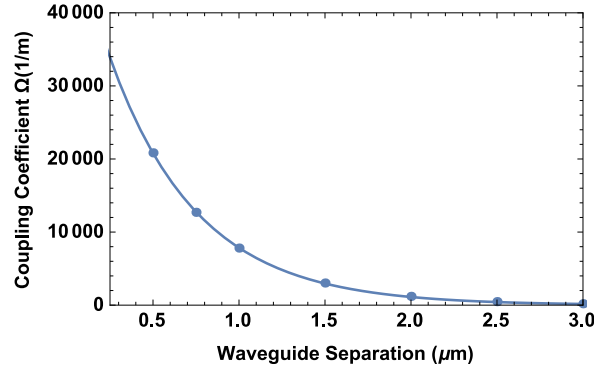
Figure 6.4: Coupling coefficients extracted from COMSOL, varying the edge-to-edge waveguide separation

an upper bound of what we might expect to be possible to fabricate on a glass substrate. Our choice of a minimum waveguide separation of 1 μm also reflects what we expect to be feasible to fabricate. This determines the maximum coupling coefficient in the device. It can be noted that at this waveguide separation, a coupling strength $\Omega = 1500$ m^{-1} can be expected, and an equivalent directional coupler would only be 2 mm long. The only free parameter remaining was the Gaussian width σ, which we varied until adiabatic passage coupling behaviour was observed. The width chosen for the Gaussian curves was $\sigma = 0.6$ cm.

For this device, the optical power P starts in the initial waveguide $|1\rangle$, and transits to the output waveguide $|3\rangle$ with a contrast approaching unity. Here, we have defined the contrast as the ratio $P_3/(P1 + P3)$. In a perfectly adiabatic device, this transition is perfectly smooth. However, oscillations are evident in the simulations, and this is a function of the adiabaticity of the device. The dark state $|2\rangle$ also has a transient, oscillatory population as a consequence of this. These oscillations should become less severe for longer devices, or
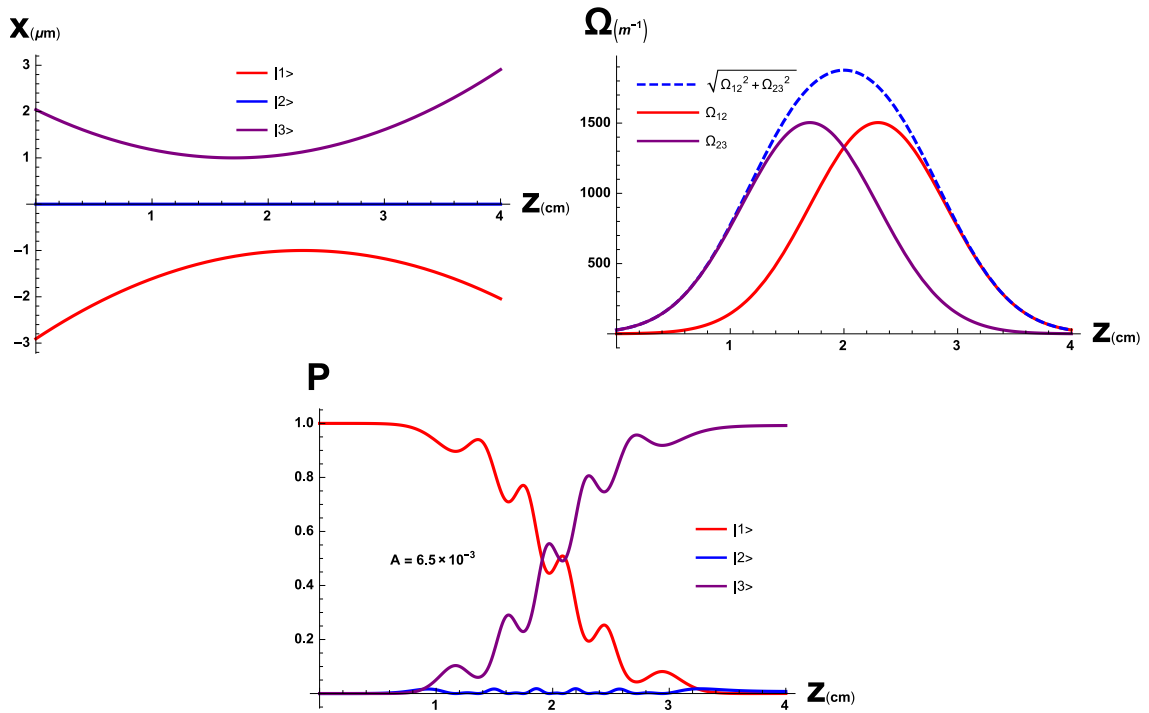
Figure 6.5: Modelled Adiabatic Passage waveguide devices, using a Gaussian tuning profile. Shown is the waveguide spatial distribution (Left) and the coupling profile (Right). The power evolution for light launched in the counter-intuitive configuration (Bottom) is also shown, showing transfer from waveguide $|1\rangle$ to $|3\rangle$, while $|2\rangle$ remains mostly empty.

devices with stronger coupling. Population in the central waveguide never exceeds 0.5% of the total population however, and this is considered sufficient for our purposes. We can further evaluate the adiabaticity of this device by defining a metric, consisting of the power in the central waveguide P_2 integrated over the length of the device z:

$$A = \frac{1}{L} \int_0^L \frac{P_2(z)}{P_0} \, \mathrm{d}z \qquad (6.10)$$

This is a unitless quantity. In the adiabatic limit, this metric gives $A = 0$, and in the case where light is fully occupying the intermediate waveguide, gives $A = 1$. For the Gaussian tuning profile shown, the adiabaticity metric gives $A = 6.5 \times 10^{-3}$.

In these devices, where adiabatic passage is facilitated by the counter-intuitive coupling order, the intuitive coupling order may also be investigated. Here, the intuitive coupling order corresponds to launching light in waveguide $|3\rangle$. This is shown in fig. 6.6. The intuitive behaviour is markedly different: many complete oscillations are evident, and no dark state is present. Unlike in the counter-intuitive order, the final output of the intuitive behaviour becomes strongly sensitive to the coupling strength and length of the device. Comparing the counter-intuitive and and intuitive configurations, it is evident that, in addition to these other properties, adiabatic passage devices also exhibit extremely asymmetric behaviour. Calculating the adiabatic metric for the intuitive case gives a value of 0.3.

To see if the adiabatic passage device could be optimised, a parameter scan was conducted. In this parameter scan, the condition given in eq. (6.9) was ignored, and the offset (z_0) and the

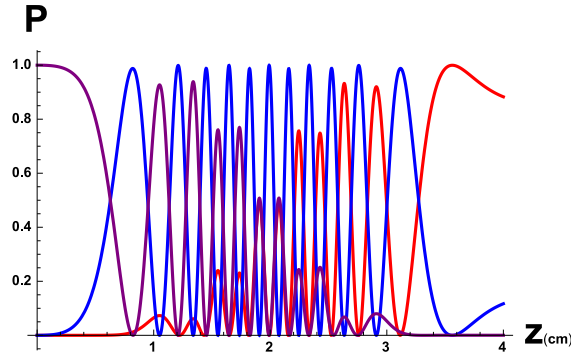Figure 6.6: Power evolution of the same device as shown in fig. 6.5, except light is launched in waveguide $|3\rangle$, corresponding to the Intuitive coupling order.

half-widths σ of the Gaussians were varied independently. The performance of the devices in this parameter range was judged by the adiabatic metric eq. (6.10), and by the final power present in the output waveguide $|3\rangle$. The results of these parameter scans are shown in fig. 6.7. The code for these parameter scans are included in appendix A.

We see that there is a large range of parameters for which the adiabatic metric is minimised. This is consistently accompanied by a power in the output waveguide approaching one. This corresponds to the adiabatic regime. Here, the device is not strongly dependent on the widths of the coupling profiles and the offset. As a result of this, the parameters used in the adiabatic passage device were left unchanged. It is also illustrative to consider the region of the parameter scan where the offset of the Gaussian coupling curves are negative. This corresponds to the coupling order being reversed, and light being coupled in the adiabatic passage intuitive configuration instead of the counter-intuitive configuration. Here, the final waveguide states are seen to vary rapidly with respect to the parameters, and the features of adiabatic passage are no longer evident.

Once the parameters for Gaussian coupling profiles had been established, several other coupling schemes were investigated. In particular, it was noted that the coupling coefficients are not required to tend to zero at the start and end of the device. With this in mind, a couple of other coupling profiles were modelled—designs which were either spatially more efficient or exhibiting greater adiabaticity. The first we call the "half-Gaussian" coupling profile:

$$
\Omega_{12} = \begin{cases} \Omega_{max} e^{\frac{-(z-z_0)^2}{2\sigma^2}} & z_0 < 0 \\ \Omega_{max} & z_0 \geq 0 \end{cases}, \tag{6.11}
$$

$$
\Omega_{23} = \begin{cases} \Omega_{max} & z_0 \leq 0 \\ \Omega_{max} e^{\frac{-(z+z_0)^2}{2\sigma^2}} & z_0 > 0 \end{cases}. \tag{6.12}
$$

The second coupling profile examined was a sinusoidal coupling profile, which is given by:

$$
\Omega_{12} = \Omega_{max} \sin^2(\frac{z}{z_{max}} \frac{\pi}{2}) \tag{6.13}
$$

$$
\Omega_{23} = \Omega_{max} \cos^2(\frac{z}{z_{max}} \frac{\pi}{2}) \tag{6.14}
$$

Using these profiles for $\{\Omega_{12}, \Omega_{23}\}$, eq. (6.4) can again be numerically integrated to determine
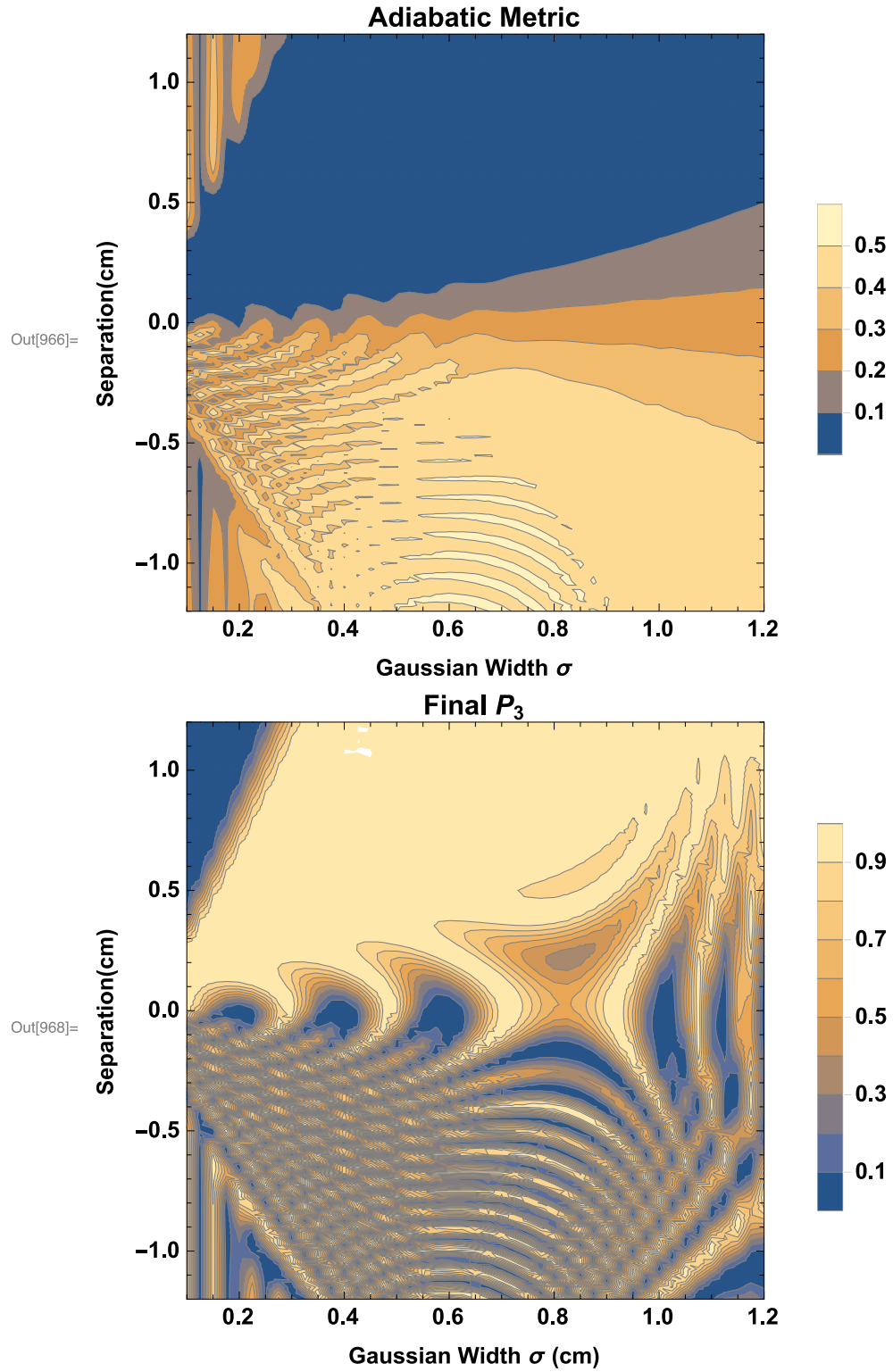
Figure 6.7: Parameter scans of the Gaussian widths σ and the offset between the Gaussian pulses z_0. Colour plots show the adiabatic metric (top) and the final power at the output P_3. Adiabatic region corresponds to the large smooth region where the adiabatic metric is minimised (blue) and the output power is maximised (yellow).

the power evolution in these waveguides. The plots for these coupling profiles are shown in figs. 6.8 and 6.9. All models were constrained to have the same minimum waveguide separation of 1 μm and the same device length of 4 cm. These designs have an adiabaticity metric equal to 9.3×10^{-4} and 1.7×10^{-3} for the half-Gaussian and the sinusoidal profiles respectively, both of which are significantly lower than in the Gaussian case examined above. These models demonstrate the flexibility that is available for implementing adiabatic passage in waveguide devices.
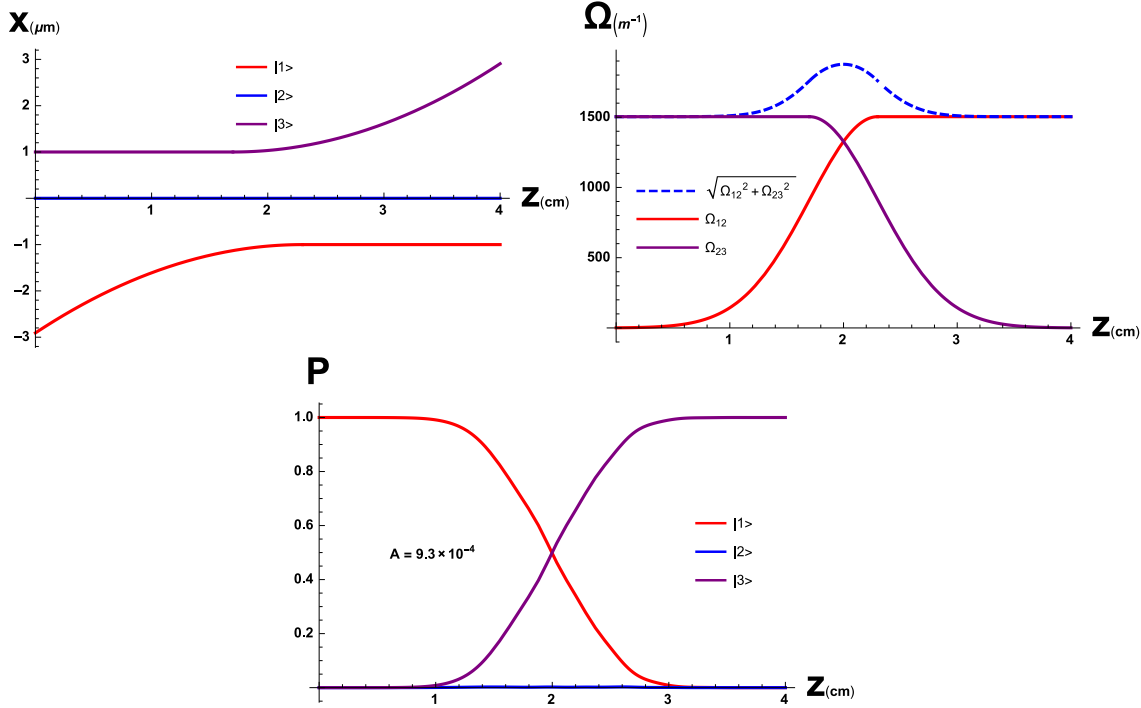
Figure 6.8: Adiabatic Passage model using the half-Gaussian coupling profile. We show the physical separation of the waveguides (Left), the coupling coefficients (Right) and the resulting power evolution (Bottom).

From here on, all models are using the half-Gausssian coupling profile, due to its high coupling efficiency and suppression of the light in the central waveguide.

6.4.1 Loss Mitigation

After establishing that adiabatic passage could be modelled with realistic values, the effect of losses on the dark state was explored. Loss in the central waveguide corresponds to an imaginary and negative Δ term in the coupled mode equations eq. (6.4). Keeping the assumption that the coupling coefficients are symmetric ($\Omega_{ij} = \Omega_{ji}$), the eigenvalues for eq. (6.4) become:

$$\lambda_0 = 0$$
$$\lambda_\pm = \frac{1}{2}(\Delta \mp \bar{\Omega}), \tag{6.15}$$
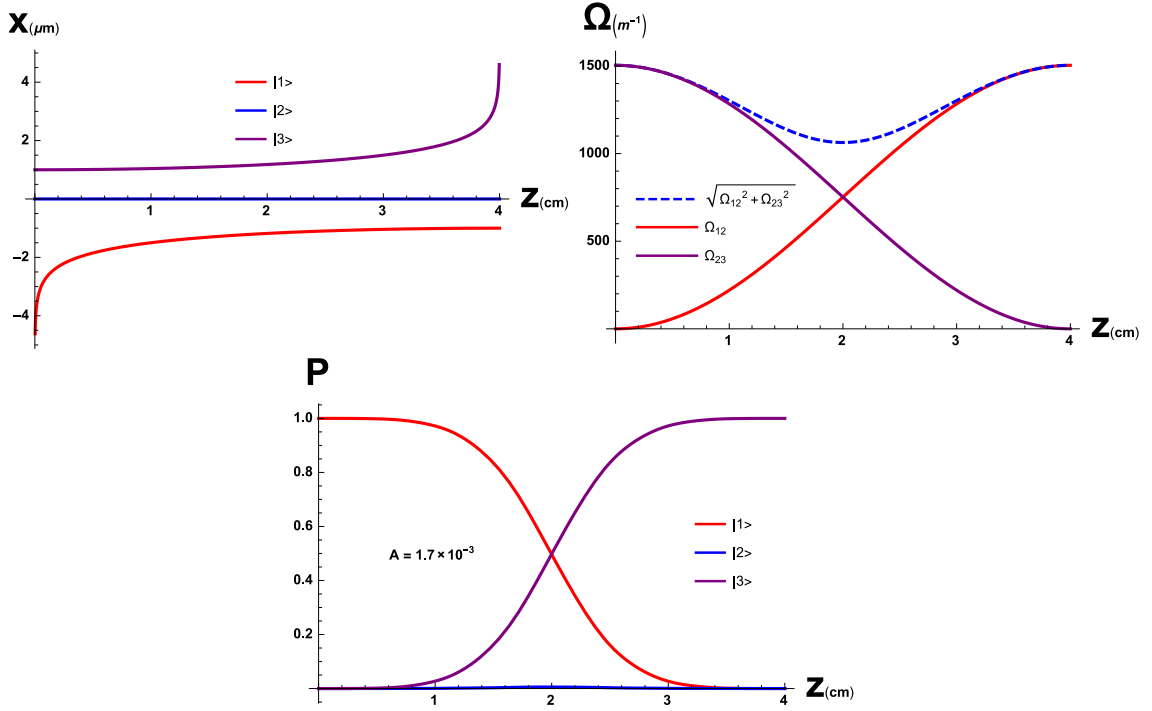
Figure 6.9: Modelled CTAP device using a sinusoidal coupling profile. (Left) Physical separation of the waveguides. (Right) Corresponding coupling profile. (Bottom) Resulting distribution in the device as light propagates in the device. Device exhibits smooth transition from $|1\rangle$ to $|3\rangle$

with the corresponding eigenvectors:

$$
v_0 = \frac{1}{\sqrt{\Omega_{12}^2 + \Omega_{23}^2}} \begin{pmatrix} \Omega_{23} \\ 0 \\ -\Omega_{12} \end{pmatrix}
$$

$$
v_{\pm} = \frac{1}{\sqrt{\Omega_{12}^2 + \Omega_{23}^2 + |\Delta \mp \bar{\Omega}|^2}} \begin{pmatrix} \Omega_{12} \\ -\Delta \pm \bar{\Omega} \\ \Omega_{23} \end{pmatrix}. \tag{6.16}
$$

In these equations we have defined $\bar{\Omega} = \sqrt{\Delta^2 + \Omega_{12}^2 + \Omega_{23}^2}$. The eigenvalue λ_0 and corresponding dark state are unaffected by the phase mismatch term Δ. Consequently, in the adiabatic limit, adiabatic passage is completely insensitive to the phase-mismatch and any losses introduced here. However, the phase-mismatch term Δ shifts the other eigenvalues $\lambda_{\pm}$ and their corresponding eigenstates. For negative and imaginary values of Δ, the real part of the eigenvalues $\lambda_{\pm}$ are shifted closer to λ_0. In practice, this means that the condition of adiabaticity needs to be more strictly enforced, as coupling between these eigenstates becomes easier, and this is detrimental to the adiabatic passage process.

Similar to the loss study in chapter 5, we introduced losses into the central waveguide in the form of a negative, imaginary component of Δ and numerically integrated the coupled mode equations 6.4. These losses were scaled with respect to to the coupling coefficient Ω. With the introduction of loss, we see in fig. 6.10 that light still couples smoothly across the device. Light in the initial waveguide $|1\rangle$ to go to zero, but much of it is lost in the

Figure 6.10: Performance of the adiabatic passage device for a phase mismatch of Im(Δ) = 0 (Top Left), Im(Δ) = $-i0.3\Omega$ (Top Right), Im(Δ) = $-i\Omega$ (Bottom Left), Im(Δ) = $-i1.7\Omega$ (Bottom Right)

intermediate waveguide $|2\rangle$, leading to a reduction in the output in $|3\rangle$. The power at the output as a function of the loss has also been plotted, and is shown in fig. 6.11. Here, we see that the transmitted power rolls off exponentially as the loss is increased, with respect to the coupling strength Ω. Using these models, direct comparisons can be made between the adiabatic passage couplers and the directional couplers studied previously. While in the directional coupler case, a loss $\Delta \approx 0.3\Omega$ reduced the efficiency of the coupler to 50%, for the adiabatic passage case, this loss is much less severe. A similar loss reduces the efficiency of the adiabatic passage coupler to 87%. The adiabatic passage coupler reaches the 50% efficiency mark for a loss of $\Delta = -i1.7\Omega$, shown in fig. 6.11, making it more than five times as resilient to losses.

In terms of plasmonic losses, a plasmon in the near-infra-red has losses between Im(β) $\approx$ 10^4–10^5 m^{-1}. This implies that, even for adiabatic passage couplers, the waveguides must be strongly coupled, with a coupling strength of a similar magnitude. Based on the modelling of chapter 5, this coupling strength is feasible.

6.4.2   Phase Mismatch

We then investigated the effect of the phase-mismatch, or the detuning. This is represented by a real Δ term. Because a plasmon tends to have a larger propagation constant than the corresponding optical mode, we chose this mismatch to be positive. In real devices, the phase mismatch between the central waveguide and the outer waveguides can generally be addressed by waveguide engineering, however, the phase-sensitivity of the device does have implications for the bandwidth of the device.

We can see from fig. 6.12 that in the case of phase mismatch, the power transfer from the
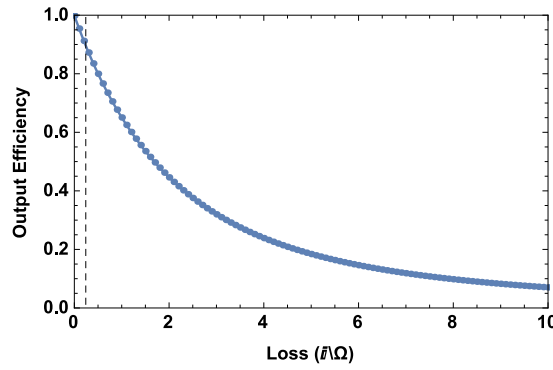
Figure 6.11: Efficiency of the adiabatic passage design with respect to loss, ranging from 0 to 10Ω. Dotted line indicates the loss at which an equivalent directional coupler drops to 50% coupling efficiency.

input to the output ($|1\rangle \rightarrow |3\rangle$) remains smooth, and the power in the intermediate waveguide $|2\rangle$ remains small. The primary effect of a large phase-mismatch is the reduction in coupling efficiency of the adiabatic passage device, with more light remaining in the initial waveguide. We can quantify the performance of the device by defining a contrast as $P_3(L)/(P_1(L)+P_3(L))$, where $\{P_1(L), P_{,3}(L)\}$ are the output powers of $|1\rangle$ and $|3\rangle$ respectively. Plotting the contrast as a function of phase mismatch (shown in fig. 6.13), we see that this reduction in coupling efficiency is not strictly monotonic, but generally decreases with increasing phase mismatch.

We can again make a comparison with the performance of similar directional coupler devices. As in the loss case, adiabatic passage is much more resilient; a directional coupler drops to a 50% transfer efficiency for a phase mismatch $\Delta = \Omega$. whereas the same occurs for this adiabatic passage design at $\Delta \approx 4\Omega$.

6.5   Comments on Fabrication

The adiabatic passage devices modelled here consist of the same materials used in chapter 5: gold, PMMA, and SU-8. As such, the adiabatic passage devices share the same constraints and obstacles in fabrication. Additionally, the small waveguide spacings are required to be tuned over the length of centimetres, demanding a high level of control. This type of control is largely incompatible with spin-coating techniques. We required a new platform, and new materials, in order to experimentally test the tolerance of adiabatic passage.

6.6   Digital Adiabatic Passage

Due to the complications in fabrication, the plasmonic adiabatic passage couplers could not be tested experimentally, and an alternate approach was taken by studying a digital version of adiabatic passage. Recently, studies have explored ideas of piecewise STIRAP [199, 200], where the coupling coefficients were tuned in discrete steps. Further studies by Jesse Vaitkus and Prof. Andrew Greentree modelled the full digitisation of the adiabatic passage dark state [201]. A photonic example of such a digital adiabatic passage device is shown in fig. 6.14. Their study shows that despite digitisation, the characteristics of adiabatic passage: broadband operation and flexibility, are maintained. Experimentally, digital adiabatic passage has many similarities to the plasmonic adiabatic passage device considered in section 6.4: The digital
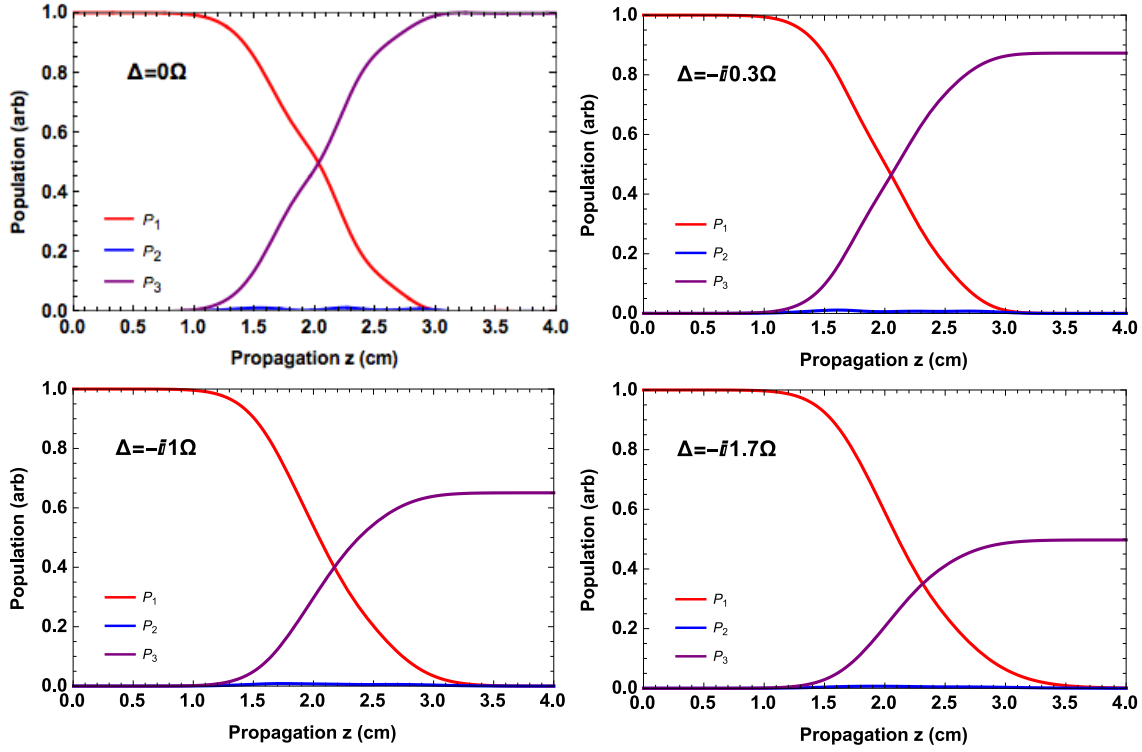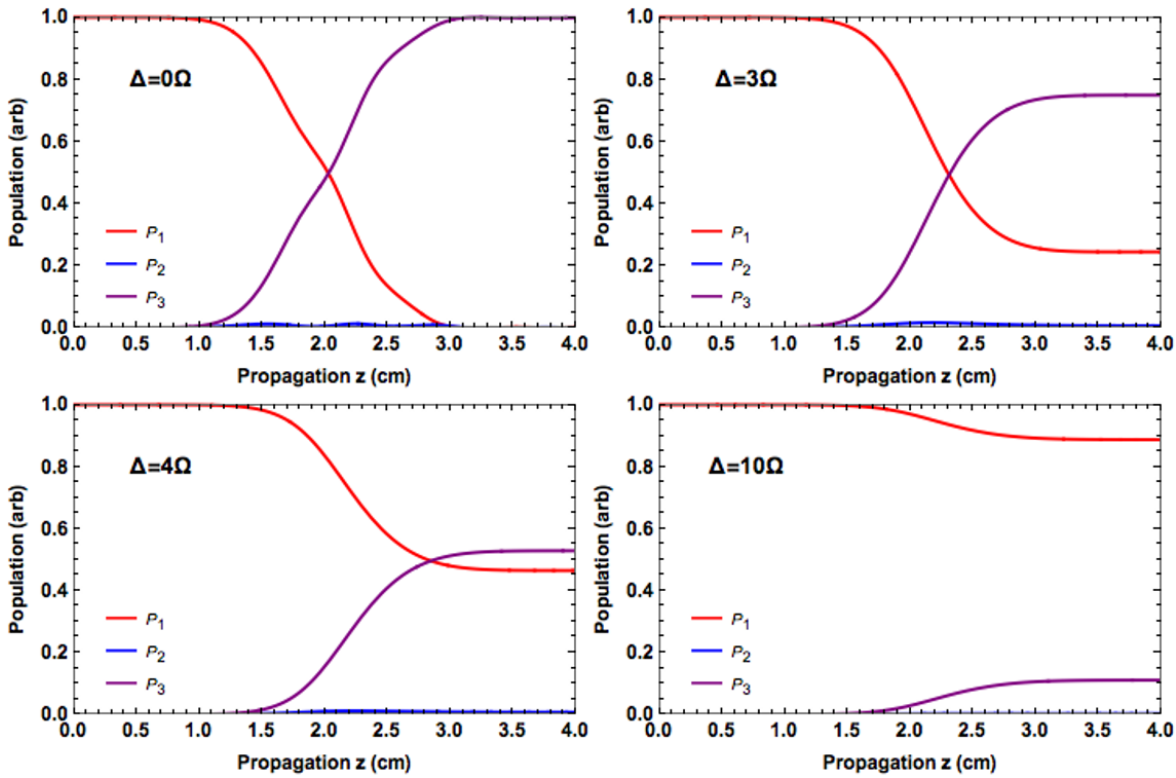
Figure 6.12: Performance of the adiabatic passage device for a phase mismatch of $\Delta = 0$ (Top Left), $\Delta = 3\Omega$ (Top Right), $\Delta = 4\Omega$ (Bottom Left), $\Delta = 10\Omega$ (Bottom Right). At large Δ, coupling is strongly inhibited.

spatial modulation of the coupling constant is analogous to phase mismatch, while the digitisation error introduces a similar loss mechanism.

In light of these features, we experimentally investigated a digital adiabatic passage design, in collaboration with Jesse Vaitkus and Prof. Andrew Greentree from RMIT, and Zachary Chaboyer from Macquarie University. The waveguide digital adiabatic passage devices were designed by Jessie Vaitkus. In these designs, the intermediate waveguide was divided into five or seven waveguide segments. These devices were then fabricated by Zachary Chaboyer from Macquarie University using an ultrafast laser inscription technique in glass, resulting in an integrated optical device. The characterisation and analysis of the digital adiabatic passage devices was then carried out by myself. In the context of this thesis, this study served to both verify the concepts of digital adiabatic passage, and to demonstrate the tolerance of adiabatic passage to these loss and phase-mismatch mechanisms, simulating conditions similar to the plasmonic case.

6.6.1 Theory

To digitise adiabatic passage, there are several of additional considerations that need to be considered. It was shown in [201] that when the intermediate state is digitised into a large number of segments (n=45), behaviour approaching regular adiabatic passage is observed, assuming a system with no losses. For digitisation into fewer segments, where the digitisation error becomes significant, adiabatic passage begins to break down. Light begins to oscillate between the waveguides, and the central waveguide is no longer dark;
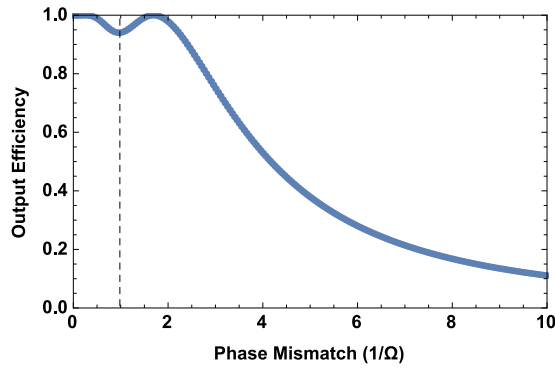
Figure 6.13: Efficiency of the adiabatic passage design with respect to phase mismatch, ranging from 0 to 10Ω. Dotted line indicates the phase-mismatch at which an equivalent directional coupler drops to 50% coupling efficiency.
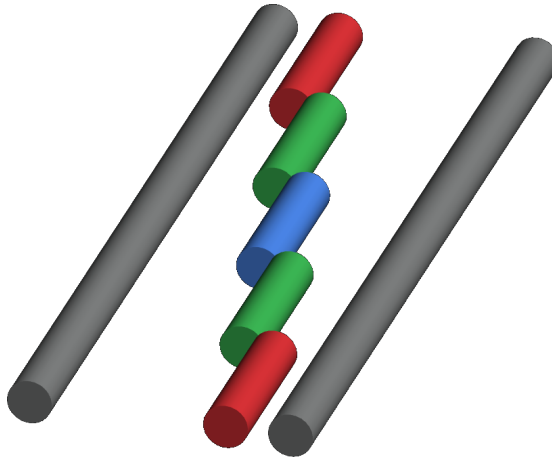
Figure 6.14: Schematic of a digitised adiabatic passage waveguide device.

a transient but significant amount of light may be observed. In addition to the degree of digitisation, the length of the individual waveguide segments must also be considered. For optimal performance, the segment lengths must be chosen such that light that couples to the waveguide segment can propagate sufficiently to couple out again. This reduces to choosing lengths such that

$$L_{opt} = \frac{(2n+1)\pi}{\sqrt{\Omega_{12}^2 + \Omega_{23}^2}}, \tag{6.17}$$

where $n = 1, 2, 3...$ and the Ω_{nm}'s are the coupling coefficients as before. The intermediate waveguide, though now consisting of many segments, will still be denoted by $|2\rangle$. It was shown in [201] that for the incorrect choice of segment lengths, resonances may occur. At these resonances the waveguide segments do not remain dark, and the model shows the light is returned to state $|1\rangle$. This model however did not include losses, and in practice this case is expected to produce large losses via scattering.

6.6.2   Device Design

By accounting for the number of segments and the length of each segment, a digital adiabatic passage device could be designed. As in the design of all adiabatic passage devices, there are a number of free parameters. Here, the constraints of the femtosecond direct write technique [202], and the physical size of the induced refractive index modification was used to constrain the minimum separation of the waveguides. We were also limited in the range of motion of the translation stages in the writing process, which constrained the maximum length of the device.

The device designs were fixed with a total device length to 70 mm, and total device width of 20 μm. The refractive index modification were of the order of $\Delta n \approx 5.6 \times 10^{-3}$, with a physical waveguide width $\rho \approx 1.6\,\mu$m. Then, by choosing the number of waveguide segments that make up the dark state and constraining their length using eq. (6.17), we optimized our digital adiabatic passage design. We chose to digitise the dark state into both 5 and 7 waveguide segments, resulting in the designs shown in table 6.1. Here, the subscripts $|2\rangle_i$ refer to the individual waveguide segments which make up the digitised waveguide $|2\rangle$. Each waveguide segment has been chosen to be separated from the previous waveguide segment by 7.5 mm. This separation was chosen to ensure that any coupling behaviour could not simply be explained by direct coupling from waveguide segment to waveguide segment. Coupling behaviour would then have to be a consequence of adiabatic passage. A schematic of the device layout is shown in fig. 6.15

			5 Segment Devices				
Waveguidelet	$|1\rangle$	$|2\rangle_1$	$|2\rangle_2$	$|2\rangle_3$	$|2\rangle_4$	$|2\rangle_5$	$|3\rangle$
L_{opt}(mm)	N/A	5.5824	9.2295	10.3775	9.2295	5.5824	N/A
x (μm)	-10.00	-2.00	-0.75	0.00	0.75	2.00	10.00

				7 Segment Devices				
Waveguidelet	$|1\rangle$	$|2\rangle_1$	$|2\rangle_2$	$|2\rangle_3$	$|2\rangle_4$	$|2\rangle_5$	$|2\rangle_6$	$|2\rangle_7$	$|3\rangle$
L_{opt}(mm)	N/A	5.5824	8.7232	9.961	10.3775	9.961	8.7232	5.5824	N/A
x (μm)	-10.00	-2.00	-0.93	-0.43	0.00	0.43	-0.93	2.00	10.00

Table 6.1: Table of positions and lengths of the waveguide segments. The relative waveguide spacing is given by x, as shown in fig. 6.15. All waveguidelet pairs $|2\rangle_{i+1}$ and $|2\rangle_i$ are separated in z by 7.5 mm to increase the total length to 70 mm

6.6.3   Fabrication

The waveguides in all devices herein were fabricated using an ultrafast laser inscription technique [202]. This consisted of taking the output of a Ti: Sapphire oscillator (Femtolasers GmbH, FEMTOSOURCE XL 500, 800 nm centre wavelength, 5.1 MHz repetition rate, <50 fs pulse duration) and focussing it into a borosilicate glass substrate (Corning Eagle2000) at a depth of 170 μm using an 100x oil immersion objective lens. Our combination of writing parameters lies within the cumulative heating regime of refractive index modification [203] in which subsequent pulses are absorbed within the focal volume before the dissipation of energy into the bulk of the material, leading to a refractive index modification dominated by thermal effects. The thermal mechanism of the index modification causes both the refractive

index modification Δn and physical size of the waveguide to increase with the amount of absorbed energy [204]. This allowed the index profile that was written to be controlled by varying the writing pulse energy. The sample was then translated with respect to the beam focus using Aerotech motion control stages with 10 nm precision, allowing us to form waveguides.

Using this writing technique, twenty-three digital adiabatic passage devices were fabricated, each written with a different writing power. The writing energy was iterated between 28.5 and 34 nJ in 0.25 nJ steps at a constant sample feedrate of 1500 mm/min in order to find the parameter space that allowed single mode operation at $\lambda = 800$ nm. The central
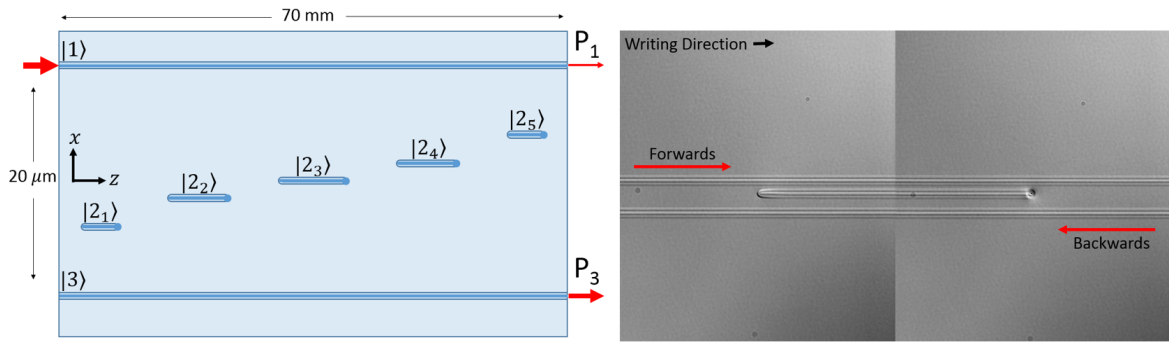
Figure 6.15: (Left) To scale schematic of a 5 segment digital adiabatic passage device. (Right)Stitched differential interference contrast (DIC) microscope image of a waveguide segment making up the dark state. Tapering is evident at the start of the segment, and a void is evident at the end.

waveguide was written by modulating the laser output with a fast RTP pockels cell. The signals that were used to trigger the pockels cell were synchronised with the motion of the translation stages in order to obtain segments of the proper length at the proper position along the length of the chip. The switching of the laser by the pockels cell leads to structuring of the waveguide segments. A taper is observed at the start of the waveguide segment, as the threshold for index modification, due to cumulative heating, is gradually reached after illumination by the laser pulses. On the other hand, the sudden turning-off of the laser at the segment end leads to a transition away from the thermal regime and the formation of a bulbous void [205]. These features are expected to introduce asymmetric losses in the device for the forward and backward launch directions. These directions are indicated in fig. 6.15.

The scattering losses are also expected to be asymmetric with respect to the intuitive and counter-intuitive configurations. The scattering is expected to be weak in the counter-intuitive configuration due to the presence of a quasi-dark-state. On the other hand, in the intuitive configuration, there is no dark state and the voids scatter strongly. Each DAP device was accompanied by a single straight waveguide acting as a reference for transmission measurements and two straight waveguides with a 20 μm spacing to verify that direct coupling between states $|1\rangle$ and $|3\rangle$ is negligible for the device being considered. Directional couplers at each writing power were also fabricated, with a waveguide spacing of 14 μm and a coupling length 50 mm. These couplers were characterised and allowed us to select the adiabatic passage device designs with the appropriate coupling strengths. The devices to be further characterised were narrowed down to the devices written with writing powers between 28.75–31.5 nJ.

6.6.4 Characterisation

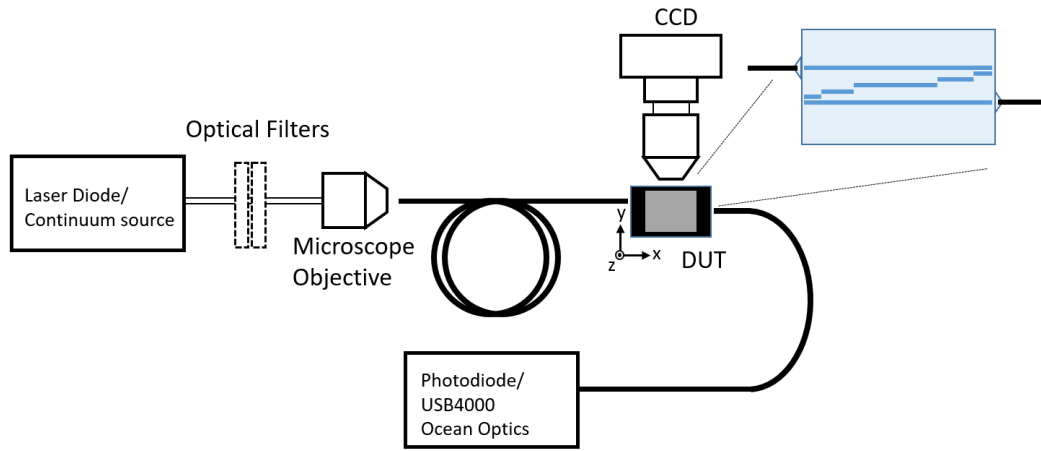Figure 6.16: Experimental schematic for characterising the digital adiabatic passage device.

To verify adiabatic passage-like behaviour, the digital adiabatic passage device was mounted on a high precision translation stage using a vacuum chuck. Light at 808 nm was coupled into a fibre, which was then coupled into the device with index matching oil. The light was coupled into the chip in the counter-intuitive configuration and the outputs were out-coupled by a fibre into a photodiode. This is shown schematically in fig. 6.16. In the ideal configuration, light is expected to transit across the device $|1\rangle \rightarrow |3\rangle$ with high contrast.

The outputs of the devices in the counter-intuitive configuration are plotted in fig. 6.17 for both the 5 and 7 segment devices, as $P_3/(P_1 + P_3)$ where P_1 and P_3 are the output powers of waveguides $|1\rangle$ and $|3\rangle$ respectively. The 11 devices tested showed little-to-no dependence on the writing energy over this range, which may be expected of an adiabatic device. Light was observed to have coupled across the DAP device in the counter-intuitive configuration in almost all cases. The largest source of variability appears to be waveguide homogeneity. On average, 89% of the output power is successfully coupled in the 5 segment devices. The 7 segment devices follow a similar trend, with a slightly diminished average output power at 86%. A slight asymmetry in fidelity is also evident in the forwards and backwards direction, with a greater fidelity in the backwards direction. This is easily explained by the position of the voids—in the backwards direction, each void is present at the beginning of the waveguidelet, where the light has yet to be coupled across and be scattered.

The outputs of both waveguides were also summed and normalised using a straight waveguide written with the same power, as shown in fig. 6.18. A large variation is evident in the transmissions between devices in the counter-intuitive performance. These variations are assumed to be due to waveguide defects, as well as intrinsic scattering due to the digitisation and gaps between segments. Despite this, the average device yields a 70% transmission. In contrast, when light is launched in the intuitive direction, the transmission is consistently suppressed, transmitting just 12% of the light. Without the dark state in the intuitive direction, the waveguidelets become strongly scattering, as shown in the insets of fig. 6.18. A slight difference in the forwards and backwards directions is also evident, with greater losses in the forwards direction. Similar behaviour can be seen for the 7 segment devices, with a strongly suppressed output in the intuitive direction. A lower overall performance can be seen when compared to the 5 segment devices, transmitting on average just 46% of the total power. A
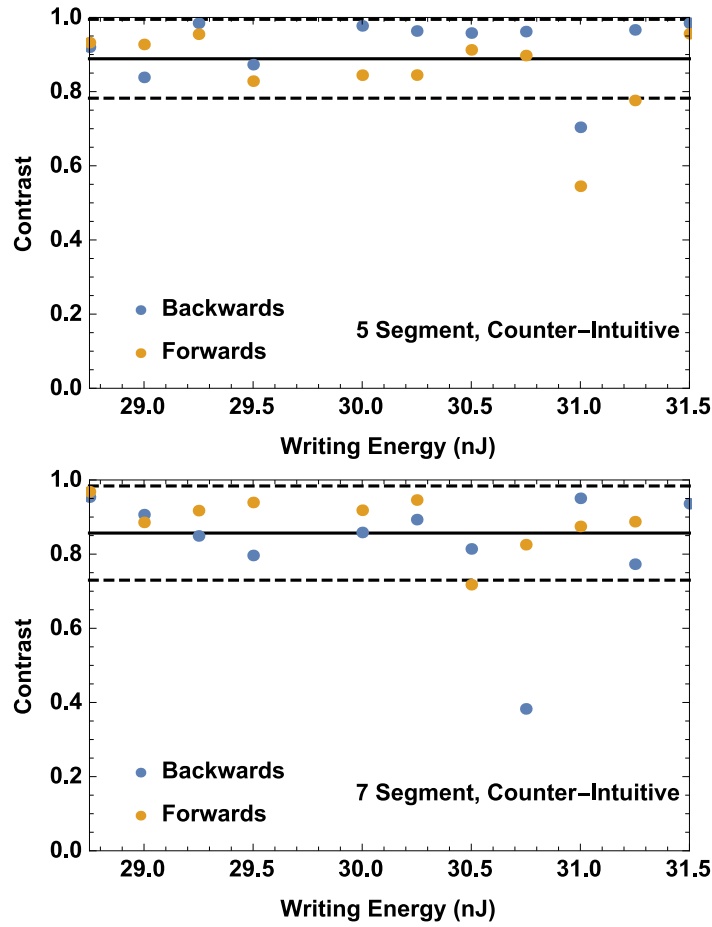
Figure 6.17: Outputs of $|1\rangle$ and $|3\rangle$ plotted as $\dfrac{P_3}{P_1 + P_3}$ in the counter-intuitive configuration. The 5 segment (Top) and 7 segment (Bottom) devices exhibit similar behaviour. The mean (solid line) and standard deviation (dashed) has been indicated.

large variance in performance between devices is also evident. Even though the additional segments in the 7 segment case should yield a better adiabatic passage performance due to a smaller digitisation error in the coupling, this is not observed experimentally—as the inclusion of additional scattering voids probably outweighs this benefit. This appears to be a feature of the femtosecond direct write implementation of digital adiabatic passage, and not a feature of digital adiabatic passage itself.

In order to test the operating bandwidth, the 5 segment devices were also characterised using a white light source (NKT Photonics SuperK Compact). The white light spectrum was narrowed down using a FGB25 colour filter in order to capture the spectral response of the devices between 700 nm and 900 nm. The output was fibre-coupled to a USB4000 OceanOptics spectrometer, yielding the raw spectra given in fig. 6.19.

The normalised waveguide outputs of some of these devices are shown in fig. 6.20. They were normalised using the straight reference waveguides in order to remove the spectral shaping caused by the filtering and the white light source itself. Across the writing powers used, it can be seen that the devices have highest fidelity not at 800 nm, but between 820–840 nm. This suggests that the induced index change Δn was greater than predicted. A greater Δn is consistent with a more strongly confined optical modes, resulting in weaker coupling
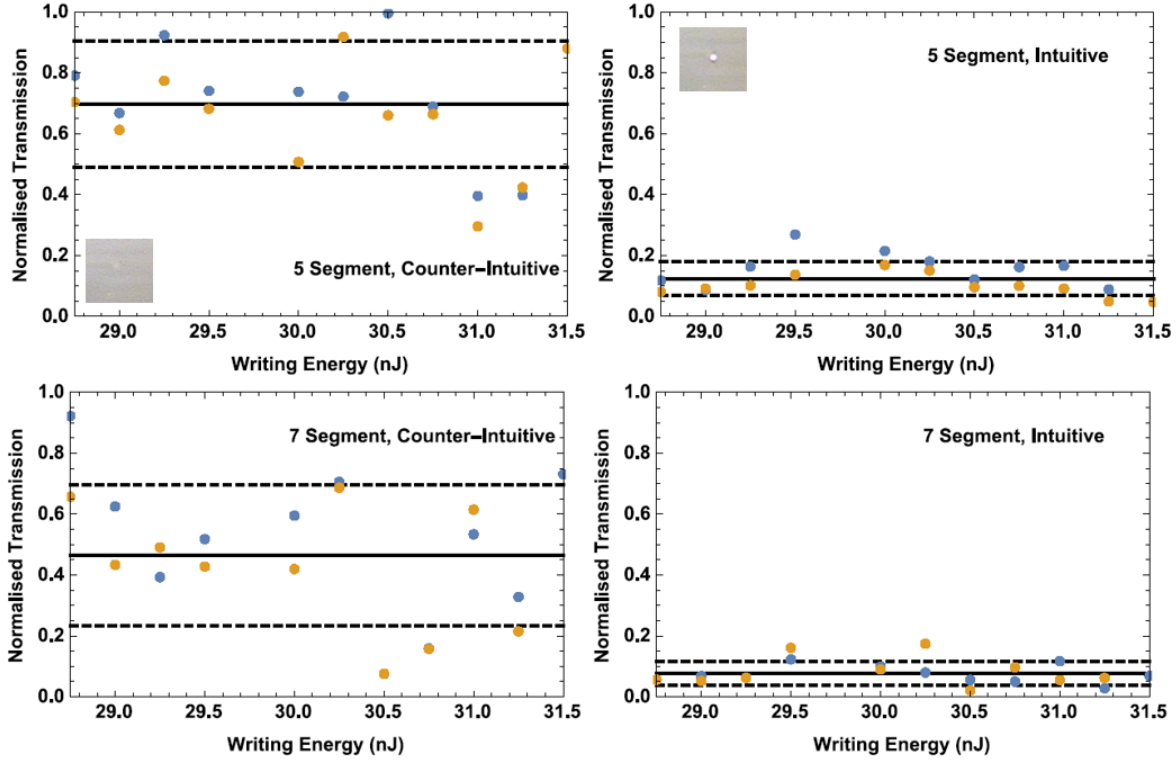
Figure 6.18: Total transmission of the 5 segment (top) and 7 segment (bottom) DAP devices, plotted as $\frac{P_1+P_3}{P_{ref}}$, plotted for the counter-intuitive (left) and intuitive (right) configurations. Mean (solid line) and standard deviation (dashed) have been indicated. Yellow and blue points correspond to the forward and backwards directions respectively. Insets correspond to an image of a void taken during the experiment from above.

coefficients, which would deteriorate the quality of the adiabatic passage performance. The optimal coupling wavelength would then be shifted to longer wavelengths, where the mode sizes are larger, and the coupling strength is recovered. At its optimal wavelength, each device exhibits fidelity above 95%, despite variability between devices. The devices remain largely insensitive to small changes in writing power, showing little shift in optimal frequency. The operational bandwidth with a fidelity above 90% is ≈ 60 nm. The optimal digital adiabatic passage performance also coincided with a suppressed throughput in the intuitive configuration < 5% as shown in fig. 6.20(b).

Outside the operational bandwidth, significant variability is observed between devices. We believe the key mechanism limiting the bandwidth is the segment lengths given by eq. (6.17): as the wavelength is varied, the coupling coefficients Ω_{ij} are varied, and the ideal length for the waveguide segments L_c no longer matches the waveguide segments in the device. The converse is true for the intuitive case: eq. (6.17) provides the condition for optimal scattering. As the wavelength and coupling coefficients are varied, the waveguide segments no longer match the condition for optimal scattering, and the intuitive configuration becomes transmissive. We also attribute the variability observed at shorter wavelengths to changes in coupling that were a consequence of the out-coupling fibre.

Figure 6.19: Raw spectral response of 5 segment DAP devices for a typical device. Counter-intuitive output is on the (left) and Intuitive is plotted on the (right). Strong spectral shaping from the laser source and filtering is evident in the reference.

6.7   Discussion

Through the characterisation of the waveguide digital adiabatic passage devices, the robustness of the adiabatic passage framework to digitisation was demonstrated. When used in the coun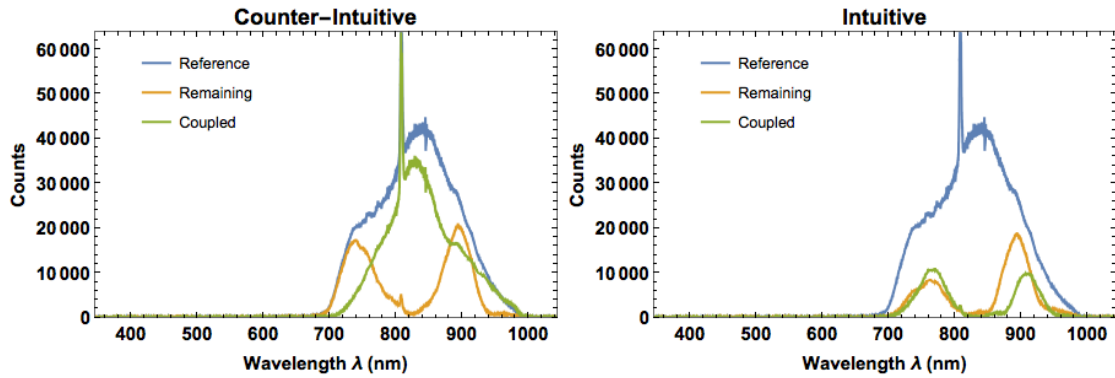ter-intuitive configuration, all of the features of adiabatic passage were evident: including robustness against variations in coupling, and robustness against strong scattering losses in the central state, which arose from both the digitisation and writing asymmetry. Additionally, as a consequence of the digitisation process, these devices also suppress the transmission for light launched in the intuitive configuration. As such, digital adiabatic passage devices also exhibit strong asymmetric behaviour. In the study of these digital adiabatic passage devices, this study also validates the feasibility of applying the adiabatic passage approach to other lossy systems, such as the plasmonic case explored earlier in this chapter.

6.8   Summary

In this chapter, we studied the more complex adiabatic passage couplers, building on the work on directional couplers in chapter 5. Compared to the directional couplers, the adiabatic passage designs considered were $\approx 4\times$ more robust against phase mismatch and $\approx 5\times$ more robust against loss than the directional couplers. This robustness is due to the presence of a dark state via the tuning of the waveguide couplings. The adiabatic passage couplers are also more flexible in design than their directional coupler counterparts, are generally tolerant to fabrication errors and require fewer engineering constraints due to relaxed phase matching conditions. However, the adiabatic passage design is also an order of magnitude longer than a typical directional coupler, and this must taken into consideration.

Adiabatic passage couplers also have several unique drawbacks: since the robustness of adiabatic passage is due to the presence of the dark state, there is no appreciable plasmonic field that accumulates at any point in the device. This makes it difficult to leverage the field confinement associated with surface plasmons. Additionally, since the device is insensitive to phase, it is also difficult to leverage the extraordinary sensitivity of the surface plasmons to local perturbations. This makes it impossible to utilise surface plasmons in this way for applications such as sensing and modulation. In light of these limitations, the usefulness of adiabatic passage to in the context of optical-plasmonic coupling is questionable.
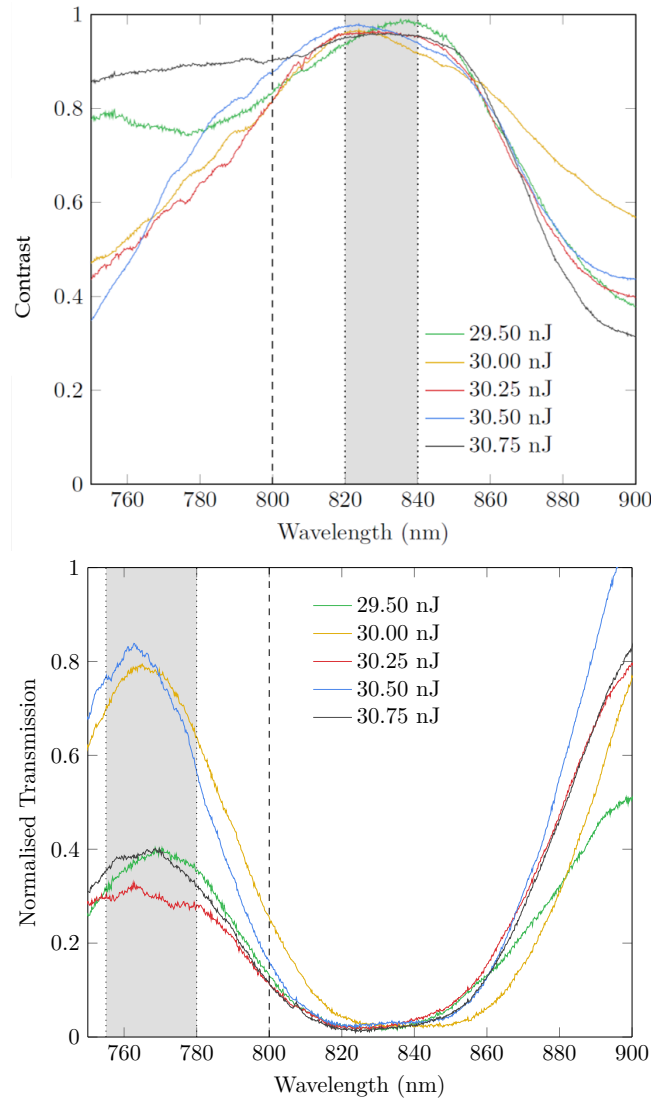
Figure 6.20: Spectral response of 5 segment DAP devices, shown for devices with writing energies between 29.50–30.75 and measured in the forwards direction. Counter-intuitive output is (top) as $\frac{P_3}{P_1+P_3}$, and Intuitive throughput is plotted (bottom) as $\frac{P_1+P_3}{P_{ref}}$.

7

Conclusion And Future Work

In this dissertation, we aimed to address both the challenges of plasmonic loss and optical-to-plasmonic coupling, in order to facilitate the development of compact surface plasmon waveguide devices. Two distinct approaches were taken: examining second-order nonlinear effects in the form of second harmonic generation and parametric down conversion, and waveguide coupling in the form of directional coupling and adiabatic passage.

7.1 Second-Order Nonlinear Effects in Propagating Surface Plasmons

In the first approach, we were able to observe a strong nonlinear response in the context of metallic, all-plasmonic second harmonic generation (chapter 3). However, the lack of available phase-matching mechanisms in the metal provided little scope for improving the conversion efficiency.

By employing dielectric nonlinear effects in lithium niobate (chapter 4) we obtained access to such phase-matching mechanisms; quasi-phase matching and birefringent phase matching; which we utilised in optically-pumped configurations. In the case of birefringent phase matching, the poor spatial overlap between the optical and plasmonic modes, arising due to the inherent disparity in mode sizes, led to low conversion efficiencies. This poor overlap diminished the benefits provided by the phase-matching. Ultimately, the nonlinear conversion was insufficient to compete with the plasmonic losses, and we were not able to observe the excitation of surface plasmons via second-order nonlinear effects.

The experiments on quasi-phase matching and second harmonic generation were inconclusive, and there is scope to carry out additional experiments. In our study, we were restricted by time and the availability of laser sources, and so our study of quasi-phase matching targeted a harmonic at 532 nm, where the plasmonic losses in gold are the most pronounced. The losses at this wavelength limited the interaction with the poling, leading to an inconclusive result. However, we believe that at longer wavelengths, where the losses become much less restrictive, a stronger interaction should be possible between the fields and the poled structures. Unfortunately, much like the birefringent phase-matching experiment, the poor spatial

overlap is still a factor which will limit the conversion efficiency.

The results of these experiments suggest that, in the planar gold-coated lithium niobate, optically-pumped configurations of second-order nonlinear effects are not feasible for providing parametric amplification in the nanosecond domain, and therefore are not feasible for plasmonic loss compensation. This is also not a useful means of enabling optical-to-plasmonic coupling.

7.2   Directional Couplers and Adiabatic Passage Couplers

The second approach taken in this dissertation covered directional coupling between optical and surface plasmon waveguides, which was then compared with similar waveguide adiabatic passage devices. In the directional coupler case, it was shown numerically that relatively short coupling lengths (10–20 μm) could be achieved using a combination of waveguide engineering and long-range surface plasmons. Using this method, a significant plasmonic field could be accumulated. Unfortunately, fabrication of such directional coupling devices using spin-coating techniques turned out to be extremely challenging and impractical. Regardless, this method was shown to be extremely sensitive to plasmonic losses, and extremely sensitive to the waveguide parameters.

In contrast, the numerical study of waveguide adiabatic passage devices with optical and plasmonic waveguides demonstrated a remarkable resilience to the plasmonic loss and phase-mismatch. The adiabatic passage devices were also extremely flexible in implementation, and were shown to be robust against variations in the waveguide parameters. These properties were further demonstrated experimentally, through the characterisation of analogous photonic digital adiabatic passage devices. These devices possessed similar losses, and were affected by scattering and digitisation errors. Despite this, when light was launched in the counter-intuitive configuration, light was transferred across the device with a coupling ratio approaching 1. Conversely, light launched in the intuitive configuration was strongly scattered and suppressed, giving the adiabatic passage couplers strongly asymmetric transmission properties. This robust behaviour of the adiabatic passage couplers is achieved with the presence of the dark state, which limits the amount of power present in the intermediate waveguide at any one time. While this property makes adiabatic passage extremely well suited to avoiding plasmonic losses, it also makes it difficult to leverage the other interesting properties of the plasmon such as the field confinement. Thus, there is limited scope for the direct application of adiabatic passage to mitigate losses in plasmonic devices.

7.3   Future Work

The studies on the second-order nonlinear conversion were conducted mostly using nanosecond laser sources. By heading towards shorter time-scales, using either picosecond or femtosecond pulse durations, a much larger nonlinear response can be expected. In the case of the quasi-phase-matching experiment, the use of longer wavelength sources should also result in a large increase in detectable signal. This could be further improved by using guided optical modes to increase the optical confinement and increase the interaction length, as suggested in [55]. This approach has the best prospects for introducing gain, as well as for launching surface plasmons via nonlinear coupling. However, these would be significantly more complex geometries.

There is also interest in investigating purely plasmonic nonlinear effects. These configurations would not be useful for introducing plasmonic gain, due to the losses present in each field. However, the large overlap between the plasmonic modes would allow the full effect of the plasmonic field enhancement to be utilised. This approach still has application for the nonlinear excitation of surface plasmons at different frequencies. This approach has been studied numerically by Duffin *et al.* [142], in the context of highly confined surface plasmon modes interacting with third-order nonlinear effects. They suggest that a nonlinear response can occur on a sufficiently short length scale that phase matching is not required. However, at longer wavelengths where the propagation lengths increase significantly, we believe that phase matching could play an important role. In such a case, phase-matching via birefringent phase-matching techniques would no longer be viable, due to the reduction in the degrees of freedom in a fully plasmonic configuration. But, in-plane methods such as quasi-phase matching could still be applied. Combining this with waveguide engineering and low loss waveguides in lithium niobate, such as suggested in [16], could result in an even larger increase in the observed nonlinear signal.

In the case of optical-plasmonic directional couplers and adiabatic passage devices, both of these approaches have been shown to be feasible numerically, however both have proved to be difficult to fabricate. By considering new materials and new fabrication techniques, it will be possible to directly characterise these devices experimentally. Such devices could have a large impact: allowing stronger coupling to propagating plasmons and enabling higher field densities in nanoscale devices. These devices could also enable better detection of plasmonic phenomena, by dirctly out-coupling to optical channels.

A
Mathematica Notebooks

Included is are several Mathematica notebooks used for several key calculations made in this thesis. In order, the notebooks are

- The Excitation angles for Second Harmonic Generation via Periodic Poling

- Crystal Cut of the Lithium Niobate for Parametric Down Conversion

- Generated Plasmon Power in Parametric Down Conversion

- Optical and Plasmonic Dispersions for Directional Coupling

- Adiabatic Passage Parameter Scan

The Excitation angles for Second Harmonic Generation via Periodic Poling

Constants

```
c = 299 792 458;
ε0 = 8.85418782 × 10⁻¹²;
μ0 = 1.25663706 × 10⁻⁶;

nano = 10⁻⁹;
```

Dielectric Properties

$$\texttt{neff[nor\_, nex\_, } \tau\texttt{\_] } = \frac{\texttt{nor nex}}{\left(\texttt{nex}^2 \texttt{ Cos}[\tau]^2 + \texttt{nor}^2 \texttt{ Sin}[\tau]^2\right)^{\frac{1}{2}}};$$

$$\texttt{nLNo}[\lambda\texttt{\_] } =$$
$$\left(4.9048 + 2.1429 * 10^{-8} \left(\texttt{T}^2 - 88\,506.25\right) + \left(0.11775 + 2.2314 * 10^{-8} \left(\texttt{T}^2 - 88\,506.25\right)\right) \Big/ \right.$$
$$\left(\left(\lambda * 10^6\right)^2 - \left(0.21802 - 2.9671 * 10^{-8} \left(\texttt{T}^2 - 88\,506.25\right)\right)^2\right) -$$
$$\left.0.027153 \left(\lambda * 10^6\right)^2\right)^{\frac{1}{2}} /. \{\texttt{T} \to 297.5\};$$

$$\texttt{nLNe}[\lambda\texttt{\_] } = \left(4.5820 + 2.2971 * 10^{-7} \left(\texttt{T}^2 - 88\,506.25\right) + \right.$$
$$\left(0.09921 + 5.716 * 10^{-8} \left(\texttt{T}^2 - 88\,506.25\right)\right) \Big/$$
$$\left(\left(\lambda * 10^6\right)^2 - \left(0.21090 - 4.9143 * 10^{-8} \left(\texttt{T}^2 - 88\,506.25\right)\right)^2\right) -$$
$$\left.0.02194 \left(\lambda * 10^6\right)^2\right)^{\frac{1}{2}} /. \{\texttt{T} \to 297.5\};$$

$$\texttt{nBK7}[\lambda\texttt{\_] } = \left(1 + \frac{1.03961212 \left(\lambda * 10^6\right)^2}{\left(\lambda * 10^6\right)^2 - 0.00600069867} + \frac{0.231792344 \left(\lambda * 10^6\right)^2}{\left(\lambda * 10^6\right)^2 - 0.0200179144} + \right.$$
$$\left.\frac{1.01046945 \left(\lambda * 10^6\right)^2}{\left(\lambda * 10^6\right)^2 - 103.560653}\right)^{\frac{1}{2}};$$

Gold Permittivity

```
imp0 = Import["METALS_Gold_Johnson.csv"];
"Column order = " <> imp0[[1, 1]] <> "," <> imp0[[1, 2]] <> "," <> imp0[[1, 3]]
imp = Take[imp0, -(Length[imp0] - 1)];
imp[[All, 1]] = imp[[All, 1]] * 10⁻⁶;
impRe = imp[[All, {1, 2}]];
impIm = imp[[All, {1, 3}]];

impEpsilon = impRe (*Dummy list*);
impEpsilon[[All, 2]] = (impRe[[All, 2]] + ⅈ impIm[[All, 2]])²;
permittivity = Interpolation[impEpsilon];
Clear[imp0, imp, impRe, impIm, impEpsilon]
```

Wave properties

```
omega[λ_] := (2 π c)/λ;

wavevectorO[λ_, n_] := (2 π n)/λ;

wavevectorSP[λ_, ϵm_, n_] := (2 π)/λ ((ϵm n^2)/(ϵm + n^2))^(1/2);
```

Main

```
λin = 1064 nano;
λout = 532 nano;

availablePeriods = {100, 200, 300, 400, 500, 600, 215, 230, 245,
    260, 275, 625, 575, 525, 475, 425, 375, 130, 140, 150, 160, 180};

kin = wavevectorO[λin, nLN[λin, 37 °]];(*No Birefringence atm*)

kout = wavevectorO[λout, nLN[λout, 37 °]];(*No Birefringence atm*)
koutp = Re[wavevectorSP[λout, permittivity[λout], nLNo[λout]]];

inputInternal[Λ_] := ArcSin[(koutp - (2 π)/(Λ nano))/(2 kin)] / °;

inputExternal[Λ_] := extϕ[nLNo[λin], nBK7[λin], ArcSin[(koutp - (2 π)/(Λ nano))/(2 kin)]] / °;

(*Internal Excitation*)
plotIn = Plot[inputInternal[Λ], {Λ, 150, 450}, Axes → False,
    Frame -> True, PlotRangePadding → None, PlotStyle → Gray](*θin*);
(*External Excitation with prisms*)
plotInExt = Plot[inputExternal[Λ]
    , {Λ, 150, 450}, PlotRange → {-60, 60}, Axes → False, Frame -> True,
    PlotRangePadding → None, PlotStyle → Gray](*θin, ext*);

discreetPlotIn = ListPlot[
    Partition[Riffle[availablePeriods, inputInternal[availablePeriods]], 2],
    PlotStyle → Gray];
discreetPlotInExt = ListPlot[Partition[Riffle[availablePeriods,
        inputExternal[availablePeriods]], 2], PlotStyle → Gray];
```

```mathematica
outputInternal[Λ_] := ArcSin[(koutp - (2 π)/(Λ nano))/kout]/°;

outputExternal[Λ_] := extϕ[nLNo[λout], nBK7[λout], ArcSin[(koutp - (2 π)/(Λ nano))/kout]]/°;
plotOut = Plot[outputInternal[Λ], {Λ, 225, 450}, Axes → False,
    Frame -> True, PlotRangePadding → None, PlotStyle → Green](*θout*);


(*External Leakage with prisms*)
plotOutExt =
   Plot[outputExternal[Λ], {Λ, 225, 450}, PlotRange → {-60, 60}, Axes → False,
    Frame -> True, PlotRangePadding → None, PlotStyle → Green](*θout ext*);

discreetPlotOut = ListPlot[
    Partition[Riffle[availablePeriods, outputInternal[availablePeriods]], 2],
    PlotStyle → Green];
discreetPlotOutExt = ListPlot[Partition[Riffle[availablePeriods,
       outputExternal[availablePeriods]], 2], PlotStyle → Green];
outplot1 = Show[{plotOut, plotIn, discreetPlotOut, discreetPlotIn},
   FrameLabel → {"Poling Period (nm)", "Internal Incident Angle (°)"}]
outplot2 = Show[{plotOutExt, plotInExt, discreetPlotOutExt, discreetPlotInExt},
   FrameLabel → {"Poling Period (nm)", "External Incident Angle (°)"}]
```

Crystal Cut of the Lithium Niobate for PDC

Constants

```
c = 299 792 458;
ε0 = 8.85418782 × 10^-12;
μ0 = 1.25663706 × 10^-6;

nano = 10^-9;
```

Dielectric Properties

$$\text{neff}[nor\_, nex\_, \tau\_] = \frac{nor\ nex}{\left(nex^2\ \text{Cos}[\tau]^2 + nor^2\ \text{Sin}[\tau]^2\right)^{\frac{1}{2}}};$$

$$\text{nLNo}[\lambda\_] = \left(4.9048 + 2.1429 * 10^{-8}\ \left(T^2 - 88506.25\right) + \right.$$

$$\frac{0.11775 + 2.2314 * 10^{-8}\ \left(T^2 - 88506.25\right)}{\left(\lambda * 10^6\right)^2 - \left(0.21802 - 2.9671 * 10^{-8}\ \left(T^2 - 88506.25\right)\right)^2} -$$

$$\left.0.027153\ \left(\lambda * 10^6\right)^2\right)^{\frac{1}{2}}\ /.\ \{T \rightarrow 297.5\};$$

$$\text{nLNe}[\lambda\_] = \left(4.5820 + 2.2971 * 10^{-7}\ \left(T^2 - 88506.25\right) + \right.$$

$$\frac{0.09921 + 5.716 * 10^{-8}\ \left(T^2 - 88506.25\right)}{\left(\lambda * 10^6\right)^2 - \left(0.21090 - 4.9143 * 10^{-8}\ \left(T^2 - 88506.25\right)\right)^2} -$$

$$\left.0.02194\ \left(\lambda * 10^6\right)^2\right)^{\frac{1}{2}}\ /.\ \{T \rightarrow 297.5\};$$

$$\text{nBK7}[\lambda\_] = \left(1 + \frac{1.03961212\ \left(\lambda * 10^6\right)^2}{\left(\lambda * 10^6\right)^2 - 0.00600069867} + \frac{0.231792344\ \left(\lambda * 10^6\right)^2}{\left(\lambda * 10^6\right)^2 - 0.0200179144} + \right.$$

$$\left.\frac{1.01046945\ \left(\lambda * 10^6\right)^2}{\left(\lambda * 10^6\right)^2 - 103.560653}\right)^{\frac{1}{2}};$$

Gold Permittivity

```
imp0 = Import["METALS_Gold_Johnson.csv"];
"Column order = " <> imp0[[1, 1]] <> "," <> imp0[[1, 2]] <> "," <> imp0[[1, 3]]
imp = Take[imp0, -(Length[imp0] - 1)];
imp[[All, 1]] = imp[[All, 1]] * 10^-6;
impRe = imp[[All, {1, 2}]];
impIm = imp[[All, {1, 3}]];

impEpsilon = impRe (*Dummy list*);
impEpsilon[[All, 2]] = (impRe[[All, 2]] + 𝕚 impIm[[All, 2]])^2;
permittivity = Interpolation[impEpsilon];
Clear[imp0, imp, impRe, impIm, impEpsilon]
```

Wave properties

```
omega[λ_] := (2 π c)/λ;

wavevectorO[λ_, n_] := (2 π n)/λ;

wavevectorSP[λ_, ϵm_, n_] := (2 π)/λ ((ϵm n²)/(ϵm + n²))^(1/2);
```

Main

```
Off[FindRoot::lstol]
Clear[λ, Λ, λp, λs, λi, ki, ks, kp, zproj, ns]
(*Special functions*)
ns[λ_, ϕdeg_, θdeg_] :=
  (*Calculates the angle of the
   input relative to the crystal axes for the signal,
   and returns the effective index. Regular methods can be used for the pump*)
  Module[{zproj, nsout},
    zproj = Sin[ϕdeg °] Cos[θdeg °];

    nsout = nLN[λ, ArcSin[zproj/1]]

  ];

(*Input Variables*)
λi = 1485.766 nano; (*Idler (Plasmonic)*)
λp = 620 nano; (*Pump (Optical)*)
λs = 1064 nano; (*Signal (Optical) (Seeded)*)


ks[ϕdeg_, θdeg_] := wavevectorO[λs, ns[λs, ϕdeg, θdeg]];
kp[θdeg_] := wavevectorO[λp, nLN[λp, (θdeg) °]];
(*Pump is an extraordinary ray*)
ki = wavevectorSP[λi, permittivity[λi], nLNo[λi]];
(*Idler is aligned along the X-axis→Ordinary ray*)

Manipulate[
 Show[
  Plot[((kp[θ] - ks[ϕ, θ]) Cos[ϕ °] - Re[ki])/
    wavevectorO[λi, nLN[λi, 43 °]], {θ, 0, 90}],
  Axes → True,
  Frame → True,
  PlotRange → {-0.06, 0.06},
  FrameLabel → {"Degrees (θ°)", "Phase-mismatch (Δn)"},
  Epilog → Inset[
    Style[StringForm["ϕ=``°", TraditionalForm[ϕ]], FontSize → 14], {80, 0.04}]
 ]
 , {{ϕ, 5}, 0, 10}
]
Manipulate[FindRoot[(kp[θ] - ks[ϕ, θ]) Cos[ϕ °] == Re[ki], {θ, 45}], {{ϕ, 5}, 0, 20}]


(*End*********************************************************************)
```

Generated Plasmon Power in Parametric Down Conversion

Constants

```
c = 299 792 458;
ε0 = 8.85418782 × 10⁻¹²;
μ0 = 1.25663706 × 10⁻⁶;

nano = 10⁻⁹;
```

Dielectric Properties

$$\text{neff}[\text{nor\_}, \text{nex\_}, \tau\_] = \frac{\text{nor nex}}{\left(\text{nex}^2 \text{Cos}[\tau]^2 + \text{nor}^2 \text{Sin}[\tau]^2\right)^{\frac{1}{2}}};$$

$$\text{nLNo}[\lambda\_] = \left(4.9048 + 2.1429 * 10^{-8}\left(T^2 - 88\,506.25\right) + \right.$$

$$\frac{0.11775 + 2.2314 * 10^{-8}\left(T^2 - 88\,506.25\right)}{\left(\lambda * 10^6\right)^2 - \left(0.21802 - 2.9671 * 10^{-8}\left(T^2 - 88\,506.25\right)\right)^2} -$$

$$\left.0.027153\left(\lambda * 10^6\right)^2\right)^{\frac{1}{2}} \text{ /. } \{T \to 297.5\};$$

$$\text{nLNe}[\lambda\_] = \left(4.5820 + 2.2971 * 10^{-7}\left(T^2 - 88\,506.25\right) + \right.$$

$$\frac{0.09921 + 5.716 * 10^{-8}\left(T^2 - 88\,506.25\right)}{\left(\lambda * 10^6\right)^2 - \left(0.21090 - 4.9143 * 10^{-8}\left(T^2 - 88\,506.25\right)\right)^2} -$$

$$\left.0.02194\left(\lambda * 10^6\right)^2\right)^{\frac{1}{2}} \text{ /. } \{T \to 297.5\};$$

$$\text{nBK7}[\lambda\_] = \left(1 + \frac{1.03961212\left(\lambda * 10^6\right)^2}{\left(\lambda * 10^6\right)^2 - 0.00600069867} + \frac{0.231792344\left(\lambda * 10^6\right)^2}{\left(\lambda * 10^6\right)^2 - 0.0200179144} + \right.$$

$$\left.\frac{1.01046945\left(\lambda * 10^6\right)^2}{\left(\lambda * 10^6\right)^2 - 103.560653}\right)^{\frac{1}{2}};$$

Gold Permittivity

```
imp0 = Import["METALS_Gold_Johnson.csv"];
"Column order = " <> imp0[[1, 1]] <> "," <> imp0[[1, 2]] <> "," <> imp0[[1, 3]]
imp = Take[imp0, -(Length[imp0] - 1)];
imp[[All, 1]] = imp[[All, 1]] * 10^-6;
impRe = imp[[All, {1, 2}]];
impIm = imp[[All, {1, 3}]];

impEpsilon = impRe (*Dummy list*);
impEpsilon[[All, 2]] = (impRe[[All, 2]] + 𝕚 impIm[[All, 2]])^2;
permittivity = Interpolation[impEpsilon];
Clear[imp0, imp, impRe, impIm, impEpsilon]
```

Wave properties

```
omega[λ_] := (2 π c)/λ;

wavevector0[λ_, n_] := (2 π n)/λ;

wavevectorSP[λ_, εm_, n_] := (2 π)/λ ((εm n^2)/(εm + n^2))^(1/2);
```

Main

```
(*Pump*)
λ1 = 620 nano;
ω1 = omega[λ1];
n1 = nLN[λ1, ϕ] /. {ϕ → 0};
k1 = wavevector0[λ1, nLN[λ1, ϕ]] /. {ϕ → 0};(*Fix angle later*)

(*Signal*)
λ2 = 1064 nano;
ω2 = omega[λ2];
n2 = nLN[λ2, ϕ] /. {ϕ → 0};
k2 = wavevector0[λ2, nLN[λ2, ϕ]] /. {ϕ → 0};

(*Idler (Plasmon)*)
λ3 = (λ1 λ2)/(λ2 - λ1);
ω3 = omega[λ3];
k3 = wavevectorSP[λ3, permittivity[λ3], nLN[λ3, ϕ]] /. {ϕ → 0};
γ = Re[evd[λ3, permittivity[λ3], nLN[λ3, ϕ]] /. {ϕ → 0}];
(*What happens if i just take this as the complex value?*)
(*Mode Profiles*)
Ψ1 = (e^(-x^2/(2 σ^2))) (e^(-y^2/(2 σ^2)));

ψ1 = Assuming[σ > 0, (Integrate[Abs[Ψ1]^2, {x, -∞, ∞}, {y, -∞, ∞}])^(1/2)]
(*For ⅆxⅆy, the square is cancelled by going from ψ1^2 to ψ1*)
Ψ2 = (e^(-x^2/(2 σ^2))) (e^(-y^2/(2 σ^2)));

ψ2 = Assuming[σ > 0, (Integrate[Abs[Ψ2]^2, {x, -∞, ∞}, {y, -∞, ∞}])^(1/2)];

Ψ3 = (e^(-k x)) (*(e^(-x^2/(2 σ^2)))*) (e^(-y^2/σ^2));(*Assuming they're all
  identical in y. I might have to actually change this one*)
```

```
ψ3 = Assuming[σ > 0 && k > 0, (Integrate[Abs[Ψ3]², {x, 0, ∞}, {y, -∞, ∞}])^(1/2)];
PwrToE[AvgPwr_, n_] :=
 Module[{Intensity, Efield, RepRate, InstPwr, PulseDuration},
   RepRate = 1 kilo;
   PulseDuration = 5 nano;
   InstPwr = AvgPwr / (RepRate * PulseDuration);

   Efield = Sqrt[2/(c n ε0) InstPwr];

   Efield

 ]


P1 = 5 milli;
E1 = PwrToE[P1, n1];

P2 = 5 milli;
E2 = PwrToE[P2, n2];
"The overlap integral:"
κa = Assuming[σ > 0 && k > 0,
    Abs[Integrate[Ψ1 Ψ2 Ψ3, {x, 0, ∞}, {y, -∞, ∞}] / (ψ1 ψ2 ψ3)]²]


"In numbers:"
κa /. {σ → 50 √2 micro, k → γ} // N
Clear[x]
sol = With[{κ = √κa /. {σ → 50 √2 micro, k → γ}, χ = 3 pico},

    DSolve[{E3'[z] == i/2 κ/Re[k3] χ (ω3/c)² E1 E2* - Im[k3] E3[z], E3[0] == 0},

     E3[z], z]] // Chop (*Check Maths re: ω3*)


func[z_] = E3[z] /. sol
Plot[ Abs[E3[z]]² / (4 nLNo[1485 nano] μ0 c) /. sol, {z, 0, 500 micro}, PlotRange → All,
  Axes → False, Frame → True, FrameLabel → {"Distance", "(Field Amplitude)²"}]
Abs[func[500 micro]]² / (2 nLNo[1485 nano] μ0 c) (*W*)
```

Optical and Plasmonic dispersions for Directional Couplers

Constants

```
c = 299 792 458;
ε0 = 8.85418782 × 10⁻¹²;
μ0 = 1.25663706 × 10⁻⁶;

nano = 10⁻⁹;
```

Dielectric Properties

```
nPMMA[λ_] =
  (2.399964 – 8.308636 * 10⁻² (λ * 10⁶)² – 1.919569 * 10⁻¹ (λ * 10⁶)⁻² + 8.720608 * 10⁻²
    (λ * 10⁶)⁻⁴ – 1.666411 * 10⁻² (λ * 10⁶)⁻⁶ + 1.169519 * 10⁻³ (λ * 10⁶)⁻⁸)^(1/2);
SellList = {{300 * 10⁻⁹, 1.7}, {365 * 10⁻⁹, 1.6387}, {400 * 10⁻⁹, 1.62},
    {500 * 10⁻⁹, 1.59}, {600 * 10⁻⁹, 1.575}, {620 * 10⁻⁹, 1.5726},
    {700 * 10⁻⁹, 1.567}, {800 * 10⁻⁹, 1.563}, {900 * 10⁻⁹, 1.5625},
    {1000 * 10⁻⁹, 1.5625}, {1100 * 10⁻⁹, 1.5625}, {1200 * 10⁻⁹, 1.5625}};
nSU8 = Interpolation[SellList];
```

Gold Permittivity

```
imp0 = Import["METALS_Gold_Johnson.csv"];
"Column order = " <> imp0[[1, 1]] <> "," <> imp0[[1, 2]] <> "," <> imp0[[1, 3]]
imp = Take[imp0, –(Length[imp0] – 1)];
imp[[All, 1]] = imp[[All, 1]] * 10⁻⁶;
impRe = imp[[All, {1, 2}]];
impIm = imp[[All, {1, 3}]];

impEpsilon = impRe (*Dummy list*);
impEpsilon[[All, 2]] = (impRe[[All, 2]] + 𝕚 impIm[[All, 2]])²;
permittivity = Interpolation[impEpsilon];
Clear[imp0, imp, impRe, impIm, impEpsilon]
```

Wave properties

```
omega[λ_] := (2 π c)/λ;

wavevector0[λ_, n_] := (2 π n)/λ;

wavevectorSP[λ_, εm_, n_] := (2 π)/λ (εm n²/(εm + n²))^(1/2);
```

Main

Calculating the Optical Waveguide Dispersion

```
λ = 633 * 10^-9;
n1 = 1.596; (*Value for SU-8 Measured at 633nm*)
ε1 = n1^2;
n2 = nPMMA[λ];
ε2 = n2^2;
ω = omega[λ];


WaveguideFunctionTM = εc/εd (hc^2 ω^2 μ0 ε0 (εc - εd)/θ^2 - 1)^(1/2);


LineLegend[{ColorData[97, 1], ColorData[97, 2], Black},
  {"Tan[k_x d]", "-Cot[k_x d]", "TM", "TE"}];
Show[Plot[{Tan[θ], -Cot[θ]}, {θ, 0, π},
  Exclusions → {Cos[θ] == 0, Sin[θ] == 0}, PlotRange → {0, 6}],
 Plot[{WaveguideFunctionTM[0.5/2 * 10^-6]}, {θ, 0, π},
  PlotStyle → {Thick, Black}, PlotRange → All]
 , Axes → False
 , Frame → True
 , FrameLabel -> {Style["k_x d", Bold, Black], Style["", Bold, Black]}
 , FrameTicksStyle → Directive[Bold, Black]
 , Epilog → Inset[%, {2.25, 4}]] (* Tan=odd Symmetry,Cot=even Symmetry,
Symmetry wrt Ez, not Ex, which determines the propagation mode profile*)


hclist = {0.25/2 micro, 0.5/2 micro, 1/2 micro}; (*half the waveguide height*)
γplotlist = {};
γlist = {};
dnum = 1;
dummy = 3;


While[dnum ≤ 3,
 λ = 400 * 10^-9;
 hc = hclist[[dnum]];
 γlist = {};
 While[λ ≤ 1 * 10^-6,
  nd = nPMMA[λ];
  εd = nd^2;
  nc = nSU8[λ];
  εc = nc^2;
  ω = omega[λ];

  sol = FindRoot[Tan[θ] - WaveguideFunctionTM == 0, {θ, 1}];
  kxvector = θ/hc /. sol;
  γ = √(kc^2 - kx^2)/wavevector0[λ, 1] /. {kx → kxvector, kc → wavevector0[λ, nc]};
  AppendTo[γlist, {λ / nano, γ}];
  λ = λ + 10^-9;
  ];
 AppendTo[γplotlist, ListLinePlot[γlist, PlotStyle → ColorData[3, dummy]]];
 dummy = dummy + 1;
 dnum = dnum + 1;
 ]
LineLegend[{Directive[Red, Dotted], Directive[Blue, Dotted],
   ColorData[3, 3], ColorData[3, 4], ColorData[3, 5]},
```

```mathematica
   {"PMMA", "SU-8", "0.25 μm Core", "0.5 μm Core", "1 μm Core"}];
Show[
 Plot[{nPMMA[Λ nano], nSU8[Λ nano]}, {Λ, 400, 1000}
   , PlotStyle → {{Dotted, Red}, {Dotted, Blue}}]
 , γplotlist
 , PlotRange → {1.47, 1.68}
 , Axes → False, Frame → True,
 FrameLabel -> {"Wavelength λ (nm)", "Effective Index"},
 FrameTicksStyle → Directive[Bold, Black]
 , Epilog → Inset[%, {850, 1.62}]
]
```

Calculating the Long-range SPP Dispersion

```mathematica
hm = 30 * 10⁻⁹; (*Metal waveguide height*)
βplotlist = {};
dlist = {30 nano, 50 nano, 10 000 nano};
dummy = 3; (*Opacity parameter*)
dnum = 1;
While[dnum ≤ 3,
 hm = dlist[[dnum]];
 λ = 400 * 10⁻⁹;
 βlist = {};
 While[λ ≤ 1 * 10⁻⁶,
  nd = nPMMA[λ];
  εd = nd²;
  εm = permittivity[λ];
  εc = nc²;
  k3d = (β² - wavevector0[λ, nd]²)^(1/2);
  k3m = (β² - εm wavevector0[λ, 1]²)^(1/2);
  βsol = FindRoot[(-εm/εd) (k3d/k3m) - Tanh[(1/2) k3m hm] == 0, {β, 1 * 10^7}];
  AppendTo[βlist, {λ / nano, Re[β] * 10⁶ /. βsol}];
  λ = λ + 10⁻⁹;
 ];
 dnum = dnum + 1;
 AppendTo[βplotlist,
  ListLinePlot[Re[βlist], PlotStyle → ColorData[52, dummy]]];
 dummy = dummy - 1;
]
(*********************************************************)


LineLegend[52,
  {"Gold Thickness ∞", "Gold Thickness 50 nm", "Gold Thickness 30 nm"}];
Show[βplotlist
 , PlotRange → All
 , Axes → False, Frame → True,
 FrameLabel -> {"Wavelength λ (nm)", "Propagation Constant (m⁻¹)"},
 FrameTicksStyle → Directive[Bold, Black]
 , Epilog → Inset[%, {600, 300}]
]
```

Plotting Optical and Plasmonic Propagation Constants

```
LineLegend[{Green, ColorData[52, 1]}, {"Optical Mode", "Plasmonic Mode"}];
Show[
 βplotlist[[1]]
 , γplotlist
 , Axes → False, Frame → True,
 FrameLabel -> {Style["Wavelength λ (nm)", Bold, Black],
    Style["Effective Index", Bold, Black]},
 FrameTicksStyle → Directive[Bold, Black]
 , Epilog → Inset[%, {850, 1.56}]
]
```

Adiabatic Passage Parameter Scan

Main

```
Clear[Δ21, γ, n, z, coeff, κ, κ12, κ23, σ, zmax, length, hamil, bwah, sep]
zmax = 0.04; (*Length of device*)
length = zmax;

κ[z_] = √(κ12[z]² + κ23[z]²) ;
hamil = {{0, κ12[z], 0}, {κ12[z], Δ21, κ23[z]}, {0, κ23[z], Δ31}};
coeff = {{1}, {0}, {0}}; (*c1,c2,c3,z*)
Δ21 = 0; Δ31 = 0;
resultslist = {};
σ = .001; (*Half Width*)

Monitor[
 While[σ ≤ 0.012 ,
   sep = -0.012;
   While[sep ≤ 0.012,

    κ23[z_] = 8000 e^(-(z - (zmax-sep)/2)²/(2 σ²)) ;

    κ12[z_] = 8000 e^(-(z - (zmax+sep)/2)²/(2 σ²)) ;
    bwah = NDSolve[
      {i {{a1'[z]}, {a2'[z]}, {a3'[z]}} == hamil.{{a1[z]}, {a2[z]}, {a3[z]}},
       {{a1[0]}, {a2[0]}, {a3[0]}} == coeff},
      {a1, a2, a3},
      {z, 0, length}];
    Inta2 = (1/length) NIntegrate[Abs[a2[z]]² /. bwah, {z, 0, length}];
    AppendTo[resultslist,
     {σ/10⁻², sep/10⁻², Inta2[[1]], Abs[a3[length]]² /. bwah[[1]]}];
    Clear[κ12, κ23];
    sep = sep + 0.00025;
   ];
   σ = σ + 0.00025;
 ]
 , {sep, σ}]
"Integrated P2"
ListContourPlot[resultslist[[All, {1, 2, 3}]],
 FrameLabel → {"Gaussian Width σ", "Separation(cm)", "Metric"},
 PlotRange → All, PlotLegends → Automatic]
"Final P3"
ListContourPlot[resultslist[[All, {1, 2, 4}]],
 FrameLabel → {"Gaussian Width σ", "Separation(cm)", "Metric"},
 PlotRange → {0, 1}, PlotLegends → Automatic]
(*Clear[Δ21,γ,n,z,coeff,κ,κ12,κ23,σ,zmax,length,hamil,bwah,sep];*)
```

B
List of Publications

Journal Publication

- V Ng, JA Vaitkus, ZJ Chaboyer, T Nguyen, JM Dawes, MJ Withford, MJ Steel, AD Greentree, *Digital waveguide adiabatic passage part 2: experiment* Optics Express **25**, 2552-2559 (2017). and arXiv 1608.07385v1

- V Ng, AM Warrier, J Lin, D Spence, JE Downes, DW Coutts, JM Dawes, *Second harmonic conversion efficiency of surface plasmons in gold films* submitted to Optics Express.

Conference Publications

- V Ng, TP Vo, DW Coutts, JM Dawes, *Nonlinear plasmonics: second harmonic generation of long range surface plasmon polaritons* AIP Congress Sydney 2012.

- J M Dawes, T P Vo, A Maleki, V Ng, L Piro, DW. Coutts, *Coupling and propagation of surface plasmons in metallic nanostructures,* invited paper International Conference on Emerging Advanced Nanomaterials, Brisbane, 2012.

- V Ng, DW.Coutts, JM. Dawes *Adiabatic Passage through a plasmon-like lossy state* OECC/ACOFT, Melbourne 2014

- V Ng, A Boes, AM Warrier, J Lin, D Spence, A Mitchell, JE Downes, DW Coutts, JM Dawes *Second harmonic generation in plasmonic lithium niobate waveguides*, European Quantum Electronics Conference, paper EHP12 Munich, Germany, (2015)

- V Ng, JA Vaitkus, ZJ Chaboyer, T Nguyen, JM Dawes, MJ Withford, MJ Steel, AD Greentree, *Does adiabatic transfer work for digitally spatially coupled waveguides?* AIP APPC congress Brisbane Dec 2016.

Digital Waveguide Adiabatic Passage Part 2: Experiment

VINCENT NG,[1,2,*] JESSE A. VAITKUS,[3] ZACHARY J. CHABOYER,[1,2] THACH NGUYEN,[1,4] JUDITH M. DAWES,[1,2] MICHAEL J. WITHFORD,[1,2] ANDREW D. GREENTREE,[3,5] AND M. J. STEEL[1,2]

[1] *ARC Centre of Excellence for Ultrahigh bandwidth Devices for Optical Systems (CUDOS)*
[2] *MQ Photonics Research Centre, Department of Physics and Astronomy, Macquarie University, NSW 2109, Australia*
[3] *Chemical and Quantum Physics, School of Science, RMIT University, Melbourne 3001, Australia*
[4] *School of Engineering, RMIT University, Melbourne 3001, Australia*
[5] *Australian Research Council Centre of Excellence for Nanoscale BioPhotonics, RMIT University, Melbourne 3001, Australia*
[*] *vincent.ng@mq.edu.au*

Abstract: Using a femtosecond laser writing technique, we fabricate and characterise three-waveguide digital adiabatic passage devices, with the central waveguide digitised into five discrete waveguidelets. Strongly asymmetric behaviour was observed, devices operated with high fidelity in the counter-intuitive scheme while strongly suppressing transmission in the intuitive. The low differential loss of the digital adiabatic passage designs potentially offers additional functionality for adiabatic passage based devices. These devices operate with a high contrast ($>90\%$) over a 60 nm bandwidth, centered at $\sim$ 823 nm.

OCIS codes: (230.7370) Waveguides; (130.3120) Integrated optics devices.

References and links

1. K. Eckert, M. Lewenstein, R. Corbalán, G. Birkl, W. Ertmer, and J. Mompart, "Three-level atom optics via the tunneling interaction," Phys. Rev. A **70**, 023606 (2004).
2. A. D. Greentree, J. H. Cole, A. R. Hamilton, and L. C. L. Hollenberg, "Coherent electronic transfer in quantum dot systems using adiabatic passage," Phys. Rev. B **70**, 235317 (2004).
3. E. Paspalakis, "Adiabatic three-waveguide directional coupler," Optics Communications **258**, 30–34 (2006).
4. R. Menchon-Enrich, A. Benseny, V. Ahufinger, A. D. Greentree, T. Busch, and J. Mompart, "Spatial adiabatic passage: a review of recent progress," Reports on Progress in Physics **79**, 74401 (2016).
5. N. V. Vitanov, A. A. Rangelov, B. W. Shore, and K. Bergmann, "Stimulated Raman adiabatic passage in physics, chemistry and beyond," Rev. Mod. Phys. (posted 3 May 2016, in press). (2016).
6. S. Longhi, G. Della Valle, M. Ornigotti, and P. Laporta, "Coherent tunneling by adiabatic passage in an optical waveguide system," Phys. Rev. B **76**, 20110(R) (2007).
7. Y. Lahini, F. Pozzi, M. Sorel, R. Morandotti, D. N. Christodoulides, and Y. Silberberg, "Effect of Nonlinearity on Adiabatic Evolution of Light," Phys. Rev. Lett. **101**, 193901 (2008).
8. R. Menchon-Enrich, A. Llobera, V. J. Cadarso, J. Mompart, and V. Ahufinger, "Adiabatic Passage of Light in CMOS-Compatible Silicon Oxide Integrated Rib Waveguides," IEEE Photonics Technology Letters **24**, 536–538 (2012).
9. G. Porat and A. Arie, "Efficient two-process frequency conversion through a dark intermediate state," Journal of the Optical Society of America B **29**, 2901 (2012).
10. F. Dreisow, M. Ornigotti, A. Szameit, M. Heinrich, R. Keil, S. Nolte, A. Tünnermann, and S. Longhi, "Polychromatic beam splitting by fractional stimulated Raman adiabatic passage," Applied Physics Letters **95**, 53–56 (2009).
11. K. Chung, T. J. Karle, M. Rab, A. D. Greentree, and S. Tomljenovic-Hanic, "Broadband and robust optical waveguide devices using coherent tunnelling adiabatic passage," Optics Express **20**, 23108 (2012).
12. C. Ciret, V. Coda, A. A. Rangelov, D. N. Neshev, and G. Montemezzani, "Planar achromatic multiple beam splitter by adiabatic light transfer." Optics letters **37**, 3789 (2012).
13. R. Menchon-Enrich, A. Llobera, J. Vila-Planas, V. J. Cadarso, J. Mompart, and V. Ahufinger, "Light spectral filtering based on spatial adiabatic passage," Light Sci Appl **2**, e90 (2013).
14. A. P. Hope, T. G. Nguyen, A. Mitchell, and A. D. Greentree, "Adiabatic two-photon quantum gate operations using a long-range photonic bus," Journal of Physics B **48**, 055503 (2015).

15. E. A. Shapiro, V. Milner, C. Menzel-Jones, and M. Shapiro, "Piecewise adiabatic passage with a series of femtosecond pulses," Phys. Rev. Lett. **99**, 033002 (2007).
16. E. A. Shapiro, V. Milner, and M. Shapiro, "Complete transfer of populations from a single state to a preselected superposition of states using piecewise adiabatic passage: Theory," Phys. Rev. A **79**, 023422 (2009).
17. A. A. Rangelov and N. V. Vitanov, "Complete population transfer in a three-state quantum system by a train of pairs of coincident pulses," Phys. Rev. A **85**, 043407 (2012).
18. J. A. Vaitkus and A. D. Greentree, "Digital three-state adiabatic passage," Phys. Rev. A **87**, 063820 (2013).
19. J. A. Vaitkus, M. J. Steel, and A. D. Greentree, "Digital Waveguide Adiabatic Passage Part 1: Theory," arXiv:1608.07384 (2016).
20. G. G. Grigoryan, G. V. Nikoghosyan, T. Halfmann, Y. T. Pashayan-Leroy, C. Leroy, and S. Guérin, "Theory of the bright-state stimulated Raman adiabatic passage," Phys. Rev. A **80**, 1–9 (2009).
21. Z. Chaboyer, T. Meany, L. G. Helt, M. J. Withford, and M. J. Steel, "Tunable quantum interference in a 3D integrated circuit," Scientific reports **5**, 9601 (2015).
22. T. G. Nguyen, R. S. Tummidi, T. L. Koch, and A. Mitchell, "Rigorous modeling of lateral leakage loss in SOI thin-ridge waveguides and couplers," IEEE Photonics Technology Letters **21**, 486–488 (2009).
23. K. M. Davis, K. Miura, N. Sugimoto, and K. Hirao, "Writing waveguides in glass with a femtosecond laser," Optics Letters **21**, 1729 (1996).
24. C. B. Schaffer, A. Brodeur, J. F. García, and E. Mazur, "Micromachining bulk glass by use of femtosecond laser pulses with nanojoule energy," Optics Letters **26**, 93–95 (2001).
25. S. M. Eaton, H. Zhang, M. L. Ng, J. Li, W.-J. Chen, S. Ho, and P. R. Herman, "Transition from thermal diffusion to heat accumulation in high repetition rate femtosecond laser writing of buried optical waveguides." Optics express **16**, 9443–9458 (2008).
26. C. T. Miese, M. J. Withford, and A. Fuerbach, "Femtosecond laser direct-writing of waveguide Bragg gratings in a quasi cumulative heating regime," Optics Express **19**, 19542 (2011).

1. Introduction

Spatial Adiabatic Passage [1–4] is the spatial analog of the Stimulated Raman Adiabatic Passage (STIRAP) protocol [5]. It is a three-state transfer framework where the coupling between states is varied to effect transfer of population from one state to another, by means of an intermediate unpopulated state. This framework is remarkably flexible and resilient to variations in implementation, leading to numerous applications in the optical domain. It has been applied directly in the design of broadband optical couplers [6–8] and optical frequency conversion [9]. The versitility of adiabatic passage has also been demonstrated in the development of optical splitters [10–12], frequency filtering [13] and optical photonic gates [14].

Recently, studies have explored adiabatic control strategies that employ digital (or piecewise) control schemes instead of continuous parameter variation [15–18]. Though the condition of adiabaticity formally requires continuity, these studies have shown that adiabatic-like behaviour is maintained. These findings provide additional flexibility when designing adiabatic passage devices, particularly in cases where precise control of the coupling coefficients is difficult.

In this paper, we use the digital adiabatic passage framework and apply it to the optical waveguide domain. We fabricate digital waveguide adiabatic passage devices where the central state has been digitised into five discrete waveguidelets. The device designs were optimised using numerical modelling, and then fabricated using a femtosecond laser direct-write inscription technique over a range of writing powers. These devices were characterised and shown to possess a highly transmissive configuration reminiscent of conventional adiabatic passage. Additionally in the opposite configuration, the transmission was strongly suppressed. This suppression is a key characteristic of the digitisation itself. High contrast operation ($>90\%$) is maintained over a 60 nm bandwidth about ~ 823 nm.

2. Digital Adiabatic Passage

The theory of digital adiabatic passage is treated in detail in [19]. In its simplest form, a system consisting of three identical coupled waveguides $\{|a\rangle, |b\rangle, |c\rangle\}$ can be described by the

Hamiltonian:

$$H = \begin{bmatrix} 0 & \Omega_{ab} & 0 \\ \Omega_{ab} & 0 & \Omega_{bc} \\ 0 & \Omega_{bc} & 0 \end{bmatrix}, \qquad |E_0\rangle = \frac{\Omega_{bc}|a\rangle - \Omega_{ab}|c\rangle}{\sqrt{\Omega_{ab}^2 + \Omega_{bc}^2}}. \tag{1}$$

where the eigenstate $|E_0\rangle$ is the so-called dark-state of H. Here, Ω_{nm} is the coupling between the nth and m^{th} waveguides and only nearest neighbour coupling has been assumed.

This eigenstate $|E_0\rangle$ is completely composed of states $|a\rangle$ and $|c\rangle$ and is not directly dependent on the coupling coefficients Ω_{nm}, but on their ratio. The process of adiabatic passage corresponds to the use of this eigenstate: starting with the coupling coefficients such that $\Omega_{bc} \gg \Omega_{ab}$ and slowly varying them such that $\Omega_{ab} \gg \Omega_{bc}$ at the end of the device, transport is effected from $|a\rangle$ to $|c\rangle$. Due to the ordering of the coupling, this is commonly called the counter-intuitive coupling scheme. When the coupling order is reversed (corresponding to launching light in $|c\rangle$ for the same coupling order), this is known as the intuitive coupling scheme, and leads to non-adiabatic oscillations, although, with central state detuning can lead to bright-state adiabatic passage [20]. As the name suggests, digital adiabatic passage devices are realised by digitising the central waveguide of standard waveguide adiabatic passage into several parallel elements which we term *waveguidelets*. For ideal systems with equal propagation terms or no direct next nearest neighbour (a–c) coupling, the *effective a–c* hopping rate [18, 19] dictates the ideal segment length:

$$L_{\text{opt}} = \pi \left(\Omega_{ab}^2 + \Omega_{bc}^2 \right)^{-1/2}. \tag{2}$$

By using Eq. 2 to digitise the adiabatic passage devices, the counter-intuitive and intuitive coupling behaviour of conventional adiabatic passage is maintained. This is demonstrated in Fig. 1.

3. Model parameters

To simulate the device, model parameters were heuristically obtained from previous work [21]. For a detailed discussion of the theoretical methods used to generate the digital adiabatic passage device see [19]. Both model parameters describing the refractive index difference between cladding and core refractive indices δ, and the $1/e$ width ρ of the Gaussian graded waveguides were varied in the software package BeamPROP until they gave a suitably good fit to the experimentally obtained mode field diameters and coupling curves. Rigorous 3D field propagation simulation was then performed to obtain the coupling lengths. This simulation was carried out using an in-house developed propagation tool based on the eigenmode expansion method [22]. Optimised lengths were found by inferring the coupling between guides from the beat length of two-waveguide systems. Although the eigenmode expansion is highly efficient, it is not able to model scattering losses. Accordingly, once a suitable design was chosen, the geometry was input into BeamPROP for accurate analysis of the scattering. Device parameters used in simulations can be found in table 1 and a simulation at these optimal parameters in the counter-intuitive and intuitive directions can be found in Fig 1.

4. Implementation

The waveguides in all devices herein were fabricated using an ultrafast laser inscription technique [23]. The output of a Ti: Sapphire oscillator (Femtolasers GmbH, FEMTOSOURCE XL 500, 800 nm centre wavelength, 5.1 MHz repetition rate, <50 fs pulse duration) was focused into a borosilicate substrate (Corning Eagle2000) at a depth of 170 μm using a 100x oil immersion objective lens. The sample was translated with respect to the beam focus using Aerotech motion control stages with 10 nm precision. Our combination of writing parameters lies within the

Table 1. Device parameters used in all calculations herein. All waveguidelets are aligned at $y = 0$ and $|a\rangle, |b\rangle_1, |c\rangle$ all begin at $z = 0$. The waveguide's center is given by x. All waveguidelet pairs $|b\rangle_{i+1}$ and $|b\rangle_i$ are separated in z by 7.5 mm to increase the total length to 70 mm to further demonstrate digitisation. ρ is the $1/e$ length of the Gaussian profile waveguides and δ is the difference between core and cladding indices. For details about the model parameters see [19].

Waveguidelet	$|a\rangle$	$|b\rangle_1$	$|b\rangle_2$	$|b\rangle_3$	$|b\rangle_4$	$|b\rangle_5$	$|c\rangle$
L_{opt}(mm)	N/A	5.5824	9.2295	10.3775	9.2295	5.5824	N/A
x (μm)	10.00	-2.00	-0.75	0.00	0.75	2.00	-10.00

ρ	1.6 μm	n_{cl}	1.4994	δ	0.0056	λ_{opt}	800 nm

cumulative heating regime of refractive index modification [24] in which consecutive pulses are absorbed within the focal volume before the dissipation of energy into the bulk of the material, leading to a refractive index modification dominated by thermal effects. The thermal mechanism of the refractive index modification causes both the peak contrast and physical size of the waveguide to increase with the amount of absorbed energy [25]. This allowed the index profile of the written waveguides to be controlled by varying the writing pulse energy. The writing pulse energy was iterated between 28.5 and 34 nJ in 0.25 nJ steps at a constant sample feedrate of 1500 mm/min. With these writing parameters, we designed our devices for optimal operation at $\lambda = 800$ nm.

The design of the fabricated adiabatic passage devices is shown in Fig. 2(a). The total device length including spaces is 70 mm. The input and output states $|a\rangle$ and $|c\rangle$ consist of straight waveguides spaced by 20 μm. This choice was made so that there would be negligible direct coupling between the outer waveguides. The central waveguide $|b\rangle$ was digitised into 5 waveguidelets that were written by modulating the laser output with a fast RTP pockels cell. A taper is observed at the start of the waveguidelet, as the threshold for index modification, due
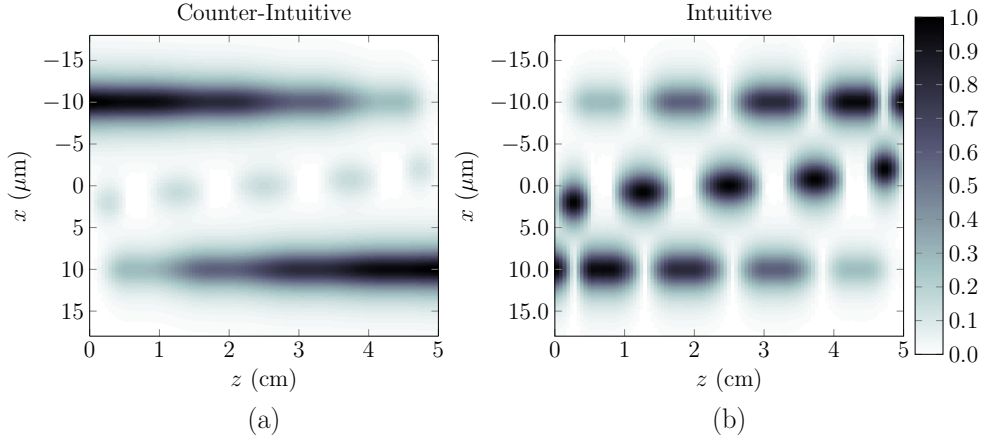
Fig. 1. Beamprop simulation of transport in structures designed in table 1 in the (a) counter intuitive and (b) intuitive directions. Images are taken at the $y = 0$ slice. In the counter-intuitive scheme, the small populations in the intermediate guides make the design tolerant to scattering losses from improper segment length, conversely the very high population in the intuitive direction makes these highly sensitive devices. Spaces of 2.5mm where added between waveguidelets to highlight digitisation.
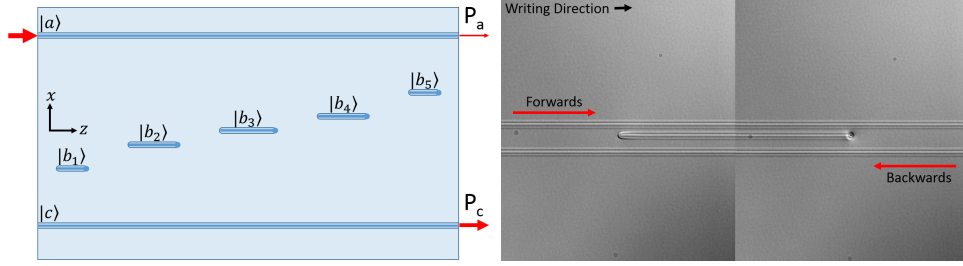
Fig. 2. (Left) Schematic of device with parameters determined by Table 1. (Right) Stitched differential interference contrast (DIC) microscope image of the start and end of a waveguidelet making up the dark state. A taper and a void are evident at either end.

to cumulative heating, is gradually reached after illumination by the laser pulses. On the other hand, the sudden turning-off of the laser at the waveguidelet end leads to a rapid transition away from the thermal regime and the formation of a bulbous void [26] as shown in Fig. 2(b). These features are expected to introduce asymmetric losses in the device for the forward and backward launch directions, indicated in Fig. 2(b).

The scattering losses are also expected to be asymmetric with respect to the intuitive and counter-intuitive configurations. The scattering is expected to be weak in the counter-intuitive configuration due to the dark-state. Conversely in the intuitive configuration, the central state is populated and the voids should scatter strongly, leading to a differential loss in the devices. Each device was accompanied by a reference waveguide for transmission measurements and two waveguides with a 20 μm spacing to verify that direct coupling between states $|a\rangle$ and $|c\rangle$ is negligible.

5. Characterisation

Eleven of the devices fabricated are characterised below, written with writing powers between 28.75–31.5 nJ per pulse, corresponding to a refractive index variation of approximately 3×10^{-4}. These devices yielded coupling coefficients most consistent with modelling. In order to verify adiabatic passage behaviour in these devices, light at 808 nm was fibre coupled into the chip in the counter-intuitive configuration and the outputs measured.

The contrast ratio between the waveguide outputs is plotted in Fig. 3(a) as $P_c/(P_a + P_c)$, for each device in the counter-intuitive configuration. Here, P_a and P_c are the output powers of waveguides $|a\rangle$ and $|c\rangle$ respectively. The 11 devices tested showed little-to-no dependence on the writing energy over this range, and light was observed to have coupled across the device in the counter-intuitive configuration in almost all cases. These demonstrate insensitivity of the devices to the effective device length, characteristic of adiabatic passage designs. The largest source of variability is believed to be waveguide inhomogeneity due to the relatively large length of the devices. On average, 89% of the output is successfully coupled. Asymmetry in fidelity is also evident in the forwards and backwards directions, with a slightly greater fidelity in the backwards direction. This is easily explained by the position of the voids—in the backwards direction, each void is present at the beginning of the waveguidelet, where the light has yet to couple across and be scattered.

In order to characterise losses in digital adiabatic passage devices, the outputs of both waveguides were also summed and normalised against a straight reference waveguide written with the same power. This is shown in Fig. 3(b). Despite scattering losses arising from digitisation, the devices have an average transmission of 70%. If we assume a propagation loss of (0.24 ± 0.06) dB/cm, typical of laser written waveguides, and including facet losses, we obtain an insertion loss
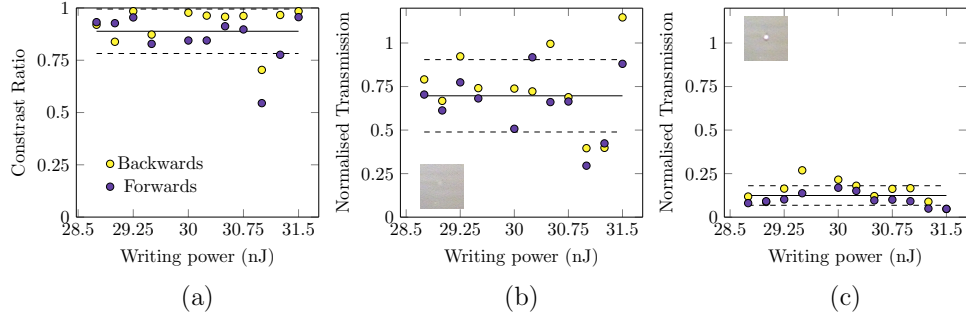
Fig. 3. Characterisation at 808 nm. The contrast ratio is plotted as $P_c/(P_a + P_c)$ for the counter-intuitive configuration (a). The total transmission is also plotted as $(P_a + P_c)/P_{\text{ref}}$, for the counter-intuitive configuration (b) and the intuitive configuration (c). Insets show a CCD image of the voids at the end of the waveguidelets. The voids are shown to be bright and strongly scattering in the intuitive configuration, but dark in the counter-intuitive configuration where they remain largely unpopulated. Transmission is higher in the backwards direction in almost all cases. Mean (solid line) and standard deviation (dashed) have been indicated.

between 3.4–4.2 dB. In contrast, light launched in the intuitive configuration is consistently suppressed, transmitting an average of 12% of the light. This corresponds to an insertion loss between 11–12 dB. Without the dark state in the intuitive direction the waveguidelets become strongly scattering, as shown in the inset of Fig. 3(c). A slight difference in the forwards and backwards directions is also evident, with greater losses in the forwards direction for reasons discussed earlier in the paper.
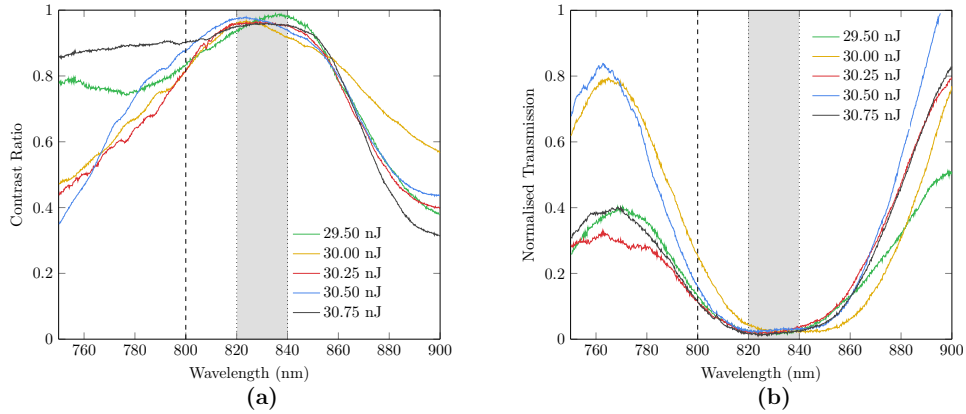
Fig. 4. Spectral response of the devices are plotted, measured in the forwards direction. (a) Counter-intuitive contrast ratio plotted as $P_c/(P_a + P_c)$, and (b) the intuitive transmission plotted as $(P_a + P_c)/P_{\text{ref}}$. Note that the optimal operating wavelength is shifted from 800 nm (dashed) to be about 830 nm (shaded). It can be seen that the broad wavelength response in the counter-intuitive configuration coincides with a suppressed response in the intuitive configuration.

To test the operating bandwidth, the devices were also characterised using a white light source (NKT Photonics SuperK Compact). The white light spectrum was narrowed down using a FGB25 colour filter to capture the spectral response of the devices between 700 nm and 900 nm. The

output was fibre-coupled to a USB4000 OceanOptics spectrometer. The devices shown were measured in the forwards direction.

The wavelength dependent performance of these devices is shown in Fig. 4. These were normalised against straight reference waveguides in order to remove the spectral shaping caused by the filtering and the white light source itself. In the counter-intuitive configuration (Fig. 4(a)), a high contrast region is consistently observed in a wavelength band centered around ~ 830 nm. This is shifted from the intended centre wavelength of 800 nm. Each device exhibits fidelity above 95% at its optimal wavelength. The devices also remain insensitive to small variations in writing power, reflected in the small shifts in optimal frequency.

The operational bandwidth with a fidelity above 90% is $\approx$ 60 nm, after which the adiabatic passage-like behaviour rolls off on either side. This can be attributed to changes in the mode size and coupling strength. As a result, Eq. 2 is no longer satisfied, and the waveguidelets are no longer the appropriate length to facilitate effective adiabatic passage. At the short wavelengths, the behaviour is further complicated by the introduction of higher order modes, resulting in variations in the roll-off behaviour.

In the intuitive case (Fig. 4(b)), the opposite is observed. The transmission is suppressed in the wavelength band around 830 nm, and we observe that the optimal conditions for the counter-intuitive performance coincide with the conditions for maximal loss in the intuitive case. The average transmission is < 5%. The increase in transmission at both longer and shorter wavelengths can then be attributed to the same effects discussed above: at wavelengths far from the optimal wavelength, the changes in coupling no longer allow Eq. 2 to be satisfied. In both cases, light oscillates between the waveguides, is more weakly scattered and is then observed at both outputs.

Switching the filter from the FGB25 to a set of long-pass and short pass filters allowed us to shift the spectral window and observe the roll off of the 30.5 nJ device shown in Fig. 5, chosen because it had the highest average transmission of all the FGB25-measured devices. The roll off of this device is smooth and is consistent with modelling [19]. The total transmission of this device using the new filter set up is also plotted in Fig. 5, where the transmission around 805 nm was omitted due to a normalisation error arising from the saturation of the spectrometer. Wavelength dependent loss is evident in this device, and is assumed to come from the scattering properties of the voids terminating the waveguidelets. On average, more than 80% of the light was transmitted across the spectrum tested.

The bandwidth of these devices, constrained by the effective $a - c$ hopping rate and the waveguidelet lengths, was measured to be narrower than predicted in [19]. Both this and the shift in the center wavelength suggests either a shift in the profile height parameter Δ or the width ρ, or that the Gaussian graded index model is an invalid approximation for estimating the refractive index profile. In principle, the bandwidth can be improved by increasing the number of waveguidelets and by removal of the spaces in between.

6. Conclusions

We have experimentally demonstrated digital adiabatic passage devices, using the design constraints investigated in [19], and fabricated using a femtosecond laser direct write technique. Despite the variability from device to device, as well as the wavelength dependent behaviour, the devices still strongly exhibit features characteristic of adiabatic passage. These features include robustness against variations in coupling, robustness against strong scattering losses in the central state, $|b\rangle$ (from both the digitisation and writing asymmetry), in the counter-intuitive configuration. Additionally, as a consequence of the digitisation process, these features are consistently accompanied by a suppression of the transmission the intuitive configuration. These characteristics suggest digital adiabatic passage may be a robust framework for designing photonic devices with novel applications.
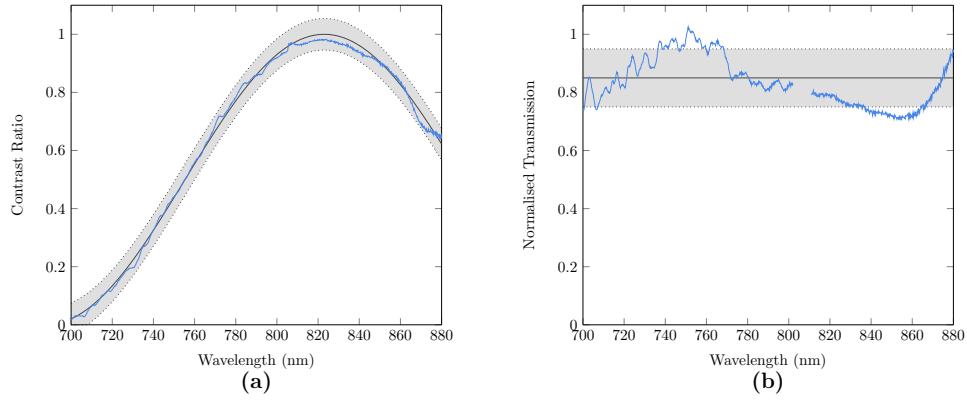
Fig. 5. Second set of measurements taken of waveguide written at 30.5nJ, using bandpass filtering. (a) Contrast ratio $P_a/(P_a+P_c)$ as a function of wavelength. Shaded area corresponds to 95% confidence interval using bisquare method. The fitted equation is $\cos^2(2\pi(\lambda - \lambda_{\text{opt}})/\lambda_\lambda)$ where $\lambda_{\text{opt}} = 823.00 \pm 0.17$ nm and $\lambda_\lambda = 541.15 \pm 1.39$ nm. (b) Device transmission $(P_a + P_c)/P_{\text{ref}}$ as a function of wavelength. A section of the transmission around 805 nm has been omitted due to a normalisation error. In the optimum region, transmission typically lies between 75% to 95% (shaded in-image)

Funding

Plasmonic Second Harmonic Generation in Gold:Lithium Niobate Thin Films

Vincent Ng[1,2,*], Aravindan M. Warrier[1], Jipeng Lin[1], David J. Spence[1], James E. Downes[1], David W. Coutts[1,2], and Judith M. Dawes[1,2]

[1] MQ Photonics, Department of Physics and Astronomy, Macquarie University, Australia
[2] Centre for Ultrahigh bandwidth Devices and Optical Systems (CUDOS)
[*] Corresponding author: vincent.ng@mq.edu.au

Using a sample consisting of a thin gold film on lithium niobate, the plasmonic second harmonic response of gold is measured simultaneously with the optical second harmonic response of lithium niobate. The non-phase-matched, bulk optical second harmonic response of the lithium niobate is used to calibrate the plasmonic signal, and these are found to be of comparable intensity over the short propagation distances which arise in this system. © 2018 Optical Society of America

1. INTRODUCTION

Surface plasmons are electromagnetic waves that propagate on the surface of conductors [1, 2]. They remain tightly bound to the surface due to the strong coupling of the field to the free electrons of the conductor. Due to their small mode sizes, surface plasmons produce extremely high field densities, and this has led to a broad range of studies which utilise the plasmonic field confinement to generate nonlinear effects. Many of these studies have focused on localised plasmons in metallic nanoparticles and nanostructures [3, 4]. In this approach, local resonance effects can be exploited to generate large enhancements of nonlinear effects in small volumes [5–8].

Others have characterised nonlinear effects arising from propagating surface plasmons using planar metal films [9–27], nanostructures and waveguides [28–32]. Here, we focus on second-order nonlinear effects. Many of the nonlinear studies on propagating surface plasmons concentrate on second-order nonlinear effects, and some are motivated by the prospect of parametric amplification [9, 11]. Despite the promise of efficient nonlinear conversion, it has been difficult to calibrate the nonlinear plasmonic response due to the short plasmonic propagation length, which limits the interaction length with the nonlinear medium to microns. In contrast, optical nonlinear processes are typically carried out over millimetres or centimetres. This inherent difference in size scale between optical and plasmonic nonlinear processes makes it difficult to make meaningful comparisons.

Furthermore, nonlinearities involving surface plasmons can arise in a variety of different ways. In addition to nonlinear effects which can arise due to different plasmon-photon combinations [10], nonlinearities may also arise by an interaction of the plasmonic field with the adjacent dielectric [11–13], or the host metal itself [14–18]. The dielectric nonlinearity is well characterised, and arises from the bulk of the dielectric. On the other hand, the metallic nonlinearity is confined to the metal surface. This surface nonlinearity consists of two main contributions [19, 20]: a truly surface-like term arising from symmetry breaking at the surface, and a bulk-like surface term related to the penetration depth of the field into the metal [21–25]. The metallic nonlinearity of metal films has been probed experimentally using optical methods [33–35]. However in optics, the contribution of the metallic nonlinearity is extremely limited due to the finite interaction that can be achieved between the optical field and the metal surface. For surface plasmons, metals form an intrinsic part of the plasmon waveguide, and the metallic nonlinearity plays a much bigger role.

The effective plasmonic nonlinearity is composed of both metallic and dielectric nonlinear responses, and each of these components can contribute to the nonlinear behaviour in different ways. This makes it difficult to characterise the plasmonic nonlinear response. In order to explore second-order plasmonic nonlinear effects it is essential to be able to both untangle these contributions and to be able to make meaningful comparisons between optical and plasmonic nonlinear effects.

Here, we isolate the metallic nonlinearity by studying plasmon-to-plasmon second harmonic generation at a gold/air interface, and we calibrate the plasmonic response by the non-phase-matched optical harmonic response of a nonlinear substrate. We use a planar plasmonic waveguide consisting of a thin film of gold deposited on lithium niobate, and by simultaneously analysing the far field leakage radiation of the harmonic plasmon and the reflected optical harmonic, we can draw direct comparisons between the effective nonlinearity provided by the gold for the surface plasmon and the optical nonlinearity of the lithium niobate.

2. DESIGN

The experiment consisted of probing a thin gold film on a z-cut stoichiometric lithium niobate substrate, exciting a plasmon at
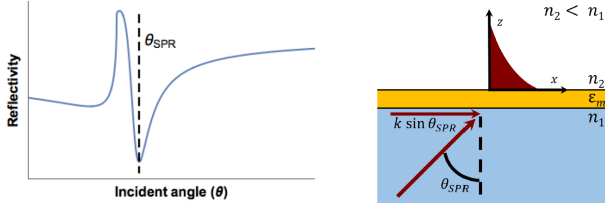
Fig. 1. A typical Kretschmann configuration for launching plasmons. The pump must be incident on the side of the film with the greater refractive index. Phase-matching is achieved by angle tuning.

the air/gold interface in a Kretschmann configuration. Gold is used due to its high conductivity and chemical stability. The birefringent crystal lithium niobate is chosen to provide the reference optical nonlinearity since it is a well-studied material with a strong second order nonlinearity of the order of 30 pm/V along its crystal axis. This geometry supports propagating surface plasmons at the air/gold interface, and was chosen as the simplest configuration. Propagating surface plasmons have well defined wavevectors, resulting in a well defined leakage radiation angle into the nonlinear substrate. We anticipate that the same approach could be applied to more complex structures such as nanowires and nanoantennas whose radiation modes are sufficiently well understood.

In order to excite the propagating surface plasmons, light was incident on the gold, passing through the lithium niobate substrate, similar to a Kretschmann configuration. The excited mode is shown in Fig. 1, and is primarily bound to the air/gold interface. This is a leaky surface plasmon mode, with the component in the lithium niobate radiating into the far field. Coupling was optimised by the choice of the gold film thickness as predicted by the Fresnel equations for a thin film:

$$R(\theta) = |r_{1m2}|^2 = |\frac{r_{1m} + r_{m2}e^{2ik_{z,m}d}}{1 + r_{1m}r_{m2}e^{2ik_{z,m}d}}|^2, \tag{1}$$

where the reflection and transmission coefficients $\{r_{ij}, t_{ij}\}$ of the individual interfaces are given by

$$r_{ij} = \frac{k_{z,i}\epsilon_j - k_{z,j}\epsilon_i}{k_{z,i}\epsilon_j + k_{z,j}\epsilon_i}, \quad t_{ij} = \frac{2n_in_jk_{z,i}}{k_{z,i}\epsilon_j + k_{z,j}\epsilon_i}. \tag{2}$$

Here, k_{z_i} corresponds to a wavevector of the incident light perpendicular to the interface, the $\{n_i, \epsilon_i\}$ correspond to the refractive indices and relative dielectric permittivities and d is the film thickness. The subscripts $\{1, m, 2\}$ refer to the lithium niobate, metal and air respectively. For an excitation at $\lambda = 1240$ nm, the refractive indices of lithium niobate are ($n_o = 2.223$, $n_e = 2.148$), and the permittivity of the gold is $\epsilon_m = -69.280 + 6.025i$. Under these conditions, the Fresnel equations predict optimal coupling to occur for a gold film thickness ~ 30 nm, as signified by a strong extinction in the reflection, and shown in Fig. 2. In practice, the actual coupling efficiency is expected to be weaker when taking into account the beam divergence and the narrow resonance of the coupling condition – it is only $\sim 0.1°$ wide.

The field distribution under these excitation conditions was simulated using Comsol Multiphysics, a finite element simulation package. The simulation was a 2D simulation of the air/gold/lithium niobate structure, using a mesh size of $\lambda/8$ in the dielectric materials and a mesh size of 4 nm in the metal. The
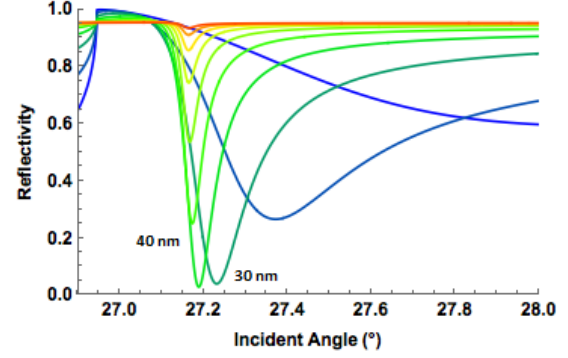
Fig. 2. Fresnel equations showing reflected power as a function of incident angle for a lithium niobate/gold/air setup, for a varying gold film thickness. Gold film thickness varies from 10 nm (blue) to 100 nm (red) in 10 nm steps.

simulation was bounded by perfectly matched absorbing boundary layers. The field distribution illustrated in Fig. 3, shows the field concentrated at the air/gold interface. No field confinement is evident in the lithium niobate. This allows us to treat the metallic nonlinear response of the gold separately from the nonlinearity of the substrate.
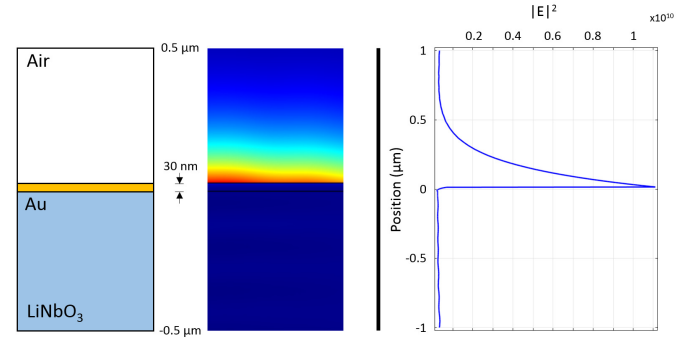
Fig. 3. Comsol simulation of the air/gold plasmon excited in a Kretschmann configuration. A to-scale schematic is shown with a colour plot (middle) and a 1D line profile (left), in $|E|^2$. The mode can be seen to be confined to the air/gold interface and no confinement is evident in the lithium niobate substrate.

3. SECOND HARMONIC GENERATION

In the Kretschmann geometry, a number of plasmon-plasmon and plasmon-photon interactions are possible, some of which are outlined in [10]. For a layout of air/gold/lithium niobate, the effective indices of the lithium niobate/gold plasmon and the air/gold plasmon are sufficiently different for the effects of mode coupling to be ignored. The remaining interactions being considered here are shown in Fig. 4.

The photon-photon generation of plasmons (Fig. 4(a)) is expected to be weak, due to the poor overlap between the photon and plasmonic modes. All-plasmonic SHG (Fig. 4(b)) possesses the strongest mode overlap, but is limited by the lack of phase matching options and requires access to the fundamental plasmonic mode. This process, which then re-radiates as a photon due to leakage, is expected to be indistinguishable from the plasmon to photon SHG process (Fig. 4(c)) identified in [10].

All-optical SHG (Fig. 4(d)) also occurs in the bulk of the lithium niobate. It is this process that we used to calibrate the plasmonic response.
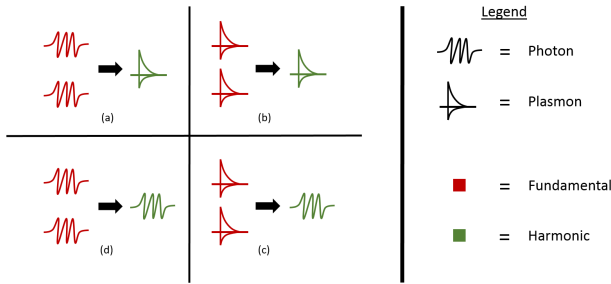
Fig. 4. Second Harmonic processes accessible in a Kretschmann geometry.

4. EXPERIMENT

A sample was prepared consisting of a z-cut wafer of stoichiometric lithium niobate, with a gold film of thickness ≈ 30 nm deposited via ion-assisted thermal deposition [36]. These samples had an arithmetic average surface roughness of $R_a \approx 1$ nm, as measured using a white light interferometer (Wyko NT 8000). With this measure of surface roughness, we concluded that any contributions from plasmonic hotspots (which could influence the harmonic efficiency) or scattering (which could influence the harmonic detection) could be neglected. The sample was then mounted on a glass prism using index matching oil in a typical Kretschmann geometry as shown in Fig. 5. The incident angle of the pump beam was varied and the reflection was measured in order to compare the sample with predictions made by the Fresnel equations. This experiment was carried out in the visible at $\lambda = 642$ nm with a bandwidth of 5 nm using a WhiteLase (SC400-4) supercontinuum source from Fianium.
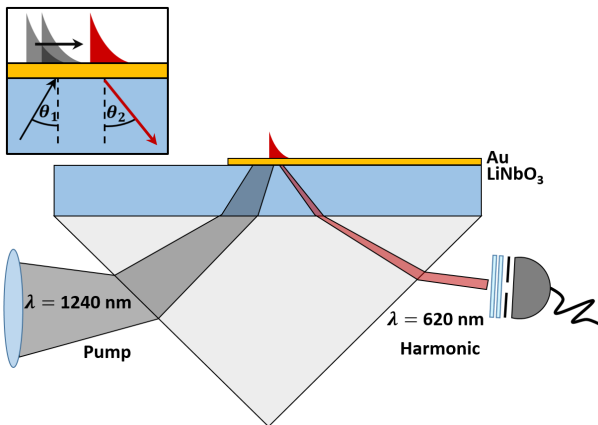

Fig. 5. Schematic of the experiment mounted in a Kretschmann configuration.

A comparison of the Fresnel equations and the measured reflection shown in Fig. 6 suggests that the samples possessed good film quality, and that the gold permittivity correlates strongly with values in the literature [37].The slight deviation is consistent with a film thickness variation of the order of nanome-

tres, and is expected to have a negligible effect on the coupling to the fundamental plasmon mode.

5. RESULTS

The sample was then probed for a nonlinear response. The pump was a diamond Raman laser at $\lambda = 1240$ nm, with a repetition rate of 80 MHz, and 600 mW of average power [38]. The corresponding second harmonic is at 620 nm. The Raman laser itself was pumped with 15 ps pulses, producing ~ 6 ps stokes shifted output pulses. The $\lambda = 1240$ nm beam was weakly focused onto the gold film using a $f = 10$ cm lens giving a beam waist of ≈ 50 μm. Tighter focusing provides high field densities but also increases the angular spread of the pump beam. This reduced the plasmonic coupling efficiency by an estimated factor of ~ 4. This pump beam was TM polarised, and the angle of incidence on the gold was varied in order to observe the harmonic response. It was verified that no optical damage occurred to the gold film and no plasma was observed during the experiments.
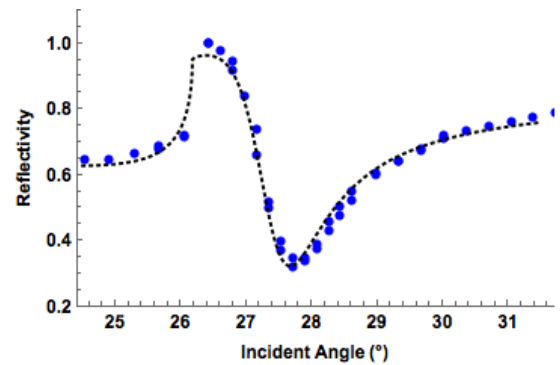
Fig. 6. Experimental reflectivity of gold at $\lambda = 642$ nm plotted with the theoretical curve using the Fresnel equations for a gold film of 32 nm. The gold permittivity was taken to be $\varepsilon_m = -12.43 + 1.15i$.

The harmonic was detected by placing a detector at the plasmon leakage angle, which was also predicted using the Fresnel equations. For a harmonic wavelength of $\lambda = 620$ nm, the refractive indices of lithium niobate are ($n_o = 2.290$, $n_e = 2.206$), and the permittivity of gold is $\varepsilon_m = -10.889 + 1.345i$. Then, for a gold film thickness ≈ 30 nm, the leakage angle corresponded to an angle of $27.2° \pm 0.1°$. Since the plasmon leakage angle had a fixed output angle, it could be distinguished from the bulk optical signal, which has an output angle determined by the reflection of the pump. By introducing a 2 mm slit in front of the detector, ~ 5 cm away from the surface, the angular collection range of the detector was reduced to an external angle of $2.3°$ ($1.2°$ internal angle). Using this slit, the optical signal would be detected when the reflection angle was in the vicinity of the harmonic leakage angle, but would otherwise be rejected. The detector itself was a photomultiplier tube (Hamamatsu H10721-20), which was preceded by a stack of dielectric filters (Schott KG5). These filters ensured no signal directly from the pump was detected.

This experiment was carried out on gold-coated lithium niobate (circles), and a bare lithium niobate sample (squares) to compare the plasmonic nonlinearity (with optical nonlinearity) and the pure optical nonlinearity. A direct measurement of the

pure plasmonic nonlinearity is difficult to obtain because suitable linear optical substrates with comparably high refractive index are rare.

The results are shown in Fig. 7(a) without any normalisation. Two features are shown, one of which is due to the bulk interaction of the pump light with the lithium niobate, and is present in both experiments ($27.2°$). The second feature at $27.45°$ is only apparent in the presence of the gold film (circles), which suggests that it is plasmonic in origin. This feature is offset from the predicted angle ($27.2°$) by $0.25°$, where we expect the fundamental beam to be optimised for plasmonic coupling. We attribute this to a small calibration error, and infer that this signal corresponds to plasmon-to-plasmon second harmonic generation. The experiment was repeated at several positions on the gold and lithium niobate, with no notable change in signal. This allowed us to conclude that there was no significant damage caused to the gold film by the incident laser radiation. It also allowed us to further confirm that there were no significant contributions from local defects or inhomogeneities. When the incident polarisation is rotated, the coupling to the plasmon is no longer possible, resulting in a reduced signal. However, for the optical nonlinearity, this coincides with tuning off the d_{33} nonlinear coefficient of the lithium niobate substrate, resulting in a reduction in the signal of the optical response.
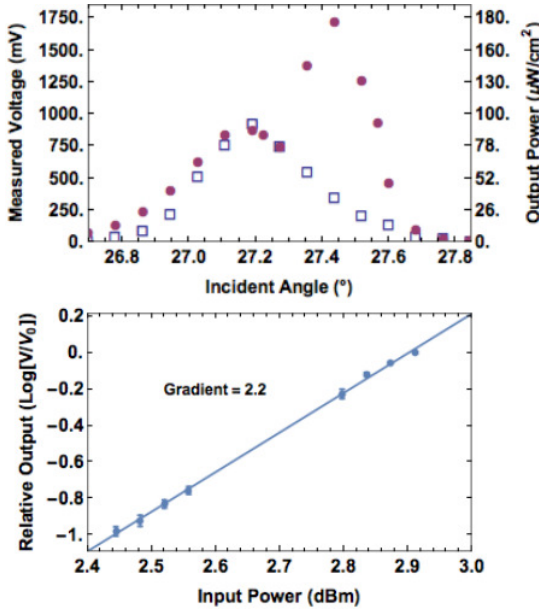

Fig. 7. (a) Harmonic output as a function of pump incident angle. The harmonic output in the absence of gold (squares) is plotted alongside the harmonic output with gold (circles), showing a distinct plasmonic signal. Quadratic dependence of the plasmonic harmonic signal is also plotted (b).

At the peak of the plasmonic signal, the pump power was scanned from 0 to 600 mW, and the signal was confirmed to scale quadratically with the pump power as shown in Fig. 7(b). This is indicative of a second-order nonlinear effect.

In a modelling study of emission and absorption of plasmonic second harmonic generation [18], Vincenti *et al.* conclude that the absorbed harmonic energy surpasses the harmonic radiated into the far field. With a different perspective, from Fig. 7, we observe that, in spite of this absorption, the plasmonic harmonic

signal can still exceed the (non-phase-matched) optical harmonic signal over the short propagation lengths encountered here.

We can further characterise the plasmonic harmonic signal by using the optical signal from the bulk lithium niobate. The harmonic field $E_{2\omega}$ generated by the lithium niobate can be calculated by the equation for the second harmonic generation in a bulk dielectric:

$$E_{2\omega} = i \frac{\omega}{c n_{2\omega}} \chi E_\omega^2 \frac{e^{i\Delta k L} - 1}{i\Delta k} \tag{3}$$

where $\Delta k = 2k_\omega - k_{2\omega}$ is the phase matching condition, L is the interaction length, E_ω is the electric field associated with the pump, and χ is the second-order susceptibility tensor of lithium niobate. Notably, the d_{33} component of the tensor has a value of ≈ 30 pm/V, making lithium niobate an excellent nonlinear optical material. We can rewrite the phase matching condition as:

$$\frac{e^{i\Delta_k L} - 1}{i\Delta_k L} = e^{i\frac{\Delta_k L}{2}} L\,\mathrm{sinc}\left(\frac{\Delta_k L}{2}\right). \tag{4}$$

This can then be related to the input and output intensities by $I = \frac{1}{2}c\epsilon_0 n|E|^2$, giving:

$$I_{2\omega} = \frac{\chi^2 \omega^2}{\epsilon_0 c^3 n_\omega^2 n_{2\omega}} I_\omega^2 L^2 \mathrm{sinc}^2\left(\frac{\Delta_k L}{2}\right). \tag{5}$$

Far from the phase-matched condition, this simplifies to a sinusoidal term with a coherence length of 4.8 μm, from which the second harmonic signals in Fig. 7 can then be calibrated. For an average power of 600 mW, a pulse duration of 6 ps, a repetition of 80 MHz and a focal spot size of 50 μm, the peak optical irradiance is found to be 60 MW/cm^2. Using Eq. 5, the optical harmonic process is found to generate a maximum of 54 μW/cm^2. This calculated irradiance for the optically generated harmonic signal can then be used as an independent reference to calibrate the signal attributed to the surface plasmon response, and convert the second harmonic signals detected in millivolts to optical intensities. This approach was robust against losses induced by optical filtering, and it resulted in a peak power of 107 μW/cm^2, corresponding to the surface plasmon leakage, as shown on the right axis in Fig. 7.

By also relating the detected leakage radiation to the power in the harmonic plasmon at the air/gold interface, the plasmon to plasmon conversion can be determined. The power in the harmonic plasmon is related to the plasmon leakage radiation by the Poynting vector, modified by a plasmon leakage rate. The Poynting vector, integrated across the plasmonic mode profile is given as:

$$|\langle S \rangle| = \frac{1}{4}\frac{1}{\mu_0 c}|E|^2 \mathrm{Re}\left[\frac{1}{n_m k_{z,m}} + \frac{1}{n_2 k_{z,2}}\right], \tag{6}$$

where a constant amplitude E_ω has been assumed. This approximation is valid under the conditions that the pump length is much greater than the propagation length of the leaky plasmon and longer than the coherence length of the nonlinear process (7.5 μm). Subscripts $\{m, 2\}$ correspond to the metal and the air respectively, as before. The leakage rate of the plasmon is calculated as [39]:

$$\alpha = Im\left[r_{1m2} e^{2ik_{z,m}d} 2\left(\frac{\omega}{c}\right)\left(\frac{\epsilon_m \epsilon_2}{\epsilon_m + \epsilon_2}\right)^{3/2}\frac{1}{\epsilon_2 - \epsilon_m}\right], \tag{7}$$

The plasmon leakage given by α competes with the plasmonic loss, given by the imaginary part of the plasmon wavevector

$Im(\beta)$. We can calculate how much of the plasmon is lost as leakage rather than absorption by calculating:

$$\eta = \frac{\int e^{-2Im(\beta)x}(1 - e^{-2\alpha x})dx}{\int e^{-2Im(\beta)x}dx}$$
$$= \frac{\alpha}{(Im(\beta) + \alpha)}. \qquad (8)$$

We find that for $\lambda = 620$ nm, the leakage efficiency is as much as $\eta = 77\%$. The detected power is then simply related to plasmon amplitude by combining Eq. 6 and 8:

$$\eta \int_a | \langle S \rangle | da = P_{2\omega,out} \qquad (9)$$

Using this approach, we find that the signal detected in the far field of 107 $\mu W/cm^2$ corresponds to harmonic field amplitude of 2×10^2 V/m at the metal surface.

To determine the field strength of the plasmon at the fundamental $\lambda = 1240$ nm, the field amplitude E_ω is obtained from the electric field of the optical excitation $E_{opt,\omega}$ and the Fresnel equations where $E_\omega = t_{1m2}E_{opt,\omega}$ and

$$t_{1m2} = \frac{t_{2m}t_{m1}e^{ik_{z,m}d}}{1 + r_{2m}r_{m1}e^{2ik_{z,m}d}}, \qquad (10)$$

and t_{ij} and r_{ij} is given by Eq. 2 as before. This is valid for a collimated or weakly focused pump beam. For a pump plasmon resonance in the IR, this is particularly pertinent due to the narrow resonance, and in practice provides an upper limit on coupling strength. By estimating a $\sim 25\%$ coupling of the 1240 nm pump, an amplitude for the fundamental plasmon can be calculated at 4.8×10^8 V/m. With the corresponding harmonic amplitude of 2×10^2 V/m, a conversion of $E_{2\omega}^2/E_\omega^2 = 2 \times 10^{-13}$ can be estimated.

6. CONCLUSION

Plasmonic second harmonic generation has been observed in a thin gold film, taking advantage of the gold surface nonlinearity, and simultaneously measured against the non-phase-matched optical harmonic response of lithium niobate. This configuration allowed the plasmon to plasmon SHG interaction to be probed and calibrated, leading to a lower bound estimation of the total efficiency as $E_{2\omega}^2/E_\omega^2 = 2 \times 10^{-13}$. Whilst far from being efficient, a nonlinear response from the surface nonlinearity of gold has been elicited that is of a similar order to that of conventional bulk nonlinear materials over much shorter propagation lengths, determined by the absorption losses at the fundamental and the harmonic wavelengths [18]. Materials like lithium niobate of course are amenable to a range of phase-matching techniques which allow the effective interaction length to be extended beyond this range, allowing efficient conversion over larger length scales. This is more difficult in the plasmonic case owing to the nature of the nonlinearity, the plasmonic dispersion and the lower dimensionality of the propagation. Until phase matching can be achieved, efficient conversion remains challenging.

7. ACKNOWLEDGEMENTS

REFERENCES

1. A. V. Zayats, I. I. Smolyaninov, and A. A. Maradudin, "Nano-optics of surface plasmon polaritons," Phys. Rep. **408**, 131–314 (2005).
2. S. Maier, "Plasmonics: Clear for launch," Nat Phys **3**, 301–303 (2007).
3. M. Kauranen and A. V. Zayats, "Nonlinear plasmonics," Nat Photon **6**, 737–748 (2012).
4. J. Butet, P.-F. Brevet, and O. J. F. Martin, "Optical Second Harmonic Generation in Plasmonic Nanostructures: From Fundamental Principles to Advanced Applications," ACS Nano **9**, 10545–10562 (2015).
5. G. Grinblat, M. Rahmani, E. Cortés, M. Caldarola, D. Comedi, S. A. Maier, and A. V. Bragas, "High-Efficiency Second Harmonic Generation from a Single Hybrid ZnO Nanowire/Au Plasmonic Nano-Oligomer," Nano Lett. **14**, 6660–6665 (2014).
6. S.-D. Liu, E. S. P. Leong, G.-C. Li, Y. Hou, J. Deng, J. H. Teng, H. C. Ong, and D. Y. Lei, "Polarization-Independent Multiple Fano Resonances in Plasmonic Nonamers for Multimode-Matching Enhanced Multiband Second-Harmonic Generation," ACS Nano **10**, 1442–1453 (2016).
7. S. Zhang, G.-C. Li, Y. Chen, X. Zhu, S.-D. Liu, D. Y. Lei, and H. Duan, "Pronounced Fano Resonance in Single Gold Split Nanodisks with 15 nm Split Gaps for Intensive Second Harmonic Generation," ACS Nano **10**, 11105–11114 (2016).
8. F. Timpu, N. R. Hendricks, M. Petrov, S. Ni, C. Renaut, H. Wolf, L. Isa, Y. Kivshar, and R. Grange, "Enhanced Second-Harmonic Generation from Sequential Capillarity-Assisted Particle Assembly of Hybrid Nanodimers," Nano Lett. **17**, 5381–5388 (2017).
9. A. T. Georges, "Parametric compensation of power losses in surface plasmon polaritons," J. Opt. Soc. Am. B **30**, 904 (2013).
10. N. B. Grosse, J. Heckmann, and U. Woggon, "Nonlinear Plasmon-Photon Interaction Resolved by k-Space Spectroscopy," Phys. Rev. Lett. **108**, 136802 (2012).
11. M. Mayy, G. Zhu, A. D. Webb, H. Ferguson, T. Norris, V. A. Podolskiy, and M. A. Noginov, "Toward parametric amplification in plasmonic systems: Second harmonic generation enhanced by surface plasmon polaritons," Opt. Express **22**, 7773–7782 (2014).
12. J. C. Quail, J. G. Rako, H. J. Simon, and R. T. Deck, "Optical Second-Harmonic Generation with Long-Range Surface Plasmons," Phys. Rev. Lett. **50**, 1987–1989 (1983).
13. R. Naraoka, H. Okawa, K. Hashimoto, and K. Kajikawa, "Surface plasmon resonance enhanced second-harmonic generation in Kretschmann configuration," Optics Communications **248**, 249–256 (2005).
14. H. J. Simon, D. E. Mitchell, and J. G. Watson, "Optical Second-Harmonic Generation with Surface Plasmons in Silver Films," Phys. Rev. Lett. **33**, 1531–1534 (1974).
15. I. I. Smolyaninov, A. V. Zayats, and C. C. Davis, "Near-field second harmonic generation from a rough metal surface," Phys. Rev. B **56**, 9290–9293 (1997).
16. G. I. Stegeman, J. J. Burke, and D. G. Hall, "Nonlinear optics of long range surface plasmons," Appl. Phys. Lett. **41**, 906–908 (1982).
17. J. Heckmann, M.-E. Kleemann, N. B. Grosse, and U. Woggon, "The dual annihilation of a surface plasmon and a photon by virtue of a three-wave mixing interaction," Opt. Express **21**, 28856–28861 (2013).
18. M. A. Vincenti, D. d. Ceglia, C. D. Angelis, and M. Scalora, "Surface-plasmon excitation of second-harmonic light: emission and absorption," J. Opt. Soc. Am. B **34**, 633–641 (2017).
19. S. S. Jha, "Theory of Optical Harmonic Generation at a Metal Surface," Phys. Rev. **140**, A2020–A2030 (1965).
20. N. Bloembergen, R. K. Chang, S. S. Jha, and C. H. Lee, "Optical Second-Harmonic Generation in Reflection from Media with Inversion Symmetry," Phys. Rev. **174**, 813–822 (1968).
21. J. Rudnick and E. A. Stern, "Second-Harmonic Radiation from Metal Surfaces," Phys. Rev. B **4**, 4274–4290 (1971).
22. J. E. Sipe, V. C. Y. So, M. Fukui, and G. I. Stegeman, "Analysis of second-harmonic generation at metal surfaces," Phys. Rev. B **21**, 4389–4402 (1980).
23. V. Mizrahi and J. E. Sipe, "Phenomenological treatment of surface second-harmonic generation," J. Opt. Soc. Am. B **5**, 660 (1988).
24. P. Guyot-Sionnest and Y. R. Shen, "Bulk contribution in surface second-

harmonic generation," Phys. Rev. B **38**, 7985–7989 (1988).

25. M. Scalora, M. A. Vincenti, D. de Ceglia, V. Roppo, M. Centini, N. Akozbek, and M. J. Bloemer, "Second- and third-harmonic generation in metal-based structures," Phys. Rev. A **82**, 043828 (2010).

26. A. T. Georges, "Theory of nonlinear excitation of surface plasmon polaritons by four-wave mixing," J. Opt. Soc. Am. B **28**, 1603–1606 (2011).

27. S. Palomba, H. Harutyunyan, J. Renger, R. Quidant, N. F. v. Hulst, and L. Novotny, "Nonlinear plasmonics at planar metal surfaces," Phil. Trans. R. Soc. A **369**, 3497–3509 (2011).

28. A. Benedetti, M. Centini, C. Sibilia, and M. Bertolotti, "Engineering the second harmonic generation pattern from coupled gold nanowires," J. Opt. Soc. Am. B **27**, 408–416 (2010).

29. A. Benedetti, M. Centini, M. Bertolotti, and C. Sibilia, "Second harmonic generation from 3d nanoantennas: on the surface and bulk contributions by far-field pattern analysis," Opt. Express **19**, 26752–26767 (2011).

30. A. de Hoogh, A. Opheij, M. Wulf, N. Rotenberg, and L. Kuipers, "Harmonics Generation by Surface Plasmon Polaritons on Single Nanowires," ACS Photonics **3**, 1446–1452 (2016).

31. T. J. Duffin, M. P. Nielsen, F. Diaz, S. Palomba, S. A. Maier, and R. F. Oulton, "Degenerate four-wave mixing in silicon hybrid plasmonic waveguides," Opt. Lett. **41**, 155–158 (2016).

32. F. J. Diaz, G. Li, C. M. d. Sterke, B. T. Kuhlmey, and S. Palomba, "Kerr effect in hybrid plasmonic waveguides," J. Opt. Soc. Am. B **33**, 957–962 (2016).

33. F. X. Wang, F. J. Rodríguez, W. M. Albers, R. Ahorinta, J. E. Sipe, and M. Kauranen, "Surface and bulk contributions to the second-order nonlinear optical response of a gold film," Phys. Rev. B **80**, 233402 (2009).

34. D. Krause, C. W. Teplin, and C. T. Rogers, "Optical surface second harmonic measurements of isotropic thin-film metals: Gold, silver, copper, aluminum, and tantalum," J. Appl. Phys. **96**, 3626–3634 (2004).

35. K. A. O'Donnell and R. Torre, "Characterization of the second-harmonic response of a silver–air interface," New J. Phys. **7**, 154 (2005).

36. P. J. Martin, W. G. Sainty, and R. P. Netterfield, "Enhanced gold film bonding by ion-assisted deposition," Appl. Opt. **23**, 2668–2669 (1984).

37. P. B. Johnson and R. W. Christy, "Optical Constants of the Noble Metals," Phys. Rev. B **6**, 4370–4379 (1972).

38. A. M. Warrier, J. Lin, H. M. Pask, R. P. Mildren, D. W. Coutts, and D. J. Spence, "Highly efficient picosecond diamond Raman laser at 1240 and 1485 nm," Opt. Express **22**, 3325–3333 (2014).

39. H. Raether, *Surface plasmons on smooth and rough surfaces and on gratings*, vol. 111 of *Springer tracts in modern physics* (Springer-Verlag, Berlin ; New York, 1988).

References

[1] A. Sommerfeld. *Ueber die Fortpflanzung elektrodynamischer Wellen längs eines Drahtes*. Annalen der Physik **303**(2), 233 (1899). URL http://onlinelibrary.wiley.com/doi/10.1002/andp.18993030202/abstract.

[2] J. Zenneck. *Über die Fortpflanzung ebener elektromagnetischer Wellen längs einer ebenen Leiterfläche und ihre Beziehung zur drahtlosen Telegraphie*. Annalen der Physik **328**(10), 846 (1907). URL http://onlinelibrary.wiley.com/doi/10.1002/andp.19073281003/abstract.

[3] E. Kretschmann and H. Raether. *Radiative Decay of Non Radiative Surface Plasmons Excited by Light*. Z. Naturforschaung **23A**, 2135 (1968).

[4] A. Otto. *Excitation of nonradiative surface plasma waves in silver by the method of frustrated total reflection*. Zeitschrift für Physik A Hadrons and nuclei **216**(4), 398 (1968). URL https://link.springer.com/article/10.1007/BF01391532.

[5] I. Pockrand, J. D. Swalen, J. G. Gordon, and M. R. Philpott. *Surface plasmon spectroscopy of organic monolayer assemblies*. Surface Science **74**, 237 (1978).

[6] J. G. Gordon and S. Ernst. *Surface plasmons as a probe of the electrochemical interface*. Surface Science **101**, 499 (1980).

[7] M. Righini, A. S. Zelenina, C. Girard, and R. Quidant. *Parallel and selective trapping in a patterned plasmonic landscape*. Nature Physics **3**(7), 477 (2007). URL https://www.nature.com/nphys/journal/v3/n7/full/nphys624.html.

[8] M. Fleischmann, P. J. Hendra, and A. J. McQuillan. *Raman spectra of pyridine adsorbed at a silver electrode*. Chemical Physics Letters **26**(2), 163 (1974). URL http://www.sciencedirect.com/science/article/pii/0009261474853881.

[9] E. Ozbay. *Plasmonics: Merging Photonics and Electronics at Nanoscale Dimensions*. Science **311**(5758), 189 (2006). URL http://www.sciencemag.org/content/311/5758/189.

[10] R. Zia, J. A. Schuller, A. Chandran, and M. L. Brongersma. *Plasmonics: the next chip-scale technology*. Materials Today **9**(7), 20 (2006). URL http://www.sciencedirect.com/science/article/pii/S1369702106715723.

[11] R. Charbonneau, N. Lahoud, G. Mattiussi, and P. Berini. *Demonstration of integrated optics elements based on long-ranging surface plasmon polaritons*. Optics Express **13**(3), 977 (2005). URL http://www.opticsexpress.org/abstract.cfm?URI=oe-13-3-977.

[12] R. Charbonneau, C. Scales, I. Breukelaar, S. Fafard, N. Lahoud, G. Mattiussi, and P. Berini. *Passive Integrated Optics Elements Based on Long-Range Surface Plasmon Polaritons*. Journal of Lightwave Technology **24**(1), 477 (2006). URL http://jlt.osa.org/abstract.cfm?URI=jlt-24-1-477.

[13] S. I. Bozhevolnyi, V. S. Volkov, E. Devaux, J.-Y. Laluet, and T. W. Ebbesen. *Channel plasmon subwavelength waveguide components including interferometers and ring resonators*. Nature **440**(7083), 508 (2006). URL http://www.nature.com/nature/journal/v440/n7083/full/nature04594.html.

[14] S. Jetté-Charbonneau, R. Charbonneau, N. Lahoud, G. Mattiussi, and P. Berini. *Demonstration of Bragg gratings based on long-ranging surface plasmon polariton waveguides*. Optics Express **13**(12), 4674 (2005). URL http://www.opticsexpress.org/abstract.cfm?URI=oe-13-12-4674.

[15] Y. H. Joo, S. H. Song, and R. Magnusson. *Long-range surface plasmon-polariton waveguide sensors with a Bragg grating?in the asymmetric double-electrode structure*. Optics Express **17**(13), 10606 (2009). URL http://www.opticsexpress.org/abstract.cfm?URI=oe-17-13-10606.

[16] P. Berini, R. Charbonneau, S. Jetté-Charbonneau, N. Lahoud, and G. Mattiussi. *Long-range surface plasmon-polariton waveguides and devices in lithium niobate*. Journal of Applied Physics **101**(11), 113114 (2007). URL http://jap.aip.org/resource/1/japiau/v101/i11/p113114_s1.

[17] H. Raether. *Surface plasmons on smooth and rough surfaces and on gratings*, vol. 111 of *Springer tracts in modern physics* (Springer-Verlag, Berlin ; New York, 1988).

[18] G. I. Stegeman and J. J. Burke. *Effects of gaps on long range surface plasmon polaritons*. Journal of Applied Physics **54**(9), 4841 (1983). URL http://jap.aip.org/resource/1/japiau/v54/i9/p4841_s1.

[19] P. Berini. *Air gaps in metal stripe waveguides supporting long-range surface plasmon polaritons*. Journal of Applied Physics **102**(3), 033112 (2007). URL http://jap.aip.org/resource/1/japiau/v102/i3/p033112_s1.

[20] J. B. Khurgin. *How to deal with the loss in plasmonics and metamaterials*. Nature Nanotechnology **10**(1), 2 (2015). URL https://www.nature.com/nnano/journal/v10/n1/full/nnano.2014.310.html.

[21] P. Berini. *Long-range surface plasmon polaritons*. Advances in Optics and Photonics **1**(3), 484 (2009). URL http://aop.osa.org/abstract.cfm?URI=aop-1-3-484.

[22] R. Zia, M. D. Selker, P. B. Catrysse, and M. L. Brongersma. *Geometries and materials for subwavelength surface plasmon modes*. Journal of the Optical Society of America A **21**(12), 2442 (2004). URL http://josaa.osa.org/abstract.cfm?URI=josaa-21-12-2442.

[23] P. Berini. *Figures of merit for surface plasmon waveguides*. Optics Express **14**(26), 13030 (2006). URL http://www.opticsexpress.org/abstract.cfm?URI=oe-14-26-13030.

[24] J. B. Khurgin and G. Sun. *Scaling of losses with size and wavelength in nanoplasmonics and metamaterials*. Applied Physics Letters **99**(21), 211106 (2011). URL http://aip.scitation.org/doi/full/10.1063/1.3664105.

[25] M. Nezhad, K. Tetz, and Y. Fainman. *Gain assisted propagation of surface plasmon polaritons on planar metallic waveguides*. Optics Express **12**(17), 4072 (2004). URL http://www.opticsexpress.org/abstract.cfm?URI=oe-12-17-4072.

[26] P. Berini and I. D. Leon. *Surface plasmon-polariton amplifiers and lasers*. Nature Photonics **6**(1), 16 (2011). URL http://www.nature.com/nphoton/journal/v6/n1/full/nphoton.2011.285.html.

[27] T. Zhang and F. Shan. *Development and Application of Surface Plasmon Polaritons on Optical Amplification*. J. Nanomaterials **2014**, 7:7 (2014). URL http://dx.doi.org/10.1155/2014/495381.

[28] M. A. Noginov, V. A. Podolskiy, G. Zhu, M. Mayy, M. Bahoura, J. A. Adegoke, B. A. Ritzo, and K. Reynolds. *Compensation of loss in propagating surface plasmon polariton by gain in adjacent dielectric medium*. Optics Express **16**(2), 1385 (2008). URL http://www.opticsexpress.org/abstract.cfm?URI=oe-16-2-1385.

[29] I. De Leon and P. Berini. *Theory of surface plasmon-polariton amplification in planar structures incorporating dipolar gain media*. Physical Review B **78**(16), 161401 (2008). URL http://link.aps.org/doi/10.1103/PhysRevB.78.161401.

[30] M. A. Noginov, G. Zhu, M. Mayy, B. A. Ritzo, N. Noginova, and V. A. Podolskiy. *Stimulated Emission of Surface Plasmon Polaritons*. Physical Review Letters **101**(22), 226806 (2008). URL http://link.aps.org/doi/10.1103/PhysRevLett.101.226806.

[31] I. D. Leon and P. Berini. *Amplification of long-range surface plasmons by a dipolar gain medium*. Nature Photonics **4**(6), 382 (2010). URL http://www.nature.com/nphoton/journal/v4/n6/full/nphoton.2010.37.html.

[32] M. C. Gather, K. Meerholz, N. Danz, and K. Leosson. *Net optical gain in a plasmonic waveguide embedded in a fluorescent polymer*. Nature Photonics **4**(7), 457 (2010). URL http://www.nature.com/nphoton/journal/v4/n7/abs/nphoton.2010.121.html.

[33] J. B. Khurgin and G. Sun. *Practicality of compensating the loss in the plasmonic waveguides using semiconductor gain medium*. Applied Physics Letters **100**(1) (2012).

[34] M. T. Hill. *Chapter 9 - Metallic and Plasmonic Nanolasers*. In A. C. B. a. C. J. James J. Coleman, ed., *Semiconductors and Semimetals*, vol. Volume 86, pp. 335–370 (Elsevier, 2012). URL http://www.sciencedirect.com/science/article/pii/B9780123910660000095.

[35] M. T. Hill, M. Marell, E. S. P. Leong, B. Smalbrugge, Y. Zhu, M. Sun, P. J. van Veldhoven, E. J. Geluk, F. Karouta, Y.-S. Oei, R. Nötzel, C.-Z. Ning, and M. K. Smit. *Lasing in metal-insulator-metal sub-wavelength plasmonic waveguides*. Optics Express **17**(13), 11107 (2009). URL http://www.opticsexpress.org/abstract.cfm?URI=oe-17-13-11107.

[36] R. A. Flynn, C. S. Kim, I. Vurgaftman, M. Kim, J. R. Meyer, A. J. Mäkinen, K. Bussmann, L. Cheng, F.-S. Choa, and J. P. Long. *A room-temperature semiconductor spaser operating near 1.5 μm*. Optics Express **19**(9), 8954 (2011). URL https://www.osapublishing.org/oe/abstract.cfm?uri=oe-19-9-8954.

[37] M. A. Noginov, G. Zhu, A. M. Belgrave, R. Bakker, V. M. Shalaev, E. E. Narimanov, S. Stout, E. Herz, T. Suteewong, and U. Wiesner. *Demonstration of a spaser-based nanolaser*. Nature **460**(7259), 1110 (2009). URL http://www.nature.com/nature/journal/v460/n7259/full/nature08318.html.

[38] T. P. H. Sidiropoulos, R. Röder, S. Geburt, O. Hess, S. A. Maier, C. Ronning, and R. F. Oulton. *Ultrafast plasmonic nanowire lasers near the surface plasmon frequency*. Nature Physics **10**(11), 870 (2014). URL http://www.nature.com/nphys/journal/v10/n11/full/nphys3103.html.

[39] T. Pickering, J. M. Hamm, A. F. Page, S. Wuestner, and O. Hess. *Cavity-free plasmonic nanolasing enabled by dispersionless stopped light*. Nature Communications **5** (2014). URL http://www.nature.com/ncomms/2014/140917/ncomms5972/full/ncomms5972.html.

[40] J. B. Khurgin and G. Sun. *Comparative analysis of spasers, vertical-cavity surface-emitting lasers and surface-plasmon-emitting diodes*. Nature Photonics **8**(6), 468 (2014). URL http://www.nature.com/nphoton/journal/v8/n6/full/nphoton.2014.94.html.

[41] L. Lafone, T. P. H. Sidiropoulos, J. M. Hamm, and R. F. Oulton. *Feasibility of GaAs-based metal strip surface plasmon nano-lasers*. IET Optoelectronics **8**(2), 122 (2014).

[42] Q. Zhang, G. Li, X. Liu, F. Qian, Y. Li, T. C. Sum, C. M. Lieber, and Q. Xiong. *A room temperature low-threshold ultraviolet plasmonic nanolaser*. Nature Communications **5**, ncomms5953 (2014). URL https://www.nature.com/articles/ncomms5953.

[43] R. W. Wood. *On a Remarkable Case of Uneven Distribution of Light in a Diffraction Grating Spectrum*. Proceedings of the Physical Society of London **18**(1), 269 (1902). URL http://stacks.iop.org/1478-7814/18/i=1/a=325.

[44] G. I. Stegeman, R. F. Wallis, and A. A. Maradudin. *Excitation of surface polaritons by end-fire coupling*. Optics Letters **8**(7), 386 (1983). URL http://ol.osa.org/abstract.cfm?URI=ol-8-7-386.

[45] D. Pohl and D. Courjon. *Near Field Optics* (Springer, 1993). URL http://www.springer.com/gp/book/9789401048736.

[46] S. A. Maier. *Plasmonics: fundamentals and applications* (New York: Springer, 2007).

[47] F. F. Lu, T. Li, J. Xu, Z. D. Xie, L. Li, S. N. Zhu, and Y. Y. Zhu. *Surface plasmon polariton enhanced by optical parametric amplification in nonlinear hybrid waveguide*. Optics Express **19**(4), 2858 (2011). URL http://www.opticsexpress.org/abstract.cfm?URI=oe-19-4-2858.

[48] A. T. Georges. *Parametric compensation of power losses in surface plasmon polaritons.* Journal of the Optical Society of America B **30**(4), 904 (2013). URL https://www.osapublishing.org/josab/abstract.cfm?uri=josab-30-4-904.

[49] S. S. Jha. *Theory of Optical Harmonic Generation at a Metal Surface.* Physical Review **140**(6A), A2020 (1965). URL http://link.aps.org/doi/10.1103/PhysRev.140.A2020.

[50] M. Fukui, S. Tago, H. Dohi, and O. Tada. *Optical second harmonic generation by long-range surface plasmon polaritons excited by a finite 1-D beam.* Applied Optics **24**(8), 1220 (1985).

[51] C.-C. Tzeng and J. T. Lue. *Nonlinear optical generation from noble metals and aluminum films in various geometric configurations.* Physical Review A **39**(1), 191 (1989). URL http://link.aps.org/doi/10.1103/PhysRevA.39.191.

[52] R. T. Deck and D. Sarid. *Enhancement of second-harmonic generation by coupling to long-range surface plasmons.* Journal of the Optical Society of America **72**(12), 1613 (1982). URL http://www.opticsinfobase.org/abstract.cfm?URI=josa-72-12-1613.

[53] A. R. Davoyan, I. V. Shadrivov, and Y. S. Kivshar. *Quadratic phase matching in nonlinearplasmonic nanoscale waveguides.* Optics Express **17**(22), 20063 (2009). URL http://www.opticsexpress.org/abstract.cfm?URI=oe-17-22-20063.

[54] Z.-j. Wu, X.-k. Hu, Z.-y. Yu, W. Hu, F. Xu, and Y.-q. Lu. *Nonlinear plasmonic frequency conversion through quasiphase matching.* Physical Review B **82**(15), 155107 (2010). URL http://link.aps.org/doi/10.1103/PhysRevB.82.155107.

[55] F. F. Lu, T. Li, X. P. Hu, Q. Q. Cheng, S. N. Zhu, and Y. Y. Zhu. *Efficient second-harmonic generation in nonlinear plasmonic waveguide.* Optics Letters **36**(17), 3371 (2011). URL http://ol.osa.org/abstract.cfm?URI=ol-36-17-3371.

[56] S. B. Hasan, C. Rockstuhl, T. Pertsch, and F. Lederer. *Second-order nonlinear frequency conversion processes in plasmonic slot waveguides.* Journal of the Optical Society of America B **29**(7), 1606 (2012). URL http://josab.osa.org/abstract.cfm?URI=josab-29-7-1606.

[57] F. M. Pigozzo, D. Modotto, and S. Wabnitz. *Second harmonic generation by modal phase matching involving optical and plasmonic modes.* Optics Letters **37**(12), 2244 (2012). URL http://ol.osa.org/abstract.cfm?URI=ol-37-12-2244.

[58] J. E. Sipe, V. C. Y. So, M. Fukui, and G. I. Stegeman. *Analysis of second-harmonic generation at metal surfaces.* Physical Review B **21**(10), 4389 (1980). URL http://link.aps.org/doi/10.1103/PhysRevB.21.4389.

[59] H. J. Simon, D. E. Mitchell, and J. G. Watson. *Optical Second-Harmonic Generation with Surface Plasmons in Silver Films.* Physical Review Letters **33**(26), 1531 (1974). URL http://link.aps.org/doi/10.1103/PhysRevLett.33.1531.

[60] R. Naraoka, H. Okawa, K. Hashimoto, and K. Kajikawa. *Surface plasmon resonance enhanced second-harmonic generation in Kretschmann configuration.* Optics Communications **248**(1–3), 249 (2005). URL http://www.sciencedirect.com/science/article/pii/S0030401804012519.

[61] N. B. Grosse, J. Heckmann, and U. Woggon. *Nonlinear Plasmon-Photon Interaction Resolved by k-Space Spectroscopy*. Physical Review Letters **108**(13), 136802 (2012). URL http://link.aps.org/doi/10.1103/PhysRevLett.108.136802.

[62] J. Heckmann, M.-E. Kleemann, N. B. Grosse, and U. Woggon. *The dual annihilation of a surface plasmon and a photon by virtue of a three-wave mixing interaction*. Optics Express **21**(23), 28856 (2013). URL http://www.opticsexpress.org/abstract.cfm?URI=oe-21-23-28856.

[63] H. J. Simon, R. E. Benner, and J. G. Rako. *Optical second harmonic generation with surface plasmons in piezoelectric crystals*. Optics Communications **23**(2), 245 (1977). URL http://www.sciencedirect.com/science/article/pii/0030401877903170.

[64] J. C. Quail, J. G. Rako, H. J. Simon, and R. T. Deck. *Optical Second-Harmonic Generation with Long-Range Surface Plasmons*. Physical Review Letters **50**(25), 1987 (1983). URL http://link.aps.org/doi/10.1103/PhysRevLett.50.1987.

[65] E. Schmidlin and H. Simon. *Observation of long range surface plasmon decay length by optical second harmonic generation*. Applied Optics **28**(16), 3323 (1989).

[66] I. R. Girling, N. A. Cade, P. V. Kolinsky, G. H. Cross, and I. R. Peterson. *Surface plasmon enhanced SHG from a hemicyanine monolayer*. Journal of Physics D: Applied Physics **19**(11), 2065 (1986). URL http://iopscience.iop.org/0022-3727/19/11/006.

[67] M. Mayy, G. Zhu, A. D. Webb, H. Ferguson, T. Norris, V. A. Podolskiy, and M. A. Noginov. *Toward parametric amplification in plasmonic systems: Second harmonic generation enhanced by surface plasmon polaritons*. Optics Express **22**(7), 7773 (2014). URL http://www.opticsexpress.org/abstract.cfm?URI=oe-22-7-7773.

[68] M. A. Vincenti, D. d. Ceglia, C. D. Angelis, and M. Scalora. *Surface-plasmon excitation of second-harmonic light: emission and absorption*. JOSA B **34**(3), 633 (2017). URL https://www.osapublishing.org/abstract.cfm?uri=josab-34-3-633.

[69] H. S. Won, K. C. Kim, S. H. Song, C.-H. Oh, P. S. Kim, S. Park, and S. I. Kim. *Vertical coupling of long-range surface plasmon polaritons*. Applied Physics Letters **88**(1), 011110 (2006). URL http://apl.aip.org/resource/1/applab/v88/i1/p011110_s1.

[70] J. R. Salgueiro and Y. S. Kivshar. *Nonlinear couplers with tapered plasmonic waveguides*. Optics Express **20**(9), 9403 (2012). URL http://www.opticsexpress.org/abstract.cfm?URI=oe-20-9-9403.

[71] D. K. Gramotnev, K. C. Vernon, and D. F. P. Pile. *Directional coupler using gap plasmon waveguides*. Applied Physics B **93**(1), 99 (2008). URL http://link.springer.com/article/10.1007/s00340-008-3206-0.

[72] Z. Chen, T. Holmgaard, S. I. Bozhevolnyi, A. V. Krasavin, A. V. Zayats, L. Markey, and A. Dereux. *Wavelength-selective directional coupling with dielectric-loaded plasmonic waveguides*. Optics Letters **34**(3), 310 (2009). URL http://ol.osa.org/abstract.cfm?URI=ol-34-3-310.

[73] T. Holmgaard, Z. Chen, S. I. Bozhevolnyi, L. Markey, and A. Dereux. *Design and Characterization of Dielectric-Loaded Plasmonic Directional Couplers*. Journal of Lightwave Technology **27**(24), 5521 (2009). URL http://jlt.osa.org/abstract.cfm?URI=jlt-27-24-5521.

[74] J. Petráček. *Nonlinear directional coupling between plasmonic slot waveguides*. Applied Physics B **112**(4), 593 (2013). URL http://link.springer.com/article/10.1007/s00340-013-5443-0.

[75] F. Liu, Y. Rao, Y. Huang, W. Zhang, and J. Peng. *Coupling between long range surface plasmon polariton mode and dielectric waveguide mode*. Applied Physics Letters **90**(14), 141101 (2007). URL http://apl.aip.org/resource/1/applab/v90/i14/p141101_s1.

[76] Y. Song, J. Wang, Q. Li, M. Yan, and M. Qiu. *Broadband coupler between silicon waveguide and hybrid plasmonic waveguide*. Optics Express **18**(12), 13173 (2010). URL http://www.opticsexpress.org/abstract.cfm?URI=oe-18-12-13173.

[77] Q. Li and M. Qiu. *Structurally-tolerant vertical directional coupling between metal-insulator-metal plasmonic waveguide and silicon dielectric waveguide*. Optics Express **18**(15), 15531 (2010). URL http://www.opticsexpress.org/abstract.cfm?URI=oe-18-15-15531.

[78] X. He, L. Yang, and T. Yang. *Optical nanofocusing by tapering coupled photonic-plasmonic waveguides*. Optics Express **19**(14), 12865 (2011). URL http://www.opticsexpress.org/abstract.cfm?URI=oe-19-14-12865.

[79] G. Magno, M. Grande, V. Petruzzelli, and A. D'Orazio. *High-efficient ultra-short vertical long-range plasmonic couplers*. Journal of Nanophotonics **6**(1), 061609 (2012). URL http://dx.doi.org/10.1117/1.JNP.6.061609.

[80] G. Magno, M. Grande, V. Petruzzelli, and A. D?Orazio. *Numerical analysis of the coupling mechanism in long-range plasmonic couplers at 1.55 µm*. Optics Letters **38**(1), 46 (2013). URL http://ol.osa.org/abstract.cfm?URI=ol-38-1-46.

[81] L. Chen, X. Li, and D. Gao. *An efficient directional coupling from dielectric waveguide to hybrid long-range plasmonic waveguide on a silicon platform*. Applied Physics B **111**(1), 15 (2013). URL http://link.springer.com/article/10.1007/s00340-012-5300-6.

[82] M. Hochberg, T. Baehr-Jones, C. Walker, and A. Scherer. *Integrated plasmon and dielectric waveguides*. Optics Express **12**(22), 5481 (2004). URL http://www.opticsexpress.org/abstract.cfm?URI=oe-12-22-5481.

[83] H. Ditlbacher, N. Galler, D. M. Koller, A. Hohenau, A. Leitner, F. R. Aussenegg, and J. R. Krenn. *Coupling dielectric waveguide modes to surface plasmon polaritons*. Optics Express **16**(14), 10455 (2008). URL http://www.opticsexpress.org/abstract.cfm?URI=oe-16-14-10455.

[84] F. Liu, R. Wan, Y. Li, Y. Huang, Y. Miura, D. Ohnishi, and J. Peng. *Extremely high efficient coupling between long range surface plasmon polariton and dielectric waveguide mode*. Applied Physics Letters **95**(9), 091104 (2009). URL http://scitation.aip.org/content/aip/journal/apl/95/9/10.1063/1.3212145.

[85] S.-Y. Park, J. T. Kim, J.-S. Shin, and S.-Y. Shin. *Hybrid vertical directional coupling between a long range surface plasmon polariton waveguide and a dielectric waveguide*. Optics Communications **282**(23), 4513 (2009). URL http://www.sciencedirect.com/science/article/pii/S0030401809007809.

[86] C. Delacour, S. Blaize, P. Grosse, J. M. Fedeli, A. Bruyant, R. Salas-Montiel, G. Lerondel, and A. Chelnokov. *Efficient Directional Coupling between Silicon and Copper Plasmonic Nanoslot Waveguides: toward Metal-Oxide-Silicon Nanophotonics*. Nano Letters **10**(8), 2922 (2010). URL http://dx.doi.org/10.1021/nl101065q.

[87] F. Liu, Y. Li, R. Wan, Y. Huang, X. Feng, and W. Zhang. *Hybrid Coupling Between Long-Range Surface Plasmon Polariton Mode and Dielectric Waveguide Mode*. Journal of Lightwave Technology **29**(9), 1265 (2011). URL http://www.osapublishing.org/abstract.cfm?uri=jlt-29-9-1265.

[88] Y. Li, F. Liu, Y. Huang, B. Fan, and R. Wan. *Coupling between second-order mode in dielectric waveguide and fundamental mode in long range surface plasmon waveguide*. Optics Communications **289**, 60 (2013). URL http://www.sciencedirect.com/science/article/pii/S0030401812011182.

[89] S. Longhi, G. Della Valle, M. Ornigotti, and P. Laporta. *Coherent tunneling by adiabatic passage in an optical waveguide system*. Physical Review B **76**(20), 201101 (2007). URL http://link.aps.org/doi/10.1103/PhysRevB.76.201101.

[90] A. Kenis, I. Vorobeichik, M. Orenstein, and N. Moiseyev. *Non-evanescent adiabatic directional coupler*. IEEE Journal of Quantum Electronics **37**(10), 1321 (2001).

[91] E. Paspalakis. *Adiabatic three-waveguide directional coupler*. Opt. Commun. **258**(1), 30 (2006).

[92] S. Longhi. *Adiabatic passage of light in coupled optical waveguides*. Physical Review E **73**(2), 026607 (2006). URL http://link.aps.org/doi/10.1103/PhysRevE.73.026607.

[93] Y. Lahini, F. Pozzi, M. Sorel, R. Morandotti, D. N. Christodoulides, and Y. Silberberg. *Effect of Nonlinearity on Adiabatic Evolution of Light*. Physical Review Letters **101**(19), 193901 (2008). URL http://link.aps.org/doi/10.1103/PhysRevLett.101.193901.

[94] F. Dreisow, A. Szameit, M. Heinrich, R. Keil, S. Nolte, A. Tünnermann, and S. Longhi. *Adiabatic transfer of light via a continuum in optical waveguides*. Opt. Lett. **34**(16), 2405 (2009).

[95] A. Salandrino, K. Makris, D. N. Christodoulides, Y. Lahini, Y. Silberberg, and R. Morandotti. *Analysis of a three-core adiabatic directional coupler*. Optics Communications **282**(23), 4524 (2009). URL http://www.sciencedirect.com/science/article/pii/S0030401809007834.

[96] F. Dreisow, M. Ornigotti, A. Szameit, M. Heinrich, R. Keil, S. Nolte, A. Tünnermann, and S. Longhi. *Polychromatic beam splitting by fractional stimulated Raman adiabatic passage*. Appl. Phys. Lett. **95**(26), 53 (2009).

[97] K. Chung, T. J. Karle, M. Rab, A. D. Greentree, and S. Tomljenovic-Hanic. *Broadband and robust optical waveguide devices using coherent tunnelling adiabatic passage.* Optics Express **20**(21), 23108 (2012). URL http://www.opticsexpress.org/abstract. cfm?URI=oe-20-21-23108.

[98] C. Ciret, V. Coda, A. A. Rangelov, D. N. Neshev, and G. Montemezzani. *Planar achromatic multiple beam splitter by adiabatic light transfer.* Optics Letters **37**(18), 3789 (2012). URL https://www.osapublishing.org/abstract.cfm?URI=ol-37-18-3789.

[99] C. Ciret, V. Coda, A. A. Rangelov, D. N. Neshev, and G. Montemezzani. *Broadband adiabatic light transfer in optically induced waveguide arrays.* Physical Review A **87**(1), 013806 (2013). URL http://link.aps.org/doi/10.1103/PhysRevA.87.013806.

[100] A. V. Zayats, I. I. Smolyaninov, and A. A. Maradudin. *Nano-optics of surface plasmon polaritons.* Physics Reports **408**(3–4), 131 (2005). URL http://www.sciencedirect. com/science/article/pii/S0370157304004600.

[101] P. B. Johnson and R. W. Christy. *Optical Constants of the Noble Metals.* Physical Review B **6**(12), 4370 (1972). URL http://link.aps.org/doi/10.1103/PhysRevB.6.4370.

[102] *SCHOTT Advanced Optics | SCHOTT AG* (2017). URL http://www.schott.com/ advanced_optics/.

[103] D. E. Zelmon, D. L. Small, and D. Jundt. *Infrared corrected Sellmeier coefficients for congruently grown lithium niobate and 5 mol.% magnesium oxide ?doped lithium niobate.* Journal of the Optical Society of America B **14**(12), 3319 (1997). URL http://josab.osa.org/abstract.cfm?URI=josab-14-12-3319.

[104] L. J. Mendoza Herrera, D. M. Arboleda, D. C. Schinca, and L. B. Scaffardi. *Determination of plasma frequency, damping constant, and size distribution from the complex dielectric function of noble metal nanoparticles.* Journal of Applied Physics **116**(23), 233105 (2014). URL https://aip.scitation.org/doi/abs/10.1063/1.4904349.

[105] C. Fisher, L. C. Botten, C. G. Poulton, R. C. McPhedran, and C. M. de Sterke. *Efficient butt-coupling of surface plasmons on a silver-air interface.* vol. 9668, pp. 966824–966824–9 (2015). URL http://dx.doi.org/10.1117/12.2202452.

[106] C. Fisher, L. C. Botten, C. G. Poulton, R. C. McPhedran, and C. M. d. Sterke. *Efficient end-fire coupling of surface plasmons in a metal waveguide.* JOSA B **32**(3), 412 (2015). URL http://www.osapublishing.org/abstract.cfm?uri=josab-32-3-412.

[107] C. Fisher, L. C. Botten, C. G. Poulton, R. C. McPhedran, and C. M. d. Sterke. *End-fire coupling efficiencies of surface plasmons for silver, gold, and plasmonic nitride compounds.* JOSA B **33**(6), 1044 (2016). URL http://www.osapublishing.org/abstract. cfm?uri=josab-33-6-1044.

[108] J. Andkjær, S. Nishiwaki, T. Nomura, and O. Sigmund. *Topology optimization of grating couplers for the efficient excitation of surface plasmons.* JOSA B **27**(9), 1828 (2010). URL https://www.osapublishing.org/abstract.cfm?uri=josab-27-9-1828.

[109] N. Rotenberg and J. E. Sipe. *Analytic model of plasmonic coupling: Surface relief gratings.* Physical Review B **83**(4), 045416 (2011). URL https://link.aps.org/doi/10. 1103/PhysRevB.83.045416.

[110] J. Lu, C. Petre, E. Yablonovitch, and J. Conway. *Numerical optimization of a grating coupler for the efficient excitation of surface plasmons at an Ag-SiO$_2$ interface.* JOSA B **24**(9), 2268 (2007). URL https://www.osapublishing.org/abstract.cfm?uri=josab-24-9-2268.

[111] S. T. Koev, A. Agrawal, H. J. Lezec, and V. A. Aksyuk. *An Efficient Large-Area Grating Coupler for Surface Plasmon Polaritons.* Plasmonics **7**(2), 269 (2012). URL https://link.springer.com/article/10.1007/s11468-011-9303-7.

[112] P. Berini. *Plasmon polariton modes guided by a metal film of finite width.* Optics Letters **24**(15), 1011 (1999). URL http://ol.osa.org/abstract.cfm?URI=ol-24-15-1011.

[113] P. Berini. *Plasmon-polariton waves guided by thin lossy metal films of finite width: Bound modes of symmetric structures.* Physical Review B **61**(15), 10484 (2000). URL http://link.aps.org/doi/10.1103/PhysRevB.61.10484.

[114] P. Berini. *Plasmon-polariton waves guided by thin lossy metal films of finite width: Bound modes of asymmetric structures.* Physical Review B **63**(12), 125417 (2001). URL http://link.aps.org/doi/10.1103/PhysRevB.63.125417.

[115] P. Berini, R. Charbonneau, N. Lahoud, and G. Mattiussi. *Characterization of long-range surface-plasmon-polariton waveguides.* Journal of Applied Physics **98**(4), 043109 (2005). URL http://jap.aip.org/resource/1/japiau/v98/i4/p043109_s1.

[116] P. Berini and J. Lu. *Curved long-range surface plasmon-polariton waveguides.* Optics Express **14**(6), 2365 (2006). URL http://www.opticsexpress.org/abstract.cfm?URI=oe-14-6-2365.

[117] I. Breukelaar, R. Charbonneau, and P. Berini. *Long-range surface plasmon-polariton mode cutoff and radiation in embedded strip waveguides.* Journal of Applied Physics **100**(4), 043104 (2006). URL http://jap.aip.org/resource/1/japiau/v100/i4/p043104_s1.

[118] G. Gagnon, N. Lahoud, G. A. Mattiussi, and P. Berini. *Thermally Activated Variable Attenuation of Long-Range Surface Plasmon-Polariton Waves.* Journal of Lightwave Technology **24**(11), 4391 (2006). URL http://jlt.osa.org/abstract.cfm?URI=jlt-24-11-4391.

[119] P. Berini, G. Mattiussi, N. Lahoud, and R. Charbonneau. *Wafer-bonded surface plasmon waveguides.* Applied Physics Letters **90**(6), 061108 (2007). URL http://scitation.aip.org/content/aip/journal/apl/90/6/10.1063/1.2468660.

[120] J. B. Khurgin and G. Sun. *The case for using gap plasmon-polaritons in second-order optical nonlinear processes.* Optics Express **20**(27), 28717 (2012). URL http://www.opticsexpress.org/abstract.cfm?URI=oe-20-27-28717.

[121] Q. Q. Cheng, T. Li, R. Y. Guo, L. Li, S. M. Wang, and S. N. Zhu. *Direct observation of guided-mode interference in polymer-loaded plasmonic waveguide.* Applied Physics Letters **101**(17), 171116 (2012). URL http://apl.aip.org/resource/1/applab/v101/i17/p171116_s1.

[122] T. Holmgaard and S. I. Bozhevolnyi. *Theoretical analysis of dielectric-loaded surface plasmon-polariton waveguides*. Physical Review B **75**(24), 245405 (2007). URL http://link.aps.org/doi/10.1103/PhysRevB.75.245405.

[123] R. F. Oulton, V. J. Sorger, D. A. Genov, D. F. P. Pile, and X. Zhang. *A hybrid plasmonic waveguide for subwavelength confinement and long-range propagation*. Nature Photonics **2**(8), 496 (2008). URL http://www.nature.com/nphoton/journal/v2/n8/full/nphoton.2008.131.html#B17.

[124] P. J. Martin, W. G. Sainty, and R. P. Netterfield. *Enhanced gold film bonding by ion-assisted deposition*. Applied Optics **23**(16), 2668 (1984). URL http://ao.osa.org/abstract.cfm?URI=ao-23-16-2668.

[125] E. Hecht. *Optics* (2017), fifth edition / global edition.. ed.

[126] R. L. Sutherland. *Handbook of nonlinear optics / Richard L. Sutherland.* Optical engineering (Marcel Dekker, Inc.) ; v. 52 (Marcel Dekker, New York, 1996).

[127] S. Palomba, H. Harutyunyan, J. Renger, R. Quidant, N. F. v. Hulst, and L. Novotny. *Nonlinear plasmonics at planar metal surfaces*. Philosophical Transactions of the Royal Society A: Mathematical, Physical and Engineering Sciences **369**(1950), 3497 (2011). URL http://rsta.royalsocietypublishing.org/content/369/1950/3497.

[128] M. Kauranen and A. V. Zayats. *Nonlinear plasmonics*. Nature Photonics **6**(11), 737 (2012). URL http://www.nature.com/nphoton/journal/v6/n11/full/nphoton.2012.244.html#ref7.

[129] R. W. Boyd, Z. Shi, and I. De Leon. *The third-order nonlinear optical susceptibility of gold*. Optics Communications **326**, 74 (2014). URL http://www.sciencedirect.com/science/article/pii/S0030401814002351.

[130] F. J. Diaz, G. Li, C. M. d. Sterke, B. T. Kuhlmey, and S. Palomba. *Kerr effect in hybrid plasmonic waveguides*. JOSA B **33**(5), 957 (2016). URL https://www.osapublishing.org/abstract.cfm?uri=josab-33-5-957.

[131] J. R. Salgueiro and Y. S. Kivshar. *Nonlinear plasmonic directional couplers*. Applied Physics Letters **97**(8), 081106 (2010). URL http://apl.aip.org/resource/1/applab/v97/i8/p081106_s1.

[132] A. R. Davoyan, I. V. Shadrivov, and Y. S. Kivshar. *Nonlinear plasmonic slot waveguides*. Optics Express **16**(26), 21209 (2008). URL http://www.opticsexpress.org/abstract.cfm?URI=oe-16-26-21209.

[133] A. R. Davoyan. *Plasmonic couplers with metal nonlinearities*. Physics Letters A **375**(14), 1615 (2011). URL http://www.sciencedirect.com/science/article/pii/S0375960111002775.

[134] E. Feigenbaum and M. Orenstein. *Plasmon-soliton*. Optics Letters **32**(6), 674 (2007). URL http://ol.osa.org/abstract.cfm?URI=ol-32-6-674.

[135] F. Ye, D. Mihalache, B. Hu, and N. C. Panoiu. *Subwavelength Plasmonic Lattice Solitons in Arrays of Metallic Nanowires*. Physical Review Letters **104**(10), 106802 (2010). URL http://link.aps.org/doi/10.1103/PhysRevLett.104.106802.

[136] A. R. Davoyan, I. V. Shadrivov, and Y. S. Kivshar. *Self-focusing and spatial plasmon-polariton solitons*. Optics Express **17**(24), 21732 (2009). URL http://www.opticsexpress.org/abstract.cfm?URI=oe-17-24-21732.

[137] A. R. Davoyan, I. V. Shadrivov, A. A. Zharov, D. K. Gramotnev, and Y. S. Kivshar. *Nonlinear Nanofocusing in Tapered Plasmonic Waveguides*. Physical Review Letters **105**(11), 116804 (2010). URL http://link.aps.org/doi/10.1103/PhysRevLett.105.116804.

[138] P. Ginzburg, A. Krasavin, and A. V. Zayats. *Cascaded Second-order Surface Plasmon Solitons due to Intrinsic Metal Nonlinearity*. arXiv:1209.3063 (2012). URL http://arxiv.org/abs/1209.3063.

[139] S. H. Crutcher, A. Osei, and A. Biswas. *Nonlinear evolution equations for surface plasmons for nano-focusing at a Kerr/metallic interface and tapered waveguide*. Optics and Laser Technology **44**(4), 1156 (2012). WOS:000300118900068.

[140] G. I. Stegeman, J. J. Burke, and D. G. Hall. *Nonlinear optics of long range surface plasmons*. Applied Physics Letters **41**(10), 906 (1982). URL http://apl.aip.org/resource/1/applab/v41/i10/p906_s1.

[141] A. T. Georges. *Theory of nonlinear excitation of surface plasmon polaritons by four-wave mixing*. JOSA B **28**(7), 1603 (2011). URL https://www.osapublishing.org/abstract.cfm?uri=josab-28-7-1603.

[142] T. J. Duffin, M. P. Nielsen, F. Diaz, S. Palomba, S. A. Maier, and R. F. Oulton. *Degenerate four-wave mixing in silicon hybrid plasmonic waveguides*. Optics Letters **41**(1), 155 (2016). URL https://www.osapublishing.org/abstract.cfm?uri=ol-41-1-155.

[143] S. Palomba and L. Novotny. *Nonlinear Excitation of Surface Plasmon Polaritons by Four-Wave Mixing*. Physical Review Letters **101**(5), 056802 (2008). URL http://link.aps.org/doi/10.1103/PhysRevLett.101.056802.

[144] J. Renger, Q. Romain, V. H. Niek, P. Stefano, and N. Lukas. *Free-Space Excitation of Propagating Surface Plasmon Polaritons by Nonlinear Four-Wave Mixing*. Physical Review Letters **103**(26), 266802 (2009).

[145] J. Renger, R. Quidant, N. van Hulst, and L. Novotny. *Surface-Enhanced Nonlinear Four-Wave Mixing*. Physical Review Letters **104**(4), 046803 (2010). URL http://link.aps.org/doi/10.1103/PhysRevLett.104.046803.

[146] S. Sederberg and A. Y. Elezzabi. *Coherent Visible-Light-Generation Enhancement in Silicon-Based Nanoplasmonic Waveguides via Third-Harmonic Conversion*. Physical Review Letters **114**(22), 227401 (2015). URL http://link.aps.org/doi/10.1103/PhysRevLett.114.227401.

[147] J. L. Coutaz, M. Neviere, E. Pic, and R. Reinisch. *Experimental study of surface-enhanced second-harmonic generation on silver gratings*. Physical Review B **32**(4), 2227 (1985). URL http://link.aps.org/doi/10.1103/PhysRevB.32.2227.

[148] I. I. Smolyaninov, A. V. Zayats, and C. C. Davis. *Near-field second harmonic generation from a rough metal surface*. Physical Review B **56**(15), 9290 (1997). URL http://link.aps.org/doi/10.1103/PhysRevB.56.9290.

[149] A. V. Zayats, T. Kalkbrenner, V. Sandoghdar, and J. Mlynek. *Second-harmonic generation from individual surface defects under local excitation*. Physical Review B **61**(7), 4545 (2000). URL http://link.aps.org/doi/10.1103/PhysRevB.61.4545.

[150] M. I. Stockman, D. J. Bergman, C. Anceau, S. Brasselet, and J. Zyss. *Enhanced Second-Harmonic Generation by Metal Surfaces with Nanoscale Roughness: Nanoscale Dephasing, Depolarization, and Correlations*. Physical Review Letters **92**(5), 057402 (2004). URL http://link.aps.org/doi/10.1103/PhysRevLett.92.057402.

[151] W. Fan, S. Zhang, N.-C. Panoiu, A. Abdenour, S. Krishna, Osgood, K. J. Malloy, and S. R. J. Brueck. *Second Harmonic Generation from a Nanopatterned Isotropic Nonlinear Material*. Nano Letters **6**(5), 1027 (2006). URL http://dx.doi.org/10.1021/nl0604457.

[152] K. Li, M. I. Stockman, and D. J. Bergman. *Enhanced second harmonic generation in a self-similar chain of metal nanospheres*. Physical Review B **72**(15), 153401 (2005). URL http://link.aps.org/doi/10.1103/PhysRevB.72.153401.

[153] K. Thyagarajan, S. Rivier, A. Lovera, and O. J. Martin. *Enhanced second-harmonic generation from double resonant plasmonic antennae*. Optics Express **20**(12), 12860 (2012). URL http://www.opticsexpress.org/abstract.cfm?URI=oe-20-12-12860.

[154] G. Hajisalem, A. Ahmed, Y. Pang, and R. Gordon. *Plasmon hybridization for enhanced nonlinear optical response*. Optics Express **20**(28), 29923 (2012). URL http://www.opticsexpress.org/abstract.cfm?URI=oe-20-28-29923.

[155] N. Bloembergen, R. K. Chang, S. S. Jha, and C. H. Lee. *Optical Second-Harmonic Generation in Reflection from Media with Inversion Symmetry*. Physical Review **174**(3), 813 (1968). URL http://link.aps.org/doi/10.1103/PhysRev.174.813.

[156] J. Rudnick and E. A. Stern. *Second-Harmonic Radiation from Metal Surfaces*. Physical Review B **4**(12), 4274 (1971). URL http://link.aps.org/doi/10.1103/PhysRevB.4.4274.

[157] V. Mizrahi and J. E. Sipe. *Phenomenological treatment of surface second-harmonic generation*. Journal of the Optical Society of America B **5**(3), 660 (1988). URL https://www.osapublishing.org/josab/abstract.cfm?uri=josab-5-3-660.

[158] P. Guyot-Sionnest and Y. R. Shen. *Bulk contribution in surface second-harmonic generation*. Physical Review B **38**(12), 7985 (1988). URL http://link.aps.org/doi/10.1103/PhysRevB.38.7985.

[159] D. Krause, C. W. Teplin, and C. T. Rogers. *Optical surface second harmonic measurements of isotropic thin-film metals: Gold, silver, copper, aluminum, and tantalum*. Journal of Applied Physics **96**(7), 3626 (2004). URL http://scitation.aip.org/content/aip/journal/jap/96/7/10.1063/1.1786341.

[160] F. X. Wang, F. J. Rodríguez, W. M. Albers, R. Ahorinta, J. E. Sipe, and M. Kauranen. *Surface and bulk contributions to the second-order nonlinear optical response of a gold film*. Physical Review B **80**(23), 233402 (2009). URL http://link.aps.org/doi/10.1103/PhysRevB.80.233402.

[161] K. A. O'Donnell and R. Torre. *Characterization of the second-harmonic response of a silver–air interface*. New Journal of Physics **7**(1), 154 (2005). URL http://iopscience.iop.org/1367-2630/7/1/154.

[162] I. I. Smolyaninov, D. L. Mazzoni, J. Mait, and C. C. Davis. *Experimental study of surface-plasmon scattering by individual surface defects*. Physical Review B **56**(3), 1601 (1997). URL http://link.aps.org/doi/10.1103/PhysRevB.56.1601.

[163] A. Yariv. *Optical waves in crystals : propagation and control of laser radiation*. Wiley series in pure and applied optics (Wiley, New York, 1984).

[164] R. S. Weis and T. K. Gaylord. *Lithium niobate: Summary of physical properties and crystal structure*. Applied Physics A Solids and Surfaces **37**(4), 191 (1985).

[165] V. G. Dmitriev, G. G. Gurzadyan, and D. N. Nikogosyan. *Handbook of Nonlinear Optical Crystals* (Springer, 2013).

[166] A. M. Warrier, J. Lin, H. M. Pask, R. P. Mildren, D. W. Coutts, and D. J. Spence. *Highly efficient picosecond diamond Raman laser at 1240 and 1485 nm*. Optics Express **22**(3), 3325 (2014). URL http://www.opticsexpress.org/abstract.cfm?URI=oe-22-3-3325.

[167] R. W. Boyd. *Nonlinear Optics* (Academic Press, 2003).

[168] J. A. Armstrong, N. Bloembergen, J. Ducuing, and P. S. Pershan. *Interactions between Light Waves in a Nonlinear Dielectric*. Physical Review **127**(6), 1918 (1962). URL http://link.aps.org/doi/10.1103/PhysRev.127.1918.

[169] M. Okada, K. Takizawa, and S. Ieiri. *Second harmonic generation by periodic laminar structure of nonlinear optical crystal*. Optics Communications **18**(3), 331 (1976). URL http://www.sciencedirect.com/science/article/pii/0030401876901449.

[170] D. E. Thompson, J. D. McMullen, and D. B. Anderson. *Second-harmonic generation in GaAs ''stack of plates'' using high-power CO2 laser radiation*. Applied Physics Letters **29**(2), 113 (1976). URL http://aip.scitation.org/doi/abs/10.1063/1.88989.

[171] A. Feisst and P. Koidl. *Current induced periodic ferroelectric domain structures in LiNbO3 applied for efficient nonlinear optical frequency mixing*. Applied Physics Letters **47**(11), 1125 (1985). URL http://aip.scitation.org/doi/abs/10.1063/1.96349.

[172] G. A. Magel, M. M. Fejer, and R. L. Byer. *Quasi-phase-matched second-harmonic generation of blue light in periodically poled LiNbO3*. Applied Physics Letters **56**(2), 108 (1990). URL http://aip.scitation.org/doi/10.1063/1.103276.

[173] D. H. Jundt, G. A. Magel, and M. M. Fejer. *Periodically poled LiNbO3 for high-efficiency second-harmonic generation*. Applied Physics Letters **59**(21), 2657 (1991). URL http://aip.scitation.org/doi/abs/10.1063/1.105929.

[174] S. Matsumoto, E. J. Lim, H. M. Hertz, and M. M. Fejer. *Quasiphase-matched second harmonic generation of blue light in electrically periodically-poled lithium tantalate waveguides*. Electronics Letters **27**(22), 2040 (1991).

[175] J. Webjorn, V. Pruneri, P. S. J. Russell, J. R. M. Barr, and D. C. Hanna. *Quasi-phase-matched blue light generation in bulk lithium niobate, electrically poled via periodic liquid electrodes.* Electronics Letters **30**(11), 894 (1994).

[176] L. E. Myers, R. C. Eckardt, M. M. Fejer, R. L. Byer, W. R. Bosenberg, and J. W. Pierce. *Quasi-phase-matched optical parametric oscillators in bulk periodically poled LiNbO₃.* JOSA B **12**(11), 2102 (1995). URL http://www.osapublishing.org/abstract.cfm?uri=josab-12-11-2102.

[177] A. C. Muir. *Interactions of Single-Crystal Lithium Niobate Surfaces with Ultra-Violet Laser Radiation.* Ph.D. thesis, University of Southampton (2008).

[178] A. Boes, D. Yudistira, T. Crasto, H. Steigerwald, V. Sivan, T. Limboeck, J. Friend, S. Mailis, E. Soergel, and A. Mitchell. *Ultraviolet laser induced domain inversion on chromium coated lithium niobate crystals.* Optical Materials Express **4**(2), 241 (2014). URL http://www.opticsinfobase.org/ome/abstract.cfm?URI=ome-4-2-241.

[179] F. Lopez-Tejeira, S. G. Rodrigo, L. Martín-Moreno, F. J. García-Vidal, E. Devaux, T. W. Ebbesen, J. R. Krenn, I. P. Radko, S. I. Bozhevolnyi, M. U. González, J. C. Weeber, and A. Dereux. *Efficient unidirectional nanoslit couplers for surface plasmons.* Nature Physics **3**(5), 324 (2007). URL http://www.nature.com/nphys/journal/v3/n5/full/nphys584.html.

[180] R. P. Mildren and J. Rabeau. *Optical engineering of diamond / edited by Richard P. Mildren and James R. Rabeau.* (Wiley-VCH Verlag GmbH & CoKGaA, Weinheim, 2013).

[181] H. A. Haus and W. Huang. *Coupled-mode theory.* Proceedings of the IEEE **79**(10), 1505 (1991).

[182] W.-P. Huang. *Coupled-mode theory for optical waveguides: an overview.* Journal of the Optical Society of America A **11**(3), 963 (1994). URL http://josaa.osa.org/abstract.cfm?URI=josaa-11-3-963.

[183] *Gersteltec.* URL http://www.gersteltec.ch/su-8-Photoresists/.

[184] *SU-8 and PMMA for optical waveguides - MicroChem.* URL http://www.microchem.com/Appl-IIIVs-Waveguides.htm.

[185] T. Tamir and R. C. Alferness. *Guided-wave optoelectronics / Theodor Tamir (ed.) ; with contributions by R.C. Alferness ... [et al.].* Springer series in electronics and photonics ; v. 26 (Springer-Verlag, Berlin ; New York, 1990), 2nd ed. ed.

[186] R. Menchon-Enrich, A. Benseny, V. Ahufinger, A. D. Greentree, T. Busch, and J. Mompart. *Spatial adiabatic passage: a review of recent progress* (2016). URL http://arxiv.org/abs/1602.06658.

[187] N. V. Vitanov, T. Halfmann, B. W. Shore, and K. Bergmann. *Laser-Induced Population Transfer by Adiabatic Passage Techniques.* Annual Review of Physical Chemistry **52**(1), 763 (2001). URL http://www.annualreviews.org/doi/abs/10.1146/annurev.physchem.52.1.763.

[188] N. V. Vitanov, A. A. Rangelov, B. W. Shore, and K. Bergmann. *Stimulated Raman adiabatic passage in physics, chemistry and beyond*. arXiv:1605.00224 [quant-ph] (2016). ArXiv: 1605.00224, URL http://arxiv.org/abs/1605.00224.

[189] J. H. Cole, A. D. Greentree, L. C. L. Hollenberg, and S. Das Sarma. *Spatial adiabatic passage in a realistic triple well structure*. Physical Review B **77**(23), 235418 (2008). URL http://link.aps.org/doi/10.1103/PhysRevB.77.235418.

[190] T. Opatrný and K. K. Das. *Conditions for vanishing central-well population in triple-well adiabatic transport*. Physical Review A **79**(1), 012113 (2009). URL http://link.aps.org/doi/10.1103/PhysRevA.79.012113.

[191] L. M. Jong, A. D. Greentree, V. I. Conrad, L. C. L. Hollenberg, and D. N. Jamieson. *Coherent tunneling adiabatic passage with the alternating coupling scheme*. Nanotechnology **20**(40), 405402 (2009). URL http://iopscience.iop.org/0957-4484/20/40/405402.

[192] A. D. Greentree, J. H. Cole, A. R. Hamilton, and L. C. L. Hollenberg. *Coherent electronic transfer in quantum dot systems using adiabatic passage*. Physical Review B **70**(23), 235317 (2004). URL http://link.aps.org/doi/10.1103/PhysRevB.70.235317.

[193] L. C. L. Hollenberg, A. D. Greentree, A. G. Fowler, and C. J. Wellard. *Two-dimensional architectures for donor-based quantum computing*. Physical Review B **74**(4), 045311 (2006). URL http://link.aps.org/doi/10.1103/PhysRevB.74.045311.

[194] L. M. Jong and A. D. Greentree. *Interferometry using spatial adiabatic passage in quantum dot networks*. Physical Review B **81**(3), 035311 (2010). URL http://link.aps.org/doi/10.1103/PhysRevB.81.035311.

[195] H. Suchowski, D. Oron, A. Arie, and Y. Silberberg. *Geometrical representation of sum frequency generation and adiabatic frequency conversion*. Physical Review A **78**(6), 063821 (2008). URL http://link.aps.org/doi/10.1103/PhysRevA.78.063821.

[196] H. Suchowski, B. D. Bruner, A. Ganany-Padowicz, I. Juwiler, A. Arie, and Y. Silberberg. *Adiabatic frequency conversion of ultrafast pulses*. Applied Physics B **105**(4), 697 (2011). URL http://link.springer.com/article/10.1007/s00340-011-4591-3.

[197] G. Porat and A. Arie. *Efficient two-process frequency conversion through a dark intermediate state*. Journal of the Optical Society of America B **29**(10), 2901 (2012). URL http://josab.osa.org/abstract.cfm?URI=josab-29-10-2901.

[198] G. Porat, Y. Silberberg, A. Arie, and H. Suchowski. *Two photon frequency conversion*. Optics Express **20**(4), 3613 (2012). URL http://www.opticsexpress.org/abstract.cfm?URI=oe-20-4-3613.

[199] E. A. Shapiro, V. Milner, C. Menzel-Jones, and M. Shapiro. *Piecewise Adiabatic Passage with a Series of Femtosecond Pulses*. Physical Review Letters **99**(3), 033002 (2007). URL http://link.aps.org/doi/10.1103/PhysRevLett.99.033002.

[200] E. A. Shapiro, V. Milner, and M. Shapiro. *Complete transfer of populations from a single state to a preselected superposition of states using piecewise adiabatic passage: Theory*. Phys. Rev. A **79**(2), 023422 (2009). URL http://journals.aps.org/pra/abstract/10.1103/PhysRevA.79.023422.

[201] J. A. Vaitkus and A. D. Greentree. *Digital three-state adiabatic passage*. Phys. Rev. A **87**(6) (2013).

[202] K. M. Davis, K. Miura, N. Sugimoto, and K. Hirao. *Writing waveguides in glass with a femtosecond laser*. Opt. Lett. **21**(21), 1729 (1996). URL http://ol.osa.org/abstract. cfm?URI=ol-21-21-1729.

[203] C. B. Schaffer, A. Brodeur, J. F. García, and E. Mazur. *Micromachining bulk glass by use of femtosecond laser pulses with nanojoule energy*. Opt. Lett. **26**(2), 93 (2001).

[204] S. M. Eaton, H. Zhang, M. L. Ng, J. Li, W.-J. Chen, S. Ho, and P. R. Herman. *Transition from thermal diffusion to heat accumulation in high repetition rate femtosecond laser writing of buried optical waveguides*. Opt. Express **16**(13), 9443 (2008).

[205] C. T. Miese, M. J. Withford, and A. Fuerbach. *Femtosecond laser direct-writing of waveguide Bragg gratings in a quasi cumulative heating regime*. Opt. Express **19**(20), 19542 (2011). URL http://www.ncbi.nlm.nih.gov/pubmed/ 21996895$\delimiter"026E30F$nhttp://www.opticsinfobase.org/abstract.cfm?URI= oe-19-20-19542.